Roger W. Burke
Keith D. Stolzenbach

Free Surface Flow Through Salt Marsh Grass

MIT Sea Grant
College Program

Massachusetts
Institute of Technology
Cambridge, MA 02139

MITSG 83-16
June 1983

FREE SURFACE FLOW THROUGH SALT MARSH GRASS

by

Roger W. Burke
Keith D. Stolzenbach

MIT Sea Grant
College Program

Massachusetts Institute
of Technology
Cambridge, MA 02139

Index No.:
Grant No. NA81AA-D-00069
Project No R/C-21
MITSG 83-16
June 1983

ABSTRACT

A numerical model is presented for predicting the vertical variation of flow through and above large obstructions, with special emphasis on tidally inundated marsh grass. Because the grass may extend through the depth of the water column, thus affecting the stress at the air–water interface, the model has the capability to extend the calculations into the overlying air layer. The model is able to compute the simultaneous vertical distribution of both horizontal velocity components.

A scaling analysis of the governing momentum equations for typical salt marsh geometrics shows that the acceleration terms are generally negligible compared to the vertical transport terms. With this approximation, the momentum equation reduces to a local force balance between the vertical momentum transport, surface pressure gradient, and vegetative drag force. A review of previous obstructed flow models solving this equation reveals that these models are generally unsuited to the purposes of this study, primarily because of an inability to provide an a priori parameterization for the vertical turbulent momentum transport, thus motivating the development of a different approach.

The two equation $k-\varepsilon$ technique parameterizes the turbulent stress using a turbulent diffusivity scheme, in which the turbulent length and velocity scales are determined from differential transport equations for the turbulent kinetic energy (k) and viscous dissipation (ε), thus allowing for the influence of diffusion on the turbulent scales, as well as the presence of more than one characterizing length scale. Modifications of the low Reynold's number form of the model (Jones & Launder, 1972, 1973) account for the additional force and turbulent energy flux caused by obstructions. The resulting model equations are solved using a finite control volume technique.

Model predictions compare favorably with a variety of analytical and experimental results for a variety of cases, including non-obstructed open channel and Couette flow, wind tunnel studies of flow through circular cylinders, a water flume study of flow through plastic strips, and field studies of flow through bean and corn crops. The model coefficients are held fixed in all comparisons, demonstrating the predictive abilities of the model for obstructed flow processes.

A study of free surface flow properties conducted in Great Sippewissett Marsh, in Falmouth, Massachusetts, provided the context for an application of the model to tidally inundated marsh grass. The measurements taken include marsh topography, wind speed and direction, water elevation at the marsh boundary, and vertical profiles of horizontal velocity at a number of locations within the marsh grass study area. The observed and predicted velocity profiles are in generally good agreement, although it was necessary to adjust the values of the grass density, which were not measured independently.

Dimensional analysis shows that the obstructed flow processes are generally dependent on three parameters, relating to the grass density (a), grass height (h_g), and the relative importance of wind stress to surface pressure. Under many conditions, the dimensionless grouping $C_d h_g a$, where C_d is the drag coefficient, is the only relevant parameter governing obstructed flows. Sensitivity studies demonstrate the relationships between the governing parameters and the vertical distribution of various variables, including velocity, kinetic energy, and dissipation.

ACKNOWLEDGMENTS

This study has been supported by a Whitaker Health Science Fund Fellowship and by a grant from NOAA, Department of Commerce, the Office of Sea Grant, Grant No. 04-7-158-44079. The research was performed at the R.M. Parsons Laboratory for Water Resources and Hydrodynamics, Department of Civil Engineering, by Mr. Roger W. Burke, Research Assistant, under the supervision of Dr. Keith D. Stolzenbach, Associate Professor.

The authors would like to thank Jayne Fifield, Bill Nuttle, and Mark Schaefer for their help in collecting the field data and for their suggestions about its meaning. We would also like to acknowledge the contribution of Dr. Harry F. Hemond, Associate Professor of Civil Engineering, for his assistance in the field work and for his general guidance of the marsh hydrology research efforts.

RELATED PUBLICATIONS:

Burke, R.W., 1979. Infiltration in a New England salt marsh. Master of Science thesis, Massachusetts Institute of Technology, Cambridge, Ma.

Burke, R.W., H.F. Hemond and K.D. Stolzenbach, 1980. An infiltrometer to measure seepage in salt marsh soils. In P. Hamilton, ed., Estuarine and Wetland Processes - With an Emphasis on Modeling. Plenum Press.

Burke, R.W., 1982. Free surface flow through salt marsh grass. Ph.D. thesis, Massachusetts Institute of Technology, Cambridge, Ma.

Burke, R.W. and K.D. Stolzenbach. A second order turbulence model of canopy flow. (in preparation)

Burke, R.W. and K.D. Stolzenbach. Measurement of free surface flow through salt marsh grass. (in preparation)

Burke, R.W. and K.D. Stolzenbach. Conveyance and friction relationship for canopy flows. (in preparation)

Fifield, J.F., 1981. Peat hydrology in two New England salt marshes: A field and model study. Master of Science thesis, Massachusetts Institute of Technology, Cambridge, Ma.

Fifield, J.L., W.K. Nuttle, and H.F. Hemond. Hydraulic properties of salt marsh peat. Water Resources Research (submitted).

Hemond, H.F., 1982. A low cost multi-channel recording piezometer system for wetland research. Water Resources Research. 18(1):182-186.

Hemond, H.F., and R. Burke, 1981. A device for the measurement of infiltration in intermittently flooded wetlands. Limnol. Oceanogr. 26(4):795-800.

Hemond, H.F., and J.L. Fifield, 1982. Subsurface flow in salt marsh peat: A model and field study. Limnol. Oceanogr. 27(1):126-136.

Hemond, H.F., W.K. Nuttle, R.W. Burke, and K.D. Stolzenbach. Surface infiltration in salt marshes: Theory and measurement. Water Resources Research (submitted).

Nuttle, W.K. 1982. The flow of water in salt marsh peat. Master of Science thesis, Massachusetts Institute of Technology, Cambridge, Ma.

Schaefer, M. and K.D. Stolzenbach. A photographic technique for the measurement of vegetation density. (in preparation)

---

copies of the above related publications may be ordered through:

Sea Grant Information Center
MIT Sea Grant College Program
Room E38-320
Massachusetts Institute of Technology
77 Massachusetts Avenue
Cambridge, MA 02139
(617)253-5944

TABLE OF CONTENTS

CHAPTER I

INTRODUCTION

Salt marshes are essentially inter-tidal systems, bordered on one side by the land, and on the other by an estuary, or the sea. A network of meandering tidal creeks, similar in appearance to a river system, connects the marsh to the open water. During flood tide, if it is of sufficient height, the water overtops the creek banks, flowing out laterally to inundate the surrounding marsh surface and it's inhabitants, the most influencial species of which is usually a type of grass called Spartina alterniflora.

The central theme of this study is to understand, and be able to predict, the vertical variation of flow through and above tidally inundated marsh grass under the combined forces of a free surface pressure gradient and wind stress. Specifically, a numerical model is proposed for simulating the local flow processes in flooded marsh grass. Such a model should permit the vertical velocity distribution to be computed for specified local values of grass density and height, free surface slope, and for the wind stress at the water surface. Since the marsh grass may extend into the air, thus affecting the stress at the air-water interface, the model should have the ability to extend the calculations into the air flow above the water. In this case, the wind velocity at a given height would be specified. The

model should be able to compute the simultaneous distribution of both horizontal velocity components.

1.1 Motivation and Background

Water motion is important to the life processes of aquatic vegetation, such as marsh grass. The microclimate in which the plants grow is regulated by the exchange of momentum, heat, and mass between the water and biologically active plant parts. This exchange enhances the uptake of nutrients, as well as the removal of gases and other substances produced during transpiration (Gerard and Mann, 1979). The rates of exchange depend strongly on the characteristics of the water motion, especially on the level of turbulence (Andersons and Charters, 1982). For these reasons, an understanding of the turbulent flow processes in the plant environment is important not only to aquatic plants, but also to terrestial systems, having applications in biology, agriculture, and forestry.

In addition to it's role in regulating the plant's microenvironment, the motion of the tidal surface waters is largely responsible for the transport of crucial nutrients in the marsh, and in the determination of residence times and concentrations of other constituents. Surface flow of water through the marsh system transports detrital material (Haines, 1976), metals (Windom, 1975), as well as a variety of other materials which may be vital or deleterious to marsh-estuarine or coastal productivity. The tidal regime may also

affect the productivity of the marshes indirectly through it's influence on such factors as salinity, pH, temperature, and light intensity. Steever et. al. (1976) has documented a close correlation between standing crop productivity and tidal range in a survey of Connecticut marshes.

Flushing by surface flow is believed to affect the response of the marsh system to artificial enrichment with fertilizers, perhaps by influencing nutrient retention (Valiela et. al., 1973; Banus et. al., 1975). The ability of an estuary or marsh to receive treated sewage will depend, among other factors, on the flushing rate by surface waters.

A subject of current debate is whether salt marshes are sources or sinks of substances such as organic carbon, inorganic nutrients, and trace metals (Nixon, 1980). Some marshes have been found to be regions of rapid deposition, such as the Flax Pond Marsh of New York (Woodwell et. al., 1977). Others, such as Great Sippewissett Marsh in Massachusetts, have been observed as being sources of various materials for the outlying open waters (Valiela et. al., 1978). Because of the great variability of the hydraulic features of coastal marshes, no single answer will fit all situations. Efforts to understand the direction of material transport in marsh systems must consider the patterns and magnitudes of circulation in the marsh, as well as between the marsh and the outlying areas.

Despite the importance of a knowledge of water transport in the

marsh ecosystem, both to research and management practice, this problem has received little attention in the past. While considerable effort has been directed towards large scale circulations in coastal bays and estuaries (Wang, S.Y., et.al., 1980), relatively little work has been done on flow models applicable to salt marsh conditions. The surface flow in a salt marsh is primarily unidirectional in the channels and creeks within the marsh, while spreading out laterally as a two-dimensional flow across the shallow grassy areas. Although tidal circulation models have been applied to the flow in a marsh channel system (Fischer, 1977), and to the flow over un-vegetated tidal flats (Abbot, 1969; Leendertse, 1970; Herrling, 1976; Holster, 1980), there is only one known previous model of lateral flow in marshes, done by Reid and Whitaker (1976). It is important to note that the limitation on this type of modeling effort has been a lack of basic knowledge regarding the hydraulic properties of surface flows through dense marsh grass. Of particular importance is the lack of information relating the turbulent flow structure to the properties of the marsh vegetation.

While there is no known study of flow resistance through marsh grass, there have been investigations of flow through other kinds of vegetation, such as that found in rivers. The value of Manning's n has been defined for several types of channel linings (Barnes, 1967). Ree and Palmer (1945) give design curves for vegetated channels found in the U.S. A summary of their results is presented in Chow (1954), as well as in Henderson (1966). In a later study, Ree and Crow (1977)

give similar design curves for earth channels of small slope planted to wheat, cotton, and other plants. These studies treat the vegetation as large boundary roughness, and provide no information about the flow within the obstructions.

In addition to the studies of vegetation resistance in rivers, considerable work, both experimental and theoretical, has been done on the subject of canopy flow fields, which are wind fields as affected by a crop or forest. Early efforts in this area are summarized by Geiger (1950). Measurements of flow characteristics have been made over various crops, such as beans (Thom, 1971), corn (Shaw et. al., 1974), as well as over forests (Oliver, 1971). Mathematicl models for the flow of air through canopies have been proposed by Inoue (1963), Cowan (1968), and Kondo (1976). In these models, the transport of momentum is parameterized by conventional eddy viscosity or mixing-length hypotheses. Higher order closure models, which solve for the individual stresses, have also been constructed (Wilson and Shaw, 1976). The obstructed flow models mentioned above are reviewed in Chapter Two, which finds these schemes generally inappropriate to the purposes of this study, prompting the development of a new approach to model obstructed flow processes.

1.2 Scope and Major Conclusions of this Study

The objective of this study is to create a computational methodology for determining the vertical distribution of flow above and within obstructions, such as tidally inundated marsh grass. A brief outline of the steps followed in the model development is given below through a description of the topics covered in each chapter of this report. Also given is a summary of the most important conclusions reached in each chapter.

The full three dimensional equations governing obstructed flow are introduced in Chapter Two. A scaling analysis of these equations, relating to typical New England marsh geometries, is then presented. This analysis shows that for flow configurations usually encountered in New England marshes the local acceleration and convective terms are generally negligible compared to the vertical transport terms. With this result, the surface flow regime in inundated marshes reduces to a local balance between the surface slope pressure gradient, vertical momentum transfer, and the drag force on the marsh grass.

Chapter Two also presents a literature review of previous empirical relationships for the drag force as a function of the obstructions and for the momentum transport. On the basis of this review it is concluded that previous obstructed flow models contain several features making them unsuited to the objectives of this study. First, these models generally take no account of the influence of diffusion on the turbulent flow structure. Second, the turbulent

length scale is almost always assumed proportional to a single scale, when in fact there are generally two length scales in obstructed flows, one associated with the depth of the obstructions, the other with their density. Third, previous obstructed flow models, with one exception (Reid and Whitaker, 1976), were designed for flow through vegetative canopies, and as such do not account for the presence of a free surface, such as will exist in tidally inundated marshes.

Chapter Three explains the concepts behind the two equations $k-\varepsilon$ closure approach proposed in this study to parameterize the momentum transport. The adaptations necessary to handle the presence of obstructions are developed; these include the addition of terms representing the production of turbulent kinetic energy by the obstructions, as well as a term accounting for the effect of the obstructions on the vertical momentum equation. Similar to the scaling analysis performed for the momentum equation, it is shown that the acceleration and horizontal gradient terms in the differential transport equations for the kinetic energy (k) and the dissipation (ε) are negligible compared to the vertical transport terms.

Following the model alterations, Chapter Two describes the iterative finite control volume technique used to solve the model equations. Model predictions are then compared with analytical and experimental results for a wide variety of cases, including non-obstructed open channel and Couette flow, wind tunnel studies of flow through circular cylinders, a water flume investigation of flow through

plastic strips, and field studies of flow through vegetative canopies such as beans and corn. The observed and predicted distributions of velocity, as well as stress in some instances, are found to be in generally good agreement. Also illustrated in this chapter is the model's ability to compute the distribution of more general turbulent properties such as turbulent kinetic energy and dissipation. The model coefficients are held fixed in all comparisons cited above, demonstrating the predictive abilities of the model for obstructed flow processes.

Chapter Four presents the results of a field study of free surface flow properties conducted at a specific study site in Great Sippewissett Marsh in Massachusetts. The data collected include marsh topography, wind speed and direction, water elevation at the marsh boundary, and the vertical profile of horizontal velocity at a number of locations within the marsh grass study area. All parameters were measured throughout a rising and falling tide during which the study area became inundated. After being analyzed, the field data is used in model simulations of the flow at the measurement stations; the grass densities, not being known, are fit so that the predicted velocities within the grass agree with the observed measurements. The same grass density profiles are used in all comparisons made at any one measurements station. In those cases where the grass extends completely through the water column, the velocity is seen to be fairly uniform with depth, as compared to those cases where the grass is

submerged beneath the water surface. This latter type of flow shows significant structure in the vertical velocity distributions, as demonstrated by both the observed and predicted results, which are seen to be in generally good agreement in the above grass region.

Chapter Five arranges the kinematic variables governing obstructed flow into dimensionless parameters. The major flow features are found to depend on three parameters, relating to the density of the obstructions, the ratio of the depth of the obstructions to the total flow depth, and the relative magnitude of the free surface pressure force to the wind stress. Investigations are then presented considering the relationships between these parameters and the vertical distribution of various variables, including velocity, kinetic energy, dissipation, as well as the turbulent diffusivity and length scale. Also considered are the depth averaged flow conveyances, and the shear stresses at the top and bottom of the obstructions.

The dimensionless parameters and the model are also used in Chapter Five to examine previous methods for determining the turbulent length scale in obstructed flows, and to calculate the values of empirical coefficients appearing in commonly used analytical expressions for flow above and within vegetative canopies. The model is shown to reproduce the observed trends in these coefficients, as well as their magnitudes.

Finally, Chapter Six discusses the areas in which future work is merited, including such topics as further applications of the model, and numerical improvements to increase the model's efficiency.

CHAPTER II

BACKGROUND

2.1 Introduction

The objective of this study, as discussed in the previous chapter, is to develop a numerical model capable of predicting the vertical variation of a basically horizontal fluid flow through and above vertically oriented obstructions, such as vegetation. In particular, the model should be able to handle those physical conditions found in tidally inundated salt marsh flats. To account for the wind stress at the air-water interface, which may lie below the top of the grass, the model should be able to solve for the air flow, as well as the underlying water movement.

This chapter presents the governing equations of motion applicable to tidal marshes. Starting from the full, three dimensional Navier Stokes or Momentum Equations, various assumptions are made in Section 2.2 to reduce the equations into a more amenable and commonly used form. Next, these equations are horizontally averaged over an area large enough to remove the influence of individual obstructions. It is this averaging process that introduces the effect of the obstructions into the momentum equations. Next, a scaling analysis of the temporally averaged momentum equations shows that the acceleration and Coriolis terms may be neglected. Finally, a review is presented of previous canopy flow models.

2.2 Governing Equations

Assuming a constant fluid density, the temporally averaged mass and momentum equations at a point within the canopy are

$$\frac{\partial u_i}{\partial x_i} = 0 \tag{2.1a}$$

$$\rho \frac{Du_i}{dt} + \rho F_i = - \frac{\partial p}{\partial x_i} + \rho g_i + \frac{\partial \tau_{ji}}{\partial x_j} \tag{2.1b}$$

where i=1,2,3 refers to the x,y, and z axis, respectively, as shown in Figure 2.1; ρ is the fluid density; p is the pressure; g_i is the gravitational force per unit mass in the ith direction, and; F_1, $F_2 = -\Omega v$, Ωu are the Coriolis forces, with Ω being the Coriolis parameter, (Ω is about 10^{-4} sec^{-1} at a latitude of 40 degrees). The z axis points vertically upward, opposite to the direction of gravity. The total derivative D/dt is

$$\frac{D}{dt} = \frac{\partial}{\partial t} + u_i \frac{\partial}{\partial x_i} \tag{2.2}$$

The stresses τ_{ij} are defined in accordance with conventional sign notation. Remembering that the velocities are time averaged, the stresses are seen to include, in addition to viscous forces, Reynold's stresses created by turbulent convection of momentum. The stresses are

$$\tau_{ij} = \mu \left(\frac{\partial u_i}{\partial x_j} + \frac{\partial u_j}{\partial x_i}\right) - \rho \overline{u_i' u_j'} \tag{2.3}$$

where μ is the molecular viscosity, u_i' = turbulent fluctuations around

the mean value, and the overbar denotes the time average over a short time interval.

Equations (2.1) are unnecessarily general for most sea or lake circulation problems, and are simplified by the boundary layer approximation, which makes the assumptions that (1) the vertical velocity and it's gradients are small compared to the horizontal velocities and their gradients, and that (2) the longitudinal and lateral variations in stress are small compared to the vertical variations, i.e., $\frac{\partial}{\partial z} >> \frac{\partial}{\partial x}, \frac{\partial}{\partial y}$. With these assumptions, the vertical momentum equation reduces to a statement of hydrostatic pressure distribution

$$p = \rho g(\eta - z) \tag{2.4}$$

where g is the acceleration due to gravity, and η is defined in Figure 2.1. Substituting (2.4) into (2.1), and making use of assumption (2), the x and y momentun equations become

$$\rho \frac{Du_i}{dt} + \rho F_i = - \rho g \frac{\partial \eta}{\partial x_i} + \frac{\partial \tau_{3i}}{\partial x_3} \tag{2.5}$$

where, from now on, i = 1,2.

Equations (2.5) are time-averaged; they apply to any point in the fluid and, as such, do not explicitly account for the presence of obstructions, the effect of which appears by averaging the equations horizontally over an area large enough to eliminate the influence of individual obstructions. This averaging process is given by Wilson and Shaw (1976), as well as Thom (1981). The additional terms generated by the averaging process represent the drag forces imposed by the

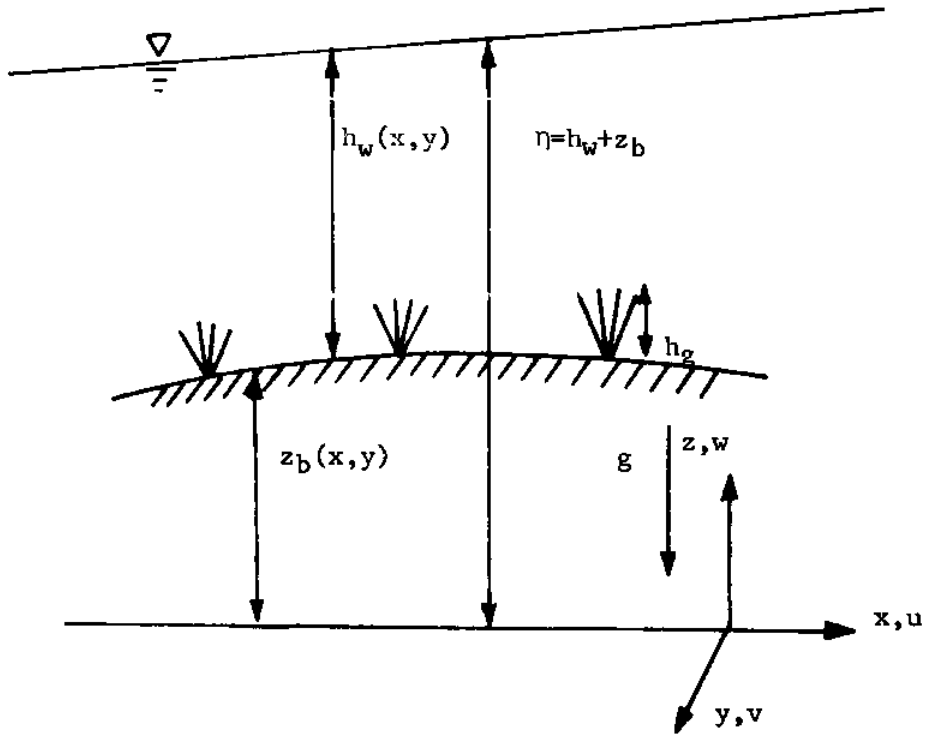

Figure 2.1 - Schematization of Flow in Tidally Inundated Marsh Grass.

obstructions in the flow. In all models known to the author, they are parameterized by a quadratic law, as follows:

$$\begin{matrix}\text{Magnitude of} \\ \text{Drag Force per} \\ \text{Unit Volume}\end{matrix} = \rho \frac{C_d a}{2} \left| u_i u_i \right|$$

where C_d is the drag coefficient, and a(z) is the vegetation density, defined as the projected area of obstructions, per unit volume at the level z, on a plane normal to the flow (Thom, 1971). Thus, for instance, in a flow through uniform cylinders of diameter (D) and spacing (S), with their axis parallel to the z direction, the value of (a) would be D/S^2.

The momentum equations can then be written as

$$\rho \frac{Du_i}{dt} + \rho F_i = -\rho g \frac{\partial \eta}{\partial x_i} + \frac{\partial \tau_{3i}}{\partial x_3} - \rho \frac{C_d a}{2} u_i (u_j u_j)^{1/2} \qquad (2.6)$$

where the horizontal velocities, as well as the stresses, are now temporally averaged to remove turbulent fluctuataions, and spatially averaged to remove influences due to interplant spacing.

The above equation assumes that the volume of the obstructions is much less than the total volume (i.e., the sum of the volume of the obstructions and the fluid volume). Making an analogy to porous media flow, this is equivalent to assuming that the porosity is near one, which is certainly a reasonable approximation for the types of situations of interest in this study. Continuing this analogy, it follows that the discharge velocity for obstructed flows will be approximately the same as the seepage velocity.

Equation (2.6) does not include an added mass term, representing the force necessary to accelerate the fluid past the obstructions (Daily and Harleman, 1966). As will be shown below, the acceleration terms for typical salt marsh geometries are generally small enough, when compared to the vertical momentum transport, that they may be neglected.

2.3 Scaling Analysis

One of the basic assumptions in this study is that the major balance in the momentum equation occurs between the shear, pressure, and drag forces, which are large compared to the total derivative and Coriolis terms. This section presents the justification for this assumption. The analysis makes no reference to the drag terms, and, as such, is independent of the presence of obstructions. Under most circumstances, of course, the drag terms will probably play an important role in determining the flow over the marsh. It is possible, however, that in some localized areas, such as algal mats, there may be little, if any, vegetation. Excluding the obstructions gives the analysis a greater generality, and width of applicability, than would have been possible by assuming a certain value of the vegetation density (a). In general, the presence of the obstructions, by retarding the flow, will tend to strengthen the basis of the approximations, as shown later.

The approach followed here will be to estimate the order of magnitude of the terms in the momentum equations, and then to show that, under various flow conditions, the size of the total derivative and Coriolis forces are small compared to the shear of pressure terms, which will be

assumed in balance (in the absence of obstructions).

To estimate the size of the various terms in the momentum equations, scaling parameters are needed relating to typical New England marshes; these parameters, given here for future reference, are

L = horizontal length scale. L will be on the order of 10^2 to 10^3 m as shown in Figure 4.1, which is a map of Great Sippewissett Marsh in Falmouth, Massachusetts.

H = vertical length scale. H will be about .1 m, the depth to which the marsh flats are inundated.

ΔH = free surface elevation change

$\Delta H/L$ = free surface slope

U = velocity scale in the horizontal direction

ΔU = velocity change due to non-uniform flow

U_* = friction velocity $(\tau/\rho)^{1/2}$. For the unobstructed flow assumed here, a relationship between U and U_* may be obtained from the friction factor expression $U_*^2 = C_f U^2$, where C_f is a friction factor of magnitude .01 for rough turbulent flow (Henderson,1976). This relationship will be assumed to hold for both tidally driven and wind driven cases.

T = time scale. T may refer to either the flooding time of the marsh flats ($T \sim 10^4$ sec.), or the time it takes for a wind set-up to become established on the marsh, determined later.

With these parameters, the various terms in the momentum equation can be estimated as

$$\frac{\partial u_i}{\partial t} + u_j \frac{\partial u_i}{\partial x_j} + F_i = - g \frac{\partial \eta}{\partial x_i} + \frac{1}{\rho} \frac{\partial \tau_{3i}}{\partial x_3} \qquad (2.7)$$

$$\left(\frac{U}{T}\right) \quad \left(\frac{U\Delta U}{L}\right) \quad (\Omega U) \quad \left(g \frac{\Delta H}{L}\right) \quad \left(\frac{U_*^2}{H}\right)$$

The following additional assumptions are also made;

(1) the slope and shear are in approximate balance, i.e., $g \frac{\Delta H}{L} = \frac{U_*^2}{H}$

(2) the terms in the continuity equation (2.1a) can be estimated as

$$\frac{\partial u_1}{\partial x_1} + \frac{\partial u_2}{\partial x_2} + \frac{\partial u_3}{\partial x_3} = 0$$

$$\left(\frac{\Delta U}{L}\right) \quad \left(\frac{\Delta U}{L}\right) \quad \left(\frac{U_3}{H}\right)$$

where U_3 is the characteristic velocity in the vertical direction. For steady flow, U_3 may be approximated using the kinematic relationship, giving $U_3 = \frac{U\Delta H}{L}$. For unsteady flow, U_3 may be taken as $U_3 = \frac{H'}{T'}$, expressing the fact that if, in a time T', the water depth changes by an amount H', then the vertical velocity will be about H'/T'. With these expressions for U_3, $\frac{\Delta U}{L}$ becomes $\frac{U\Delta H}{HL}$ and $\frac{H'}{HT'}$ for steady and unsteady flow, respectively.

Using the relationships in (1) and (2) above, as well as the friction factor expression, it is possible to show that the D/dt and Coriolis terms are generally smaller than the slope or shear terms. This will be done by considering various flow configurations typical of marsh flow

situations; as shown in Table 2.1, three configurations will be considered; (1) tidally steady flow, (2) tidally unsteady flow, and (3) wind driven flow. For each configuration, Table 2.1 gives the values of the scaling parameters, as well as the magnitudes of the terms in (2.7). Two general situations are considered, one with $L = 10^2$m, the other with $L = 10^3$ m. For each flow configuration, certain of the parameters will be uniquely defined; knowing the values of these parameters, it is then possible, using the relationships described above, to obtain the remainder of the scaling parameters. The parameters unique to each configuration are given below, together with a description of the physical circumstances under which each case might occur.

(1) Tidally steady flow

This might occur during flood, or ebb, tide on sections of marsh bordered by tidal creeks. The water slope $(\frac{\Delta H}{L})$ is then uniquely defined by the tide; from measurements taken in the field (see Chapter four), $\frac{\Delta H}{L}$ will be about 10^{-4}. Knowing L, it is then possible to calculate ΔH, and the remainder of the parameters $(U_*^2 = gH\frac{\Delta H}{L}$; $U = \frac{1}{\sqrt{C_f}} U_*$; $\Delta U = \frac{U\Delta H}{H})$

(2) Tidally unsteady flow

This might occur on dead-end sections of marsh bordered on one side by an open water body, such as a creek, and on the other side by a solid boundary, such as an upland. The velocities U and ΔU are uniquely defined: as discussed earlier, $\frac{\Delta U}{L}$ for unsteady flow is about $\frac{H'}{HT'}$; in this case, $H'=H$, and $T'=T \sim 10^4$ sec. Noting that the velocity at the solid boundary will be zero, the velocity change ΔU over the length L is seen to be

Case	H (m)	L (m)	T (sec)	ΔH (m)	U_* ($\frac{m}{sec}$)	U ($\frac{m}{sec}$)	ΔU ($\frac{m}{sec}$)	ΩU ($\frac{m}{sec^2}$)	$\frac{\partial u}{\partial t} \sim \frac{U}{T}$	$\frac{u\partial u}{\partial x} \sim \frac{U\Delta U}{L}$	$g\frac{\partial h}{\partial x} \sim \frac{1}{\rho}\frac{\partial \tau}{\partial z}$ $g\frac{\Delta H}{L} \sim \frac{U_*^2}{H}$
tidally steady											
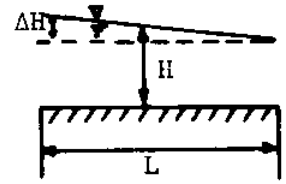 1A	.1	10^2	10^4	.01	.01	.1	.01	10^{-5}	10^{-5}	10^{-5}	10^{-3}
1B	.1	10^3	10^4	.1	.01	.1	.1	10^{-5}	10^{-5}	10^{-5}	10^{-3}
tidally unsteady											
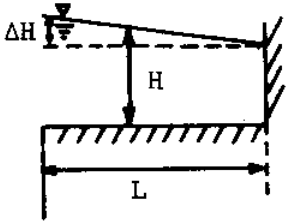 2A	.1	10^2	10^4	10^{-4}	.001	.01	.01	10^{-6}	10^{-6}	10^{-6}	10^{-5}
2B	.1	10^3	10^4	.1	.01	.1	.1	10^{-5}	10^{-5}	10^{-5}	10^{-3}
wind driven											
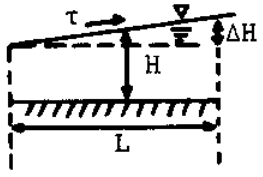 3A	.1	10^2	10^2	.01	.01	.1	.01	10^{-5}	10^{-3}	10^{-5}	10^{-3}
3B	.1	10^3	10^4	.1	.01	.1	.1	10^{-5}	10^{-5}	10^{-5}	10^{-3}
3C	.1	10^2	10^3	10^{-4}	.001	.01	10^{-5}	10^{-6}	10^{-3}	10^{-9}	10^{-5}
3D	.1	10^3	10^3	10^{-3}	.001	.01	10^{-4}	10^{-6}	10^{-5}	10^{-9}	10^{-5}

Table 2.1 - Scaling Parameters for Typical Salt Marsh Geometries.

about the same as U, giving $U \sim \Delta U \sim L/T$. Using the known values of L and T to find $U \sim \Delta U$, the rest of the parameters can then be obtained ($U_* = \sqrt{C_f}\, U$; $\Delta H = \frac{U_*^2}{H}\frac{L}{g}$).

(3) Wind driven flow

This case corresponds to wind blowing over the water surface, creating a slope $\frac{\Delta H}{L}$. The time it takes for the slope to become established, assuming an initially flat surface, can be estimated most simply by recognizing that, from continuity, $\frac{dA}{dt} = U \cdot H$, where A is the volume of water displaced by the wind. Taking $A=O(\Delta HL)$ gives $\Delta HL = UHT$, or $T = \frac{\Delta HL}{UH}$.

The value of U_* is defined by the wind stress. From Wu (1969), the wind stress (τ_s) can be taken as approximately $\tau_s = \rho_a(.001\ U_{10}^2)$, where U_{10} is the wind speed at a reference height of 10m, and ρ_a is the density or air ($\rho_a \sim 1$ kg/m^3). Estimating the range of U_{10} to be between 1 and 10 m/sec., with $\rho_\omega = 1000$ kg/m^3, the corresponding values of $U_* = (\tau_s/\rho_\omega)^{1/2}$ become .001 and .01 m/sec. Having determined U_*, and the expression for T, it is then possible to calculate the rest of the parameters ($U=\frac{1}{\sqrt{C_f}}\, U_*$; $\Delta H = \frac{U_*^2}{H}\frac{L}{g}$; $T = \frac{\Delta HL}{UH}$; $\Delta U = \frac{U\Delta H}{H}$)

Reviewing Table 2.1, the Coriolis forces are seen to be at least an order of magnitude less than the pressure or slope terms for all cases. For most cases, the unsteady and convective terms are also small enough to be neglected. The three exceptions to this are cases 3A, 3C, and 3D, where the unsteady terms are as large, or greater, than the slope terms. The reason for the large magnitude of these terms can be traced back to the relatively small values of T; as the time it takes

for the wind set-up to become established decreases, $\frac{du}{dt} \sim \frac{U}{T}$ becomes relatively larger.

In these three cases, the unsteady terms will play a role in the momentum equations during the time T before steady state conditions are established. Because this period is small compared to the marsh flooding time, it will be ignored, on the grounds that the conditions existing during this unsteady period are not representative of those encountered during most of the time the marsh is flooded, and would not have much of an effect on the overall flow field.

In summary, for the conditions typical of coastal New England salt marshes, the total derivative DU_i/dt and Coriolis forces have been shown in the above analysis to be negligible compared to the pressure or slope terms, or important over a period of time short enough that it can be overlooked. Again, no reference has been made to obstructions, such as vegetation, the presence of which would increase the friction factor C_f, thus further supporting the approximations.

Without the acceleration or Coriolis terms, the momentum equation reduces to the form shown in(2.8), which represents the final form of the momentum equations used in this study.

$$\frac{\partial \tau_{3i}}{\partial x_3} = \rho g \frac{\partial \eta}{\partial x_i} + \rho \frac{Cda}{2} u_i (u_j u_j)^{1/2} \qquad (2.8)$$

The vertical velocity distribution at any location in the marsh is thus taken to be established quickly, as determined by a local horizontal force balance, and is relatively independent of unsteadiness, or horizontal convection. The relative unimportance of these factors will also be

used in the next chapter to simplify the transport equations for other variables.

This assumption does not imply, however, that there is no lateral connection at all between different locations in the marsh. Such interaction would arise through the continuity equation; as the water moves from one location to the next, the water height, as well as the slope, would likely change, thus altering the pressure forces in the momentum equation.

2.4 Previous Canopy Flow Models

This section reviews previous attempts to solve for the flow through and above vegetative canopies. Almost exclusively, the models presented here were developed for airflow, and take no account of a free surface, such as will exist in marsh flow. The only model known to the author that treats water flow through vegetation was done by Reid (1976).

Most airflow canopy models assume the pressure term in (2.8) is small, and the x axis is aligned with the direction of mean wind, so that the momentum equation becomes

$$\frac{d\tau}{dz} = \rho \frac{Cda}{2} u|u| \qquad (2.9)$$

where τ refers only to the turbulent stress $\rho\overline{u'w'}$.

2.4.1 Flow above the Canopy

Many researchers, uninterested in the flow through the canopy layer, have treated the vegetation as roughness elements. Analogous to classical theories of flow over rough surfaces, the influence upon the flow of a

canopy of height h_g is felt throughout a roughness layer that may extend well above $z=h_g$. At its upper limit, the roughness sublayer merges with an inertial sublayer in which the velocity may be expressed by the semi-logarithmic law (Monin and Yaglom, 1971)

$$u = \frac{u_*}{\kappa} \ln \left(\frac{z-d}{z_o}\right) \tag{2.10}$$

where u_* is the friction velocity in the inertial sublayer; κ is the von Karman constant; z_o is the roughness length; and d is the zero-plane displacement height, usually thought of as the level to which the effective surface must be raised to make the wind profile in the inertial sublayer obey the semi-logarithmic law (Thom, 1981). If the vegetation is small enough, d may be taken as zero, in which case (2.10) reverts back to its familiar form.

Determination of z_o and d for vegetative surfaces is best done by experimental determination from wind velocity profile measurements. Brutsaert (1982) summarizes roughness parameters for various surfaces, with z_o ranging from .001 cm for ice to 165 cm for Tokyo, Japan.

In the absence of experimental data, it becomes necessary to estimate z_o and d from empirical relationships. Brutsaert (1982) suggests that, as a first approximation, z_o/h_g and d/h_g may be taken as 1/8 and 2/3, respectively. In reality, of course, these ratios will be complicated functions of surface characteristics, such as vegetation density. Nevertheless, in the absence of wind profile data, practically the only recourse is to make use of these, or similar, relationships.

Reid and Whitaker (1976), in a model of wind driven water flow through and above obstructions, divided the water depth into two layers, one within the canopy, and one above it. The equations of motion were then averaged over each layer. The interfacial stress at the canopy top was formulated in terms of a coupling coefficient (f') and the velocity difference between the two layers. The value of f' was determined by fitting the model predictions to a laboratory study by Tickner (1957) on the effects of wire screens on wind set-up in a model channel. Having thus determined f', Reid was able to solve for the flow in each layer.

There are several drawbacks to Reid's approach. Probably the most important is that no evidence is presented to show that the chosen value of f' yields satisfactory predictions for any data other than Tickner's. It seems unlikely whether a single value of f' would apply for all vegetation densities, under all conditions. To the extent that f' must be reevaluated for different values of (a), water depth, and other variables, the predictive abilities of the model are restricted.

2.4.2 Flow within the Canopy

Solution of (2.9) for flow within the canopy requires specification of (C_d) and (a), and a turbulence closure assumption for the shear stress. These subjects are dealt with below.

Determination of (C_d) and (a)

The drag term in (2.9) contains the parameters (a) and (C_d). The vegetation density (a), defined earlier as the frontal area of the obstructions per unit volume, is usually determined from field experiments.

A common method for determining (a) for commerical crops such as corn or beans is to take several plants from the field and superimpose them on a large grid drawn on sheets of paper. Plant shapes are then drawn on the grid, measured, and used to calculate plant area as a function of height. This approach is less practicable for vegetation such as marsh grass, having a higher density of plants, many of which are interlinked with each other.

The drag coefficient (C_d) may be taken as (Brutsaert, 1982)

$$C_d = b \cdot R_e^c$$

where $R_e = (\rho u L_L / \mu)$, L_L is a characteristic length scale of the leaves, and b and c are approximately constants. For isolated objects having simple geometries, such as a cylinder or plastic strip, b and c can be estimated (Schlichting, 1968). Studies have also been done on the drag coefficients of isolated elements of vegetation canopies, such as spruce shoots (Landberg and Thom, 1971), these being representative of a forest company. Thom (1968), in a wind tunnel study of bean leaves, found the drag, not surprisingly, to depend strongly on the angle of incidence (Θ) of the leaf to the mean flow, with C_d ranging from .03 for Θ=0° to .8 for Θ=90°. At typical angles of incidence encountered in the field (Θ=20°), the drag was found to be a mixture of form and skin friction, with a ratio of about three to one, and a magnitude of .3.

In-situ measurements of (C_d) within canopies have also been performed, usually by first determining the stress, such as with a hot wire anemometer;

knowing u, (a), and τ, (2.9) is then solved for (C_d). Representative values of (C_d) for various crops are .32 for corn (den Hartog and Shaw, 1975), .08 for beans (Thom, 1971), and .8 for spruce trees (Raymer, 1962).

The drag coefficient measured in situ within a canopy has been found to be usually several times smaller than that of an isolated element in an equivalent uniform flow, i.e., a flow having the same velocity as that measured in the spaces between the elements of the canopy (Thom, 1981). Note, for example, the difference in C_d between the bean leaves and the bean crop, mentioned above. The ratio of (C_d) for the individual element to that of the canopy is called the shelter factor (p).

Although not entirely understood, (p) is generally believed to be caused by mutual aerodynamic interference of neighboring obstructions, although other factors, such as leaf movement, may also play a role. Field values of (p) are usually between three and four, as determined by Thom (1971) for a bean crop, and Steward and Thom (1973) for a pine forest. Seginer (1976), in a wind tunnel study of circular cylinders having $R_e \approx 1000$, also found $p \approx 3$; however, Thom (1971), in a similar canopy with $R_e \approx 60$, found $p \approx 1$, thus suggesting a possible Reynold's number effect.

Seginer (1976), studying the data of compact heat exchangers at $R_e \simeq 1000$, noted that the drag coefficient of circular cylinders decreased with increasing density, going from a value of C_d=1 for a=0 to C_d=.3 for a=50m^{-1}. Further investigation into the heat exchanger data literature revealed that the values of (a) were consistently above 50m^{-1}, an order of magnitude larger than that found in vegetative canopies. Such large

differences in (a), and the accompanying large differences in the flow interference patterns, make use of the heat exchanger data impractical for applications relating to natural vegetation.

Reviewing the above discussion, the drag coefficient for vegetative canopies is seen to depend on the size and shape of the elements, their angles of attack relative to the flow, and their mutual interference, making extrapolation from laboratory studies difficult. Given these complexities, models of canopy flow usually either rely on experimental observations of (C_d) taken in the canopy of interest, or, more often, determine (C_d) by trial and error to give the best fit to the data.

Turbulence Closure Assumptions

Solution of (2.9) requires some turbulence closure assumption about the stress. Almost universally, previous models have made recourse to the turbulent diffusivity approach, in which

$$\tau = \mu_t \frac{\partial u}{\partial z} \tag{2.11}$$

where μ_t is the turbulent diffusivity. The closure problem then shifts from τ to μ_t. Unlike μ, the molecular viscosity, μ_t is not a property of the fluid, but rather of the local state of turbulence (at least, that is what is assumed). Continuing this line of thought, μ_t is frequencly expressed as

$$\mu_t = \rho V_t \ell_t$$

where V_t is the velocity scale of the turbulence, and ℓ_t is the turbulent length scale. Determination of μ_t for canopy flow models has usually followed one of two routes; the mixing-length approach, or the diffusivity

approach.

The mixing-length approach, based on the Prandtl von Karman theory for turbulent boundary layers, maintains that

$$\mu_t = \ell^2 \left|\frac{\partial u}{\partial z}\right|$$

where $\ell_t = \ell$ is called the mixing length and $V_t = \ell\left|\frac{\partial u}{\partial z}\right|$ is the turbulent velocity scale. With the assumption of a constant mixing length ℓ_c and $C_d a$ = constant, one solution of (2.9) is

$$\frac{u(z)}{u(h_g)} = \exp(\alpha_c(z/h_g - 1))$$

where $u(h_g)$ is the velocity at the top of the canopy ($z=h_g$), and α_c is the attenuation coefficients, given as $(\frac{1}{4} C_d a\, h_g^3 \ell_t^{-2})^{1/3}$. This derivation, introduced independently by Inoue (1963) and Cionco (1965), yields an exponential wind profile. There are too many assumptions in it to be regarded as anything more than an empirical fit. In addition, it does not satisfy the lower boundary condition that u=0 at z=0 and hence, while empirically convenient, is mathematically arbitrary (Thom, 1981). Nonetheless, this approach is widely used, largely because, by suitably fitting the parameter α_c, reasonable predictions of the upper part of various canopy wind profiles have been otained. Cionco (1972) summarizes the best values of α_c for numerous canopies.

The diffusivity approach relates μ_t directly to other variables in the momentum equation, and makes no mixing length assumption. Cowan (1968) assuming $\mu_t/u = [\mu_t(h_g)/u(h_g)]$ and $C_d a$ = constant, generated the

hyperbolic wind profile

$$\frac{u}{u(h_g)} = \left[\frac{\sinh(a_\omega z)}{\sinh(a_\omega h_g)}\right]^{1/2} \tag{2.14}$$

where a_ω is a parameter; this result satisfies the lower boundary condition. Assuming that both μ_t and $C_d a$ are constant, one obtains (Landsberg and James, 1971; Thom, 1971)

$$\frac{u}{u(h_g)} = [1 + a'_\omega\ (1 - \frac{z}{h_g})]^{-2} \tag{2.15}$$

where a'_ω is another parameter. As with the exponential profile, this result does not satisfy the lower boundary condition. While both a_ω and a'_ω can be expressed in terms of the parameters governing (2.9) and μ_t, they are operationally empirical coefficients, determined by comparison against experimental observations.

Despite the different ways in which (2.13), (2.14) and (2.15) were derived, they all give wind profiles that have similar shapes, and that decay monotonically with depth. These models rely heavily on fitting parameters for their success, and can not handle vertically non-homogeneous canopies without direct integration.

Another disadvantage of these models is that, while describing the shape ($u/u(h_g)$) of the velocity profiles, they say nothing about it's magnitude. Values of $u(h_g)$ and $\mu_t(h_g)$ required in the expressions must be either known from experiments, or calculated by joining the equations to the corresponding formulation of the inertial sublayer (i.e., (2.10))

at $z=h_g$. This embodies the assumption, not necessarily accurate, that the mean height of the plants h_g coincides with the lower boundary of the inertial sublayer. Accordingly, the turbulent diffusivity $\mu_t(h_g)$ in (2.14) becomes, by virtue of (2.10) and (2.11), $\mu_t(h_g) = ku_*(h_g-d)$, where u_* is the friction velocity in the inertial sublayer. The value of $u(h_g)$ is found by substituting $z=h_g$ into (2.10), thus requiring knowledge of z_o and d.

To overcome these difficulties, numerical models have been developed that extended the calculations above the level $z=h_g$. Kondo and Akashi (1976), in one such model, parameterized the shear stress using a mixing length approach, in which ℓ was taken as being proportional to $1/C_d a$. To prevent ℓ from becoming infinite above the canopy layer, the following restriction was added,

$$\left|\frac{d\ell}{dz}\right| < \kappa$$

The proportionality between ℓ and $C_d a$ is based on the assumptions that (1) the production of kinetic energy by the vegetation (P_d) is in approximate balance with the viscous dissipation of turbulent energy (ε), and (2) the mean velocity (u) scales with $k^{3/2}$, where $k = \frac{1}{2}\overline{u_1'u_1'}$ is the turbulent kinetic energy. As discussed fully in Chapter three, $P_d \sim (C_d a u^3)$ and $\varepsilon \sim (k^{3/2}/\ell)$; with these estimates, and assumptions (1) and (2), it is seen that $\ell \sim 1/C_d a$.

This model contains several weaknesses. The first concerns the ability of the mixing length approach to adequately describe the turbulent transport. A general feature of all mixing length models is that

they are equivalent to assuming that the turbulence produced at a point is dissipated by viscous action at the same point (see Section 3.2.5). No account is made of the influence of diffusion on the turbulent length scale. This is a potentially serious flaw for canopy flow, where downward diffusion of turbulence will likely play an important role in the transport of momentum, as well as other quantities, such as heat or water vapor.

In addition to this drawback, there are questions concerning the validity of the assumptions on which the proportionality between ℓ and $C_d a$ are based. It seems unlikely, for instance, that the diffusion of kinetic energy, and production by shear gradients, will always be small, as implied by assumption (1) above. Another concern is that, besides preventing abrupt changes in ℓ when (a) becomes small, no physical justification is given why $d\ell/dz$ should be less than κ. Tennekes and Lumley (1972) note that algebraic prescription of turbulent scales is best done when these scales are unique. This will not be the case for marsh flow problems, in which there will usually be two length scales, one associated with the mean velocity gradients, and one with the wake generated eddies.

Despite these drawbacks, this formulation for the turbulent length scale is used by Wilson and Shaw (1976), who closed (2.9) using a second order technique. Their model consists of five equations for five variables: velocity, Reynold's stress, and the three components of the turbulent kinetic energy. Higher order terms were parameterized with the help of three length scales, assumed proportional to a master length scale ℓ, prescribed in a similar fashion as in Kondo's model. The constant of proportionality between ℓ and $C_d a$ was determined by trial and error to

give the best fit to a set of experimental observations within a corn crop. In formulating the bottom boundary conditions, Wilson & Shaw assumed the existence of a logarithmic layer, without giving any justification for it. The presence of obstructions may well alter the near-wall turbulence structure from that in conventional open channel flow situations.

One of the main reasons behind Wilson & Shaw's use of a second order closure technique was to be able to predict reversals of wind gradient ($\frac{\partial u}{\partial z} < 0$) when solving (2.9). Such regions of wind gradient reversal have been observed in the lower parts of some canopies (Lemon et al., 1970; Oliver, 1975). That a turbulent diffusivity closure approach can not cope with this phenomenon can be seen by noting that, for flow governed by (2.9), the shear stress will be a monotonically increasing function of height. The eddy viscosity expression $\tau = \mu_t \frac{\partial u}{\partial z}$ dictates that the velocity will then also increase steadily (assuming μ_t is not negative). This limitation arises because of the imposition of the flux-gradient model, and is not necessarily implied by the basic flow equation (2.9).

Shaw (1977), from the equation for the local rate of change of the Reynold's stress $\overline{u'w'}$, showed that, under certain conditions, the mean wind gradient can reverse in direction within a canopy. The allowable conditions for this to occur are most readily satisfied by canopies, such as trees, having a large, leafy surface near the top, and a rather sparse trunk space lower down. It is for these kinds of canopies that wind gradient reversals are most common (Brutsaert, 1982). For obstructions such as marsh grass, having a more uniform distribution of vegetation density, with the highest values occuring near the bottom, such reversals in velocity gradient are

much less likely to occur, and, as such, do not seem a serious concern for this study.

Lewellen and Sheng (1980) expanded Wilson and Shaw's model to include other effects, such as skin friction, but did not alter the basic model formulations. They did, however, extend the calculations to the canopy floor, where the velocities, as well as the gradients of the turbulent fluxes, were set to zero. While including viscous terms in the momentum equations, no such terms were added to the equations for the Reynold's stress, or the components of the kinetic energy.

The models of Kondo, Wilson and Shaw, and Lewellen and Sheng have been demonstrated by their authors to describe with reasonable accuracy experimental observations of wind canopy flow. Universally, however, one data set was used for comparison, raising questions as to the ability of the models to handle other situations, having different surface characteristics. Wilson and Shaw smoothed the gradient of the Reynold's stress in the region above the canopy to yield better fit to the data; to the extent that this will always be necessary, the predictive abilities of the model are reduced.

This section has described previous turbulent closure assumptions used in canopy flow models. The main features of these models are summarized in the next section, and are compared with the desired attribures of a flow model for inundated marsh flats.

2.5 Summary and Conclusions

Table 2.2 sumarizes the main features of the canopy flow models discussed previously. That these models are inappropriate to the study of flow through inundated marsh flats can be seen by reviewing the requisites of such a model.

Obviously, any marsh flow model should be able to handle a free surface. In order to predict the wind stress at the air-water interface, which may lie below the top of the vegetation, the model should also be able to solve for the overlying air flow. Ideally, the same set of equations should be used in both cases, the differences appearing only through the boundary conditions.

A second desirable attribute, relating to the parameterization of the turbulent transport terms, is that the model should contain no a priori specification of turbulent length or velocity scales. As discussed earlier, such specification (1) does not account for the influence of diffusion, (2) is difficult to implement unless the scales are unique, which will not be the case within a canopy, and (3) requires different formulations, depending on whether or not the water or air flow is being solved.

A third desirable attribute of a marsh flow canopy model is that it takes into consideration the fact that, in the presence of obstructions such as vegetation, the near-wall variation of mean and turbulent quantities will differ from those found in non-obstructed flow situations. If the model equations are extended to the canopy floor, terms should be added to include near-wall viscous effects. Because a large fraction

Author	Turbulence Closure Assumption	Vertically Non-homogeneous Canopy	Turbulent Length Scale	Free Surface	Near-wall Viscous Effects
Inoue* (1963)	mixing-length	no	prescribed	no	no
Cowan * (1968)	diffusivity	no	prescribed	no	no
Landsberg & Thom* (1971)	diffusivity	no	prescribed	no	no
Reid (1976) and Whitaker	none (Eq. are vert. avg.)	no	N.A.	yes	no
Kondo, (1976)	mixing length	yes	prescribed	no	no
Wilson & Shaw (1976)	2nd order technique	yes	prescribed	no	no
Lewellen & Scheng (1980)	2nd order technique	yes	prescribed	no	partially
This study	k-ε	yes	not necessary to prescribe	yes	yes

*analytic solution

Table 2.2

Main Features of Various Canopy Flow Models

of the total change of a variable may occur in the region near the wall, it is important that this zone be modeled correctly.

A fourth requisite of a marsh canopy flow model is that it be able to handle a wide range of geometries and physical conditions. In particular, this refers to the vegetation density (a): the model should be able to handle cases ranging from very little, or no vegetation (a=0), up to values of (a) as high, if not exceeding, those expected in the marsh. Any sacrifices in simplicity or economy incurred by following such a route are offset by the greater generality and width of applicability of the model.

As seen from Table 2.2, these desired attributes are generally not met by previous canopy flow models. The analytic solutions, i.e. those of Inoue, Cowan or Landsberg and James, contain too many limitations to be useful for the application considered here. The numerical models of Kondo, Wilson and Shaw, and Lewellen and Sheng do not consider the presence of a free surface. More importantly, they all rely on an algebraic prescription of the turbulent length scale, do not generally account for the influence of obstructions on the near-wall turbulence structure, and, from the available literature, do not seem to have been very well compared against experimental data. The same criticism applies to Reid's model.

The inability of previous canopy models to meet the objectives of this study prompted a search for an alternative approach to closing the momentum equations. The chosen method is discussed in the next chapter.

CHAPTER III

MODEL FORMULATION AND VERIFICATION

3.1 Introduction

The last chapter developed the governing momentum equations for obstructed flow, with special attention to tidal marsh conditions. Reviewing previous obstructed flow models, it was concluded that the methods used to parameterize the turbulent stress terms do not generally meet the objectives of this study.

Looking for an alternate way to parameterize the turbulent stresses, it was decided to use a two-equation k-ε low Reynold's model. This technique accounts for the influence of diffusion on the turbulent scales, requires no a priori specification of μ_t, and takes account of near-wall viscous effects.

This chapter begins by reviewing the concepts behind the standard k-ε model, followed by a development of the modifications allowing the model to handle flow through vegetation, or other obstructions. Next, the numerical solution method is described. Finally, model verification is provided by comparing numerical solutions to analytical and experimental results.

3.2 Governing Features of k-ε Model

The k-ε model, proposed by Chou (1945), Harlow-Nakayama (1968), and Jones-Launder (1972), parameterizes the turbulent shear stress using a

conventional eddy viscosity technique, whereby

$$-\overline{u_i' u_j'} = \frac{\mu_t}{\rho} \left(\frac{\partial u_i}{\partial x_j} + \frac{\partial u_j}{\partial x_i} \right) \tag{3.1}$$

Following the practice of earlier workers (e.g., Emmons, 1954), the turbulent viscosity μ_t is taken as being uniquely determined by the density, turbulent kinetic energy $k = \frac{1}{2} \overline{u_i' u_i'}$ and a turbulent length scale ℓ, in the form

$$\mu_t = \rho k^{1/2} \ell \tag{3.2}$$

At high Reynolds' number, ℓ may be related to the turbulent dissipation rate ε by (Tennekes & Lumley, 1972)

$$\ell = C_\mu \frac{k^{3/2}}{\varepsilon} \tag{3.3}$$

where C_μ is a constant. Substituting this expression for ℓ into (3.2) yields the important final result

$$\mu_t = \rho C_\mu \frac{k^2}{\varepsilon} \tag{3.4}$$

The turbulent kinetic energy k and the dissipation rate ε are determined by differential transport equations, as discussed in the following sections.

The distinguishing feature of the k-ε model is the way in which it determines ℓ. Other researchers, all starting from (3.2), have proposed different ways of determining the length scale ℓ, resulting in different sets of transport equations. These models are reviewed by Launder and Spalding (1972). The dissipation equation approach for

finding ℓ has become popular, owing largely to the relative ease with which the ε equation is derived (Rodi, 1981).

3.2.1 The k Equation

An exact equation for k can be derived from the Navier Stokes equations (Hinze, 1975). For high Reynolds number flow this equation reads

$$\rho \frac{Dk}{dt} = \frac{\partial}{\partial x_i}\left[\rho \overline{u_i'\left(\frac{u_j'u_j'}{2} + \frac{p'}{\rho}\right)}\right] - \overline{\rho u_i'u_j'}\frac{\partial u_i}{\partial x_j} - \mu \overline{\frac{\partial u_i'}{\partial x_j}\frac{\partial u_i'}{\partial x_j}}$$

convective flux; diffusive transport; P_s = production; ε = viscous dissipation

(3.5)

The total derivative of k is balanced by diffusive transport due to the velocity and pressure fluctuations, the production of k by the interaction of Reynolds stress and mean velocity gradients, and the dissipation of k by the action of viscosity.

Before this equation can be used in a turbulence model, some approximations must be introduced for the unknown turbulent correlation appearing in the diffusion term. Analagous to the diffusion term for momentum, the rate of transport of k is taken as

$$\overline{\rho u_i'\left(\frac{u_j'u_j'}{2} + \frac{p'}{\rho}\right)} = \frac{\mu_t}{\sigma_k}\frac{\partial k}{\partial x_i} \tag{3.6}$$

where σ_k is an effective Prandl number for the diffusion of kinetic energy. With this approximation, and the eddy viscosity expression for $\overline{u_i'u_j'}$, the modeled form of the k equation becomes

$$\rho \frac{Dk}{dt} = \frac{\partial}{\partial x_i} \left(\frac{\mu_t}{\sigma_k} \frac{\partial k}{\partial x_i}\right) + \mu_t \left(\frac{\partial u_i}{\partial x_j} + \frac{\partial u_j}{\partial x_i}\right) \frac{\partial u_i}{\partial x_j} - \rho\varepsilon \qquad (3.7)$$

3.2.2 The ε Equation

The dissipation equation as it appears in the k-ε model was first developed and used by Hanjalic (1970); his derivation starts with the fact that for high Reynolds number, locally isotropic flow, the rate of dissipation can be shown to be equal to the product of the molecular kinematic viscosity and the fluctuating vorticity (Hinze, 1975). Next, the Navier Stokes equations are manipulated to produce an equation for the fluctuating vorticity, and thus for the dissipation rate. Finally, modeling assumptions are made to express the higher order turbulence correlations in terms of known quantities, similar to what was done for the exact k equations. These model assumptions are fairly involved and will not be discussed in detail here. The end result, shown below, contains terms representing the rate of change, convection, diffusion, and generation of vorticity due to vortex stretching, and viscous destruction of vorticity.

$$\rho \frac{D\varepsilon}{dt} = \frac{\partial}{\partial x_i}\left(\frac{\mu_t}{\sigma_\varepsilon} \frac{\partial \varepsilon}{\partial x_i}\right) + \frac{C_1\varepsilon}{k} (P_s) - \rho \frac{C_2\varepsilon^2}{k} \qquad (3.8)$$

Convective Flux — Diffusion — generation-destruction

Operationally, (3.8) serves not as a transport equation for dissipation, but rather for a quantity that scales with $k^{3/2}/\ell$; in essence, it is an equation for determining ℓ.

3.2.3 Constants

The values of the constants appearing in the k and ε equations were determined from experiments, as discussed in detail by Hanjalic and Launder (1972). Briefly, C_μ (.09) was determined from the requirement that in a constant stress layer $\frac{\tau}{\rho k} = C_\mu^{1/2}$ (see Section 3.2.5); C_2(1.92) was determined by reference to the decay of grid turbulence; and C_1(1.44) was chosen so that von Karman's constant equals .42. The diffusion coefficients σ_k and σ_ε were assumed to be close to unity, and were determined by computer optimisation with a variety of free shear flows (Launder et. al., 1973).

3.2.4 Applications

The form of the k-ε model given above (i.e., with fixed constants) has been applied with good results to many kinds of flow, including 2-D wall boundary layer (Jones and Launder, 1972), duct flows (Stephenson, 1976), free shear layers (Launder et. al, 1973), and recirculating flows (Gosman et. al., 1979).

Flows where this version of the k-ε model has not given entirely satisfactory predictions are (1) axisymmetric jets in stagnant surroundings (Rodi, 1976), (2) flows, such as far field jets or wakes, where the change in velocity across the flow is a small fraction of the translational velocity of the flow (Launder et. al., 1973), and (3) thin shear flows over curved surfaces (Launder, 1975). The reasons behind the lack of agreement with experimental data for these cases are mentioned at the end of Section 3.3.

3.2.5 Inferences from Near Wall Turbulence

In the vicinity of a wall the convection and diffusion of turbulent kinetic energy will be small, leaving a balance in the kinetic energy equation (3.7) between P_s and ε, or

$$\mu_t \left(\frac{\partial u}{\partial z}\right)^2 = \rho C_\mu \frac{k^{3/2}}{\ell} \tag{3.9}$$

where v has been set to zero for simplicity. Multiplying the left hand side of this expression by μ_t, and the right-hand side by $\rho k^{1/2} \ell$, leads to the result

$$\frac{\tau^2}{\rho^2} = C_\mu k^2 \tag{3.10}$$

This relationship between τ and k is borne out by experiment, with the ratio $(\tau/\rho k)^2$ being found to be .09 in fully turbulent flow.

Another useful relationship can be had by eliminating k from the dissipation term by introducing the definition of μ_t, giving

$$\tau = C_\mu^{-1/2} \rho \ell^2 \left(\frac{\partial u}{\partial z}\right)^2 \tag{3.11}$$

which may be recognized as the mixing length hypothesis, where the mixing length is seen to be equivalent to $C_\mu^{-1/4} \ell$. This derivation shows why the mixing length model is referred to as a local equilibrium model, as it is the form to which the kinetic energy equation reduces when diffusion and convection are neglected, implying that k is both produced and dissipated at the same location.

3.3 Viscous Effects

The form of the model presented above applies only to fully turbulent regions; close to a solid surface, or other interface, the Reynold's number will become low enough for molecular viscosity to be important. Although this viscosity-affected region may be several orders of magnitude smaller than the total flow depth, it is nonetheless important, since a large fraction of the total change of a variable may occur in this region. The complexities of the viscosity-affected region may be avoided by utilizing the fact that, for many turbulent flows, the near-wall variation of the mean turbulent quantities are functions only of the normal distance from the wall (provided the variables are non-dimensionalized by the wall shear stress, the density, and the fluid viscosity). These universal patterns, called wall functions, are determined empirically. Thus, in making flow calculations, the first grid point of a finite difference grid on which the flow is to be computed is chosen so that it's distance from the wall is just above the viscosity-affected region. Boundary values of the dependent variables u, v, k and ε at this point are then determined from the wall functions, given by Launder and Spalding (1973).

The wall functions, however, are not sufficiently universal to be used in all situations: severe streamwise pressure gradients, steep property gradients, the influence of buoyancy or body forces - all these may substantially disturb the near-wall flow. Accurate predicitions of such flows preclude the wall functions mentioned earlier; instead,

the finite difference calculations should be carried out through the viscous layer right down to the wall. Jones & Launder (1972, 1973) expanded the capability of the k-ε model to include viscous effects. The complete form of their model is given in Table 3.1, in which R_t denotes the turbulent Reynolds number ($k^2/\nu\tilde{\varepsilon}$) and $C_{\mu\infty}$ and $C_{2\infty}$ are the values assumed by C_μ and C_2 in the fully turbulent region, i.e., the values given in Section 3.2.3.

The set of equations in Table 3.1 differ from the high Reynolds number form of the k-ε model in four major ways: these are

(1) inclusion of viscous diffusion of k and $\tilde{\varepsilon}$

(2) replacement of ε by $\tilde{\varepsilon}$ as the independent variable in the dissipation equation where

$$\tilde{\varepsilon} \equiv \varepsilon - 2\mu \left(\frac{\partial k^{1/2}}{\partial x_j}\right)^2 \tag{3.13}$$

This change was motivated by computational rather than physical reasons. Measurements show that ε is approximately constant very near the wall, i.e., for $\frac{zu_*}{\nu} < 5$. This suggests a no-flux boundary condition for the ε equation. Jones & Launder (1972), however, could not get this approach to work, so instead they decided to replace ε by $\tilde{\varepsilon}$, letting $\tilde{\varepsilon}$ go to zero at the wall, and introduced into the k equation the extra term shown above, which is equal to the dissipation rate in the immediate vicinity of the wall (Jones & Launder, 1972). Away from the wall, the term goes to zero.

$$\rho\frac{Dk}{dt} = \frac{\partial}{\partial x_j}[(\frac{\mu_t}{\sigma_k} + \mu)\frac{\partial k}{\partial x_j}] + \mu_t \frac{\partial u_i}{\partial x_j}(\frac{\partial u_i}{\partial x_j} + \frac{\partial u_j}{\partial x_i}) - \rho\tilde{\epsilon} - 2\mu(\frac{\partial k^{1/2}}{\partial x_j})^2 \tag{3.12a}$$

$$\rho\frac{D\tilde{\epsilon}}{dt} = \frac{\partial}{\partial x_j}[(\frac{\mu_t}{\sigma_\epsilon} + \mu)\frac{\partial\tilde{\epsilon}}{\partial x_j}] + \frac{C_1\tilde{\epsilon}}{k}[\mu_t \frac{\partial u_i}{\partial x_j}(\frac{\partial u_i}{\partial x_j} + \frac{\partial u_j}{\partial x_i})] - \rho\frac{C_2\hat{\epsilon}^2}{k} \tag{3.12b}$$

$$+ 2\frac{\mu\cdot\mu_t}{\rho}(\frac{\partial^2 u_i}{\partial x_j \partial x_j})^2$$

$$\mu_t = \rho\frac{C_\mu k^2}{\epsilon} \tag{3.12c}$$

where,

$$C_u = C_{u\infty}\exp(-2.5/(1+R_t/50)$$

$$C_2 = C_{2\infty}(1-.3\exp-R_t^2)$$

$$R_t = k^2/\nu\tilde{\epsilon}$$

Table 3.1

Standard Low Reynold's Form of the k-ε model

(3) Dependance of C_μ and C_2 on the turbulent Reynolds number R_t $(=k^2/\nu\tilde{\varepsilon})$.

The functional form of the dependencies was determined experimentally; C_μ was determined by considering constant stress Couette flow: C_2 by analyzing the decay rate of isotropic grid turbulence (Jones and Launder, 1972).

(4) Addition of an extra term on the right-hand side of the $\tilde{\varepsilon}$ equation.

There is no physical argument for this term's adoption; it was included to produce satisfactory variation of k with distance from the wall.

Equations (3.12) represent the standard, low Reynolds number k-ε model as developed by Jones & Launder (1972, 1973). It has been extensively studied by many researchers, and found to give good agreement with experimental data for a variety of different applications, such as equilibrium sink-flow boundary layers (Jones and Launder, 1972), flow on a spinning disc (Launder and Sharma, 1974), and prediction of heat transfer coefficients on the pressure surface of a turbine blade (Turner, 1971). Classes of flow not adequately predicted by the model are strongly heated flows, and flows with large gradients of fluid properites (Launder, 1976).

It should be mentioned here that Jones and Launder's model assumes an hydraulically smooth surface, and takes no account of boundary roughness, or large obstructions like canopy elements. The effect of flow obstructions such as marsh grass is covered in the next section.

3.4 Inclusion of Obstructions in the Low Reynold's Number Model

The presence of obstructions in the flow field will affect the generation, transport, and destruction of the turbulence quantities, requiring modifications in the standard low Reynold's Number form of the k-ε model (Table 3.1). Including these modifications, the complete and final form of the turbulence closure model used in this study is given in Table 3.2.

Comparison of this set of equations with Table 3.1 reveals several basic differences; these are

(1) neglect of acceleration (D /dt) and horizontal gradients.

For typical marsh flows, as discussed in Chapter II, the ratio of the length scale in the horizontal direction (L) to that in the vertical direction (H) will be on the order of 10^3-10^4. It follows from this that the longitudinal and lateral variations of a variable will be small compared to the vertical variations (i.e., $\frac{\partial}{\partial z} >> \frac{\partial}{\partial x}, \frac{\partial}{\partial y}$)

The total derivative terms D /dt may be shown to be small by comparing them to the diffusive transport terms. As was done in the momentum equation analysis, no reference will be made to the drag related terms. The order of magnitude of the various terms can be estimated as

$$0 = \frac{\partial}{\partial z}\left[\left(\frac{\mu_t}{\sigma_k} + \mu\right)\frac{\partial k}{\partial z}\right] + \mu_t\left[\left(\frac{\partial u}{\partial z}\right)^2 + \left(\frac{\partial v}{\partial z}\right)^2\right] + \rho \frac{.01R_t}{1+.01R_t} \frac{C_d a}{2} (u^2+v^2)^{3/2}$$

$$P_s \qquad\qquad P_d$$

$$- \rho\tilde{\varepsilon} - 2\mu\left(\frac{\partial k^{1/2}}{\partial z}\right)^2 \tag{3.14a}$$

$$0 = \frac{\partial}{\partial z}\left[\left(\frac{\mu_t}{\sigma_\varepsilon} + \mu\right)\frac{\partial \tilde{\varepsilon}}{\partial z}\right] + \frac{C_1\tilde{\varepsilon}}{k}(P_s + C_1' P_d) - \rho\frac{C_2\tilde{\varepsilon}^2}{k}$$

$$+ 2\frac{\mu \cdot \mu_t}{\rho}\left[\left(\frac{\partial^2 u}{\partial z^2}\right)^2 + \left(\frac{\partial^2 v}{\partial z^2}\right)^2\right] \tag{3.14b}$$

$$\mu_t = \rho \frac{C_\mu}{\left(1 + C_\mu' \frac{P_d}{\rho\tilde{\varepsilon}}\right)} \frac{k^2}{\tilde{\varepsilon}} \tag{3.14c}$$

where

$C_\mu = C_{\mu\infty} \exp[-2.5/(1+R_t/50)]$ $\qquad$ $C_2 = C_{2\infty}(1.0-.3\exp -R_t^2)$

$C_1' = C_2/C_1$ $\qquad$ $C_\mu' = 2.6$

$R_t = k^2/\nu\tilde{\varepsilon}$

Table 3.2

Modified Version of Low Reynold's Number k-ε Model

$$u_i \frac{\partial k}{\partial x_i} = O(\frac{U\upsilon^2}{L}) \quad , \quad u_i \frac{\partial \tilde{\varepsilon}}{\partial x_i} = O(\frac{U\varepsilon}{L})$$

$$\frac{\partial k}{\partial t} = O(\frac{\upsilon^2}{T}) \quad , \quad \frac{\partial \tilde{\varepsilon}}{\partial t} = O(\frac{\varepsilon}{T})$$

$$\frac{\partial}{\partial z}(\overline{\omega'(\frac{u_i'u_i'}{2} + \frac{p'}{\rho})}) = O(\frac{\upsilon^3}{H}) \quad , \quad \frac{\partial}{\partial z}(\overline{\nu\omega'(\frac{\partial u_i'}{\partial x_j})^2} + (\frac{\nu}{\rho}\overline{\frac{\partial p}{\partial x_i}\frac{\partial \omega'}{\partial x_i}}) = O(\frac{\upsilon\varepsilon}{H})$$

where υ is the order of magnitude of the turbulent fluctuations, and U is the characteristic velocity scale. Many of the above approximations were drawn from Tennekes & Lumley (1972), as was the exact form of the transport term for the dissipation equation (Note that, for isotropic turbulence $\varepsilon = \overline{\nu(\frac{\partial u_i'}{\partial x_j})^2}$).

The ratio of the diffusive transport to $u_i \partial/\partial x_i$ is $(\frac{L}{H}\frac{\upsilon}{U})$. The value of $\frac{\upsilon}{U}$ may be roughly approximated from the friction factor expression, giving $\frac{\upsilon}{U} \sim \frac{U_*}{U} \sim .1$, as discussed earlier. The value of $(\frac{L}{H}\frac{\upsilon}{U})$ then becomes about 10^2 (with $L = 10^3$ m), large enough to justify neglecting the convective terms.

The ratio of the diffusive transport to $\partial/\partial t$ is $\frac{\upsilon T}{H} \sim \frac{.1UT}{H}$. Using the values of U, H, and T given in Table 2.1, this ratio is seen to be greater than 10, with the exception of Case 3C; as discussed earlier, the short duration of this case ($\sim$10 sec.) allows it to be ignored. In general, then, the unsteady terms may be neglected compared to the diffusive transport terms.

The physical significance of these approximations is that the vertical turbulent structure is steady, and establishes itself quickly relative to horizontal changes. Similar considerations in Chapter II led to the neglect of the Du_i/dt terms.

(2) addition of terms representing the production of turbulent kinetic energy by obstructions.

The total production of turbulent kinetic energy (P) is now

$$P = \underbrace{\mu_t\left[\left(\frac{\partial u}{\partial z}\right)^2 + \left(\frac{\partial v}{\partial z}\right)^2\right]}_{P_s} + \underbrace{\frac{.01R_t}{1+.01R_t}\,\frac{\rho C_d a}{2}\,(u^2+v^2)^{3/2}}_{P_d}$$

where the first term represents production of k due to shear (P_s) and the second production due to obstructions (P_d). The factor $\frac{.01Rt}{1+.01Rt}$ is added to force P_d to zero in the viscous zone at the water surface. In the main flow, where R_t is high, this factor approaches one.

The term P given above appears directly in the k equation; before being used in the $\tilde{\varepsilon}$ equation, P_d is multiplied by the factor $C_1'=C_2/C_1$. This ratio was chosen so that the dissipation equation would be in balance under conditions of uniform obstructed flow, in which all vertical gradients are zero. (This might happen, for instance, in flow through infinitely long cylinders, driven by a pressure gradient). The k equation under these conditions reduces to a balance between P_d and $\tilde{\varepsilon}$; the dissipation equation becomes $\frac{C_1\tilde{\varepsilon}}{k}(C_1'P_d) = \frac{C_2\rho\tilde{\varepsilon}^2}{k}$, which is in balance if $C_1'=C_2/C_1$.

(3) addition of a term reducing the effect of k on μ_t.

The motivation behind this alteration can best be explained by considering fluid flow past an idealized, vertically oriented obstruction. Most of the eddies produced in the wake of this element will have vertical vorticity; while adding to u' and v', they will have relatively less of an effect on w'. This idea is corroborated by investigations of Seginer (1976) and Shaw et al (1974), who found that u' > v' > w' within the canopies they studied. The effect of this is that, while the obstruction produced eddies contribute to k (via u'u' and v'v'), they contribute relatively less to u'w' shear, and to the vertical diffusion of turbulence. To reduce the effect of k on μ_t, the following relationship was proposed,

$$\mu_t = \rho \frac{C_\mu}{(1+C'_\mu \frac{P_d}{\rho\tilde{\varepsilon}})} \frac{k^2}{\tilde{\varepsilon}}$$

where $C'_\mu = 2.6$ was determined by trial and error to give the best fit to experimental data from four laboratory studies of obstructed flow, discussed in Section 3.7.2. Figures 3.1 and 3.2 show the results of two of these studies, conducted by Plate (1965) and Thom (1971) in a wind tunnel. The motion within the obstructions is driven by energy diffused downward from the top of the canopy. At any level within the canopy, some of this energy is expended in overcoming the drag forces.

Also shown in Figure 3.2 are model predictions made with $C'_\mu = 0$, 1.3, 2.6, and 3.9. The reasons behind the different shapes of the velocity profiles are given below.

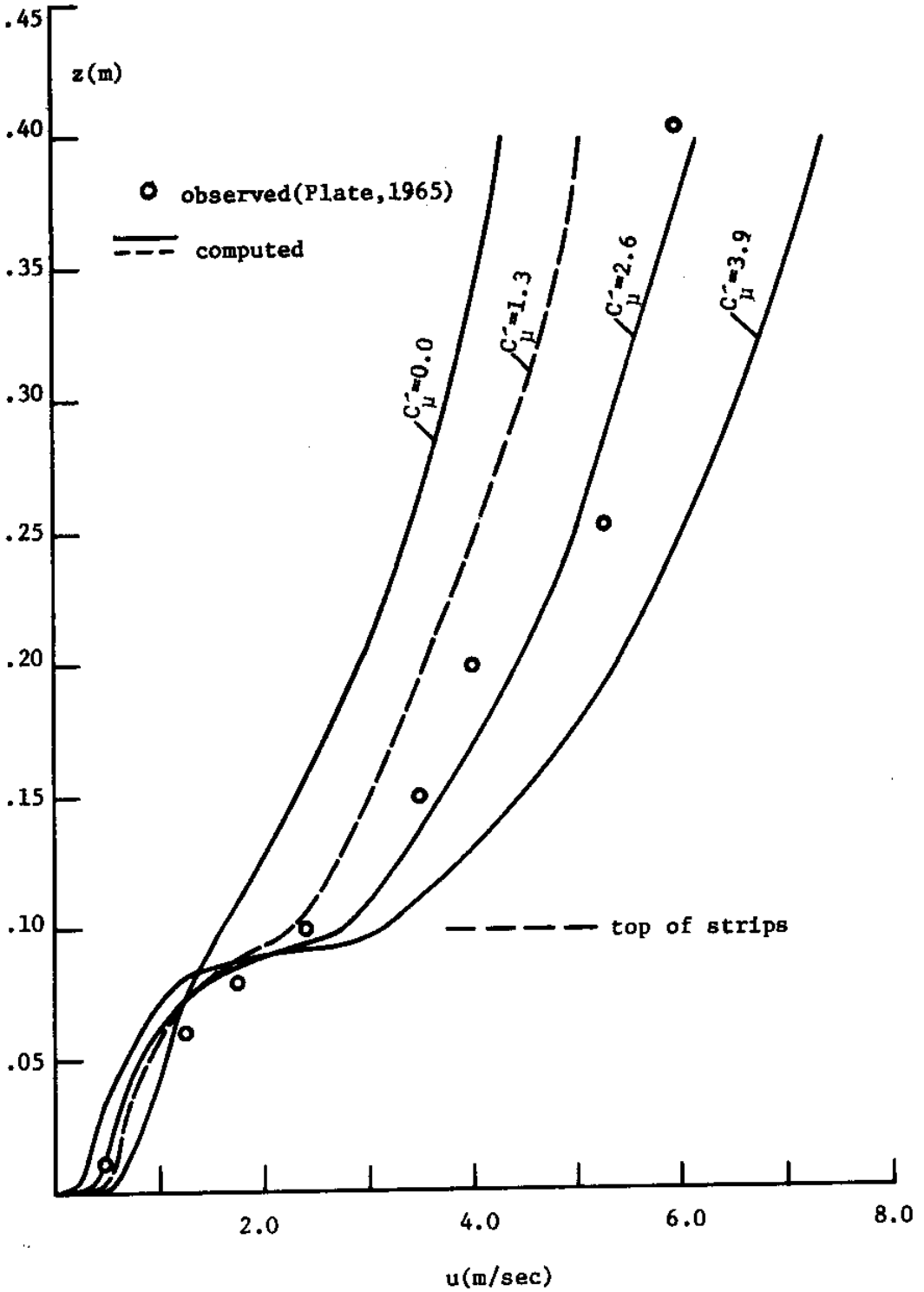

Figure 3.1 - Model Runs Illustrating Effect of C'_μ on Velocity Profiles in Rectangular Strips.

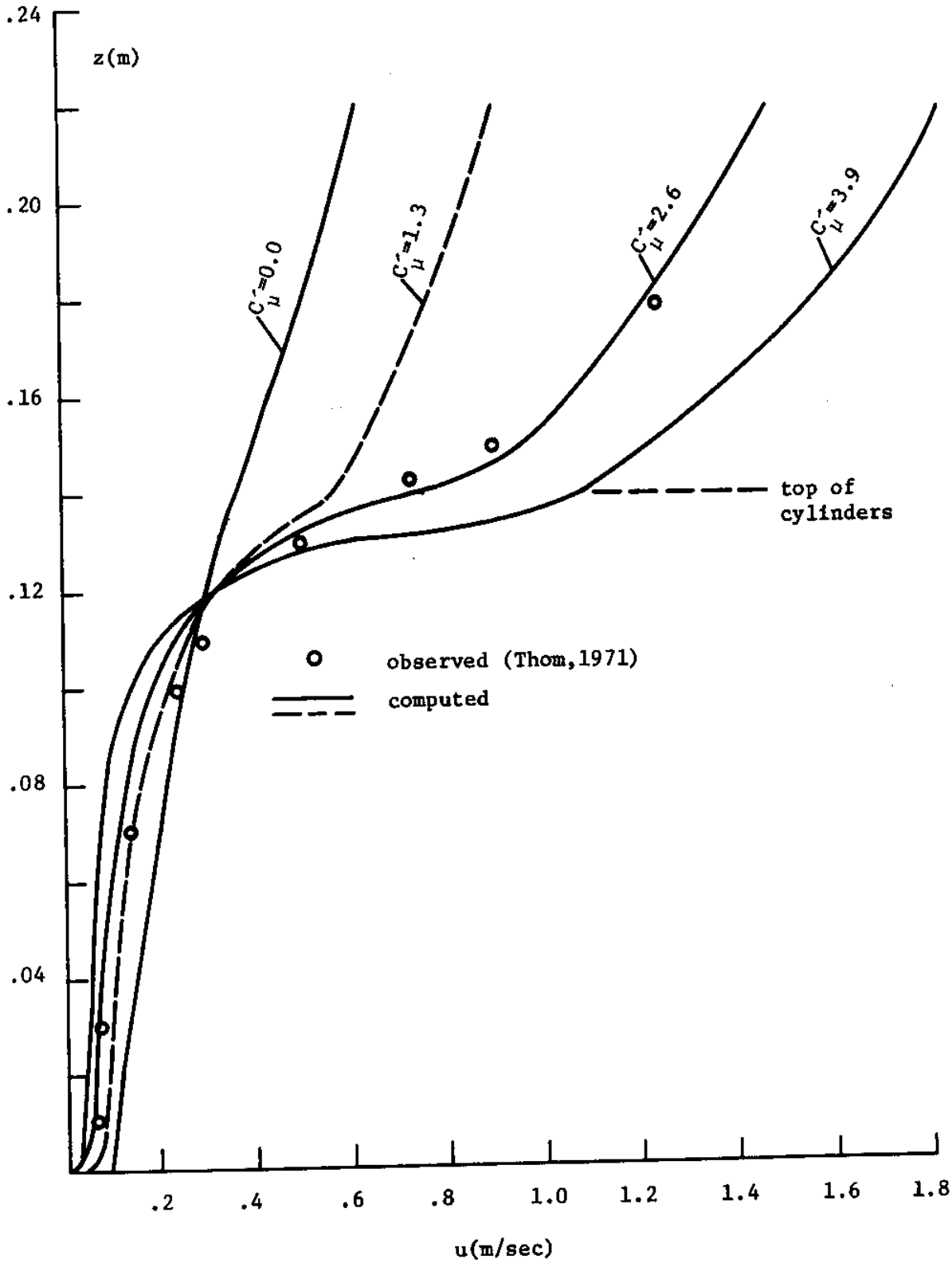

Figure 3.2 - Model Runs Illustrating Effect of C'_μ on Velocity Profiles in Circular Cylinders.

As seen from the above expression, μ_t varies inversely with C_μ', other factors being kept constant. For C_μ' equal to 0 or 1.3, k contributes a relatively large amount to μ_t. The resulting large values of μ_t imply a higher level of turbulence, and thus more downward diffusion of energy; since this energy drives the flow, the velocity profiles within the canopy are larger, and more uniform, compared to the predictions made with higher values of C_μ'. In these cases, μ_t is relatively smaller, and there is less downward diffusion of energy; subsequently, the stress, as well as the velocity, attenuate more quickly in the canopy. This is especially true near the top of the canopy, where the larger gradients affect the profiles above, as well as below, the level $z=h_g$. These trends are seen in Figures 3.1 and 3.2.

Above the obstructions, P_d is zero, and μ_t reverts back to the form proposed by Launder and Spalding. At $z=h_g$, where P_d changes suddenly to zero, μ_t increases sharply; for the case with $C_\mu' = 2.6$, μ_t changes by a factor of about six between the two grid points lying just below and just above the top of the obstructions. (All other variables, u, v, k, ε and τ change smoothly in this region.)

Remembering that $\mu_t = k^{1/2}\ell$, this sudden, discontinuous, change in μ_t implies a correspondingly abrupt change in the turbulent length scale (ℓ). On physical grounds, one would like ℓ to be a continuous function of height. Still, however, it is possible to argue that, by drastically altering the flow environment at $z=h_g$, equally drastic changes may be induced in ℓ. Additionally, if the vegetation density (a) goes gradually to zero, P_d will also change gradually, as will ℓ.

The variation of μ_t proposed here has extended the range of applicability of the k-ε model. Different functions for μ_t have been put forth by other researchers to obtain more acceptable predictions with certain kinds of flows. One such function was introduced by Rodi (1972) for flows, such as far field jets or wakes, where the velocity differences across the flow are small compared to the free stream velocity, and where the turbulence is weakly strained by the mean flow. Correlating the experimental data, Rodi proposed a function $C_\mu = g(P/\varepsilon)$ which was found by others (Launder et. al., 1973) to significantly improve the predictions over those obtained by using the standard high Reynold's form of C_μ (i.e., $C_\mu = .09$).

The reason why $C_\mu = .09$ did not work well in these cases can be traced to the fact that this value was chosen on the basis of experiments in which the production P and dissipation ε were in approximate balance. For the types of flow mentioned above, P/ε is much less than unity, requiring different values of C_μ. A detailed analysis of the conditions under which $C_\mu = .09$ is given by Rodi (1975).

At this point, the model formulation is complete. Before proceeding to the boundary conditions, and the numerical solution scheme, some discussion will be given concerning the limitations of the k-ε approach as it relates to the objectives of this study.

One limitation of the model is that it is unable to account for bottom roughness, which is equivalent to saying that an hydraulically smooth surface is assumed in all calculations. For most situations involving obstructed flow, however, it seems likely that this will not be a

very serious concern. In contrast to non-obstructed flow situations, such as open channel flow, where most of the turbulence is generated at the bottom, and then diffuses upward, much of the turbulence in obstructed-flow cases will be generated in the main flow region, and then diffuse downward. Thus, it seems probable that the near-wall turbulence will be dominated by downward diffusion from above, and will be relatively unaffected by the bottom roughness.

A second limitation of the model is that it assumes the local state of turbulence can be characterized by one velocity and one length scale, and that the Reynold's stresses can all be related to these scales by an eddy viscosity expression. This relation often implies that the transport of the individual stresses is not adequately accounted for, even if the transport of the characterizing scales are (Rodi, 1981). In particular, the model can not distinguish between shear and wake-generated turbulence. As noted by Thom (1981), the wake produced turbulence will have a length scale on the order of the size of the obstructions, which will usually be smaller than the characteristic length scale of the shear generated turbulence. The wake generated turbulence is thus more quickly dissipated into heat (the dissipation rate being inversely proportional to the length scale), and so is short-lived in the canopy environment, having less effect on the total canopy turbulence. The model takes no account of this phenomenon.

To the author's knowledge, there is no existing canopy model that handles this effect, owing largely to the difficulties involved in separately treating the dissipation generated by the obstructions.

Wilson and Shaw (1976) note that a model including separate treatment of wake generated turbulence would provide a better understanding of the processes governing the interactions between the fluid and the obstructions, but would not likely produce major changes in the calculated flow field.

Allowing for more than one turbulent length or velocity scale would require a higher order model, involving transport equations for the individual turbulent stresses, with each new equation introducing additional turbulent correlations to be simulated. Launder and Spalding (1972) state that, in general circumstances, a length scale equation is needed more than transport equations for the individual Reynold's stresses. The complexity of these higher order models, and the uncertain benefits in accuracy for obstructed flows, made them seem inappropriate for the purposes of this study.

3.5 Boundary Conditions

Figure 3.3 shows the two basic flow regimes (free surface water flow and overlying air flow) found in marsh flow applications. The primary interest in the air flow is to predict the wind stress (τ) at the air-water interface. Each of these regimes has its own boundary conditions. For the free surface flow, the lower and upper boundary conditions are

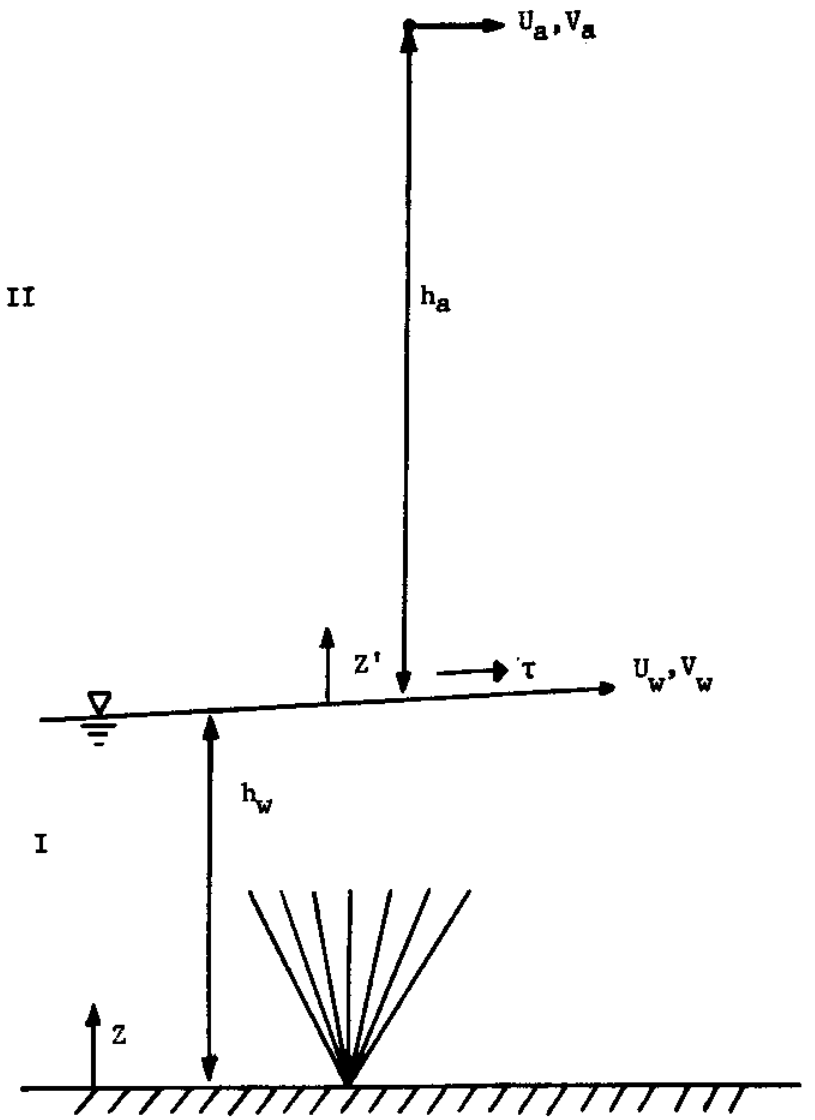

Figure 3.3 - Two Flow Regimes (confined and unconfined) Considered in Model Simulations.

$$u=v=0 \qquad @\ z=0 \qquad (3.15a)$$
$$k=\tilde{\varepsilon}=0$$

$$k=\tilde{\varepsilon}=0$$
$$\mu\frac{du}{dz} = \tau_x \qquad @\ z=h_w \qquad (3.15b)$$
$$\mu\frac{dv}{dz} = \tau_y$$

For the air flow, the upper boundary conditions are

$$u = U_a$$
$$v = V_a \qquad @\ z'=h_a \qquad (3.16a)$$
$$\mu_t \frac{d\tilde{\varepsilon}}{dz} = \mu_t \frac{dk}{dz} = 0$$

where U_a and V_a are prescribed velocities at some reference height h_a. The lower boundary conditions are

$$u = U_w$$
$$v = V_w \qquad @\ z'=0 \qquad (3.16b)$$
$$\tilde{\varepsilon} = k = 0$$

where U_w and V_w are the velocities of the water surface. For virtually all practical applications, U_w and V_w will be at least an order of magnitude less than the velocities in the air, allowing U_w and V_w to be set equal to zero. This greatly simplifies the calculations, avoiding the need for iterating back and forth between the air and water flow computations.

The boundary conditions may be altered as the need arises; for instance, in a wind tunnel study, the same boundary conditions

($u=v=k=\tilde{\varepsilon}=0$) may be applied at both upper and lower surfaces. If warranted, as for example in computing the wind stress in a case where the grass is completely submerged baneath the water surface, recourse may be had to the wall functions described earlier.

3.6 Solution Technique

Having arrived at the model equations (3.14), it remains to devise a method for solving them numerically. The equations have the simplifying feature of being one-dimensional: on the other hand, they are complex, inter-linked, and non-linear, making them hard to evaluate numerically, prone to instability, and requiring an iterative solution technique. A finite control volume approach was decided upon as the best way of discretizing the equations. This approach is developed by Patanker (1980), from which much of the following discussion is taken.

3.6.1 General Discretization Equation

The differential equations of the model may all be cast into the general form

$$\frac{d}{dz}\left(\Gamma \frac{dT}{dr}\right) + S = 0 \qquad (3.17)$$

where T is the dependent variable, Γ is the diffusion coefficient, and S is a source term. This is an important time-saving step; as a consequence, it is only necessary to be concerned with the numerical solution of (3.17); the equations for velocity, kinetic energy, and dissipation are particular cases of (3.17), with different forms of Γ

and S, and with appropriate boundary conditions.

Equation (3.17) is solved numerically using the control volume approach, whereby the calculation domain is divided into a number of non-overlapping control volumes, each of which surrounds a single grid point. The differential equation is integrated over each control volume, resulting in a set of linear algebraic equations that are then solved simultaneously.

To derive the discretization equation, consider Figure 3.4, showing a single control volume (dashed lines) surrounding a grid point P, with neighboring points U and D. Integrating (3.17) over the control volume, of unit depth and length Δz, leads to

$$\left(\frac{\Gamma dT}{dz}\right)_u - \left(\frac{\Gamma dT}{dz}\right)_d + \bar{S}\,\Delta z = 0 \qquad (3.18)$$

where $\bar{S}$ is the average value of S over the control volume.

$\bar{S}$ may be a function of the dependent variable T, and it is then desirable to incorporate this dependence directly into the discretization equation. Only a linear dependence is allowed, because as will be seen later on, the discretization equations will be solved using the techniques of linear algebraic equations. $\bar{S}$ is linearized in the form

$$\bar{S} = S_c + S_p \cdot T_p \qquad (3.19)$$

where S_c is the constant part of S, and S_p is the coefficient of T_p.

Evaluating $\frac{\Gamma dT}{dz}$ with a linear profile, and using the above expression for $\bar{S}$, (3.18) becomes

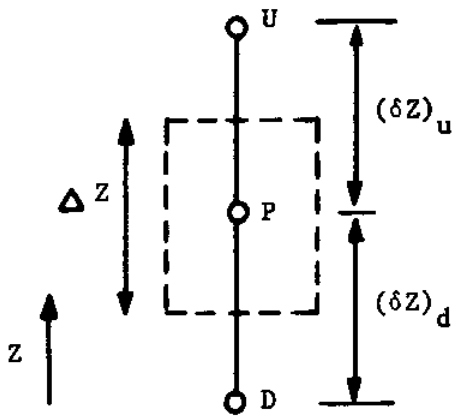

Figure 3.4 - Control Volume Surrounding Grid Point P.

$$\frac{\Gamma_u(T_U - T_P)}{(\delta z)_u} - \frac{\Gamma_d(T_P - T_D)}{(\delta z)_d} + (S_c + S_p T_p)\,\Delta z = 0 \qquad (3.20)$$

or, rearranging

$$a_P T_P = a_U T_U + a_D T_D + b \qquad (3.21)$$

where

$$a_U = \frac{\Gamma_u}{(\delta z)_u} \qquad (3.22a)$$

$$a_D = \frac{\Gamma_d}{(\delta z)_d} \qquad (3.22b)$$

$$a_P = a_D + a_U - S_P\,\Delta z \qquad (3.22c)$$

$$b = S_c\,\Delta z \qquad (3.22d)$$

Equation (3.21) is the final form of the discretization equation for the control volume surrounding point P. The coefficients in the discretization equation contain source terms S_c and S_p, as well as conductivity terms Γ_u and Γ_d. The method of determining these terms is described below.

Treatment of Conductivity Terms

Inspection of (3.21) shows that Γ_u, Γ_d represent the value of Γ at the control-volume interfaces; typically, however, the values of

Γ will only be known at the grid points D, P, U. It then becomes necessary to evaluate the interface conductivity, say Γ_d, in terms of these grid point values. Following the suggestion of Pantanker (1980), the interface conductivities are found using the harmonic mean of the neighboring points. Thus, for instance, Γ_d is given by

$$\Gamma_d = \frac{\partial \cdot \Gamma_P \cdot \Gamma_D}{\Gamma_P + \Gamma_D} \tag{3.23}$$

Equation (3.23) assumes that the control voluem face lies halfway between the grid points, which will be true for this study.

Treatment of Source Terms

When linearizing the source terms as $\bar{S} = S_c + S_p \cdot T_p$, specific rules must be followed in determining S_c and S_p if instabilities and physically unrealistic solutions are to be avoided. S_p should be less than or equal to zero, because only then will the coefficient a_P be always-positive. This is one of the paramount rules of the control volume approach; all coefficients a_U, a_D, a_P must always be positive. Pantanker (1980), explaining this rule, states

> "Most situations of interest here will be such that the value of a dependent variable at a grid point is influenced by the values at heighboring grid points only through the process of convection and diffusion. Then it follows that an increase in the value at one grid point should, with other conditions remaining equal, lead to an increase, and not a decrease, in the value at the neighboring grid point. In (3.21) if an increase in T_U must lead to an increase in T_P, it follows that the coefficients a_U and a_P must have the same sign. We can, of course, choose to make them all positive, or all negative".

A second rule for physically realistic solutions is that S_c be positive in the discretization equations for kinetic energy and dissipation. The physical interpretation of k and $\tilde{\epsilon}$ requires that their values be positive; to ensure this, the appropriate values of S_c must be always-positive. As a general rule, positive values of S_c in the discretization equation for a dependent variable T guarantee that no negative values of T will arise in the solution. Since negative values of velocity are allowable, at times even desirable, this requirement does not apply to the momentum equation.

This section has outlined the general rules used in linearizing the source terms; the explicit relationships for S_c and S_p appropriate to the different model equations are shown in Table 3.3. From this table, it is seen that for all equations S_p is less than zero; for the kinetic energy and dissipation equations, S_c is greater than zero, while for the momentum equation S_c may be either positive or negative, depending on the sign of $\frac{\partial n}{\partial x}$

3.6.2 Boundary Conditions

Consider Figure 3.5, showing a string of grid points. A discretization equation like (3.21) can be written for the control volumes surrounding the internal points (I, D, P, U). The end points

Equation	S_c	S_p
Momentum (2.8)	$-\rho g \frac{\partial \eta}{\partial x_i}$	$\frac{-\rho C_d a}{2}(u_{jj})^{1/2}$
Kinetic Energy (3.14a)	$\mu_t((\frac{\partial u}{\partial z})^2+(\frac{\partial v}{\partial z})^2]+\rho(\frac{.01R_t}{1+.01R_t})\frac{C_d a}{2}(u^2+v^2)^{3/2}$ P_s $\quad$ P_d	$\frac{-\rho\tilde{\epsilon}}{k}\frac{-2\mu}{k}(\frac{\partial k^{1/2}}{\partial z})^2$
Dissipation (3.14b)	$\frac{C_1\tilde{\epsilon}}{k}(P_s+C_1'P_d) + \frac{2\mu.\mu_t}{\rho}[(\frac{\partial^2 u}{\partial z^2})^2+(\frac{\partial^2 v}{\partial z^2})^2]$	$\frac{-C_2\rho\tilde{\epsilon}}{k}$

Table 3.3

Source Term Coefficients

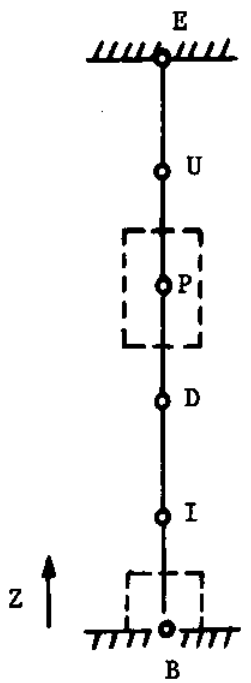

Figure 3.5 - Sample Calculation Domain

B and E require special attention, as it is through them that the boundary conditions enter the numerical scheme. There are two kinds of boundary conditions encountered in this study: (1) T specified, and (2) flux of T specified. For the rest of this discussion, attention will be focused on the lower boundary B.

If T_B is specified, no additional equations are required. If the flux is specified, an additional equation is needed for T_B. This is achieved by integrating the differential equation over the "half" control volume, an enlarged view of which is shown in Figure 3.6.

Proceeding along the lines of the last section leads to

$$q_B - \frac{\Gamma_i(T_B-T_I)}{(\delta z)_i} + (S_c+S_p \cdot T_B)\ \Delta z = 0 \qquad (3.24)$$

where $q_B = -\left(\frac{\Gamma dT}{dz}\right)_B$ is the boundary flux. Rearranging this expression into the standard form gives

$$a_B T_B = a_I T_I + b \qquad (3.25)$$

where

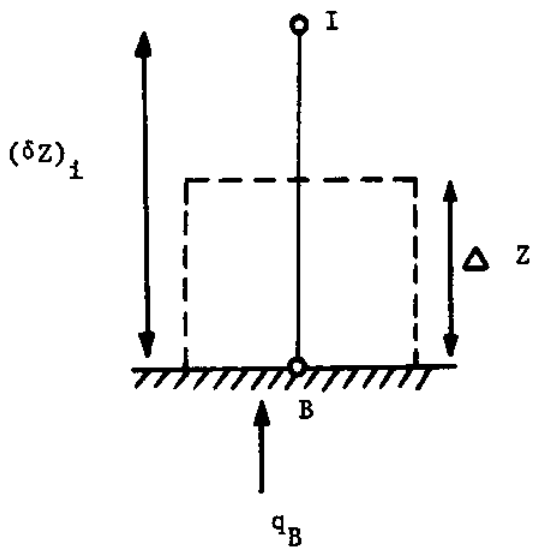

Figure 3.6 - Half Control Volume at Boundary

$$a_I = \frac{\Gamma_i}{(\delta z)_i} \tag{3.26a}$$

$$b = S_c \cdot \Delta z + q_B \tag{3.26b}$$

$$a_B = a_I - S_p \cdot \Delta z \tag{3.26c}$$

In this manner the discretization equations for the boundary grid points are constructed; combining these equations with those for the internal grid points gives the required number of equations for the unknown variables. The equations are nominally linear and tridiagonal - as such, they can be solved directly using the Thomas algorithm (Pinder and Gray, 1977).

3.6.3 Grid Spacing

It is not necessary that the grid points in Figure 3.5 be equally distant apart; indeed, there are decisive advantages for not having uniform grid spacing. Near solid surfaces, or other interfaces, where the variable gradients are steep, a finer grid spacing is needed than in the main flow region, where the gradients are relatively smaller. A variable grid scheme provides efficient use of the program's computing power, deploying it to those areas where it is needed most.

There are no universal rules concerning the correct spacing of adjacent grid points. The scheme used in this study was to start out from the wall using a certain grid size (Δz_w), doubling or tripling

the grid size every five steps until some maximum grid size (Δz_{max}) was reached. The size of Δz_{max} was about .05m for water flow, and about .25m for air flow.

Proper resolution of the viscous sublayer was found to require very small values of Δz_w, and consequently large numbers of grid points. For typical marsh flow, as an example, the turbulent Reynold's number R_t becomes equal to one at about $z=.1x10^{-3}$m. Assuming 10 grid points are needed to resolve the zone between the point and the wall, Δz_w must be about $.1x10^{-4}$m. With this value, and Δz_{max}=.05m, 137 grid points are necessary to cover a .20m water column, with a viscous zone at each end.

The need for so many grid points is one of the less desirable features of the model, and one in which more work would be useful. It is possible, for instance, that the value of Δz_w could be relaxed, without a disproportionate loss of accuracy in the solutions. Ideally, the viscous zone could be avoided by developing wall functions similar to those discussed earlier for non-obstructed flows.

3.6.4 Outline of Solution Scheme

The model equations are solved using an iterative technique. The steps of this process are:

(1) Guess, or estimate, the value of the dependent variables ($u,v,k,\tilde{\epsilon},\mu_t$) at all grid points.

Obviously, the closer the initial guess to the final results, the less work involved in reaching a solution. If the initial guess is

too far off, the whole process may diverge. Where possible, it is recommended to use as an initial guess the solution to a previous run, similar to the one being studied. If no such numbers are available, realistic profiles of the variables calculated analytically should be used. In the presence of grass, where such profiles may be unknown, a good idea is to start out by solving a no-grass case having the same geometry and forcing functions; using these solutions as an initial guess, the grass is then introduced by stages, the output of one stage forming the input of the next stage, until the final results are obtained.

(2) Using the guessed values, solve the model equations to get new values of the dependent variables.

Following the principles outlined in Section 3.6.1, the differential equations of the model have now all been cast into nominally linear form. The coefficients of these linear equations are calculated using the estimated values from step one. The nominally linear algebraic equations for one dependent variable at a time are then solved using the Thomas Algorithm. The discretization equations for k and $\tilde{\varepsilon}$ are solved twice for each calculation of the velocities (u,v); this slows down the rate of change of k and $\tilde{\varepsilon}$, thus helping to prevent instabilities.

(3) Under-relax the new values of the dependent variables.

This is a crucial step in the solution scheme. By slowing down the change, from iteration to iteration, in the values of the variables, under-relaxation helps to avoid divergence. The general under-relaxation scheme is

$$T = \alpha \cdot T_{new} + (1-\alpha) \cdot T_{old} \tag{3.27}$$

where α is the under-relaxation factor, T_{old} and T_{new} are the old and new values of T, respectively. Gosman (1976) suggests using α in the range .5-.7. A commonly used value in this study was α = .75. The importance of under-relaxation can not be overstated. If all the variables (u,v,k, $\tilde{\varepsilon}$, μ_t) are not under-relaxed after every iteration, numerical instabilities will inevitably result.

(4) With the under-relaxed variables as better guesses, return to Step (2) and repeat the process until further iterations produce no significant changes in the values of the dependent variables.

The iteration process is terminated when some convergence criterion is satisfied. Following the suggestion of Pantanker (1980), convergence is monitored by examining how perfectly the current values of the dependent variables satisfy the discretization equations. For each grid point, a residual R can be defined as

$$R = a_P T_P - a_U T_U - a_D T_D - b \tag{3.28}$$

Obviously, when R is zero, the equation is completely satisfied. The criterion used in this study is to require R to be less than some small percentage of $a_P T_P$, which will generally be the biggest term on the right-hand side of (3.28). The convergence criterion can be written as

$$\frac{|R|}{a_P T_P} < \text{eps} \qquad (3.29)$$

A value of eps = .001 was found to yield good agreement with analytical and experimental results, without requiring excessive iterations.

An alternative procedure to measuring the percent change in R would have been to monitor the magnitude of R, requiring it to be less than some small number. Accurate specification of this number would depend on the physical circumstances, which would likely change from one problem to the next, requiring recalculation of the convergence criterion number. This problem is avoided by using a percent change approach.

3.7 Model Verification

The computer program, having been written and coded, was tested by comparing numerical solutions against analytical and experimental results. As a first step, non-obstructed flows were examined, as they were the simplest, and best understood. These comparisons served to determine whether the model equations were being solved correctly, and to evaluate the convergence formulation.

The next step in the verification process was to examine obstructed flows. The goals here were to determine the empirical coefficient C'_μ

(discussed in Section 3.3), analyze the correctness of the model idealizations, and their applicability under natural conditions.

3.7.1 Flows without Obstructions

Open Channel Flow - Smooth Bottom

The first case considered here is that of water flowing down a smooth slope. Figure 3.7 shows the physical set-up, along with plots of u/u_* as predicted by the model, observed by Nagakawa et. al., (1975) and determined analytically using the formula (Schlichting, 1968)

$$\frac{u}{u_*} = 2.5 \ln \left(\frac{u_* z}{\nu}\right) + 5.5 \qquad (3.30)$$

This relationship, although derived for the region close to the wall, has been found to approximate the velocity throughout the channel depth. The friction factor for smooth surfaces at large Reynolds numbers is (Schlichting, 1968)

$$\frac{1}{\sqrt{f}} = 2 \log(R\cdot\sqrt{f}) - .8 \qquad (3.31)$$

where U = average channel velocity, R=Reynold's number $(R=\frac{4Uh}{\nu})$, h=channel depth, and f = friction factor $(f=8(u_*/U)^2)$. The value of f calculated using the above formula and that predicted by the model are .015 and .016, respectively $(R=3\cdot10^5)$.

In Figure 3.8 dimensionless profiles of k and ϵ predicted by the model are compared with experiments for developed open channel flow by Nagakawa et. al., (1975). The good agreement reconfirms that the model equations are being solved correctly.

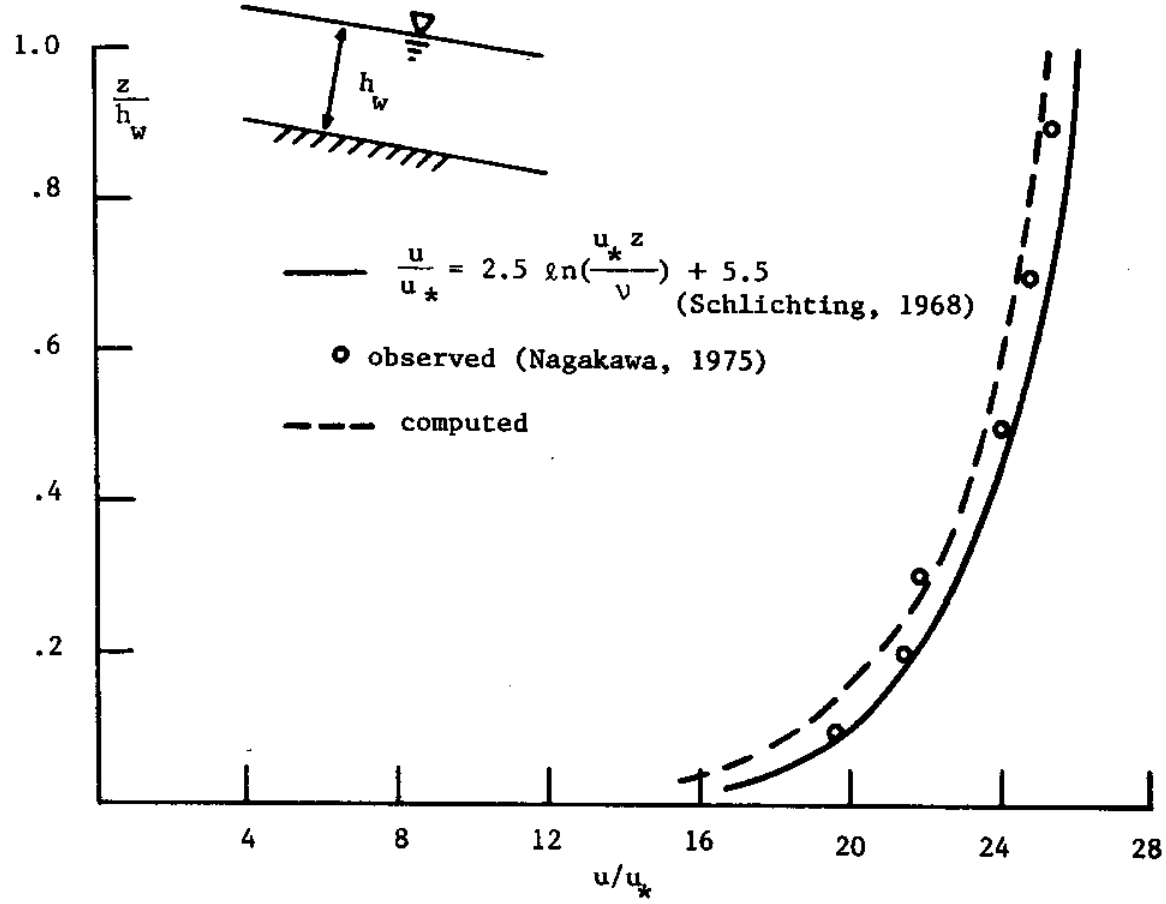

Figure 3.7 - Open Channel Flow

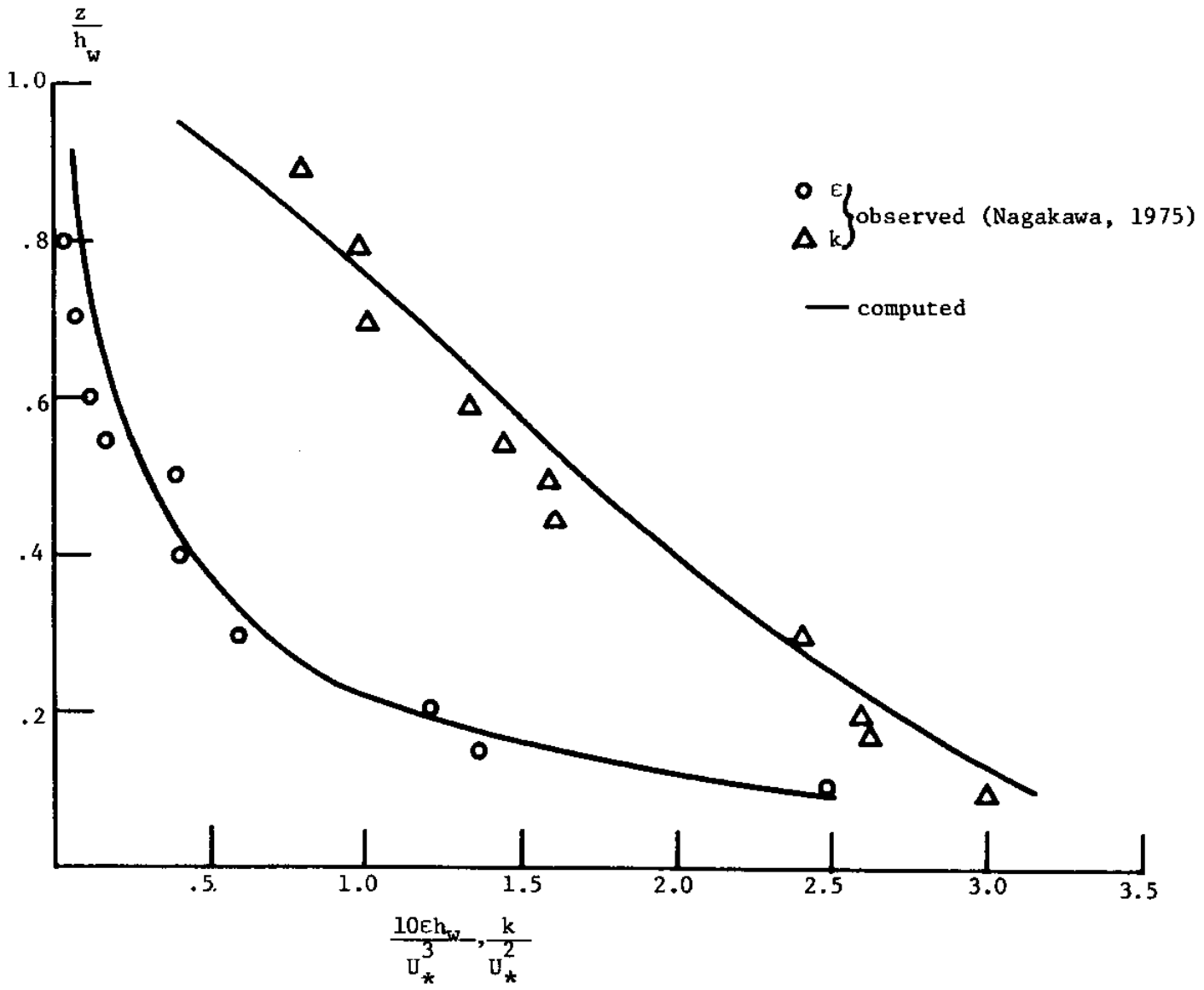

Figure 3.8 - Comparison of Experimental Results (Nagakawa, 1975) and Numerical Model Solutions for Smooth Bottom Open Channel Flow.

Couette Flow

The second non-grass flow case examined was plane Couette flow in a smooth channel. Model predictions were compared against the experimental data of Robertson (1959). Figure 3.9 shows the observed and predicted values of u/u_* against depth. Since the velocity profile is symmetric about the channel center-line, only values for half the channel depth are given. (The fact that the computer program exhibited the expected symmetry is in itself one check of the program). The observed and predicted values of the friction factor f are .0187 and .0183, respectively.

3.7.2 Obstructed Flow Studies

The next step in the verification process was to look at obstructed flow experiments. A review of the literature turned up numerous investigations of flow in canopies, conducted both in the laboratory, and in the field. Owing to their more controlled nature, the laboratory studies were used to determine the empirical coefficient C'_μ. Once determined, the value of this coefficient was held constant in all subsequent work.

Laboratory Studies of Canopy Flow

Four laboratory studies were examined; three were conducted in wind tunnels, the fourth in a water flume. Table 3.4 gives the physical description of each experiment. For Kouwen's water flume (1969) study, u, k, and $\tilde{\varepsilon}$ were set to zero at the bottom of the flume; at the surface, τ, k, and $\tilde{\varepsilon}$ were set to zero. For Plate (1965) and Thom (1971), u, k,

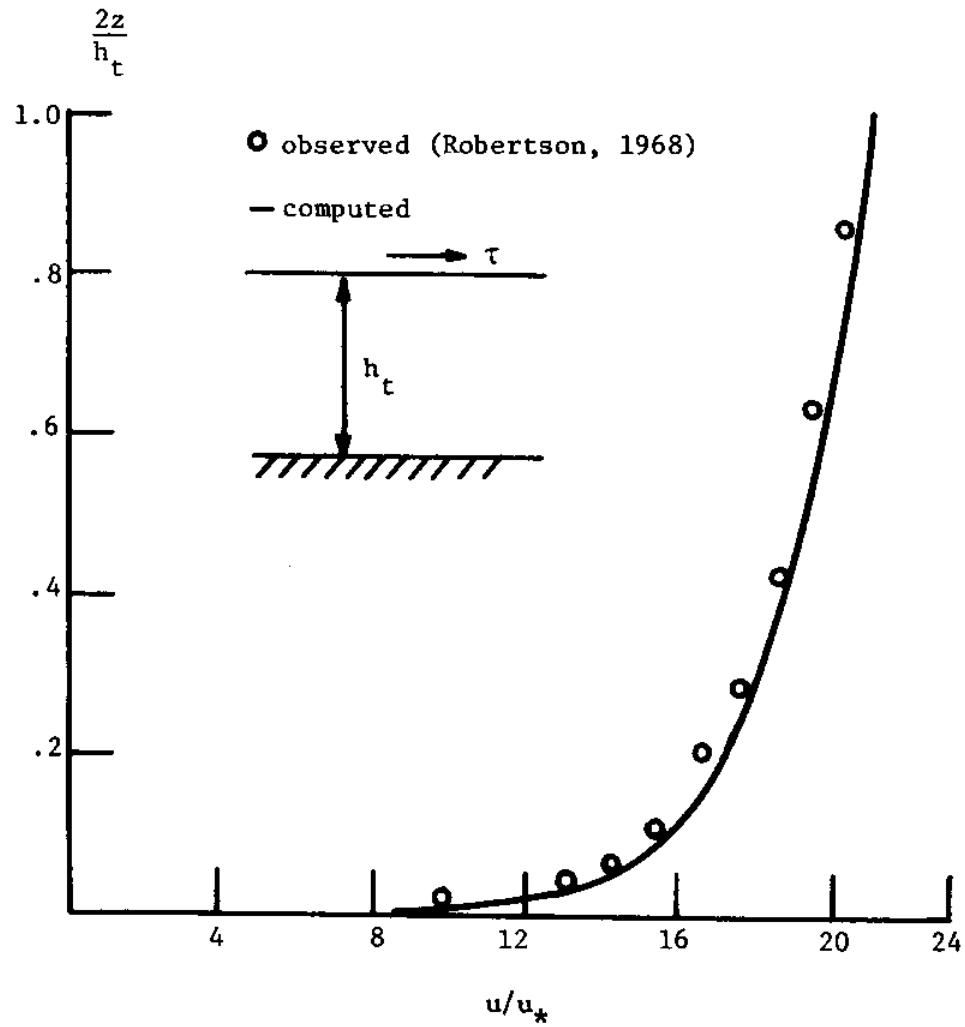

Figure 3.9 - Comparison of Experimental Results (Robertson, 1968) and Numerical Model Solutions for Smooth Boundary Couette Flow.

Author	Type of Canopy	$a(m^{-1})$	C_d	Experimental Apparatus	Boundary Conditions
Thom (1971)	c. cylinder with dia.=.001m	10	c. cylinder*	wind tunnel	$u=k=\tilde{\epsilon}=0$ @ $z=0,h_t$**
Plate (1965)	rectangular strips	5	2.0	wind tunnel	$u=k=\tilde{\epsilon}=0$ @ $z=0,h_t$**
Seginer (1976)	c. cylinder with dia.=.003m	5	$\frac{\text{c.cylinder*}}{3}$	wind tunnel	$u=k=\tilde{\epsilon}=0$ @ $z=0$ F_k+$=F_u=F_{\tilde{\epsilon}}=0$ @ $z=.53m$
Kouwen (1969)	rectangular strips	25	2.0	water flume	$u=k=\tilde{\epsilon}=0$ @ $z=0$ $F_u=k=\tilde{\epsilon}=0$

*as given by Schlichting (1968)

**h_t = height of wind tunnel

+F = vertical flux

Table 3.4

Laboratory Studies used in Model Comparisons

and $\tilde{\varepsilon}$ were set to zero at the top and bottom of the wind tunnel. For Seginer (1976), the upper boundary conditions were changed, in that the fluxes of the variables were set to zero at z= .53 m, where $\frac{du}{dz}$ was given to be zero.

A pressure gradient was assumed to drive the flow in the three wind tunnel studies. Seginer (1976) claims to have made $\frac{dp}{dx} = 0$ by adjusting the wind tunnel ceiling. Nonetheless, the variation of shear stress above the canopy is linear, as it would be in pressure driven flow. Seginer maintains that this is due to convection, implying that the flow decelerates as it moves down the tunnel. Whether $\frac{dp}{dx}$ is actually zero is not certain; the velocity and stress profiles are very similar to those expected in pressure driven flow, and this is what was assumed. Neither Plate or Thom make any reference to this matter.

The values of C_d used in the model predictions for Thom and Seginer were those determined experimentally by the authors. The factor of 1/3 in Seginer's estimate of C_d may be interpreted as the ratio of the drag coefficient measured in situ within the canopy to that measured for a single element in an equivalent uniform wind. This ratio is commonly called the shelter effect, as discussed in Chapter II. The value of C_d used in Kouwen and Plate's comparisons were taken to be that of a rectangular strip (Daily and Harleman, 1973).

A value of $C'_\mu = 2.6$ was found by trial and error to give the best fit to the four data sets, as discussed in Section 3.4. Figures 3.10-3.13 show the observed and predicted velocity profiles for the

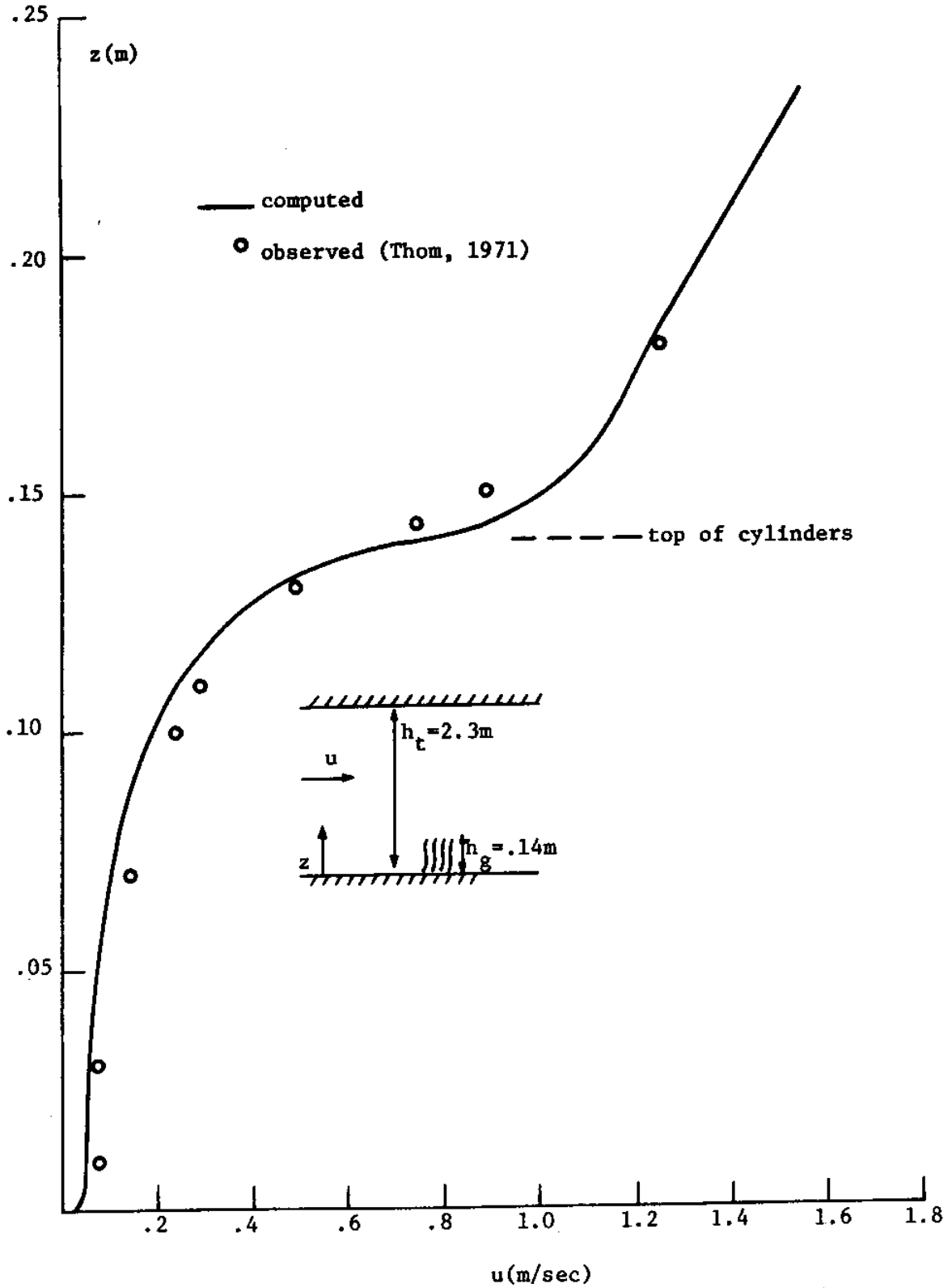

Figure 3.10 - Comparison of Observed Velocity Measurements (Thom, 1971) and Computed Model Value for Wind Tunnel Study of Flow through Circular Cylinders

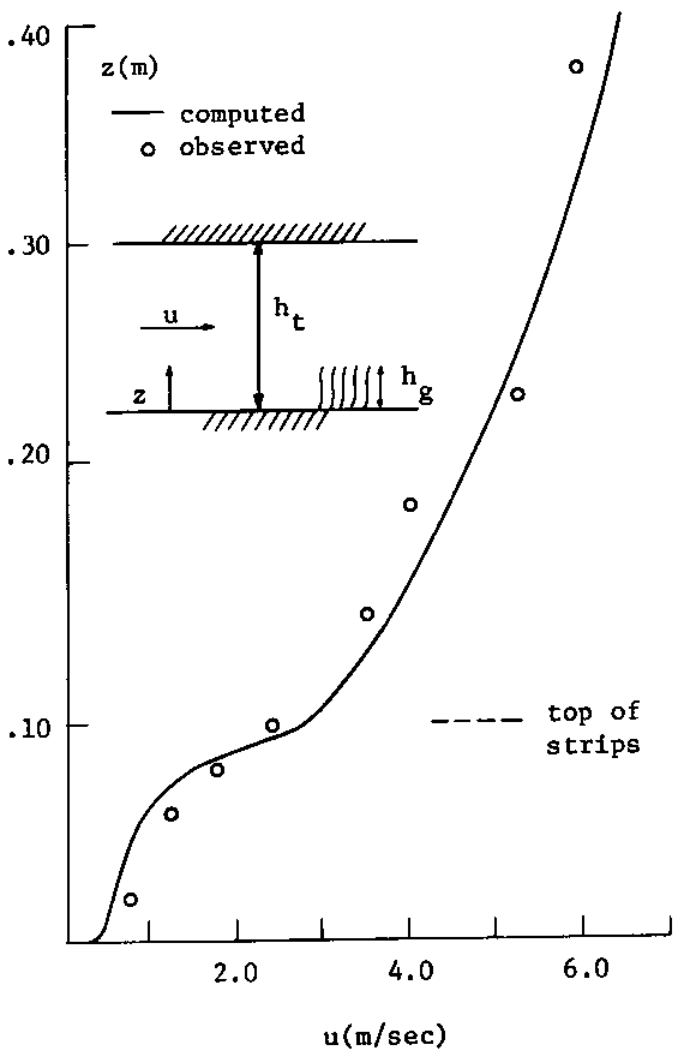

Figure 3.11 - Comparison of Observed (Plate, 1965) and Computed Model Values of Flow through Rectangular Strips.

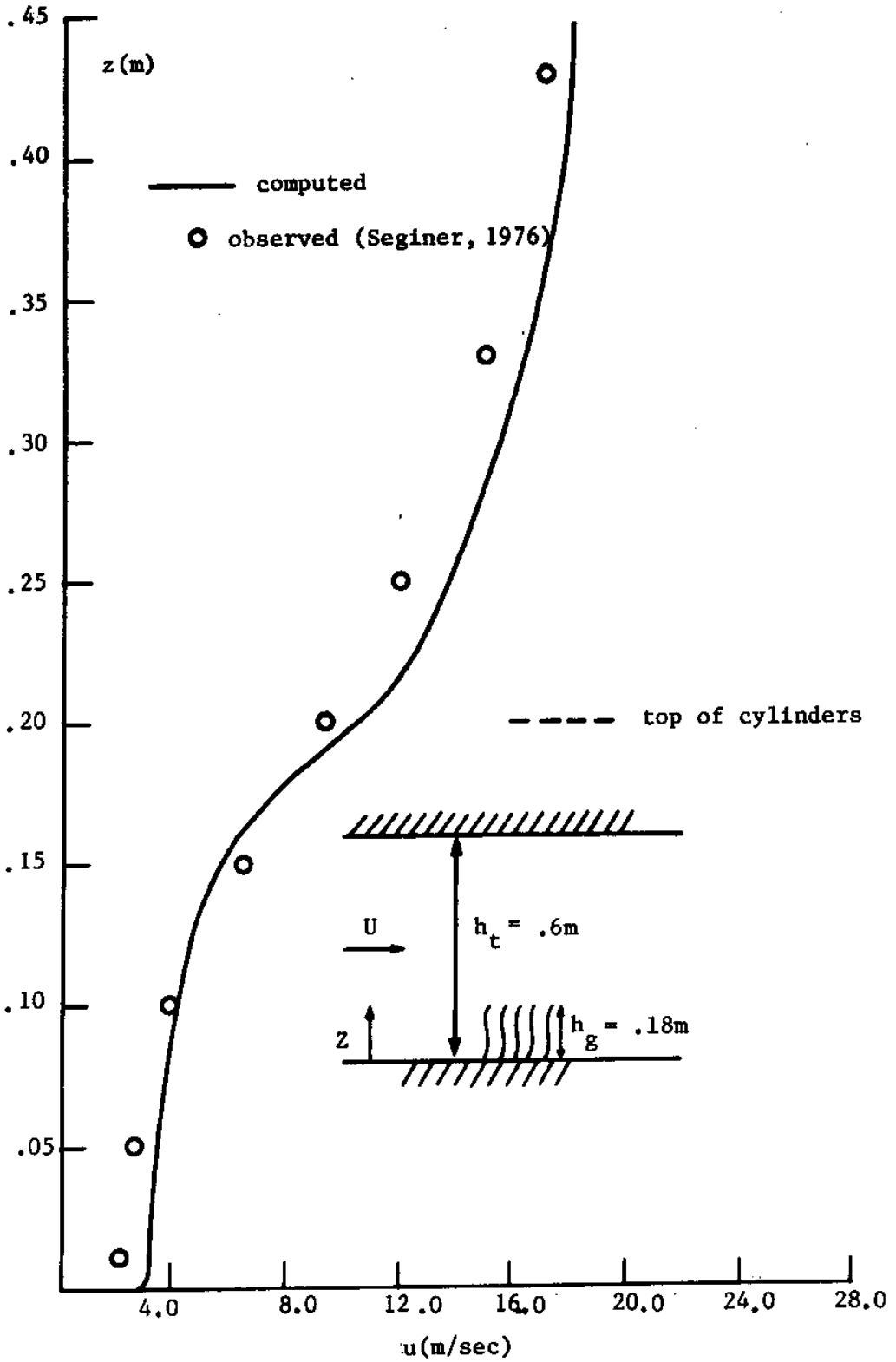

Figure 3.12 - Comparison of Observed Velocity Measurements (Seginer, 1976) and Computed Model Values for Wind Tunnel Flow through Circular Cylinders.

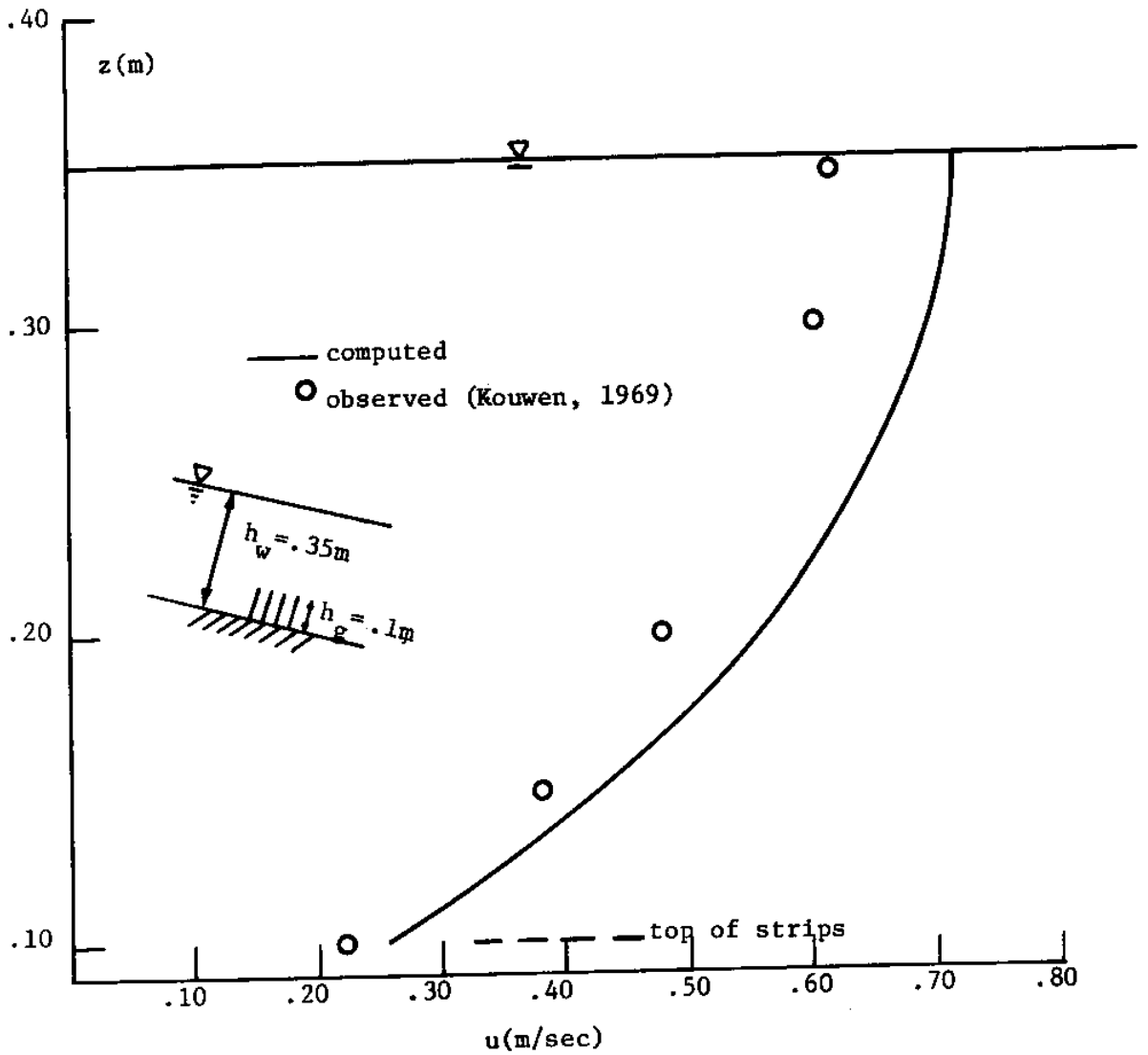

Figure 3.13 - Comparison of Observed Velocity Measurements (Kouwen, 1969) and Computed Model Values for Water Flow through Rectangular Strips.

studies. The profiles are in good agreement, giving confidence in the correctness of the model structure.

In addition to velocity, stress measurements were also taken by Seginer and Thom. Seginer measured the turbulent shear stress within the canopy using a hot wire anemometer, the observed and predicted results being shown in Figure 3.14. The sharp decline in stress within the canopy has important implications for the marsh; it indicates that, in situations where the grass protrudes through the water column, the wind stress at the air-water interface will be significantly reduced from it's value over the grass.

Thom measured the total drag force on the cylinders with a moment balance. Assuming that $\tau = \int_0^{h_g} \frac{C_d a}{2} u^2 dz$, and that the bottom stress is negligible, the drag force then gives an estimate of the shear stress at $z=h_g$. The value found by Thom in this way was $.11 n/m^2$, as compared to $.096\ n/m^2$ predicted by the model.

Plate did not measure the stress directly, but estimated it from the expression $\frac{u}{u_*} = \kappa \ln (\frac{z-d}{z_o})$; taking $d=h_g$, he then fitted the data above the canopy to determine $z_o \simeq .1 h_g$ and $u_* \sim .94$ m/sec, compared to a model prediction of .78. The discrepancy between the u_* values obtained from the model and the semi-log law approach is discussed in the next section.

Seginer used a hot wire anemometer to measure the three components of the turbulent intensity i_1, i_2, i_3, where in general $i_j = \sqrt{\overline{u_j'^2}}/u$. No error analysis was presented for these measurements. A summation gives $(\frac{1}{2} \sum_{j=1}^{3} i_j^2)^{1/2} = \sqrt{k}/u$; the observed and predicted profiles of

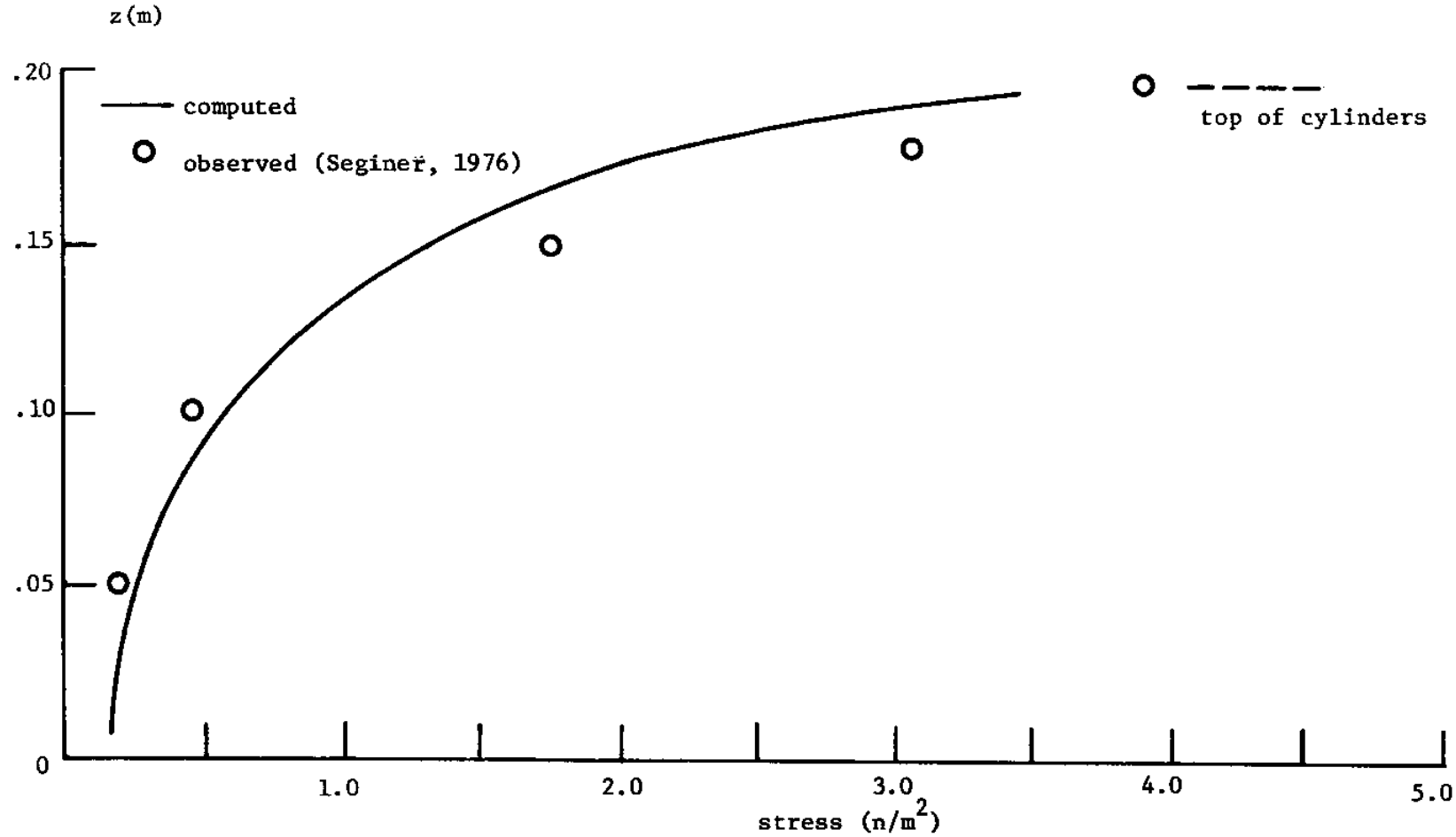

Figure 3.14 - Comparison of Experimental Observations (Seginen, 1976) and Computed Model Values of Stress in Circular Cylinders.

this quantity are presented in Figure 3.15. From the observed values of u, k was then determined, and is compared with model predictions in Figure 3.16. Also shown, for $z > h_g$, are values of k derived from the relation $k = \frac{\tau/\rho}{C_\mu^{1/2}}$ (values of τ/ρ were those given by Seginer, which matched closely the model predictions). As discussed in Section 3.2.5, this expression applies when diffusion and convection of k are negligible, leaving a balance in the k equation between production and dissipation. The model predictions are seen to agree closely with the values of k obtained analytically using the above expression, whereas the observed values are consistently higher. This suggests the possibility of downstream convection of k in the wind tunnel, or perhaps upward diffusion from within the canopy by a mechanism not accounted for by the model (see model limitations in Section 3.4).

Field Studies of Canopy Flow

In addition to laboratory studies, two field studies measuring velocities in corn (Wilson & Shaw, 1977) and beans (Thom, 1971) were also examined. Figures 3.17 and 3.18 show the observed and predicted velocity profiles for each of these cases. Figure 3.19 shows observed and predicted profiles of τ/τ_{h_g} for Wilson & Shaw's study, where τ_{h_g} is the shear stress at the top of the corn crop.

The values of (a) used in the model predictions were determined experimentally by the authors. The values of (C_d) were assumed close to those predicted by the authors, and were determined by trial and error. Thom estimated C_d=.07 using an analytic approach; Wilson & Shaw found C_c=.04 by trial and error to give the best fit between the

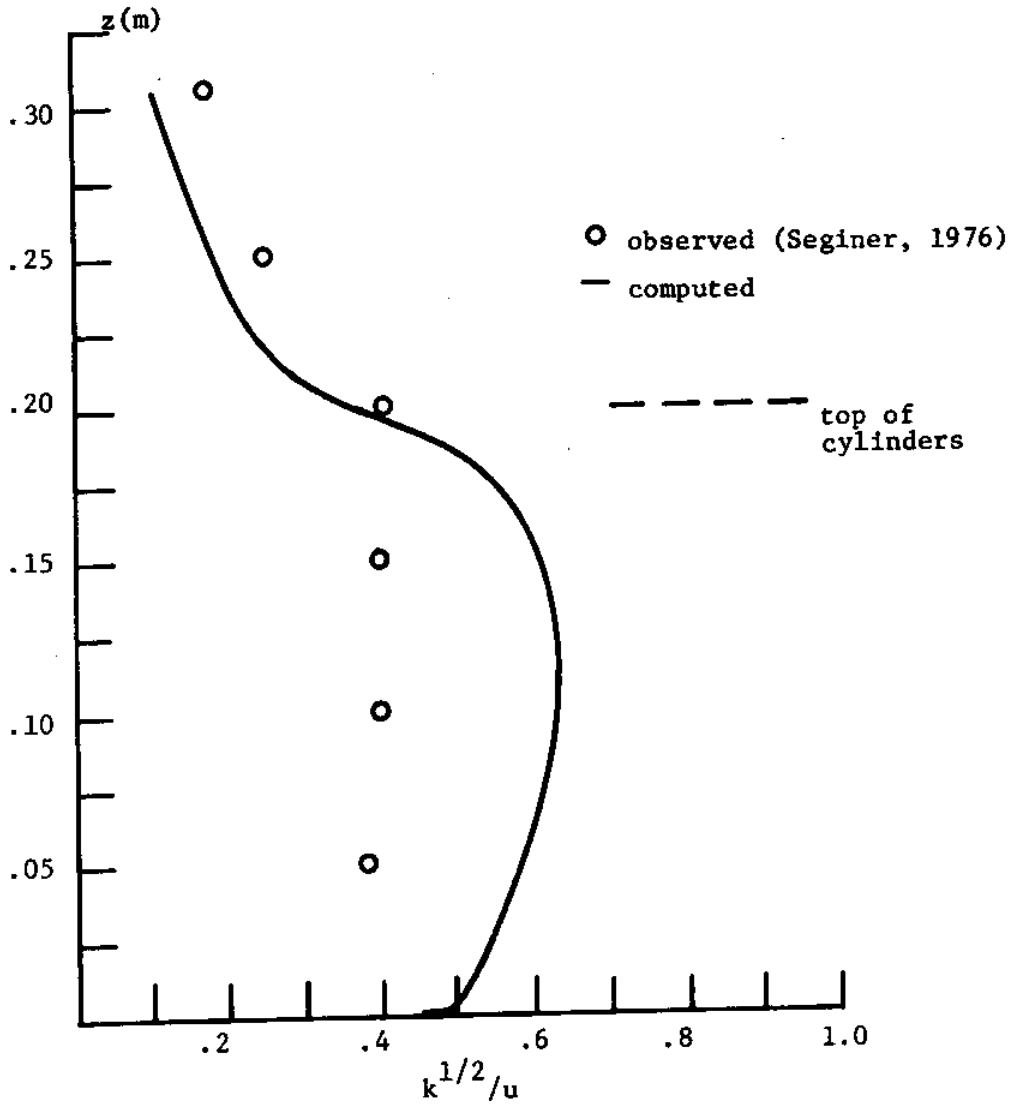

Figure 3.15 - Comparison of Observed (Seginer, 1976) and Computed Model Values for Flow in Circular Cylinders.

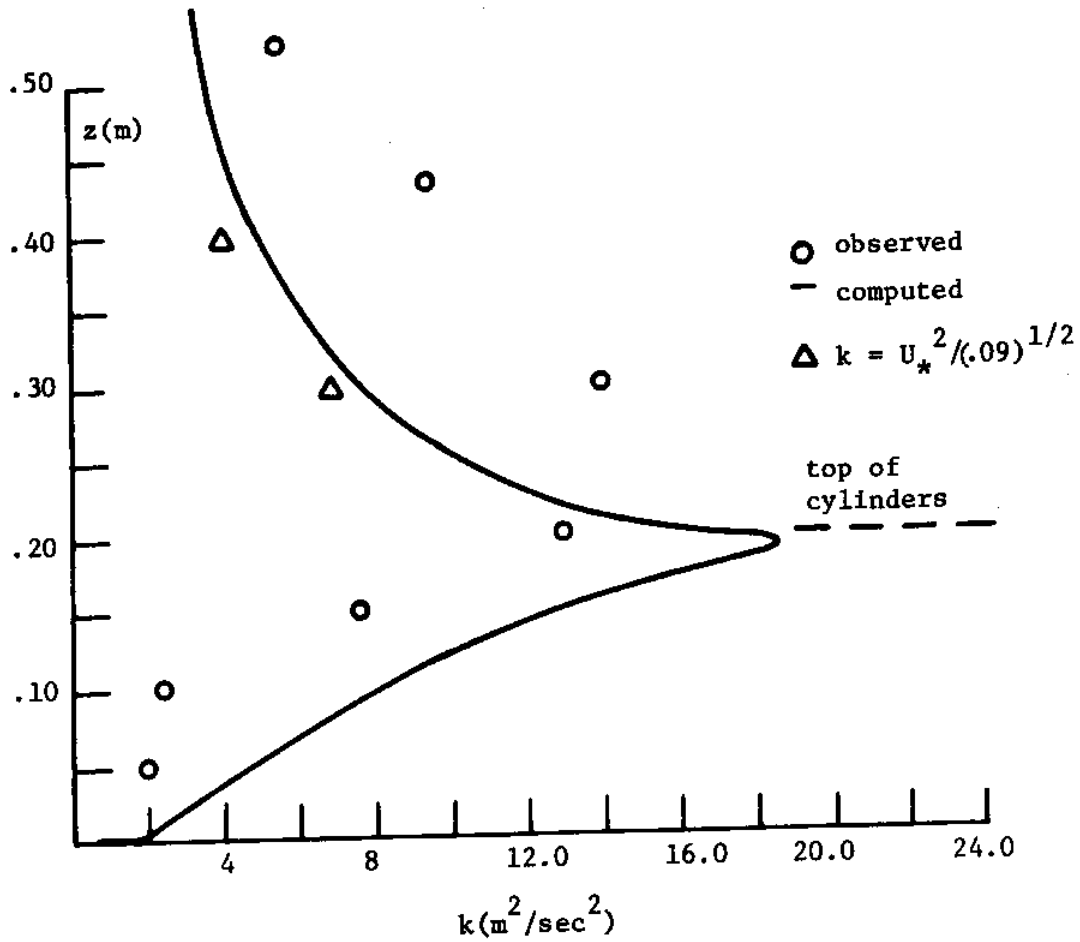

Figure 3.16 - Comparison of Observed (Seginer, 1976) and Computed Model Values of Kinetic Energy for Flow in Circular Cylinders.

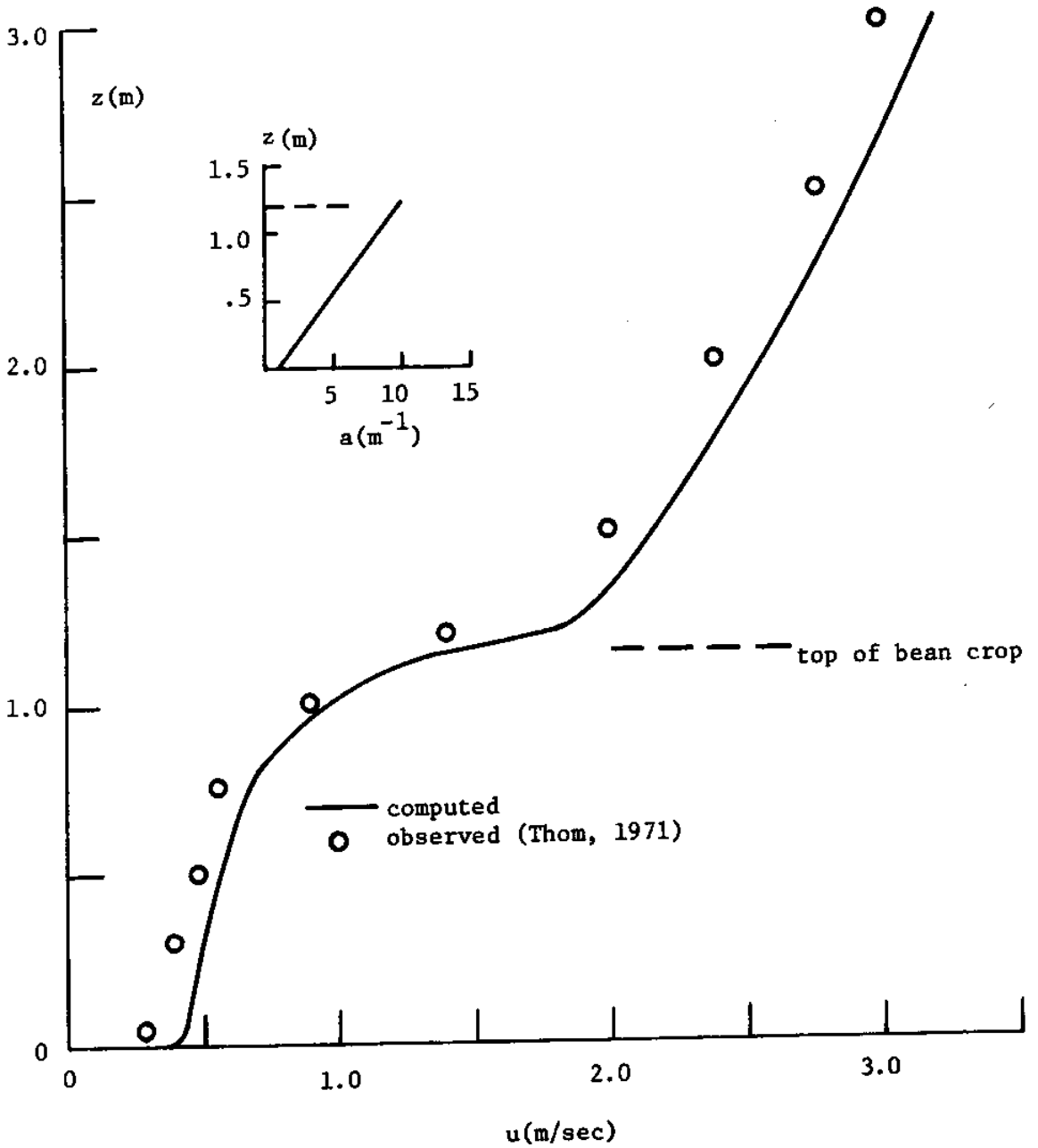

Figure 3.17 - Comparison of Observed (Thom, 1971) and Computed Model Values for Flow within a Bean Crop.

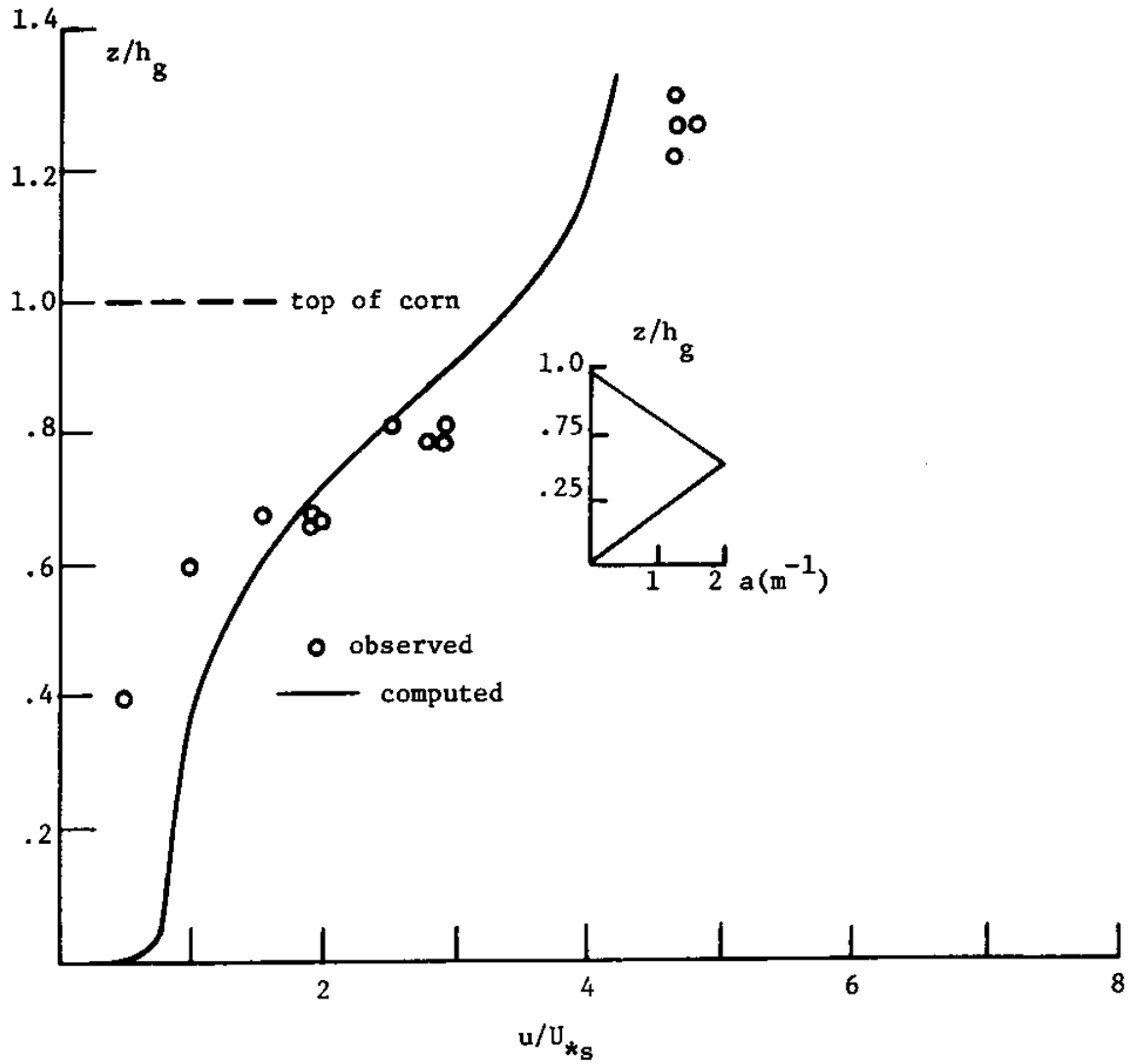

Figure 3.18 - Comparison of Observed (Wilson and Shaw, 1976) and Computed Model Vaues for Flow in a Corn Crop.

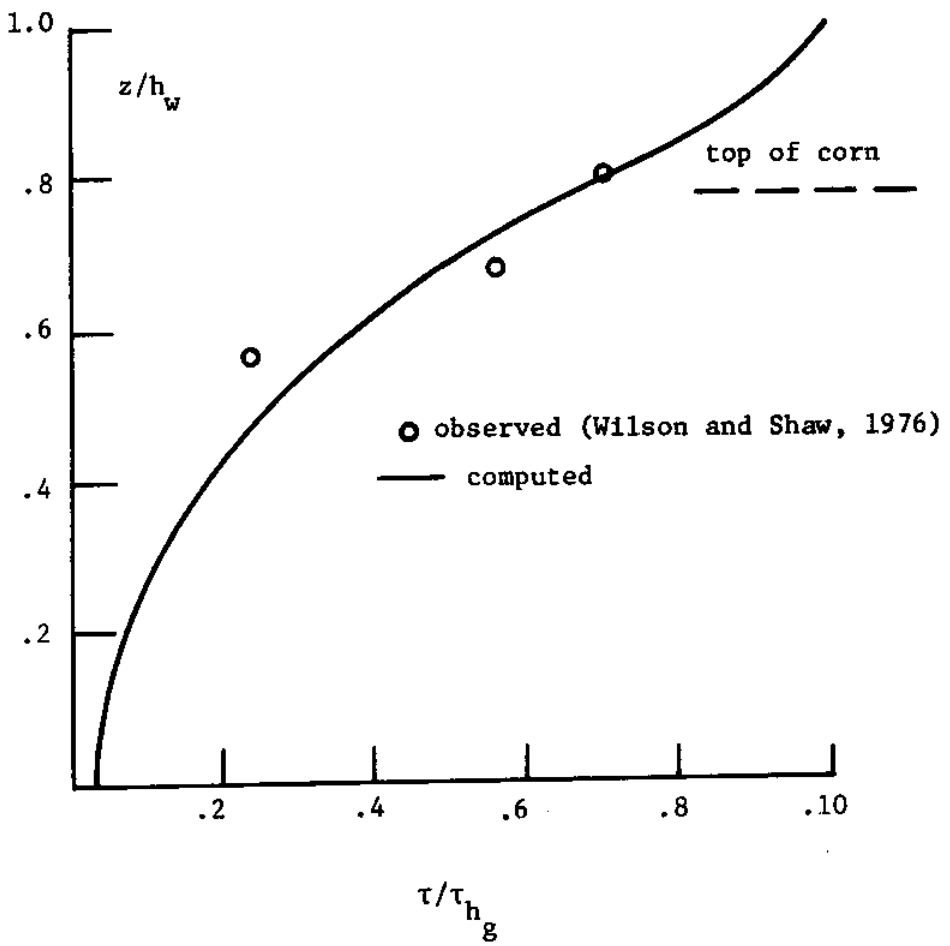

Figure 3.19 - Comparison of Observed (Wilson and Shaw, 1976) and Computed Model Values for Flow in a Corn Crop.

data and their model predictions. (In contrast to the laboratory studies, where well defined values of (C_d) were available for use in the model comparisons, no such information was available for the field studies. The values provided by Thom and Wilson and Shaw did not seem of sufficient accuracy to require their use in the comparisons.)

Following a similar approach to Plate (1965), Thom estimated u_* at the top of the bean crop to be about .35m/sec., as compared to a predicted value of .5. The difference in shear stress, which varies as u_*^2, is about a factor of two.

Without direct measurement, it is not possible to compare the accuracy of these two stresses. The small (10%) difference between the observed and predicted u_*^2 values of the laboratory studies, mentioned earlier, lends some support to the k-ε predictions. As noted by Brutsaert (1982), the depth of the canopy sublayer may extend considerably above $z=h_g$, making it possible that many of Thom's measurements, which extend a distance of $3h_g$ above the top of the bean crop, may lie within this sublayer, and are thus not governed by the semi-log law. This is corroborated by the observation that using the semi-log formula to find u_* for Seginer's study, with his value of d=.14m, leads to a u_* of roughly 2.5m/sec., as compared to a measured value of about two. Seginer's measurements also extended a distance of about $3h_g$ above the top of the canopy.

Figure 3.20 shows the observed and predicted profile of $\frac{\sqrt{k}}{u}$ for Wilson and Shaw's study. The observed values were deduced from turbulence intensity data given by Shaw et.al., (1976), in the same manner

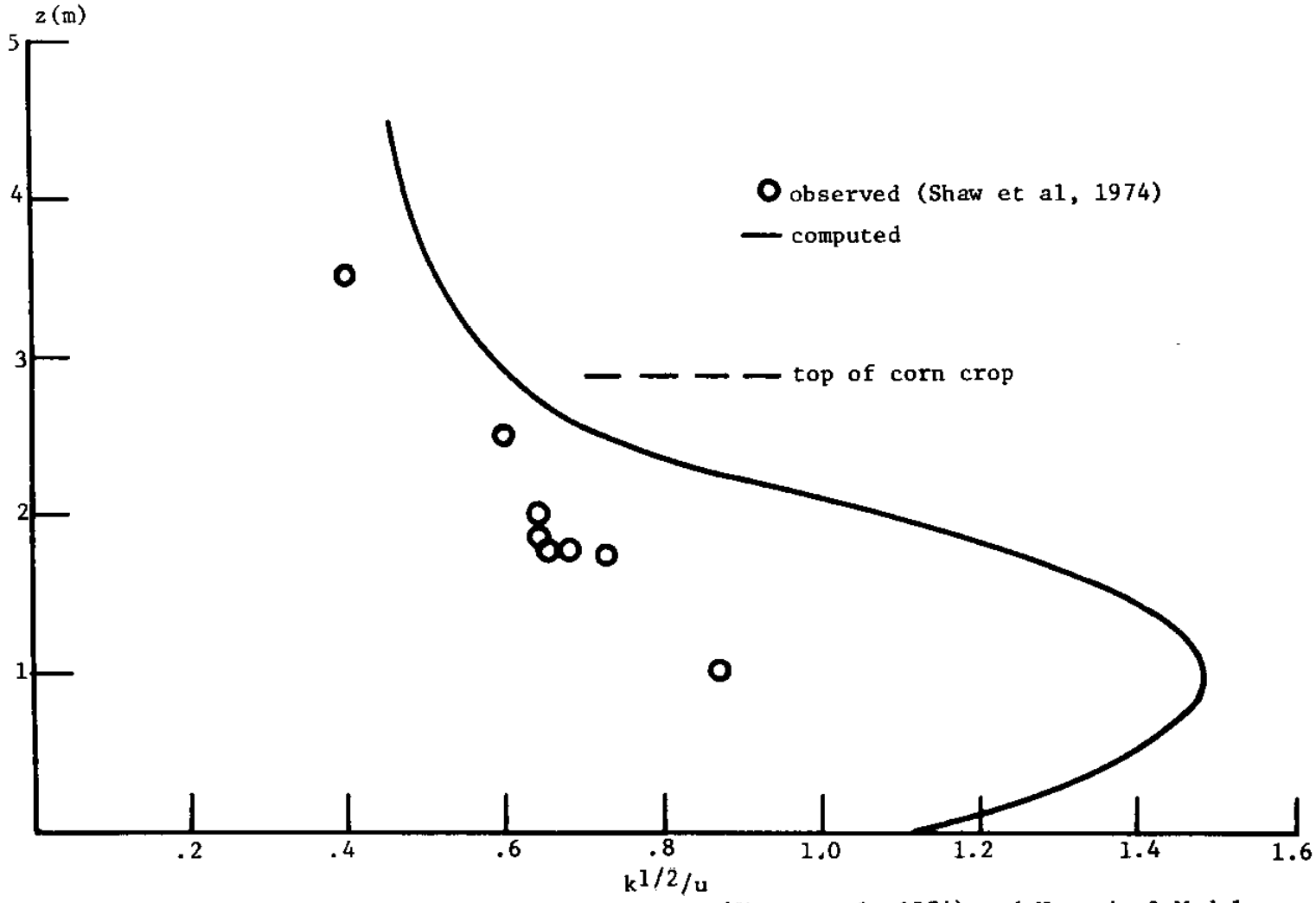

Figure 3.20 - Comparison of Experimental Results (Shaw et al, 1974) and Numerical Model Solution for Corn Crop

as described in the last section. Similar to the results found in the laboratory study of Seginer (1976), the predicted values of $\sqrt{k}/u$ are consistently higher than the observed measurements. Both observed and predicted profiles follow the shape of the vegetation density profile (a). This trend, observed in other canopies (Thom, 1981) as well, agrees with what might be expected; as (a) increases, so does the kinetic energy produced by the obstructions.

Examining the results in this section for velocity, stress, and kinetic energy, the agreement between observed and model values is generally not as close as that obtained for the laboratory studies. The major reason for the relatively poorer fit in the field studies can be traced to the presence of large, leafy surfaces in the bean and corn crops of the field studies. The leaves will affect the physics of the flow, and thus the model parameterization, in three major ways.

First, the leaves will exert drag on the flow through skin friction, as well as pressure forces. This will require redefinition of (a) to include surface area per unit volume, as well as reformulation of C_d.

Second, the leaves may also dissipate kinetic energy by skin friction, requiring an additional sink term in the kinetic energy equation. Lewellen and Sheng (1980) include such a term in their canopy flow model.

Third, the movement of leaves in the wind may generate eddies affecting the turbulent transport of momentum, as well as kinetic energy. The value of C_μ' in the expression for μ_t was derived on the

basis of the lab studies, having vertical obstructions that may have bent over in the wind, but almost certainly did not move back and forth, such as might be expected of leaves. This fluttering action could conceivably produce eddies having different orientations than those generated by vertical, stationary obstructions, thus requiring modification of the C_{μ}' term.

While inclusion of these effects would probably lead to better results for crops such as beans or corn, they would not likely have much of an impact on the modeling of marsh grass, which does not have the large, leafy surfaces responsible for the phenomena described above, and which is the major concern of this study.

3.8 Summary

The model presented here solves the momentum equations (2.8) for flow through and above obstructions, using a modified two-equation k-ε approach to parameterize the turbulent stresses. Turbulence closure is achieved without the need for a priori specification of the turbulent scales, these being determined by transport equations, in conjunction with specified obstruction geometry, and other boundary conditions. The model solves the equations through the viscous-affected regions near solid boundaries or free surfaces, and makes no empirical assumptions about the variation of mean or turbulent quantities in these regions.

The model formulation was tested by comparing numerical predictions against experimental data from the literature. Six experimental studies

were chosen for investigation. The empirical model coefficients were kept at the same values in all predictions, thereby avoiding any curve-fitting connotations associated with changing the coefficients from one case to the next. Experimentally determined values of the obstruction parameters (a) and (C_d) were used whenever possible.

The case studies can be divided into two groups, those conducted in the laboratory, and those conducted in the field. The laboratory studies, being more controlled, were used to find the value of the model coefficient C'_μ, which was subsequently held fixed at a value of 2.6. Consisting of three wind tunnel studies and one water flume test, the laboratory studies had varying model parameters, with the obstruction based Reynold's number (defined in Section 2.4.2) varying from 60 to 1000, and with ($h_g a$) ranging from .5 to 2.5. The model predictions agreed closely with observed measurements of velocity and stress; model predictions of kinetic energy were consistently high, but correct within a factor of two.

In addition to the laboratory studies, two field investigations of flow in a corn and bean crop were also analyzed. Despite the complexities introduced by the presence of large, leafy surfaces, the model predictions and observed results were generally in good agreement, although not as close as for the laboratory studies.

In the next chapter the model is used to calculate the flow in tidally inundated marsh grass, the numerical predictions being compared with experimental results.

CHAPTER IV

FLOW IN TIDALLY INUNDATED MARSH GRASS

4.1 Introduction

This chapter discusses a study by the author of flow in tidally inundated marsh grass. After some general background information about the area chosen for the measurements, a description of the experimental apparatus is given. Next, the operating procedure followed on a typical field day is outlined. A discussion of the experimental results, together with an error analysis, is then presented. Finally, observed velocity distributions are compared with predictions of the numerical model described in the foregoing chapter.

4.2 Background

To investigate the flow in tidally inundated marshes, and to provide a basis for model comparison, a field study of water movement was conducted during the summer of 1980 in Great Sippewissett Marsh, located outside of Falmouth, Massachusetts. Great Sippewissett has an area of about one-quarter square kilometers, with a single entrance for the tidal water. The tidal range is about one and one-half meters. Figure 4.1 shows a map of the marsh, including the area chosen for the field study.

An enlarged view of the study area is shown in Figure 4.2. This location was chosen because it is surrounded on three sides by open

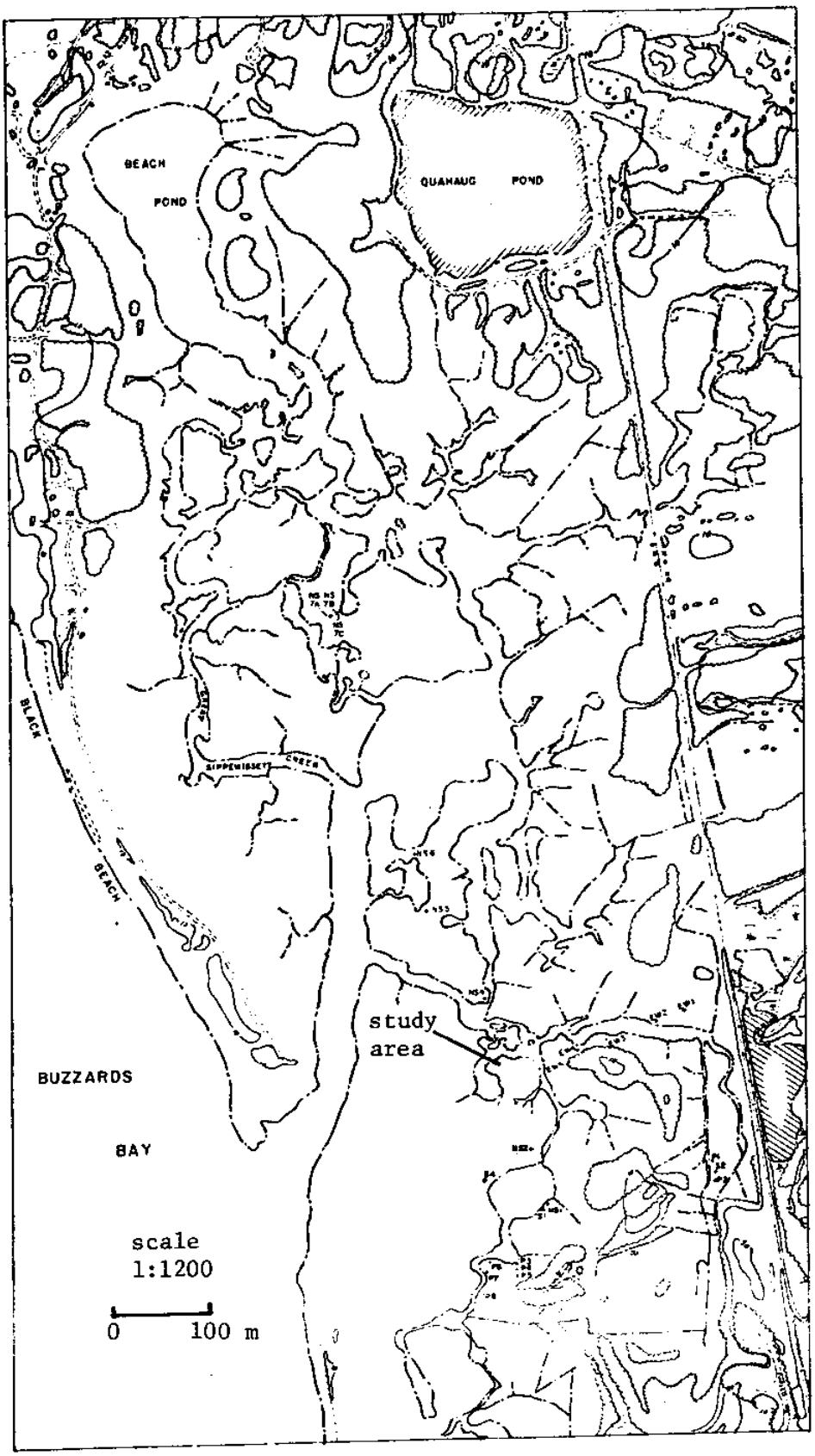

Figure 4.1 - Great Sippewisett Salt Marsh.

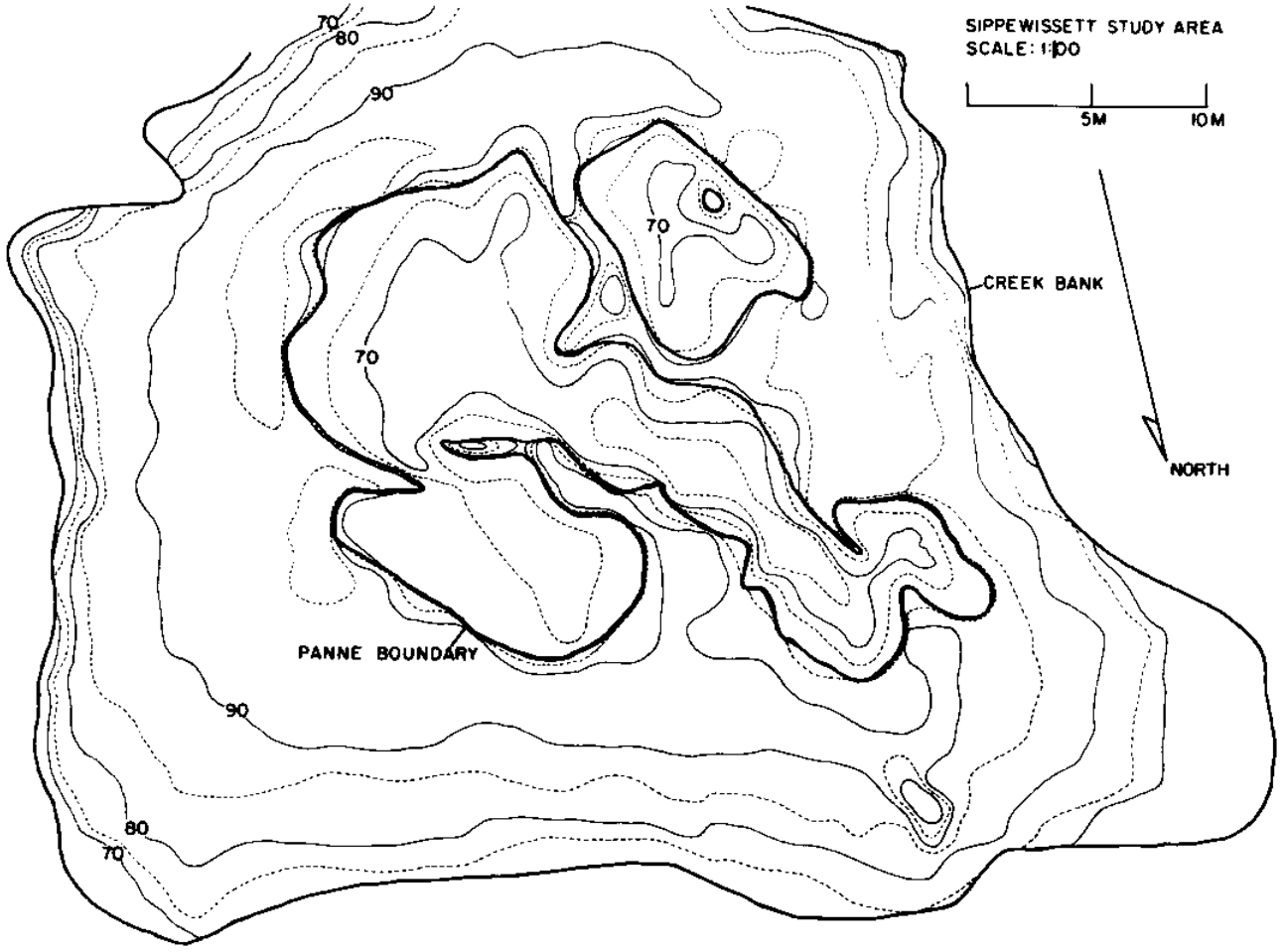

Figure 4.2 - Topographical Map of Study Area (Elevation in Centimeters above an Arbritary Datum.)

water, thus allowing a net water flow across the study area during flood and ebb tide. This situation was preferred to that found in dead-end areas bordered by solid boundaries, where the water movement would be more restricted. The contours in Figure 4.2 represent the results of a topographical survey of the study area. The low-lying regions in the center of the study area are continually filled with water, support no vegetation, and are called pannes. Excluding these regions, the vegetation of the study area is almost exclusively a type of grass called short form Spartina alterniflora, ranging in height from about five to twenty-five centimeters. In certain areas near the creek bank, tall form Spartina, about one meter tall, can be found. The study area is about forty meters long on each side.

During flood tide, the water level in the surrounding creeks rises; if the tide is high enough, the study area becomes completely innundated. With the turn of the tide, the water level starts to fall until, once again, the study area is exposed.

It is during the period of tidal innundation that the field experiments are carried out. Figure 4.3 shows the stations where the velocity measurements were taken. Table 4.1 shows the sampling dates of each station. At each station, profiles of velocity versus depth were obtained by taking measurements at roughly five centimeter intervals throughout the water column. Typically, several such profiles were taken at each station, during both flood and ebb tide. Depending on the tidal stage, the grass may have extended through the

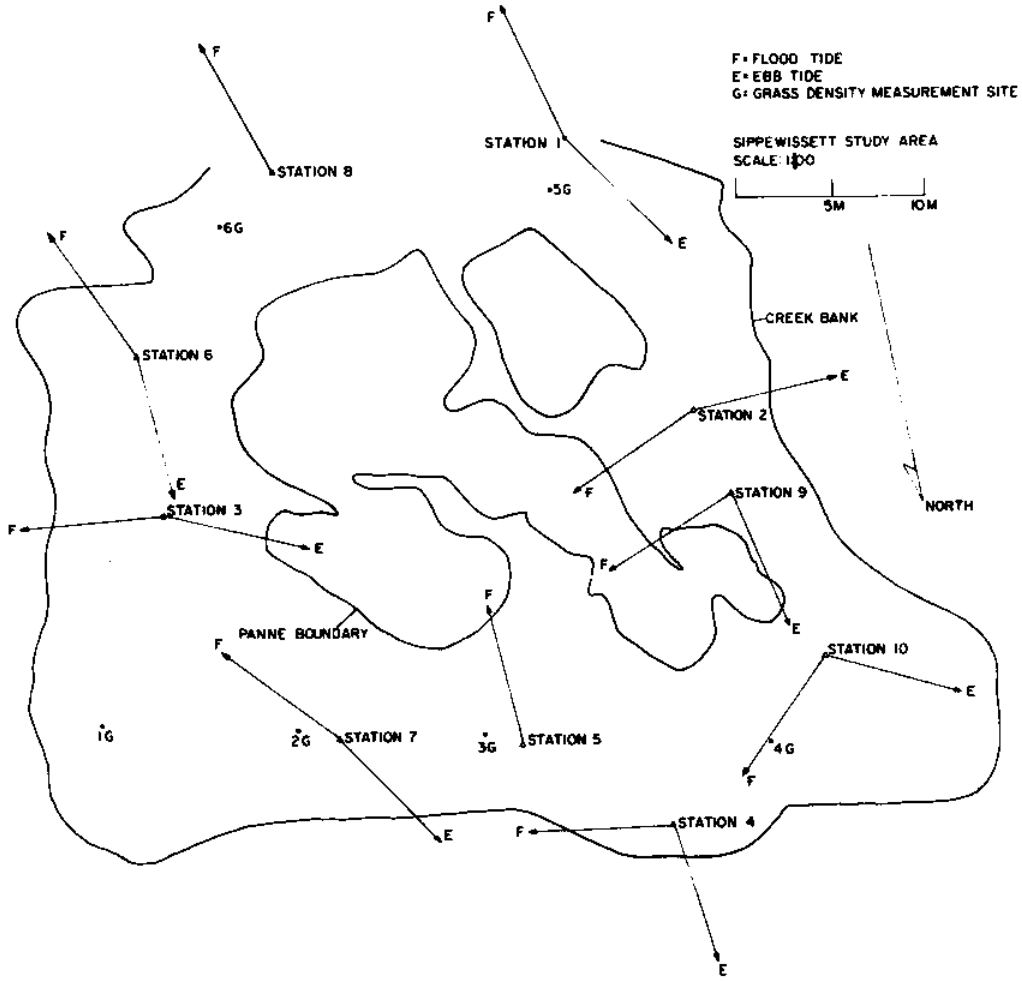

Figure 4.3 - Location of Velocity Profile Stations and Grass Density Measurement Sites on Study Area. Arrows Indicate Observed Direction of Flow during Flood and Ebb Tide.

Date	Stations Sampled
8/29/80	1
8/30/80	2,3
8/31/80	4,5,6
9/1/80	7,8
9/2/80	9,10

TABLE 4.1

Velocity Measurement Stations and Dates Sampled

water column or been completely submerged below the surface. In conjunction with the velocity measurements, wind speed and stage height at the boundary of the study area were recorded.

4.3 Experimental Apparatus

4.3.1 Flow-Metering Device

A measuring device suitable for tidally inundated marsh flats must meet two basic requirements; (1) ability to measure low velocities (on the order of .01 m/sec) in dense grass without disturbing the flow, and (2) insensitivity to the presence of foreign material, such as detritus or pieces of grass, in the water. These two requisites precluded most conventional flow metering techniques of relatively low cost, and prompted the design and construction of a special measuring device, shown schematically in Figure 4.4. The device operates on a time-of-travel technique: dye pulses, released into the water by means of a solenoid pump, are photographed at intervals by a camera; a digital clock, located in the camera's field of view, provides a time scale. A transparent grid, laid over the developed prints, provides a distance scale with which to measure how far the dye has moved between prints. The orientation of the clock, having been recorded in the field, indicates the direction of flow relative to the study area.

The dye solution was prepared at the beginning of every field day by mixing one-quarter teaspoon of rhodamine with five hundred milliliters of water from the nearest creek. The solution was placed

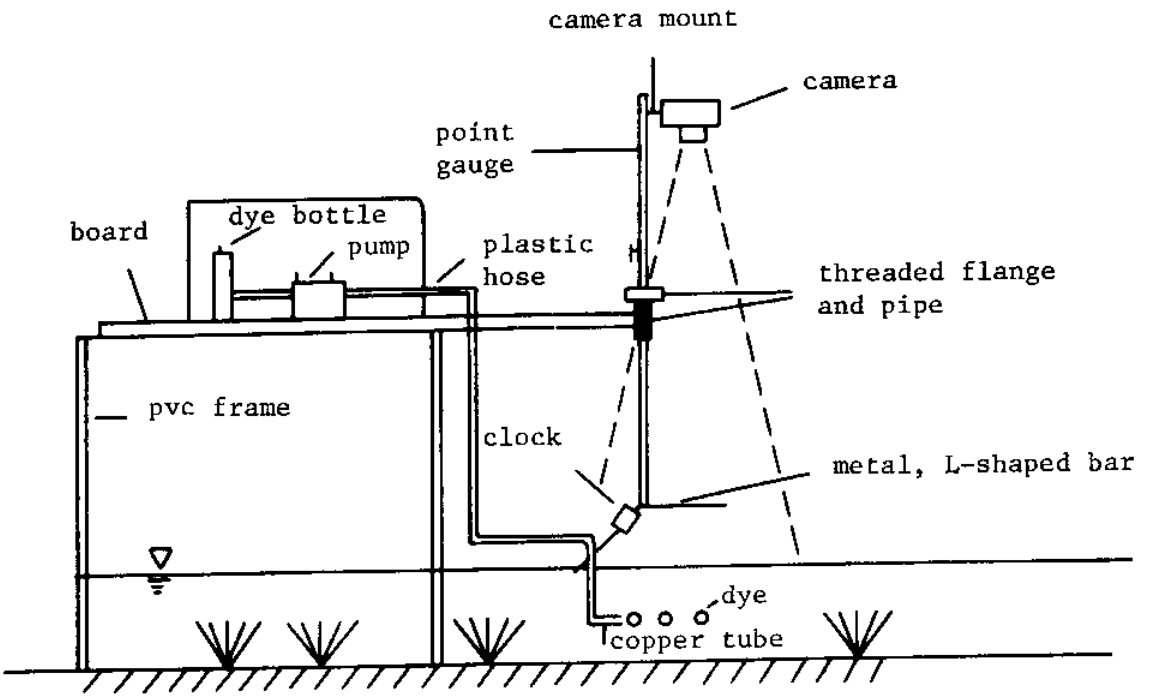

Figure 4.4 - Flow Metering Device

in a plastic bottle which, together with a solenoid pump, was housed in a converted tool box for ease in transportation.

The solenoid pump (Valco, Inc., Model # PV-500) injected the dye via a copper tube into the water. The pump was remotely activated by a hand held switch, connected to the pump by a two meter cord. By adjusting the strength of the piston stroke, it was possible to create one-half centimeter spheres of dye. The spheres were released perpendicular to the direction of water flow, thereby reducing the chance of any pump-related inertial effects from entering the velocity measurements.

An Olympus 10 camera was used to track the dye's motion. The camera was equipped with a wide angle lens, to give a sufficient field of view to track the dye, and an autowinder, which wound the film at a rate of two frames per second. While in the field the camera was kept in a watertight, plastic diving case. The case allowed for adjustments by means of a "glove" built into the plastic. The camera was remotely operated by a shutter release attached to the autowinder. Color film was used in the camera.

A Casio PQ-10 brand pocket-sized digital clock was used as the time scale. The clock was operated in it's stop-watch mode, accurate to one-tenth of a second. The quartz display (black numbers on a white back ground) provided the sharp contrast needed to read the time from the prints.

The dye-injecting copper tube, camera, and clock were secured to a

modified point gauge, as shown in Figure 4.4. The relative position of these instruments remained constant during the course of the experiments. By turning the dial on the point gauge, the whole apparatus could be moved up or down as desired to take measurements at different water depths.

The modified point gauge was held in position by attaching it to one end of a board, the other end of which was clamped to a frame made of three-quarter inch pvc pipes fastened together with aluminum connectors, to prevent rust. The tool box containing the solenoid pump and dye were also placed on this frame.

In addition to the components of the metering device described so far, there is one auxillary piece of equipment that should also be mentioned. An umbrella was held over the sampling station to reduce reflection of the sun's rays off the water surface. Without the umbrella, nothing could be seen in the prints but a shiny, mirror-like surface (Polarizing filters were tried, but did not work as well as the umbrella).

4.3.2 Stage Height and Meteorological Data

The water height at four or five locations surrounding the study area was recorded at roughly one-half hour intervals using meter sticks inserted into the peat. The meter sticks were marked to one-tenth of a centimeter. At each meter stick location, the height above some arbitrary datum was obtained using a level, also accurate to about

.001m. With these two measurements, it was then possible to calculate the water surface elevation $\eta = h_w + z_b$ at the meter stick location.

The wind speed and direction at the study area were measured using a portable meteorological station (#474-2 Electronic Weather Station, manufactured by Science Associates). Specifically, a cup anemometer and wind vane were mounted on a three meter collapsible mast. The information was recorded on a strip chart recorder, driven by two six volt batteries.

4.4 Operating Procedure

This section describes a typical field day, involving the operation of the apparatus described in the previous section. Two people were required to collect the data. At the beginning of the field day the equipment was carried out to the study site and assembled in anticipation of the flooding tide. Assembly took about one hour. To minimize flow disturbances at the sampling site, the metering device was oriented so as to be downstream of the dye injection area. The procedure followed in operating the equipment is given below.

(1) After the tide flooded the sampling site, the point gauge dial was turned until the bottom of the copper tube touched the water surface. The dial reading and the water level on a nearby meter stick were then recorded. (Knowing these two measurements enabled later determination of the position of the dye pulse).

(2) When the water reached the desired depth of the first profile, measurements were begun. One of the two workers, holding the umbrella with one hand, used the other hand to hold an identification card marked with the number "1" in the camera's field of view. The other worker then released a dye pulse, and took pictures of it's motion., Typically, three to four pictures were taken, during which the dye moved about twenty centimeters. This constituted one run, with one or two such runs being performed at each depth. This process was then repeated every five centimeters until the profile was completed. At each depth, the identification card was changed, so that a different number appeared in the prints. Given a water depth of twenty centimeters, about ten minutes were needed to complete one profile.

(3) Having finished one or two profiles, stage height readings were taken. One worker remained by a designated "base" stage stick, while the other worker went to each of the other stage sticks circumbscribing the study area. Simultaneous readings were then taken at the base stick and each of the other stage sticks in turn.

Steps (2) and (3) were repeated until the time arrived to move the metering device, either to a different station, or because the tide had changed, and the water was flowing in the opposite direction. In the latter case, the device was swung around 180 degrees, so that velocity measurements were taken at the same location as during flood tide. Having moved the device, it was necessary to redo step (1).

Once the water drained off the marsh study area, the stage sticks

were levelled in; this enabled later calculations of z_b (see Figure 2.1).

4.5 Data Reduction

4.5.1 Velocity Measurements

Determination of Distance Scale

As mentioned earlier, the flow-metering device contains a time scale, but no distance scale. Before being able to calculate the flow velocities from the dye prints, it was necessary to find a way to measure how far the dye had moved between prints. Because the dye could be located anywhere from right at the water surface to a depth of over twenty centimeters, the possibility that refraction of light passing across the air-water interface might affect the distance measurements was first investigated.

Investigation of the refraction effects was carried out by taking pictures of a wire screen (mesh spacing $\simeq$.008m) submerged to various water depths, ranging from zero to twenty-five centimeters. In order to simulate field conditions, the distance between the camera and grid was held constant at the same value as that between the camera and the dye release point on the flow-metering device. Film positives of the wire screen were then enlarged to the same size as the dye prints. The film positives, being transparant, were laid on top of each other, from which it was seen that the difference in size between the grid not covered with water and that covered to a depth of ten centimeters was

about two percent; similarly, the difference between this grid and that submerged to twenty-five centimeters was also about two percent. This error, when compared to the other sources of error discussed later, was considered small enough to be neglected.

Aside from investigating refraction effects, this procedure provided the necessary means for determining the dye's motion; specifically, the film positive of the grid submerged to a depth of ten centimeters was chosen as the distance scale. The grid was laid over each of the dye prints, the position of the center of the dye patch then being recorded in terms of a cartesion coordinate system drawn on the grid. Obviously, the orientation of the grid had to be kept the same from print to print. This was done by aligning the x and y axis of the grid with an L shaped metal bar holding the clock. The compass bearing of the metal bar, having been recorded in the field, indicated the direction of dye movement relative to the study area.

Once all the prints had been analyzed, the information was stored on a data file. It was then a relatively straightforward matter to calculate, for any two successive prints, the direction and magnitude of the velocity.

Error Analysis

There are two sources of error in determining the velocity; those associated with the measurement of the distance, and those associated with time. The relative contribution of these two effects can be seen by considering the most probable fractional error of velocity $(\frac{\delta v}{v})$

defined as (Topping, 1982)

$$\left(\frac{\delta v}{v}\right) = \left(\left(\frac{\delta x}{x}\right)^2 + \left(\frac{\delta t}{t}\right)^2\right)^{1/2} \qquad (4.1)$$

where x is the measured distance traveled by the dye in a measured time t, v is the measured velocity ($v=\frac{x}{t}$), and δx, δt are the measured errors in distance and time respectively.

In order to calculate the fractional errors $\frac{\delta x}{x}$ and $\frac{\delta t}{t}$ various estimates of distance and time are required. These estimates are defined below:

x_p - distance traveled by dye between two prints

t_p - elapsed time between two prints

x_{max} - total distance dye's motion is followed

t_{max} - total time dye's motion is followed

$\delta x_i, \delta t_i$ - errors in distance and time due to instrument imprecision

d_v, d_h - vertical and horizontal distance spread by dye over x_{max}

Values of these quantities are given in Table 4.2 for the regions above and below the grass. These estimates were derived on a qualitative basis for the purpose of calculating the fractional errors in distance and time. These errors are discussed below, and summarized in Table 4.2.

Region	(1) x_p (m)	(2) t_p (sec)	(3) $v = \frac{x_p}{t_p}$ (m/sec)	(4) x_{max} (m)	(5) $t_{max} = \frac{(4)}{(3)}$ (sec)	(6) μ_t/ρ (m^2/sec)	(7) d_v (m)	(8) d_h (m)	(9) $\frac{\delta t_i}{t_p}$	(10) $\frac{\delta x_i}{x_p}$	(11) $\frac{d_h}{2x_{max}}$	(12) $\frac{\delta v}{v} = ((9)^2+(10)^2+(11)^2)^{1/2}$
Above grass	.10	.7	.15	.2	1.3	10^{-4}	.02	.02	.14	.08	.05	.17
Below grass	.07	2.5	.03	.2	7	10^{-4}	.03	.05	.04	.11	.13	.19

Table 4.2

Fractional Errors in Velocity Measurements

The fractional error in time $\frac{\delta t}{t}$ is almost entirely the result of lack of precision in the digital clock. The digital clock is accurate to one-tenth of a second ($\delta t_i \sim .1S$); the fractional error in time can then be estimated as $\delta t_i / t_p$, values of which are given in Table 4.2.

The fractional error in distance $\frac{\delta x}{x}$ arises from two major sources; instrument imprecision, and spreading of the dye pulse. The error arising from the lack of precision of the distance scale can be estimated by recalling that the mesh size of the grid is about .008m ($\delta x_i \sim .008m$); the fractional error in distance is then $\delta x_i / x_p$, as shown in Table 4.2.

The other major source of distance error relates to the spreading of the dye pulse. At the time of release, the dye, having a length of about .005m, spreads horizontally and vertically under the influence of various forces.

The vertical spreading of the dye will be caused largely by turbulent diffusion. The vertical distance (d_v) over which the dye spreads may be estimated as (Fischer et al., 1979)

$$d_v = \sqrt{\ell_o + \frac{\mu_t}{\rho} t_{max}} \qquad (4.2)$$

where ℓ_o is the initial length of the dye pulse ($\ell_o \sim .005m$). The turbulent diffusivity μ_t can be approximated from model comparisons against the marsh flow data; representative values for the region above and below the grass are given in Table 4.2. The larger predicted

values of d_v for the region below the vegetation are due to the longer time it's motion is followed.

As the dye spreads vertically, it will be sheared by mean velocity gradients, causing a horizontal dispersion of the dye. If the velocity gradients are linear, the horizontal spreading will be more or less symmetric about the center of the dye patch (in the absence of other forces). In this case, the motion of the center of the dye patch would reflect the fluid's motion; assuming the center of the dye could be accurately determined, the vertical diffusion would not likely have a significant effect on the fractional error in distance.

For marsh flow situations, where the velocity gradients are not linear, the horizontal spreading will not be symmetric about the center of the dye, the location of which no longer provides the most accurate measure of the fluid's motion. Other factors contributing to the asymetric spreading of the dye will be collision with grass blades, and turbulent diffusion. Under the influence of these phenomena, the dye will disperse horizontally, obtaining a size (d_h) over the distance (x_{max}) it's motion is followed. Values of d_h for the regions above and below the grass are shown in Table 4.2. These values were obtained qualitatively from inspection of the dye prints. Even though the velocity gradients are significantly higher above the grass (see the data in Section 4.6), the size of the dye patch is generally larger within the vegetation, owing to the obstruction related effects mentioned earlier. The horizontal spreading of the dye is seen to be

generally larger than the vertical spreading.

In measuring the dye's motion, it did not seem practicable to try and correct for the asymettric spreading of the dye, the nature of which would depend on the effects described above. Instead, the procedure used was to follow the center of the dye patch, determined qualitatively for each print. The fractional error associated with this approach can be estimated as $\frac{d_h}{2x_{max}}$, where $\delta x = \frac{d_h}{2}$ is the measured error in distance.

The fractional error in velocity $(\frac{\delta v}{v})$ expected for any one measurement is found by summing the individual contributions described above. As shown in Table 4.2, the total error is about twenty percent. This estimate is borne out in the next section, which presents the observed velocity measurements. From Table 4.2, most of the error for the region above the grass is due to instrument imprecision, while for the region within the grass most of the error is related to the horizontal spreading of the dye.

While it is believed that this discussion has included all those errors of practical importance, there may still be other unexplained and unexpected errors. One such source of error may be flow disturbances resulting from the presence of the metering device, and the field workers, standing in the water. As mentioned earlier, attention was taken to minimize this possibility by restricting all activity to the area downstream of the sampling site.

4.5.2 Stage Height

Calculation of Slope from Stage Height Data

The water heights at various locations surrounding the study area were recorded at roughly one-half hour intervals during the period of tidal inundation. The water heights were determined by meter sticks inserted into the peat. At each meter stock location, the elevation above some arbitrary datum was determined with a level. With these measurements, it was then possible to calculate the total elevation $\eta = h_w + z_b$ at the meter stick locations.

Knowing η at these points surrounding the study area, some way was needed of using this information to calculate the water slopes at the velocity measurement stations (The object being to then use the slopes in the model comparisons). Given the information available, it was decided to assume the water surface over the entire study area was a plane, given by the equation

$$\eta = b_1 + b_2 x + b_3 y \tag{4.3}$$

where b_1, b_2 and b_3 were determined by applying a least squares regression analysis to the known values of η at the meter stick locations. Obviously, this procedure could only be carried out at those times when measurements of η had been recorded. At intermediate times, the slopes were obtained by linear interpolation of the coefficients $b_2 = \frac{\partial \eta}{\partial x}$ and $b_3 = \frac{\partial \eta}{\partial y}$.

In general, values of η were not available at all the meter sticks at the same time. As discussed earlier in Section 4.3.2, values of η were recorded simultaneously at a designated base stage stick, and at each of the other meter sticks in succession. Each such pair of readings was separated by roughly a one minute interval, during which the tide changed by about .002m. Simultaneous readings at all the meter sticks were obtained by linear interpolation, using the base stage stick readings to determine how much change should be made at other locations. The resulting set of simultaneous measurement were then used to find the equation of the plane, as described above.

Error Analysis

The coefficients b_2 and b_3 determined by the above method are only valid when the marsh is completely flooded. Under conditions of partial inundation, it would not be very meaningful to assume the water slope will be approximated by a plane, the equation of which will depend on variables at points that may be separated by dry ground. The period of complete tidal inundation was determined for each field day with the aid of the topographic survey, and field notes made on that day.

Even when the study area is completely flooded, the water surface may not be a plane. One way of testing whether the data are consistent with this assumption is to estimate the standard error of the

coefficients b_2 and b_3. These standard errors, shown as the error bars in Figures 4.10-4.14, vary between twenty to forty percent of the magnitude of b_2 or b_3.

Aside from the error associated with the fit of the data, there will also be an error associated with the measurement process. As a simple, one-dimensional case, consider that the slope (s) between two points is

$$s = \frac{|\eta_2 - \eta_1|}{x_s} \tag{4.4}$$

where η_1, η_2 are the elevations at two meter sticks, separated by a distance x_s.

Similar to the procedure used in Section 4.5.1, the most probable error in the slope can be estimated as

$$(\frac{\delta s}{s})^2 = 2(\frac{\delta \eta_1}{(\eta_2 - \eta_1)})^2 + (\frac{\delta x_s}{x_s})^2 \tag{4.5}$$

where δ refers to the error of the associated quantity. The above expression assumes that the errors in η_1 and η_2 will be about the same. As average values, x_s may be taken as 40m; the corresponding value of $(\eta_2 - \eta_1)$ will be about .01m. With these estimates, it is possible to determine the fractional errors in distance and elevation, as follows.

(1) Fractional error in distance

The tape measure used to determine x_s is marked to .01m. In

reality, however, the error will be larger than this, owing to the unevenness of the tape as it passes through the grass. Estimating this error to be about .1m gives an error $(\frac{\delta x_s}{x_s})$ of $3x10^{-3}$.

(2) Fractional error in elevation

To determine the error $2(\frac{\delta\eta_1}{\eta_2-\eta_1})^2$, it should first be remembered that, in general, the values of η used in the slope calculations were determined by liner interpolation with three meter stick readings. The most likely error $\delta\eta_1$ is then estimated as $(\delta\eta_1)^2=3(\delta\eta)^2$, where $\delta\eta$ is the error of the individual elevation readings. Recalling that $\eta = h_w+z_b$, it follows that $(\delta\eta)^2=(\delta h)^2+(\delta z_b)^2$, where $\delta h = \delta z_b = .001m$ (see Section 4.3.3). Inserting this into the above expression for $\delta\eta_1$, gives a value of $\delta\eta_1 = .003m$. The fractional error $\sqrt{2}(\frac{\delta\eta_1}{\eta_2-\eta_1})$ then becomes .35.

For practical purposes, the entire error is seen to be caused by imprecision in resolving the differences in elevation. The fractional error $\delta s/s$ is about the same magnitude as the standard error of the coefficients b_2 and b_3, suggesting the possibility that the size of the standard errors is not so much a reflection of the assumption of a plane water surface, as of inaccuracies in the measurement technique.

4.5.3 Wind Speed and Direction

The wind speed and direction were recorded by pens striking against pressure sensitive paper. The frequency of recording was about once every two seconds. The recording paper was marked to 1/2 m/sec and 10

degrees for the speed and direction transmitters, respectively. On a typical field day, the recorded velocity varied over about 3m/sec, with an average magnitude of about 5 m/sec. Assuming negligible inaccuracies in the sensing devices, the fractional error in the value of the velocity used in the model comparisons may be taken as $\frac{3/2}{5} \sim$ 30%. Similarly, the error in the wind direction is about ± 5 degrees. As discussed later, the wind has little influence on the flow field for the cases considered here, making the errors in wind speed or direction of minor practical importance.

4.6 Presentation of Results

4.6.1 Velocity Measurements

Figure 4.3 shows the location of each velocity measurement station on the study area, as well as the observed direction of flow during flood and ebb tide. No measurements were taken in the panne occupying the center of the study area. This region had no vegetation, and was at a lower level than the surrounding marsh surface, with the result that the water depth during tidal inundation generally exceeded the capabilities of the metering device.

Depending on the tide, the direction of flow is seen from Figure 4.3 to be fairly constant over the study area; remembering that these measurements were taken over a period of about a week, it is also seen that the flow direction is constant from day to day, as would be expected for tidally driven flow.

The velocity profiles taken at each station are shown in Figures 4.5-4.9. Each profile is marked with an identification number giving the station number and profile number, in that order. The position of the tide (i.e. flood or ebb) and time of day is also given for each profile. The range of measurements observed at each depth indicates a velocity error of about twenty to thirty percent, which agrees with the estimates made in the previous section. The generally higher velocities observed during flood than ebb tide are caused by the larger water slopes, presented in the next section.

The grass height for each profile is identified with a dashed line. The grass is seen to be either completely submerged below the water surface or, more often, protruding through the entire water column. Further discussion of the velocity measurements is postponed until Section 4.7, which compares the experimental results against model predictions.

4.6.2 Stage Height and Water Slope

Figures 4.10-4.14 present the results of the stage height measurements, with each figure corresponding to a different field day. The figures are divided into three sections. The uppermost section of each figure plots total elevation η against time for the northern most meter stick.

The middle section of the figure shows the water slopes in the north and west direction, calculated by assuming the water surface over

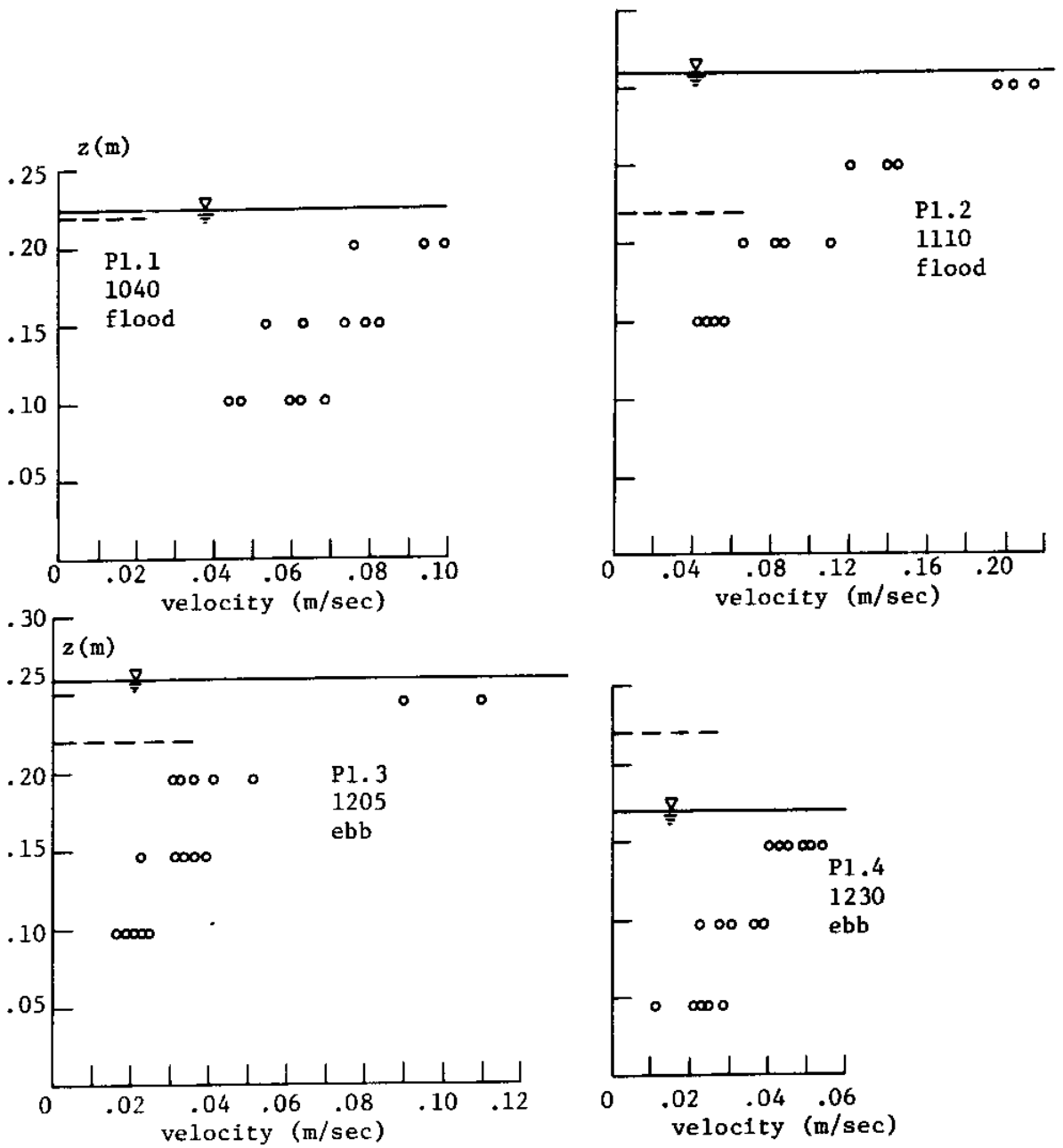

Figure 4.5 - Observed Velocity Profiles at Station 1

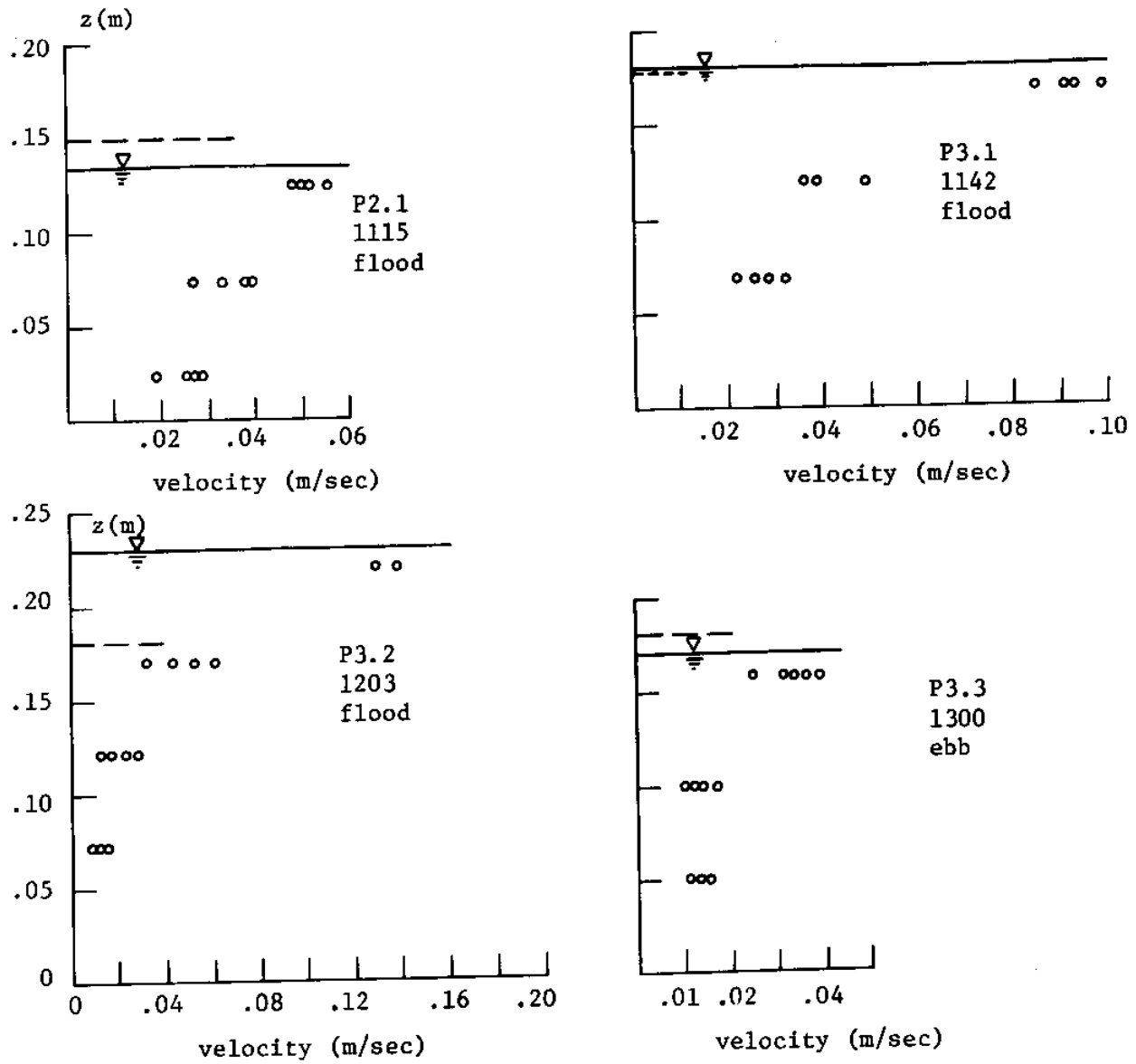

Figure 4.6 - Observed Velocity Profiles at Stations 2 and 3

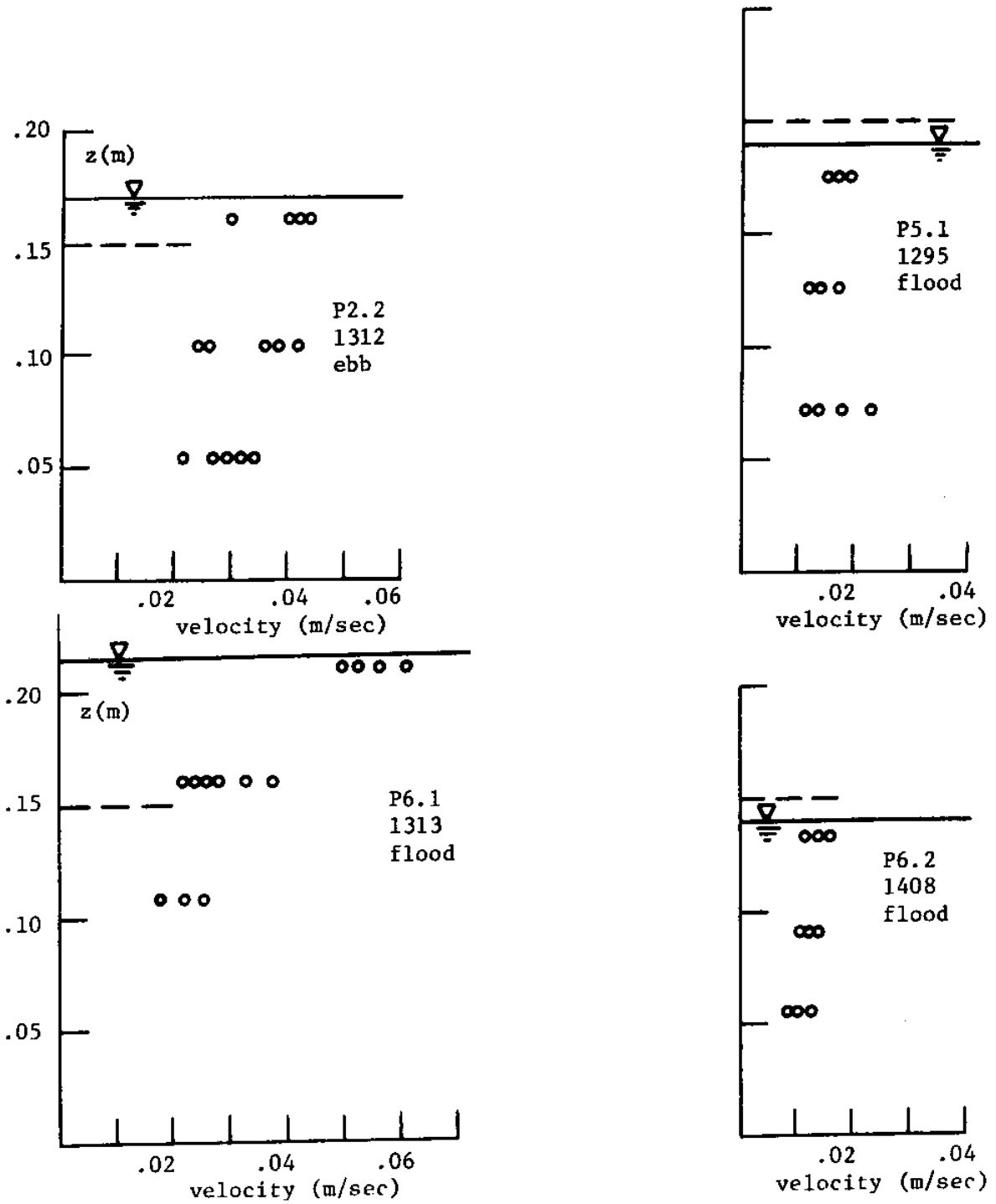

Figure 4.7 - Observed Velocity Profiles at Stations 2, 5 and 6.

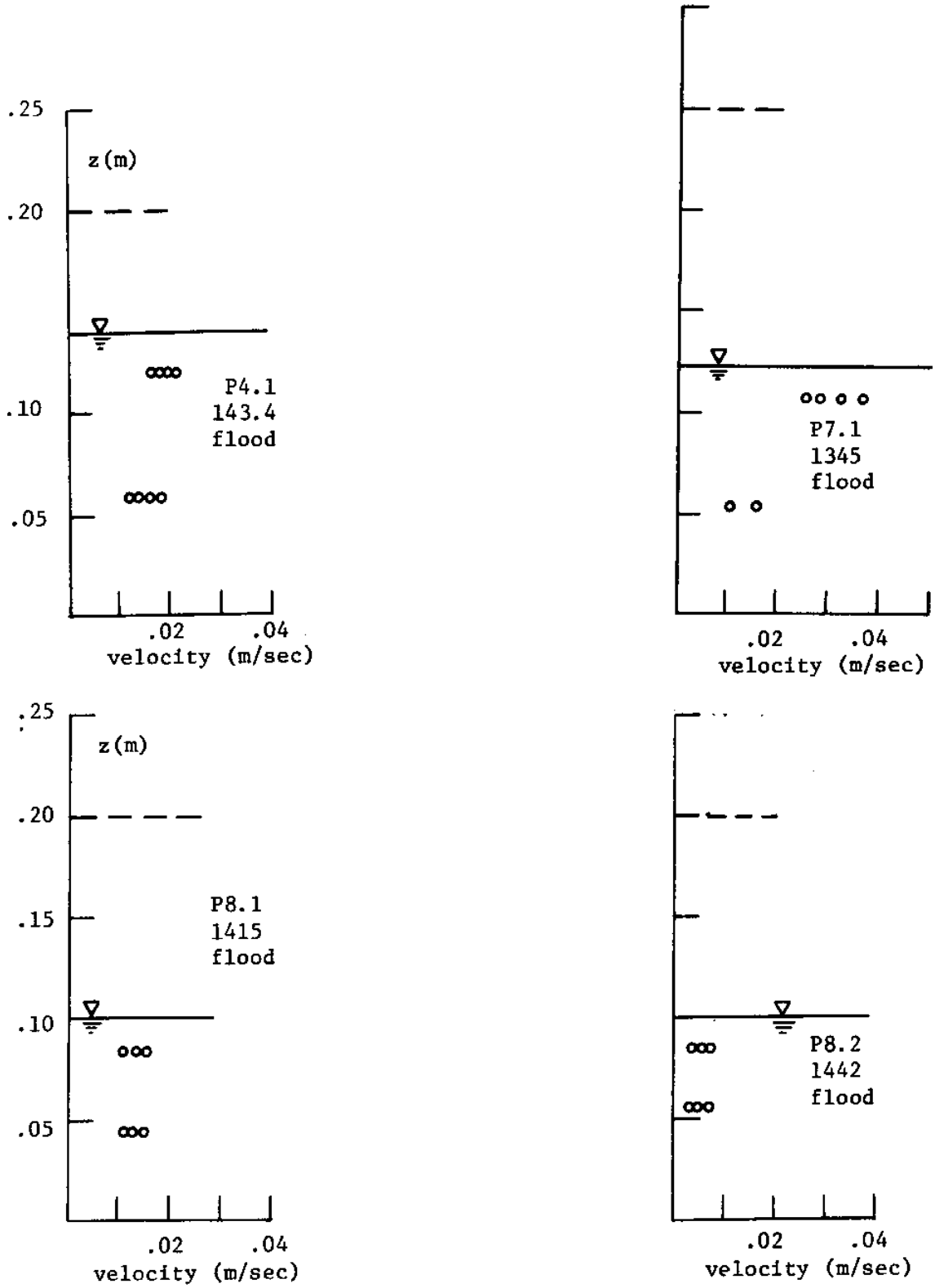

Figure 4.8 - Observed Velocity Profiles at Stations 4, 7 & 8

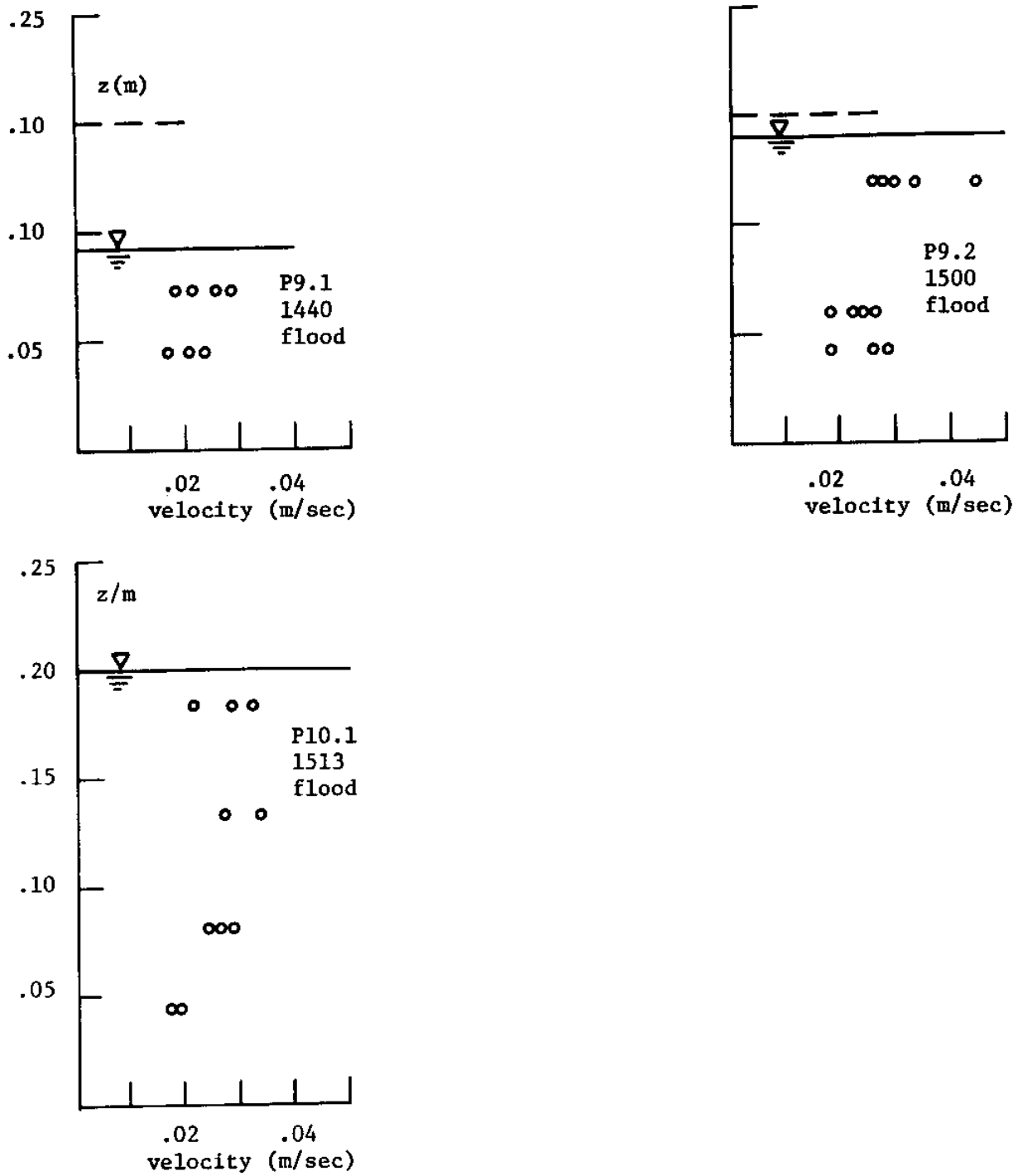

Figure 4.9 - Observed Velocity Profiles at Stations 9 and 10.

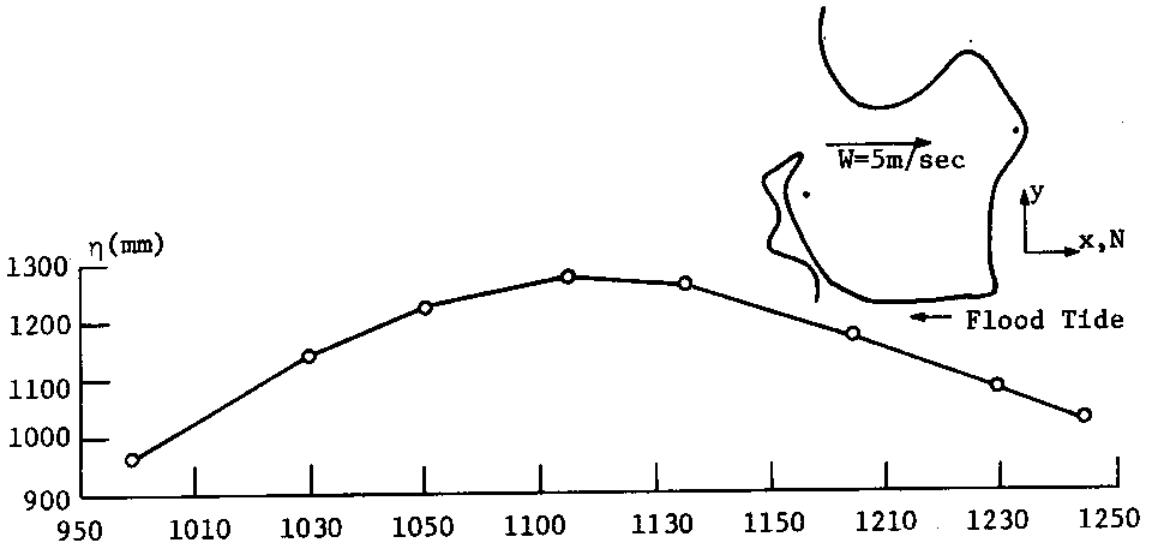

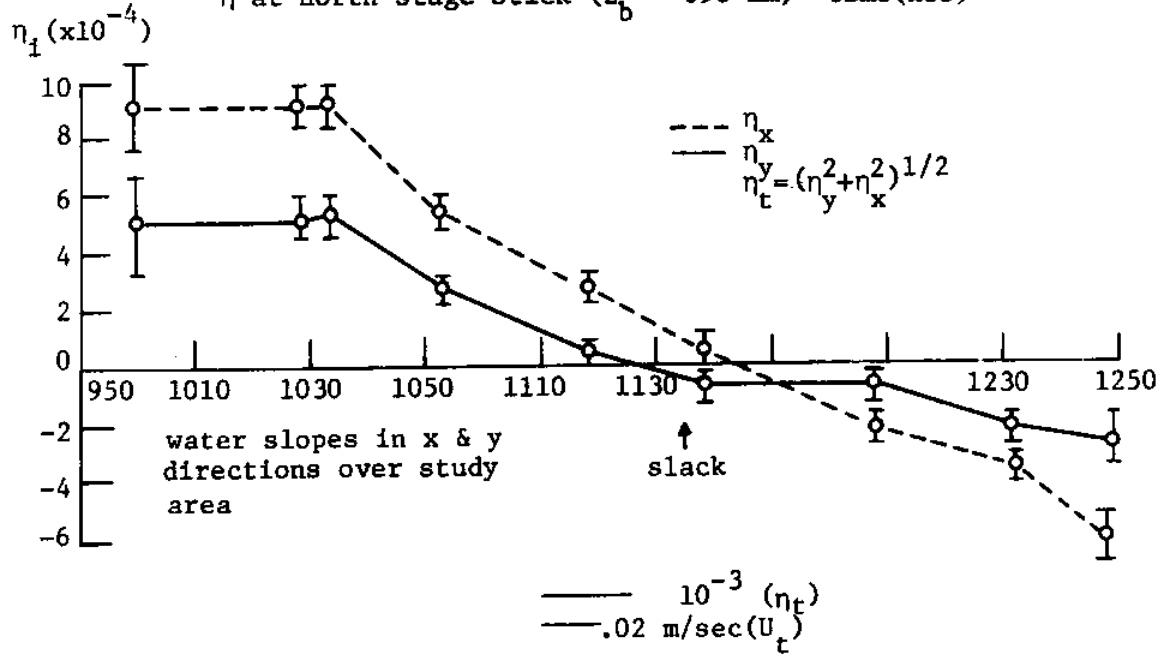

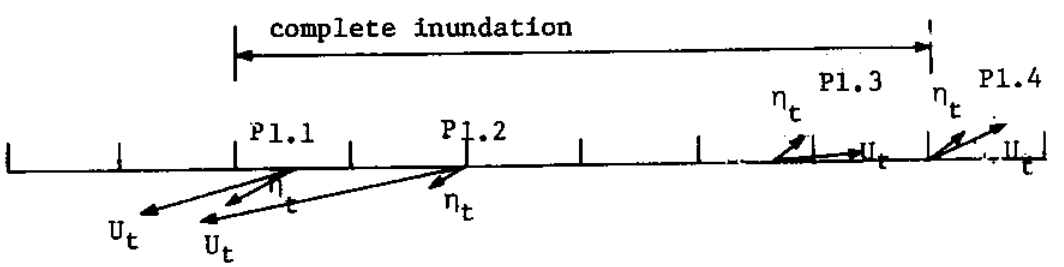

direction and magnitude of η_t and U_t at sampling stations at time of measurements.

Figure 4.10 - Stage Data for 8/29/80.

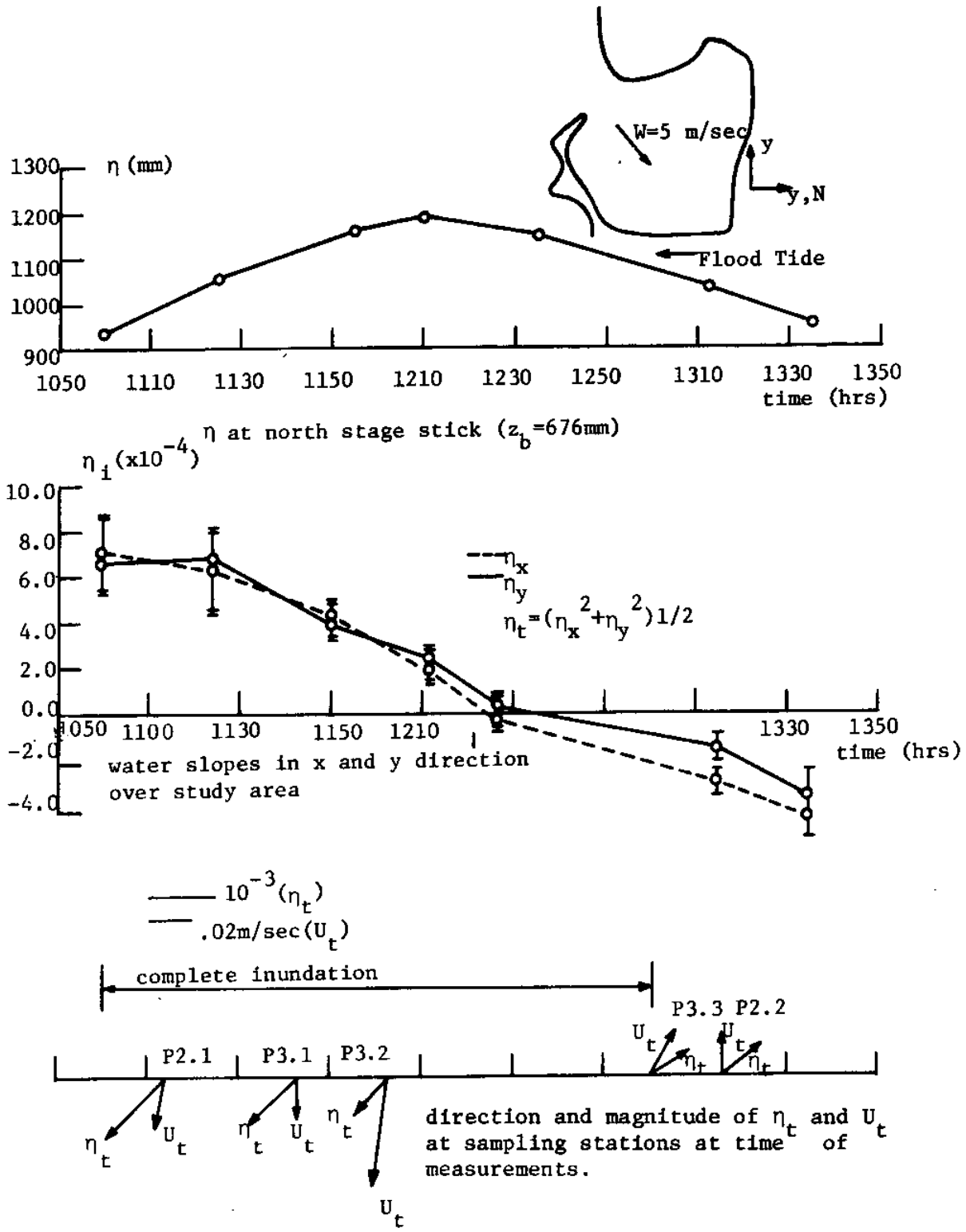

Figure 4.11 Stage Data for 8/30/80.

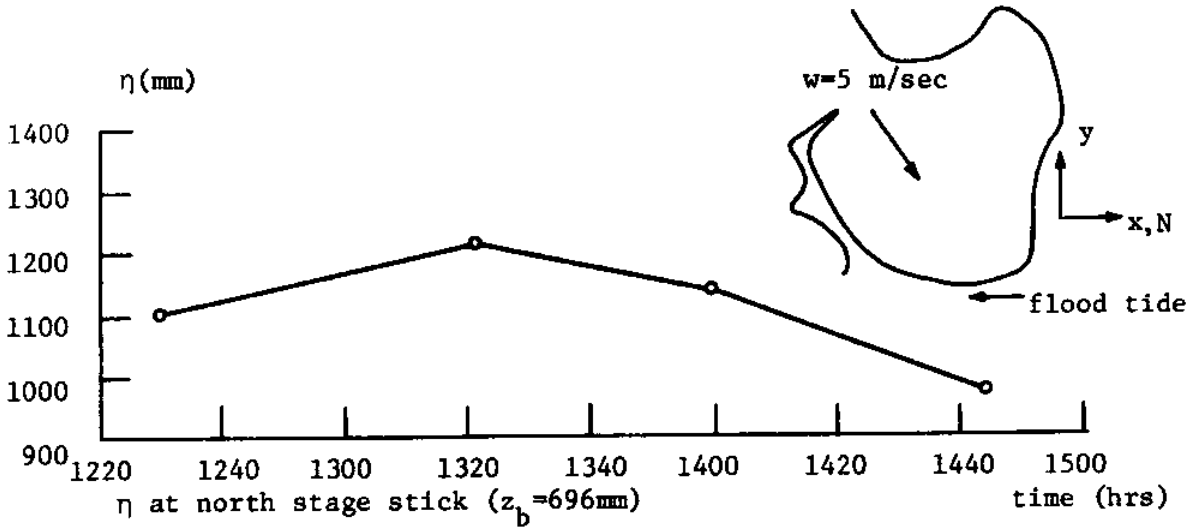

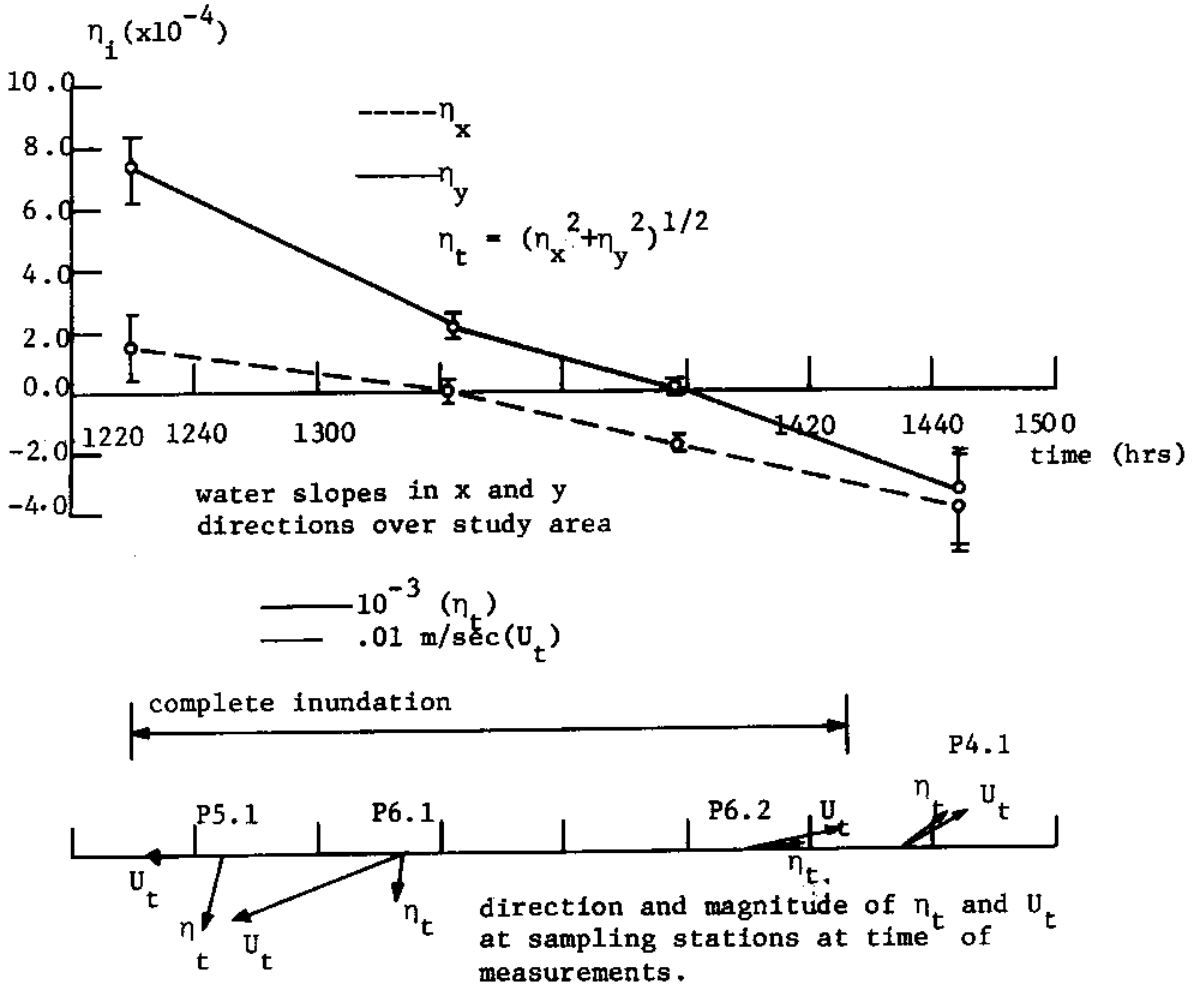

Figure 4.12 - Stage Data for 8/31/80.

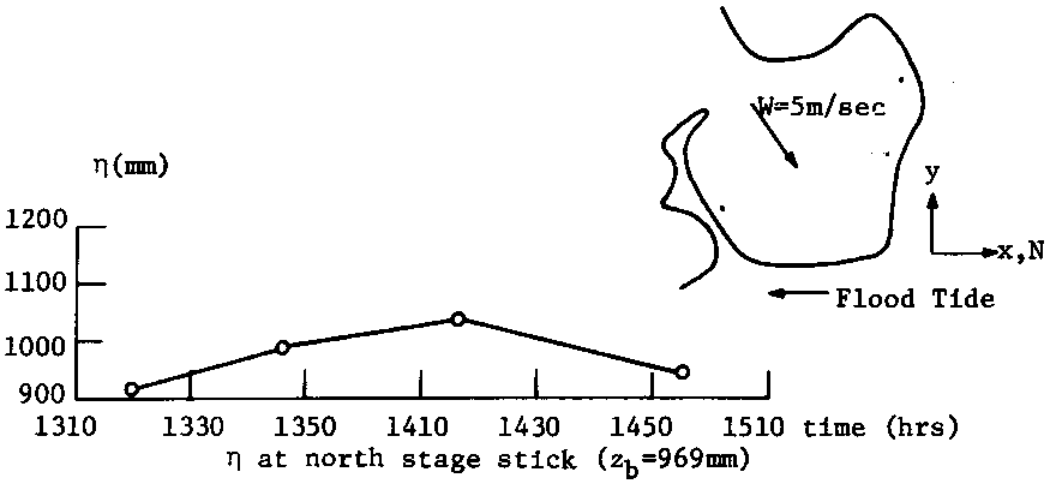

η at north stage stick (z_b=969mm)

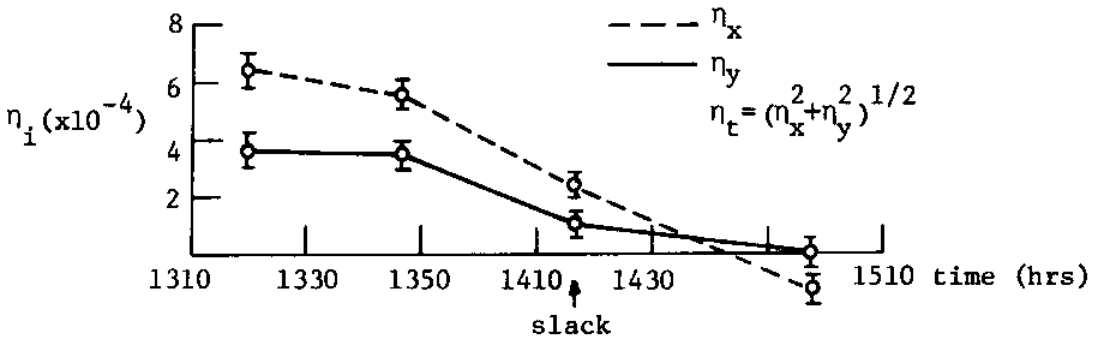

water slopes x and y directions over study area

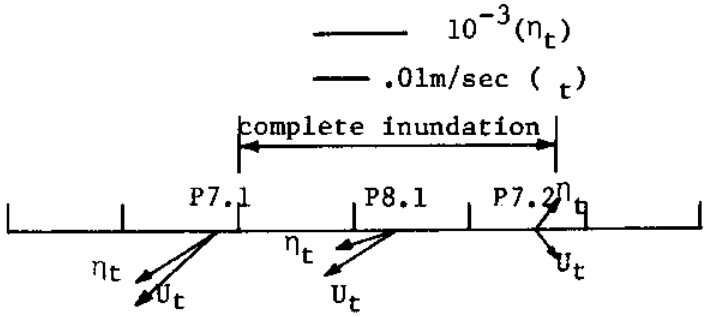

direction and magnitude of η_t and U_t at sampling stations at time of velocity measurements

Figure 4.13 - Stage Data for 9/1/80.

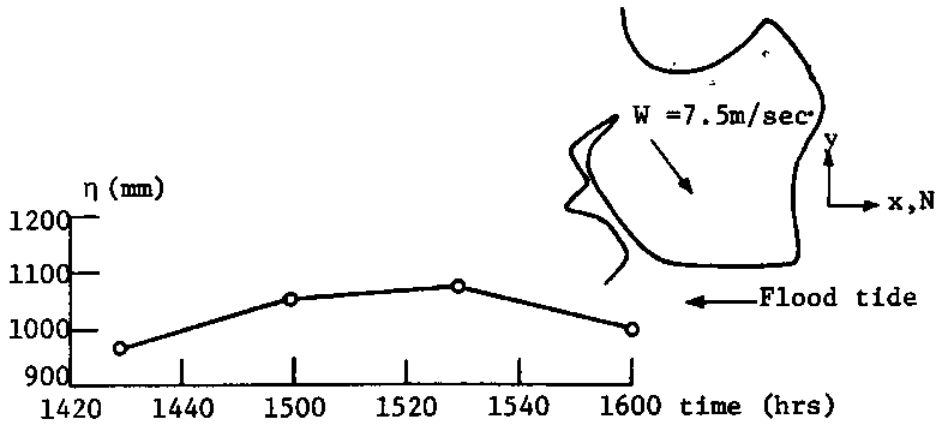

η at north stage stick (z_b=658mm)

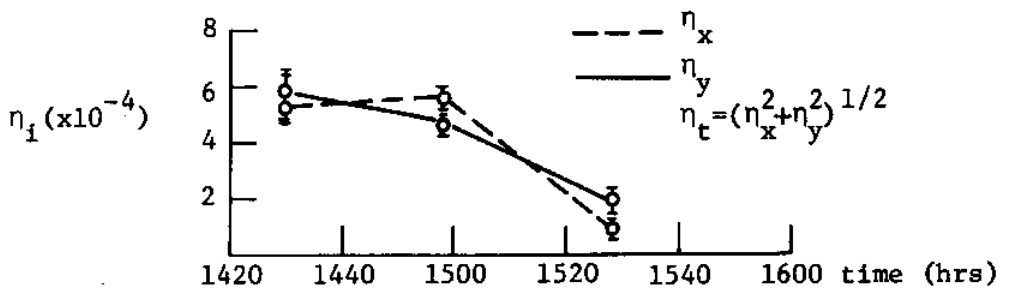

water slopes in x and y direction over study area

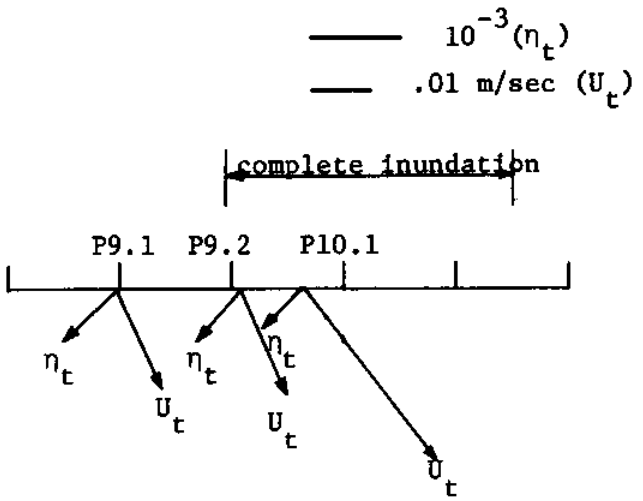

direction and magnitude of η_t and U_t at sampling stations at time of velocity measurements

Figure 4.14 - Stage Data for 9/2/80.

the entire study area to be a plane, as discussed previously. The error bars represent the standard error of the coefficients of the equation of the plane. The water slopes are seen to be asymmetric about slack tide, with higher values during flood than ebb tide. The asymmetric nature of marsh tidal flow, as applied to the creeks, has been noted by Boon (1975), among others.

The bottom section of each figure shows the net direction of water slope and velocity at the time each profile was taken. Depending on the tide, the direction of water slope is seen to be fairly constant from day to day. Also shown in the bottom section is the period during which the study area was completely inundated, as determined with the topographic survey, and the aid of the field notes. Except for the profiles taken around the time when the study area was only partially inundated, the water slope and direction of flow are in roughly the same direction. The most notable exception to this occurs for stations 2 and 9 (Figures 4.11 and 4.14), both of which are located in the same part of the study area. The water slope and velocity in these cases are approximately perpendicular; although the wind is in the same direction as the water flow, it's magnitude is too small to account for the observed velocities in the grass. The water flow in this part of the study area is significantly different from that at the other stations, and seems to be governed by local conditions that do not apply elsewhere on the marsh.

4.6.3 Wind Speed and Direction

Figure 4.15 presents a weather station record of wind speed and direction for a typical field day. Both the magnitude and direction are seen to be rather steady; as might be expected for an area bordering the sea, the direction of the wind was almost always landward, with a heading of about seventy degrees from north. The magnitude and direction of the wind for each field day is noted in Figures 4.10-4.14.

4.7 Comparison of Field Data and Model Predictions

Having analyzed the field data, it was then possible to use this information in model comparisons. Only those profiles in which the study area was completely flooded, and in which the water slope and velocity had approximately the same direction, were used in model predictions. Figures 4.16-4.23 show the observed and predicted profiles for each case. For simplicity, and ease of comparison, only the velocity magnitudes are shown in the figures.

In order to make meaningful comparisons between the observed and predicted results, it was necessary to simulate the physical condititons existing at the time the profiles were taken; this was done in terms of the following model parameters.

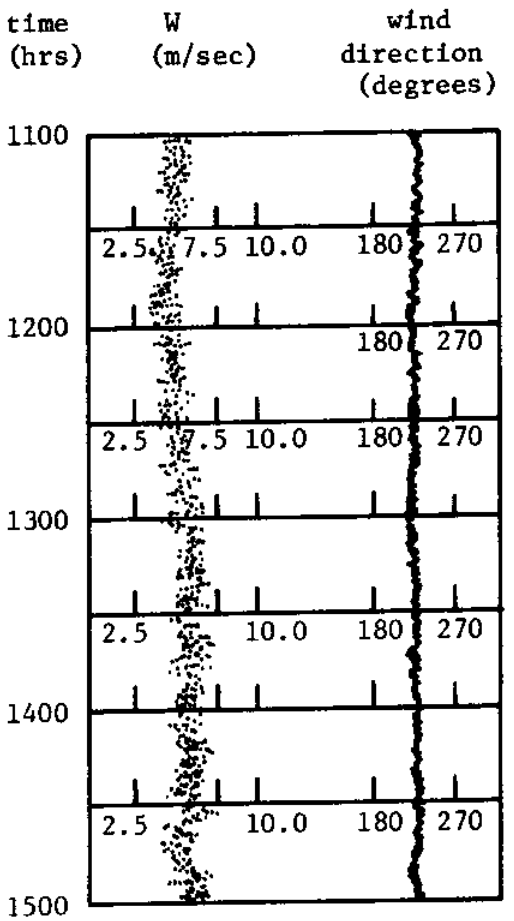

Figure 4.15- Wind Speed and Direction for 9/1/80

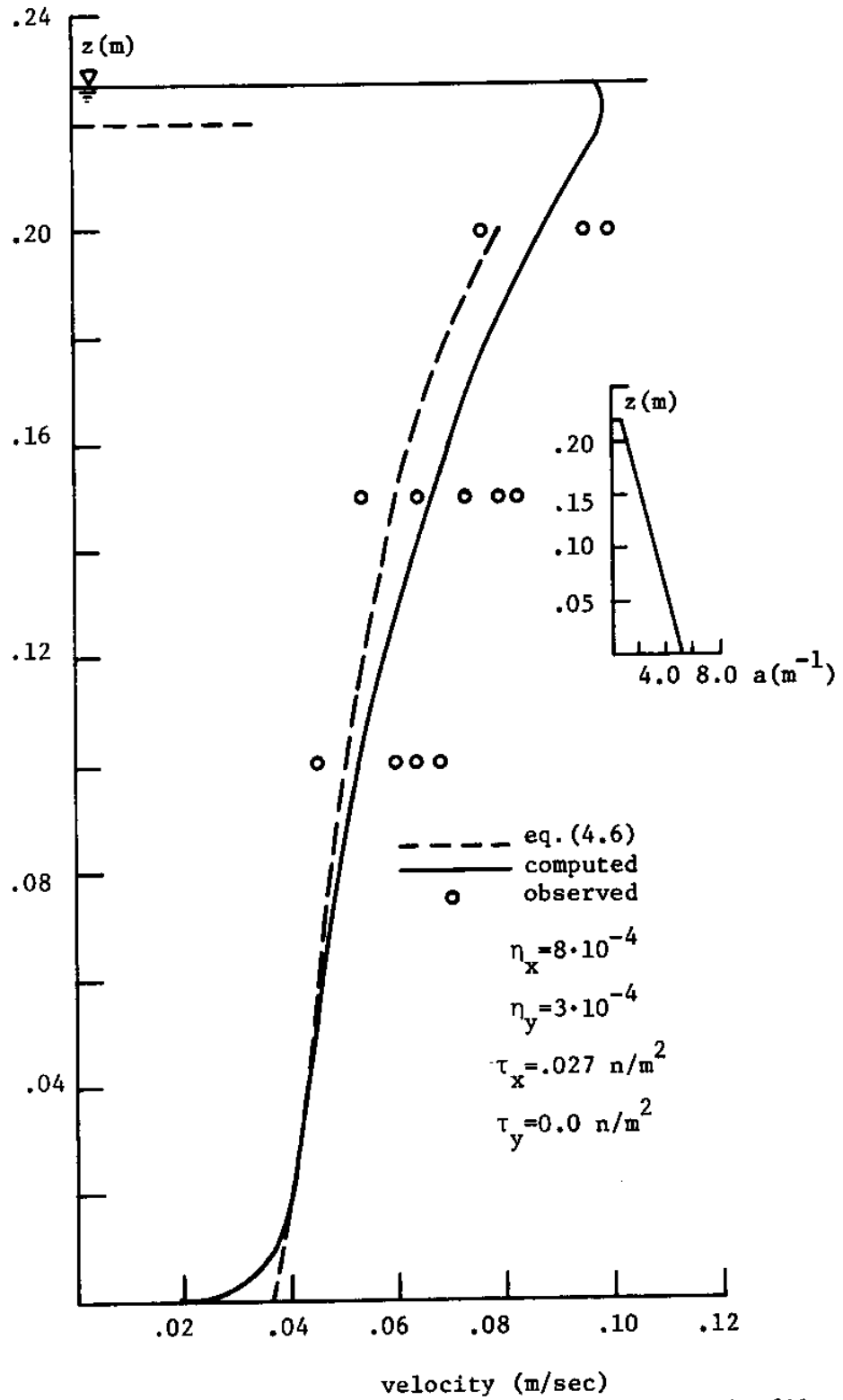

Figure 4.16 - Observed and Computed Velocity Profiles for Pl.1

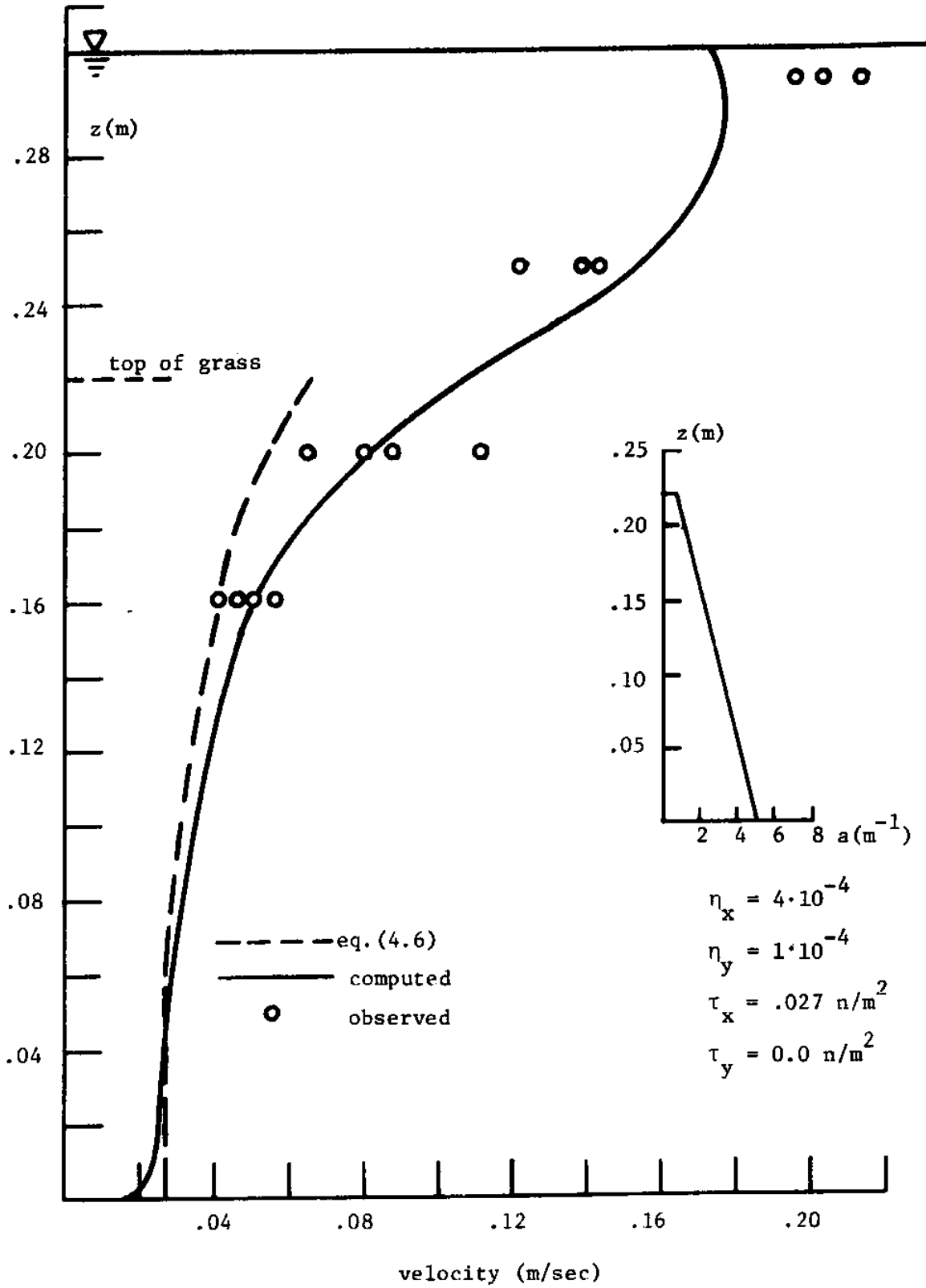

Figure 4.17 - Observed Velocity Profile for P1.2

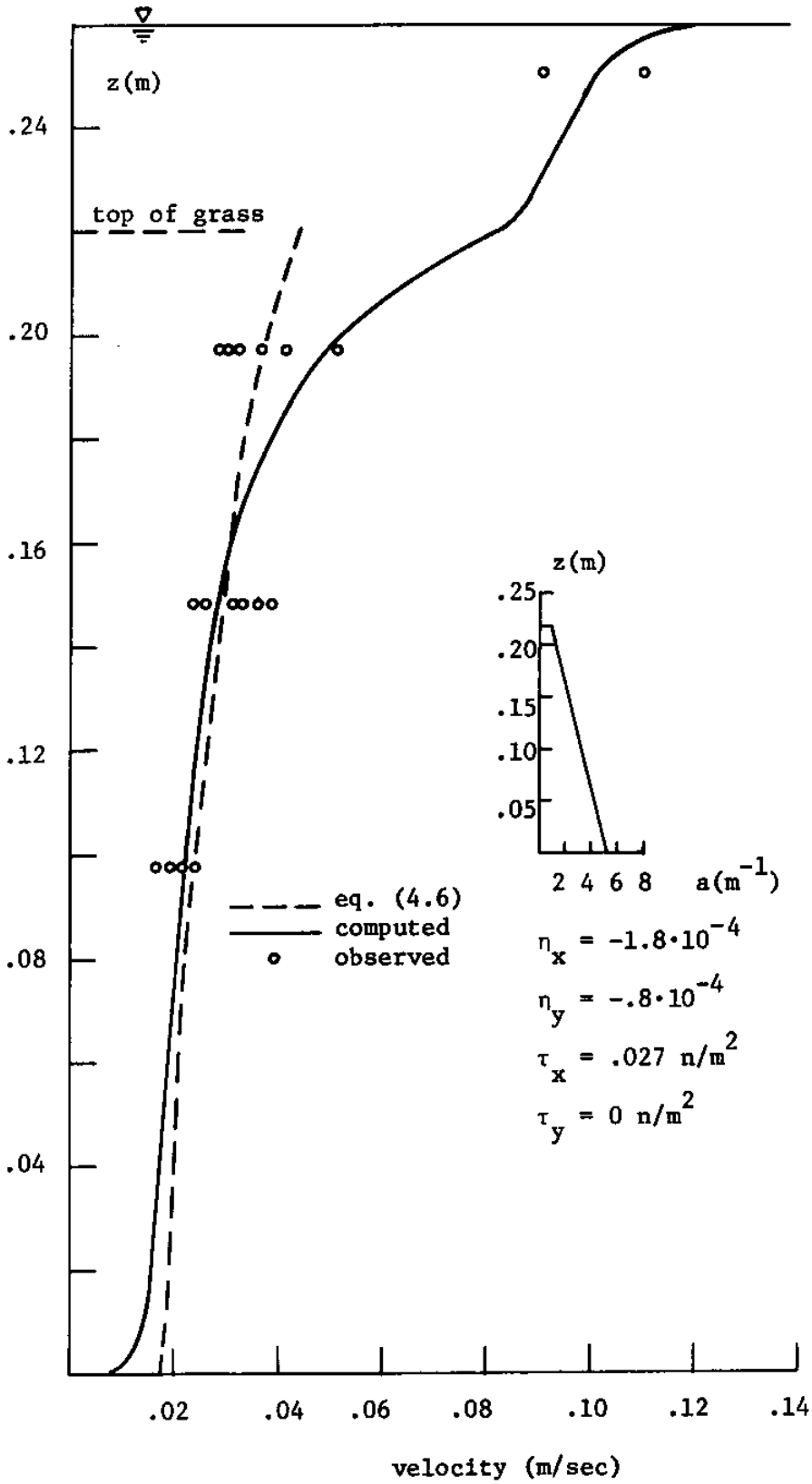

Figure 4.18 - Velocity Profile for P1.3

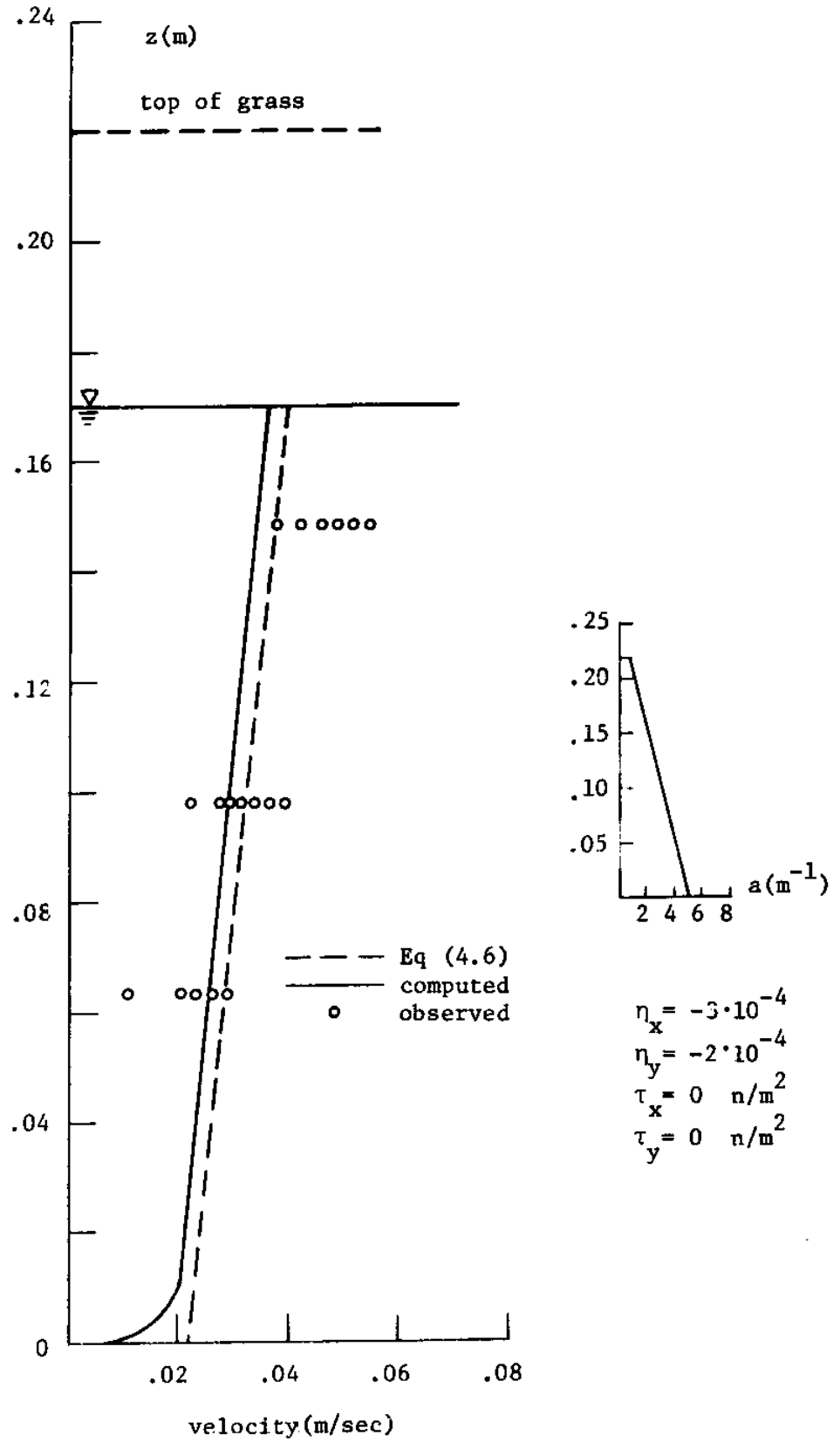

Figure 4.19 - Velocity Profile for Pl.4

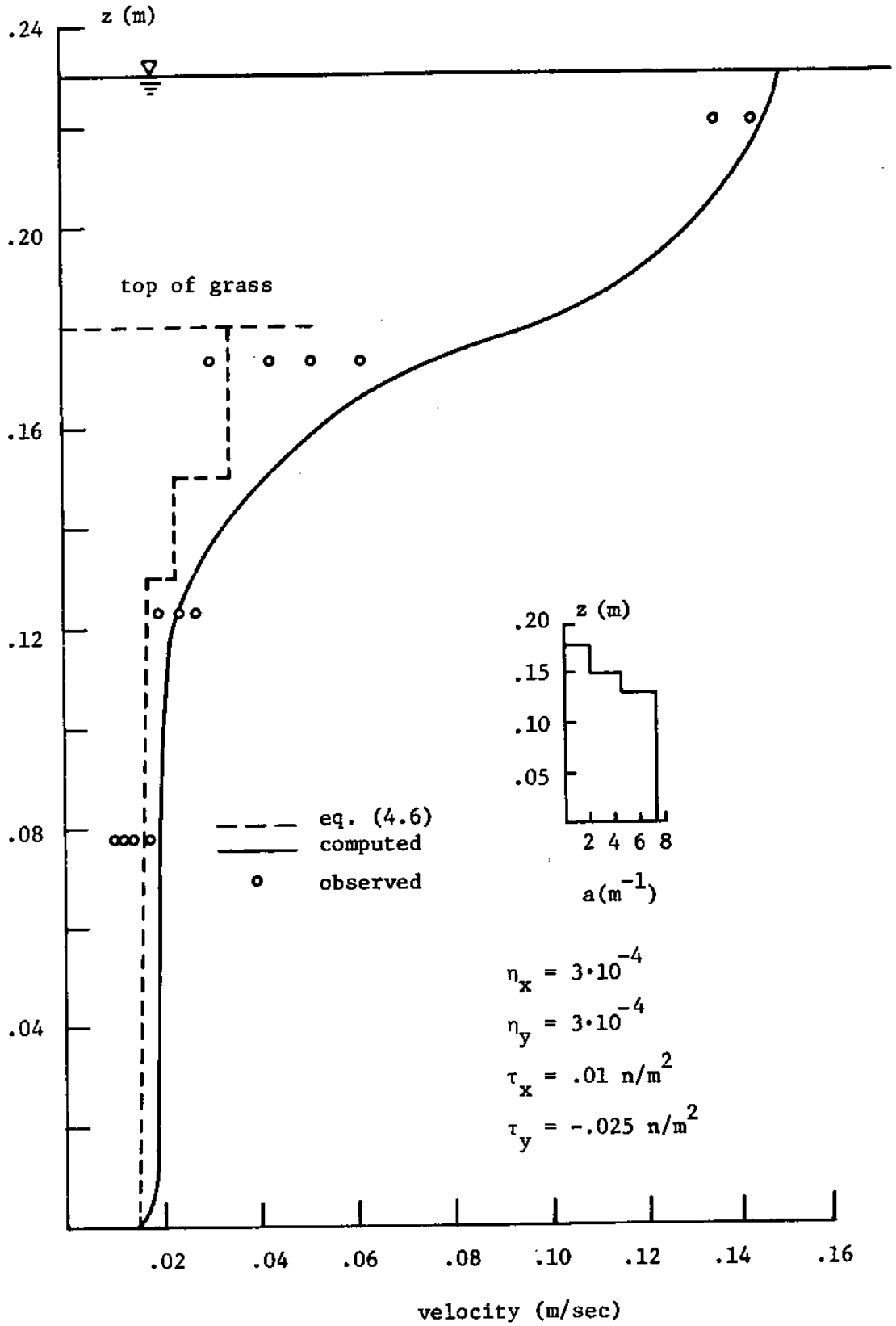

Figure 4.20 - Velocity Profile for P3.2

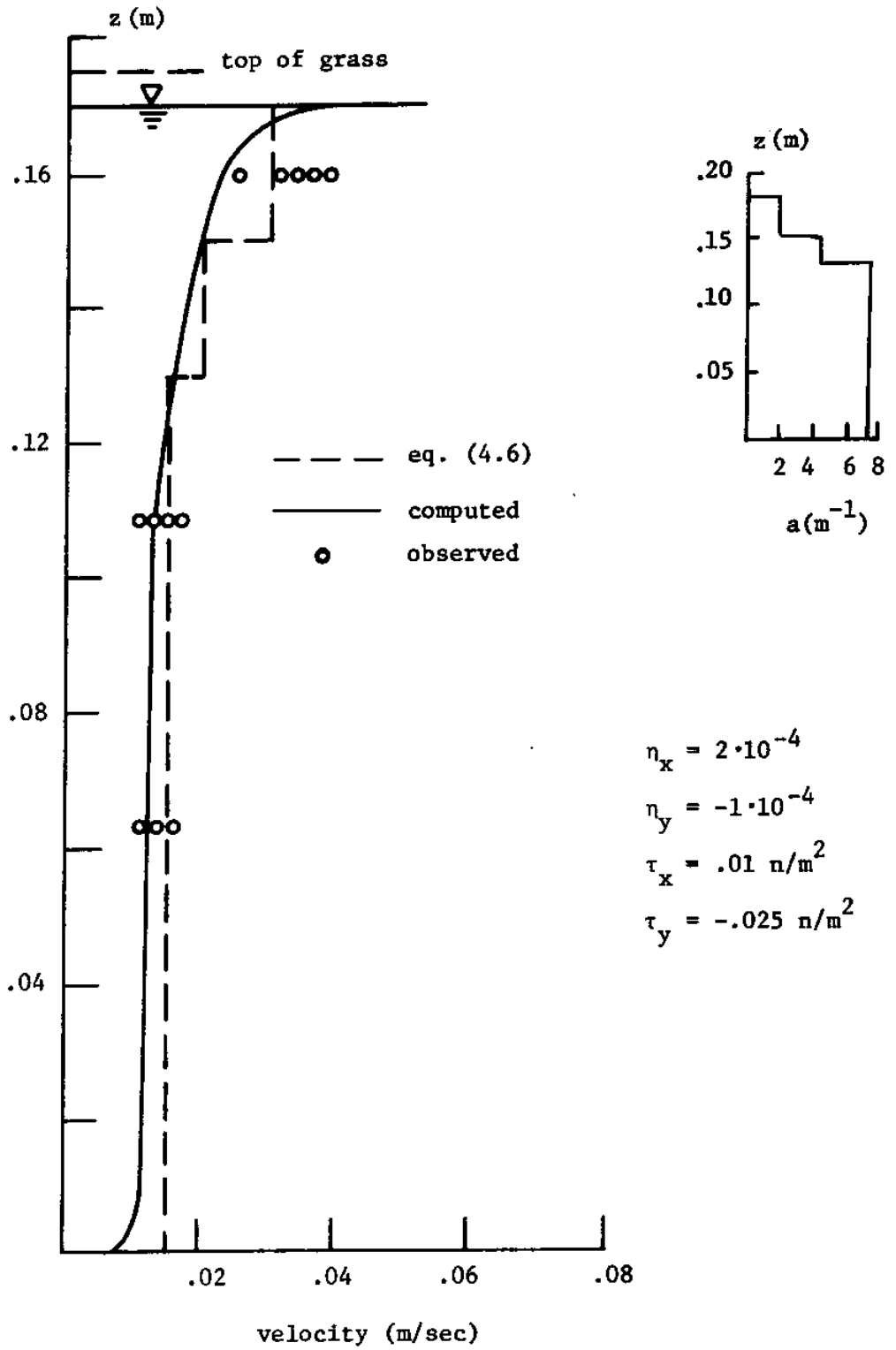

Figure 4.21 - Velocity Profile for P3.3

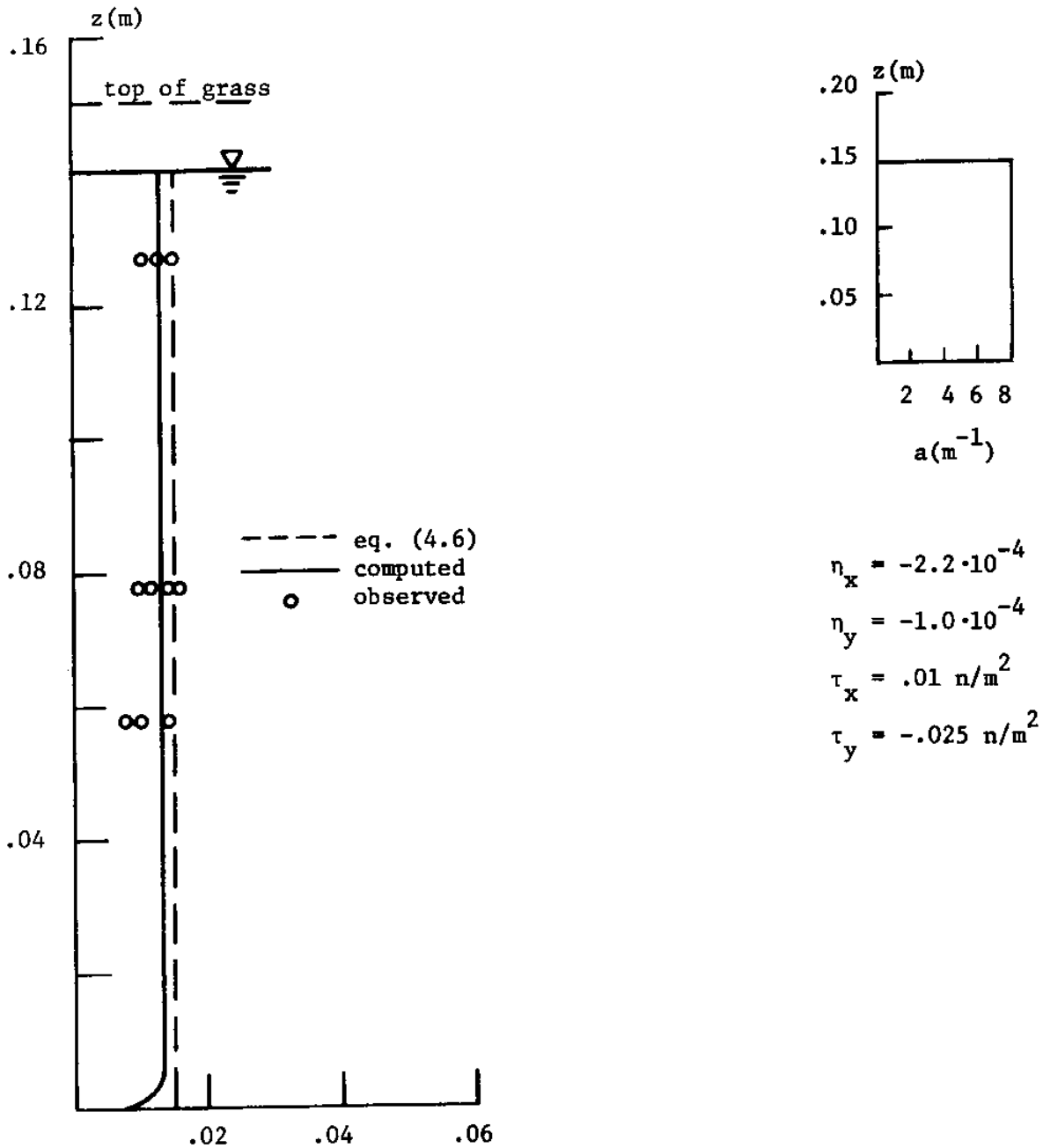

Figure 4.22 - Velocity Profile for P6.2

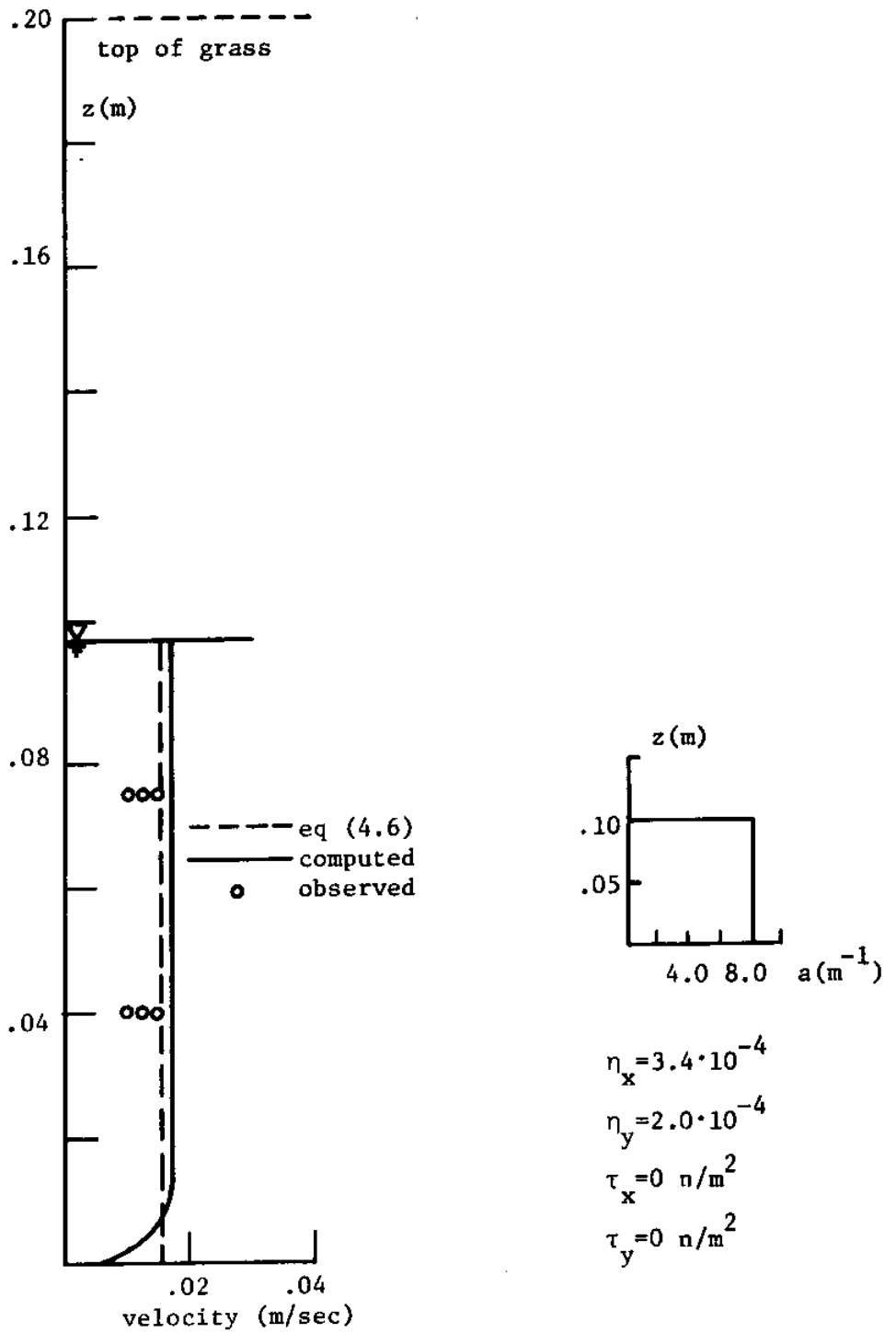

Figure 4.23 - Observed Velocity Profile for P8.1

4.7.1 Water Slopes

The water slopes $(\frac{\partial \eta}{\partial x}, \frac{\partial \eta}{\partial y})$ at the time of each profile were obtained by reference to Figures 4.10-4.14. As discussed later, the wind has little effect on the flow, from which it follows that the direction of flow predicted by the model will coincide with the direction of the net water slope.

4.7.2 Grass Characteristics

The vegetation was modeled as a collection of circular cylinders of different lengths. Three parameters characterize the cylinders. The first one is the height of the tallest cylinders; in general, this was taken to be the same as the depth of the grass recorded in the field. In those cases where the grass was completely submerged, this height was adjusted slightly (by about ten percent) to give a better fit to the data in the region above the grass. This change is within the error with which the grass height was measured.

The second parameter is the drag coefficient (C_d), which was taken to be that of a circular cylinder of .001m diameter (d=.001m). (C_d) was thus a function of the obstruction-based Reynold's number ($R_e=\sqrt{u^2+v^2}\,d/\nu$) as given by Schlighting (1968).

The third parameter is the vegetation density (a) which appears together with (C_d) in the drag term. As discussed in Chapter two, the drag of a single, isolated element is generally not the same as that of a group of such elements. This sheltering effect is usually accounted

for by assuming that (a) is given, and then adjusting (C_d) to fit the data. Not knowing (a) at the velocity measurement station, it was decided to specify (C_d), and then adjust (a).

Using a constant value of (a) in the model was found to yield unsatisfactory agreement with the data; to obtain better results, (a) was allowed to vary with height, it's magnitude being determined to give a reasonable fit to the data. The distribution of (a) used in each model prediction is shown in the appropriate figure. The same (a) profile was used in all comparisons made at any one station.

As mentioned above, the sheltering effect is accounted for in the value of (a). Common values of the sheltering coefficients (p_d) recorded in vegetative canopies, such as corn, are about 3 (see Section 3.4.1). Thom (1971), in a wind tunnel study of flow through circular cylinders of .001m diameter, and obstruction-based Reynold's number (R_e) of about 60, found (p_d) to be about one. For marsh grass, having similar geometry, and R_e values, it seems possible that the same (p_d) would apply, in which case the computed values of (a) would not be significantly different from those determined directly from the grass geometry. The maximum difference expected between the computed and actual values would be about a factor of three.

The only literature known to the author about marsh grass densities is in a paper by Valiela et al (1978). Using their values of stem diameter (about .002m), and stem density/m^2 (about 1000), a value of $a = 2m^{-1}$ is computed. This number is compatible with those found by

model predictions. The trend of decreasing (a) with height is not surprising, and is in accord with what might be expected for a tall grass, having most of it's mass near the bottom, and getting progressively thinner with height.

These ideas are corroborated by Schaefer et al (1982), who determined the vertical (a) distributions at six sites within the same study area used in this investigation. The location of each site is shown in Figure 4.3. The observed (a) distributions are displayed in Figure 4.24. The higher values of (a) recorded at site 6 are due to the predominance of the grass Distichlis spicata at this location; at the other five sites, Spartina alterniflora was the major species. (The velocity measurements were all taken in Spartina alterniflora). Comparing the (a) profiles determined by Schaeffer with those predicted by the model, the following points are observed;

(1) As with the model predictions, the recorded (a) profiles are not the same for each site, reflecting the spatial variation mentioned above.

(2) For $z > .05$ m, the observed (a) profiles are seen to be in good agreement with those determined by the model, both in terms of shape, as well as range of magnitudes. For $z < .05$ m, the model values are generally lower; this is most likely due to the fact that few velocity measurements were taken in this range, thus requiring extrapolation of (a) from higher regions, where velocity measurements did exist. The higher observed grass densities near the bottom

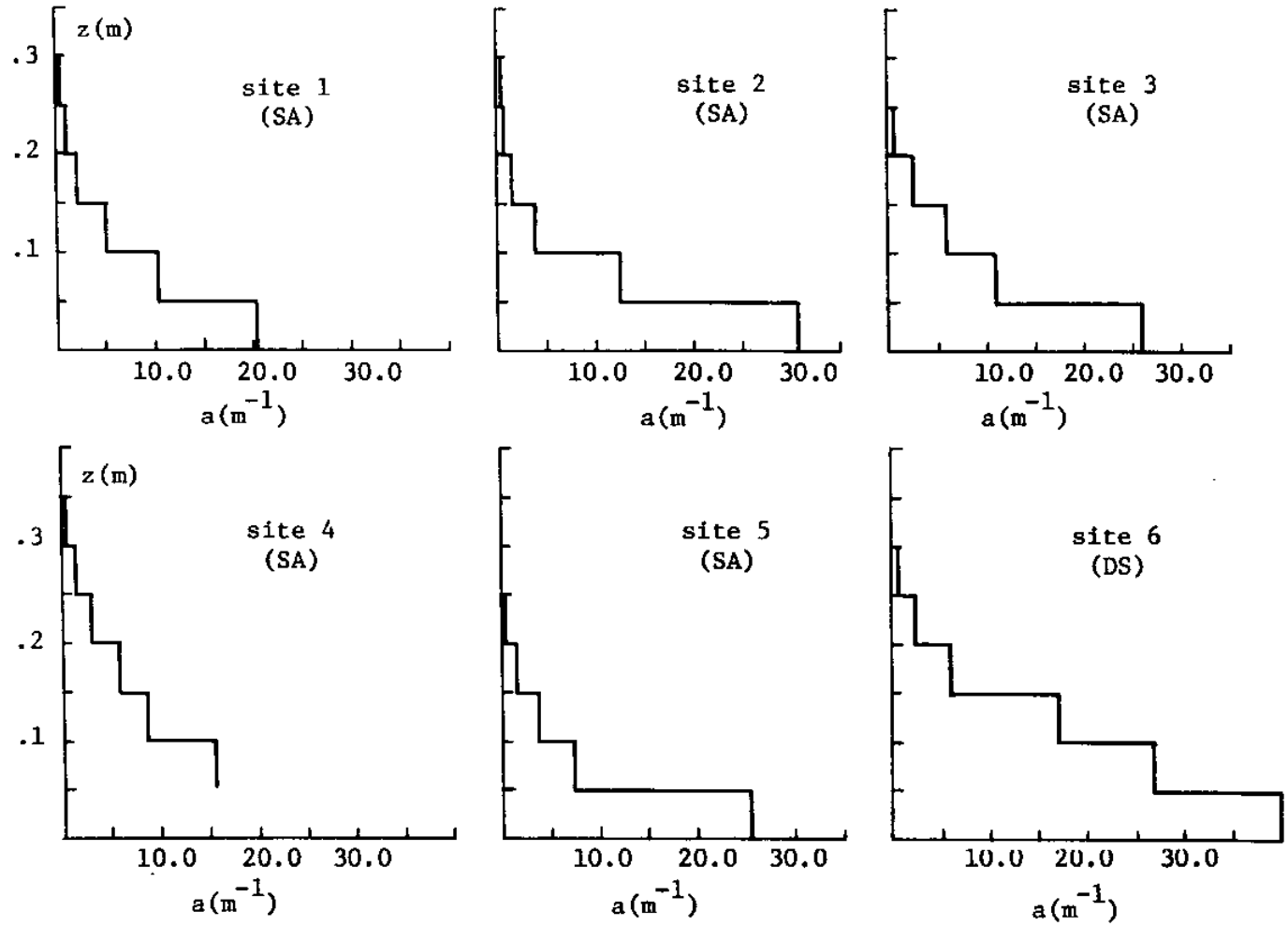

Figure 4.24 - Profiles of (a) at Six Sites on Study Area (SA = Spartina alterniflora; DS = Distichlis Spicata)

indicate that the velocities in this region will probably be less than those predicted by the model in Figures 4.16-4.23.

Except for the near-bottom region, it is seen that the model has reproduced the same general (a) distributions as found by the measurements of Schaefer. This supports the belief that (a) did not serve as merely a fitting parameter in the model calculations, but represented the conditions in the field.

4.7.3 Wind Stress

The wind stress was obtained by solving the model equations (2.9) for the overlying air flow. The predicted values of stress for each profile are shown in Figures 4.16-4.23. For the cases considered here, the wind stress will have little effect on the flow, except for a thin region near the water surface. That this is so can be seen by noting that the average velocity recorded over the study area was about 5m/sec; using the relationships defined in Section 2.3, this gives a value of stress of about .03 n/m^2, compared to a pressure force ($\rho g \frac{\partial \eta}{\partial x} h_w$) of about .2 n/m^2. In the presence of grass extending into the air, the effect of the wind would be even less. For practical purposes, the wind stress could have been set to zero for the cases examined here, without appreciably affecting the results. In general, however, this may not be true; thus, for instance, at slack tide, or in dead-end regions of the marsh, the wind may be important. The following discussion, while directed specifically at the procedure used

in the trial calculations, serves also as a guideline for those situations in which the wind stress may play a role in determining the velocity.

The boundary conditions for the air flow situations are given in Section 3.5. In review, the upper boundary conditions on the velocity are prescribed values of U_a and V_a at a reference height h_a. These were determined with the help of the meteorological station data, which provided the wind speed (W) and direction at a height of three meters. Aligning the x axis with the direction of the wind allowed V_a to be set equal to zero. Using a reference height of ten meters (h_a = 10m), the velocity U_a was adjusted until the velocity predicted by the model at three meters coincided with W. An alterenate procedure would have been to set h_a = 3m, and U_a = W. This route was not followed because of the concern that, at a height of three meters, $\frac{\partial \varepsilon}{\partial z}$ and $\frac{\partial k}{\partial z}$ would not be zero, as prescribed in the boundary conditions. The dependence of model results on h_a is discussed in the next Chapter.

In addition to knowing the reference velocities, solution of the model equations required knowledge of the grass properties. In principle, the vegetation density should have been changed for each station, in accordance with the spatial variation of the grass parameters. Considering the small magnitude of the wind stress, compared to the tidal forces, this seemed unnecessary for the cases considered here; instead, a value of $a = 4m^{-1}$ was used in all comparisons. For similar reasons, the wind stress was set equal to

zero for those cases where the water surface was more than five centimeters below the top of the grass.

In accordance with the model's inability to handle bottom roughness, these wind calculations assume that the water surface is hydraulically smooth. This is almost certainly a resonable assumption for the low wind cases (about 5m/sec), studied here. Given the great reduction of stress within the grass, as shown in Figure 3.15, it seems likely that, as long as the grass protrudes well above the water column, the water surface may be taken as smooth with no appreciable influence on the results. If, however, the grass is completely submerged, or nearly so, the water surface may become rough enough under the action of a strong wind that the smooth surface assumption would no longer be valid. In this case, recourse could be had to the wall functions, discussed in Section 3.3.

4.8 Discussion

The agreement between the observed and predicted velocities shown in Figures 4.16-4.23 is generally quite good, both below and above the grass. While it is true that the vegetation density (a), and in some cases the grass height (h_g) as well, were adjusted to obtain a better fit, it should be remembered that the same values were applied to all profiles taken at one station; in particular, this refers to Figures 4.16-4.21, in which a total of six profiles were studied using two (a) distributions, one for each station. This gives some

indication that (a) was not merely a fitting parameter, but represented the conditions found in the marsh. The profiles of (a) seem reasonable, and are compatible with the admittedly scant available literature, as well as the observations in Great Sippewissett Marsh. The variation of (a) between stations could be said to reflect the spatial variation of the grass properties.

Both the observed and predicted velocity profiles share certain general trends; among these are,

(1) nearly uniform velocity within the grass. This is due to the dominance of the pressure forces over shear effects. Neglecting the shear stresses, the momentum equation expresses a balance between the drag and pressure, giving a uniform velocity of

$$(u^2+v^2)^{1/2} = [((g\frac{\partial\eta}{\partial x})^2+(g\frac{\partial\eta}{\partial y})^2)^{1/2}\frac{2}{C_d a}]^{1/2} \qquad (4.6)$$

The velocities predicted in this manner for each profile are shown in Figures 4.16-4.23. The drag coefficient was taken as 2.5, which is roughly the same as that used in the model calculations, and corresponds to the value of (C_d) for a circular cylinder with a diameter of .001m, and a velocity of about .01m/sec.

This simple model is seen to yield close agreement with the data in those cases where the grass protrudes throughout the entire water column. As long as the wind speed is small, compared to the pressure forces, (4.6) will accurately predict this type of flow. As discussed

later, however, the wind stress may not always be negligible.

For those cases where the grass is completely submerged (i.e. Figures 4.17, 4.18, 4.20) (4.6) also fits the data fairly well within the vegetation. In general, however, this will not be true. In situations where the grass is completely submerged, a shear stress will be created in the grass by the overlying layer of water. This shear will induce velocities within the grass larger than those predicted by (4.6). This trend is not very noticable in the data of Figures 4.17, 4.18, 4.20 owing to the relatively large grass depth (h_g) compared to the depth of water. For cases having smaller values of h_g/h_w, the shear will have more of an influence on the velocity profiles, making (4.6) less useful. The effect of $\frac{h_g}{h_w}$ is discussed in the next chapter.

Finally, (4.6) can not handle the layer of water lying above the top of the grass in Figures 4.17, 4.18, 4.20.

(2) velocities in the water above the grass considerably larger than within the grass. This result is observed both in the data and the model predictions, the two of which are in generally good agreement in the above grass region. The larger velocities imply that, although the above grass region is not as deep as the canopy layer, it may still play a major role in the overall marsh circulation patterns. As such, it is important to have a model that can handle this region.

(3) negligible wind effect. As discussed in detail in the previous section, the wind forcing is generally an order of magnitude

smaller than the pressure forces. While characterizing the profiles studied here, this is not a general feature of all marsh flow situations. It is conceivable, for instance, that under certain circumstances, such as at slack tide, or in closed-end marsh areas, the wind could be the dominant driving force.

The above discussion has stressed the point that the flow conditions represented in Figures 4.16-4.23 do not include all possible situations that may be encountered in tidally inundated marshes. In particular, this refers to shear effects; while relatively unimportant for most of the studies studied here, the influence of shear on the velocity profiles will become greater under conditions of lower grass to water depth ratios, or larger wind stresses. Of the three cases discussed in Chapter two, the profiles examined here most closely resemble case 1, i.e., steady, tidally driven flow.

4.9 Summary

A time of travel flow-metering device, capable of measuring velocities of about .01m/sec in marsh vegetation, was designed, built, and used in a field study of water movement in Great Sippewissett Marsh. Vertical velocity profiles were obtained at various locations on a study area, bordered on three sides by open water, thus allowing a net flow during flood, and ebb tide. Stage height readings around the perimeter of the study area and wind speed and direction were also recorded. The water slopes corresponding to the times of the velocity

profiles were derived from the stage stick readings by assuming the water surface over the study area to be a plane.

Using this information, model comparisons against the flow data were performed. The vegetation density (a), not being known, was determined by using the model to obtain a reasonable fit to the data. The same (a) distribution was used in all predictions made at any one location. The drag coefficients (C_d) was taken as that of a circular cylinder having a .001m diameter. The wind stress was determined by solving the model equations in the overlying air flow.

The generally close agreement between model predictions and experimental results lends further support to the correctness of the model formulation, and indicates the ability of the model to predict the flow in tidally inundated marshes.

The degree to which the velocity profiles are affected by changes in the driving forces, grass characteristics, and other parameters, is investigated in the next chapter.

Chapter V

Generalized Solution

5.1 Introduction

This chapter identifies the dimensionless parameters governing obstructed flow, relating to such effects as the geometry of the obstructions, or the relative magnitude of the shear and pressure forces, and uses the model developed in Chapter III to investigate the sensitivity of the flow field to variation of these parameters.

Three basic flow geometries are considered; these are shown in Figure 5.1. The water movement in inundated salt marsh grass may belong to either flow types I or II, or to a combination of these two cases. The overlying air movement belongs to flow type III, which may be thought of as a limiting case of flow type II in which the ratio of the depth of the obstructions to the flow depth approaches zero. For simplicity, only uni-directional flow is considered, and the drag coefficient (C_d) is set equal to one.

5.2 Dimensional Analysis

The kinematic dimensional parameters governing obstructed flow situations may be taken as

h_g = depth of obstructions

h_w = water depth

h_a = height above bottom at which velocity is specified

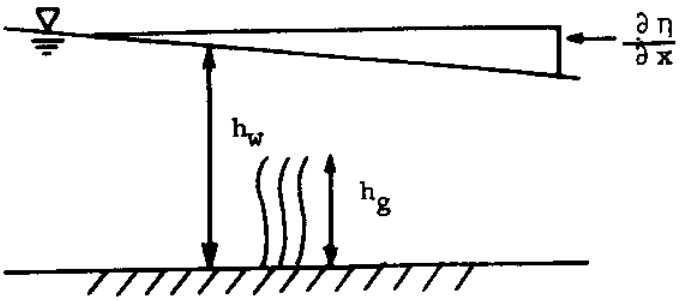

I - confined, pressure driven flow

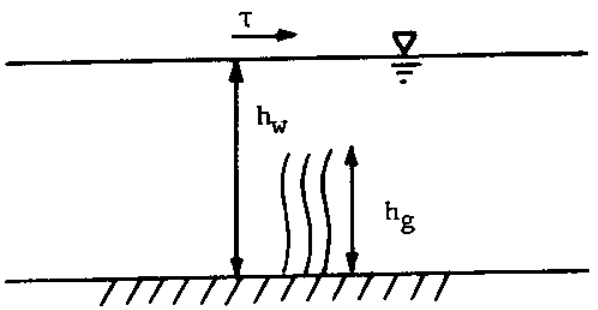

II - confined, shear driven flow

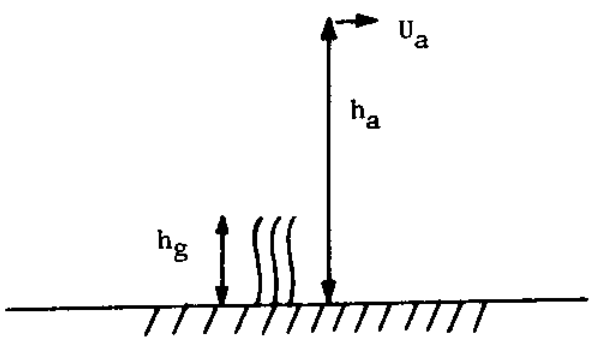

III - unconfined flow

Figure 5.1 - Three Flow Geometries Considered in Generalized Solutions.

$C_d a$ = effective grass density

$U_* = (\frac{\tau}{\rho})^{1/2}$ = friction velocity at h_w (type II flow)

$U_\eta = (g \frac{\partial \eta}{\partial x} h_w)^{1/2}$ = characteristic velocity for pressure driven flow (type I flow)

U_a = specified velocity at h_a (type III flow)

ν = kinematic viscosity of the fluid

These parameters may be arranged to form the following dimensionless group (assuming that U_a is relevant only for type III flow)

$\frac{h_a}{h_g}$ = ratio of height at which velocity is specified to depth of obstructions.

$\frac{h_w}{h_g}$ = ratio of depth of confined flow to depth of obstructions

$C_d h_g a$ = effective area normal to the direction of flow per unit horizontal area.

$\frac{U_*^2}{U_m^2}$ = relative magnitude of shear force to total driving force

$\frac{\hat{U}\hat{h}}{\nu}$ = Reynold's number

where $U_m = (U_*^2 + U_\eta^2)^{1/2}$, and $\hat{U}$, $\hat{h}$ are appropriate scales for defining a Reynold's number. As will be seen later, the velocity scale $U_g = U_m(\frac{2}{C_d h_g a})^{1/2}$ is often applicable, representing a momentum balance

between the driving force (U_* and/or U_η) and the drag on the obstacles. Table 5.1 presents the values of the above defined parameters for the model runs considered in this chapter.

Before considering the effect of the dimensionless parameters on the flow field, the influence on the model predictions of grid spacing, and initial conditions, was investigated by modeling two flow systems, geometrically and dynamically similar, but differing in scale by a factor of two. The systems were of type I, as defined in Figure 5.1. Reynold's number effects were eliminated by reducing ν by a factor of $2^{3/2}$ in the smaller configuration. To maintain geometrical similarity, the nodal point grid spacing for the smaller configuration was half that of the larger configuration. The various model runs performed for each geometry are detailed in Table 5.1 (runs 1-4). The non-dimensionalized velocity profiles for each run are shown in Figure 5.2.

From this figure, it is seen that the velocity profiles for the two runs having different initial conditions are about 1% apart, compared to about 10% for the two runs having dissimilar grid spacing. (The grid spacing for the smaller configuration was kept at the same value as that for the larger configuration, instead of being reduced by a factor of two). The velocity profiles for the runs having the same initial conditions, and similar grid spacing, are seen to be practically identical. The close agreement between these two runs serves as a check of the model formulation, and of the completeness of the set of dimensionless parameters.

Run #	h_g m	a m^{-1}	h_w m	h_a m	U_*^2 $(\frac{m}{sec})^2$	$g\frac{\partial \eta}{\partial x}$ $\frac{m}{sec^2}$	ν $(x10^{-6})$ m^2/sec	U_a	$\frac{h_a}{h_g}$	$\frac{h_w}{h_g}$	$C_d h_g a$	$(\frac{U_*}{U_m})^2$
1	.1	5	.2	-	0	$5\cdot10^{-3}$	1.83	-	-	.5	.5	0
2	.05	10	.1	-	0	$5\cdot10^{-3}$	.647	-	-	.5	.5	0
3	.05	10	.1	-	0	$5\cdot10^{-3}$	.647	-	-	.5	.5	0
4	.05	10	.1	-	0	$5\cdot10^{-3}$	.647	-	-	.5	.5	0
5	.1	5	.1	-	0	10^{-3}	1.83	-	-	1	.5	0
6	.1	5	.1	-	0	10^{-2}	1.83	-	-	1	.5	0
7	.1	5	.1	-	0	.01	15	-	-	1	.5	0
8	.1	5	.1	-	.21	.042	15	-	-	1	.5	.98
9	.1	5	.1	-	.83	.017	1.8	-	-	1	.5	.98
10	.1	0	0	-	0	$5\cdot10^{-3}$	1.8	-	-	0	0	0
11	.1	.1	.1	-	0	$5\cdot10^{-3}$	1.8	-	-	1	.01	0
12	.1	1.0	.1	-	0	$5\cdot10^{-3}$	1.8	-	-	1	.1	0
13	.1	10.0	.1	-	0	$5\cdot10^{-3}$	1.8	-	-	0	1.0	0
14	.2	0	-	-	0	.42	15	-	-	1	0	1
15	.2	.05	.2	-	0	.42	15	-	-	1	0.1	1
16	.2	.5	.2	-	0	.42	15	-	-	1	.1	1
17	.2	5	.1	-	0	.42	15	-	-	1	0	1
18	.1	0	-	10	-	-	15	7	100	-	.01	-
19	.1	.1	-	10	-	-	15	7	100	-	.1	-
20	.1	1.0	-	10	-	-	15	7	100	-	1.0	-
21	.1	10.0	-	10	-	-	15	7	100	-	5.0	-
22	.1	50.0	-	10	-	-	15	7	100	-	.5	-
23	.1	5	.1	-	0	10^{-3}	1.8	-	-	1	.5	0
24	.1	5	.1	-	10^{-4}	$5\cdot10^{-3}$	1.8	-	-	.1	.5	.17
25	.1	5	.1	-	.42	.42	15	-	-	1	.5	.5
26	.1	5	.1	-	.42	.42	15	-	-	1	.5	.83
27	.1	5	.1	-	.42	.42	15	-	-	1	1.0	1.0
28	.2	5	.2	-	0	0	15	-	-	1	1.0	0
29	.15	6.7	.2	-	0	0	15	-	-	.75	1.0	0
30	.05	20	.2	-	0	0	15	-	-	.01	1.0	0
31	.2	5	.2	-	.42	.42	15	-	-	1	1.0	1
32	.15	6.66	.2	-	.42	.42	15	-	-	.75	1.0	1
33	.05	20.0	.2	-	.42	.42	15	-	-	.05	1.0	1
34	2.8	*	-	6	-	-	15	2.3	2.14	-	*	-
35	2.8	*	-	10	-	-	15	3.0	3.57	-	*	-
36	2.8	*	-	20	-	-	15	4.0	7.14	-	*	-

*See Figure 3.18

TABLE 5.1

Model Simulation Parameters

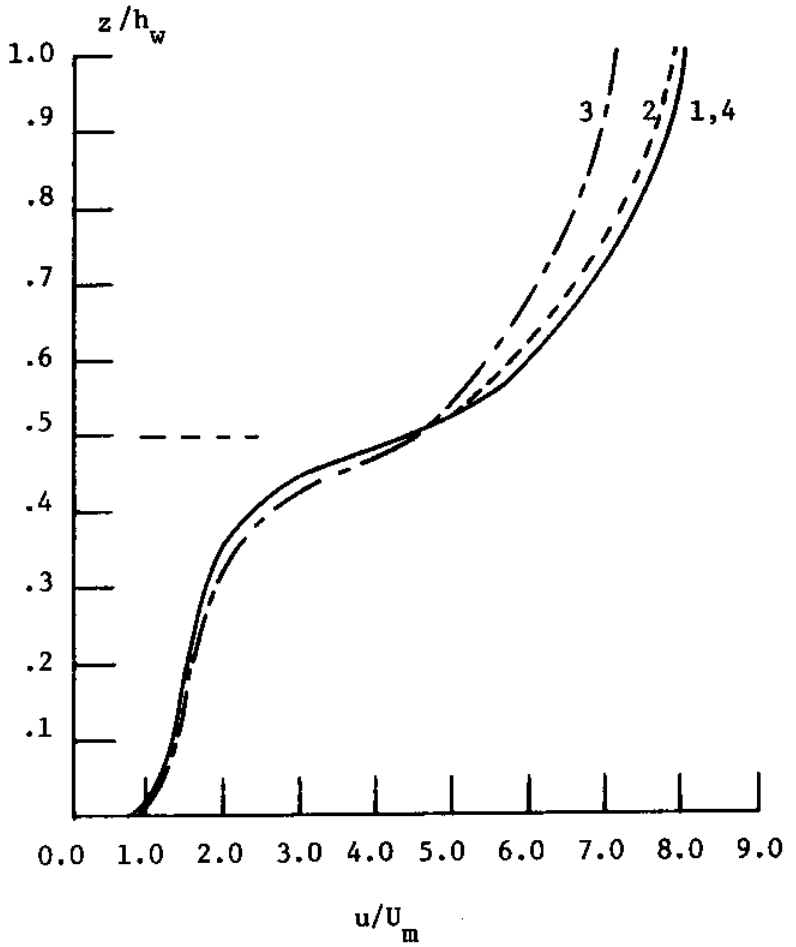

Figure 5.2 - Model Runs Investigating Scale Effects. Runs 1 and 2 Have Different Initial Conditions; Runs 1 and 3 Have Dissimilar Grid Spacing; Runs 1 and 4 Have the Same Initial Conditions, and Similar Grid Spacing.

A study was next done on the effect of a Reynold's number based on the water depth, defined as $R = U_t h_w/\nu$, where U_t is the average velocity over the flow depth h_w. For typical marsh flow situations, R will be about 1000. At this value, non-obstructed flow would be on the verge of changing from viscous to turbulent conditions. For obstructed flow, where the individual elements serve as sources of turbulence, this transition will likely occur for lower values of R. Although the flow will thus be turbulent, it seemed plausible that at $R \sim 1000$, viscous effects might still play a role in determining the flow field. This was investigated through two experiments, in each of which all dimensionless parameters except R were kept constant.

The conditions of the first experiment are detailed in Table 5.1, (runs 5-7), as well as Figure 5.3. Under these circumstances (i.e. type I flow with $h_g/h_w=1$), the velocity will be given by U_g throughout much of the flow depth, so that the value of the Reynold's number becomes $R \sim U_g h_w/\nu$. The value of R was varied between 1.1×10^3 and 1.1×10^4 by chanaging the slope $g \frac{\partial \eta}{\partial x}$, as shown in Table 5.1.

From Figure 5.3 it is seen that near the bottom the velocity deviates from U_g to satisafy the no-slip condition at the bottom. As R increases, the flow near the bottom assumes a more uniform shape, in accordance with the greater momentum transfer caused by the more turbulent motion. Over the range of R considered, viscous bottom effects are seen from Figure 5.3 to extend about 10% into the flow.

The second experiment used to study Reynold's number effects

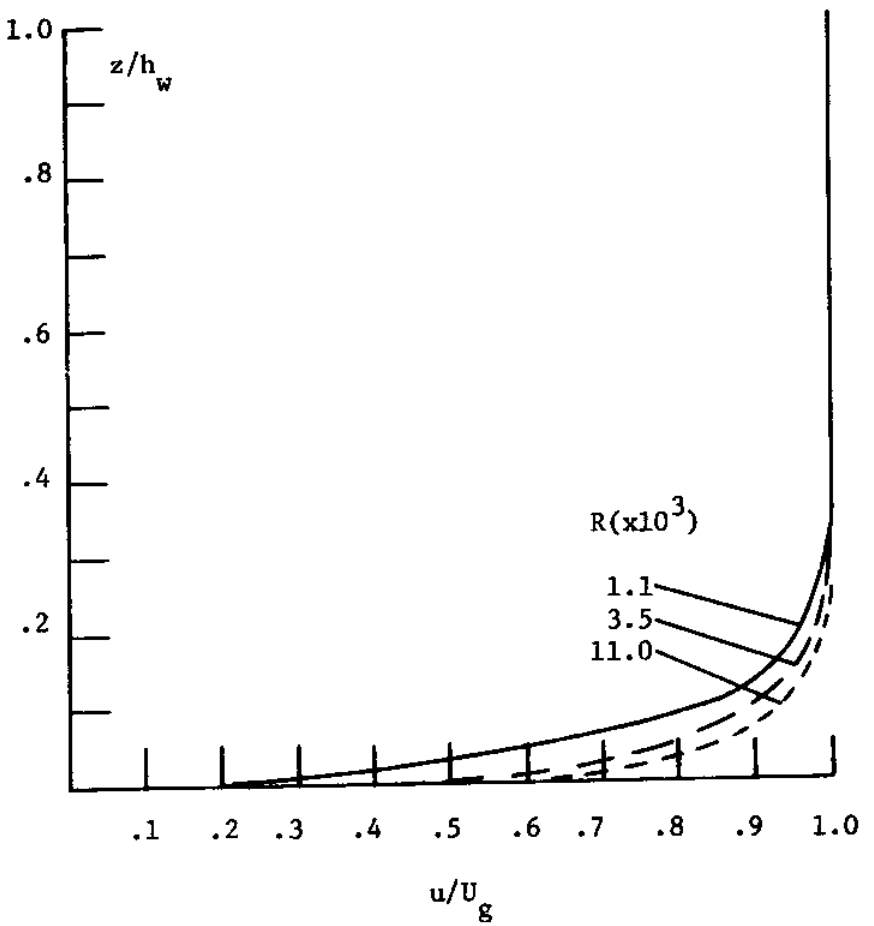

Figure 5.3 - Effect of Reynold's Number ($R=U_t h_w/\gamma$) on Type I Flow with $h_g/h_w=1$, $C_d h_g a=1$. (Runs 5-7).

involved a situation having both shear and pressure forces. Two model runs were performed, each having different magnitudes of the shear and pressure forces, but the same ratio $(\frac{U_*}{U_m})^2$. As such, R was the only dimensionless parameter that varied; the range of R was between 2700-6000. The two velocity profiles were found to differ by about 10%, as shown in Figure 5.4.

In the above two experiments, having R on the order of 1000, the major features of the flow were found to be relatively insensitive to R. To minimize Reynold's number effects on the model runs performed in this chapter, the value of R was kept as constant as possible, not usually varying by more than a factor of three during the course of any one set of runs. On this basis, and considering the small impact on the major flow features, Reynold's number effects are not considered in this chapter.

The following three sections present discussions concerning the effect of the dimensionless parameters on the vertical variation of velocity, the flow conveyance, and the turbulent structure for each of the types of flow in Figure 5.1. Comparisons are made between the turbulence closure theories used in other studies and the closure approach adopted here. Next, the variation of shear stress at the top and bottom of obstructions is considered, with the model results being used to determine the empirical coefficients appearing in previous obstructed flow models. The predicted values of the coefficients are compared with observed values. Finally, a summary of the most important

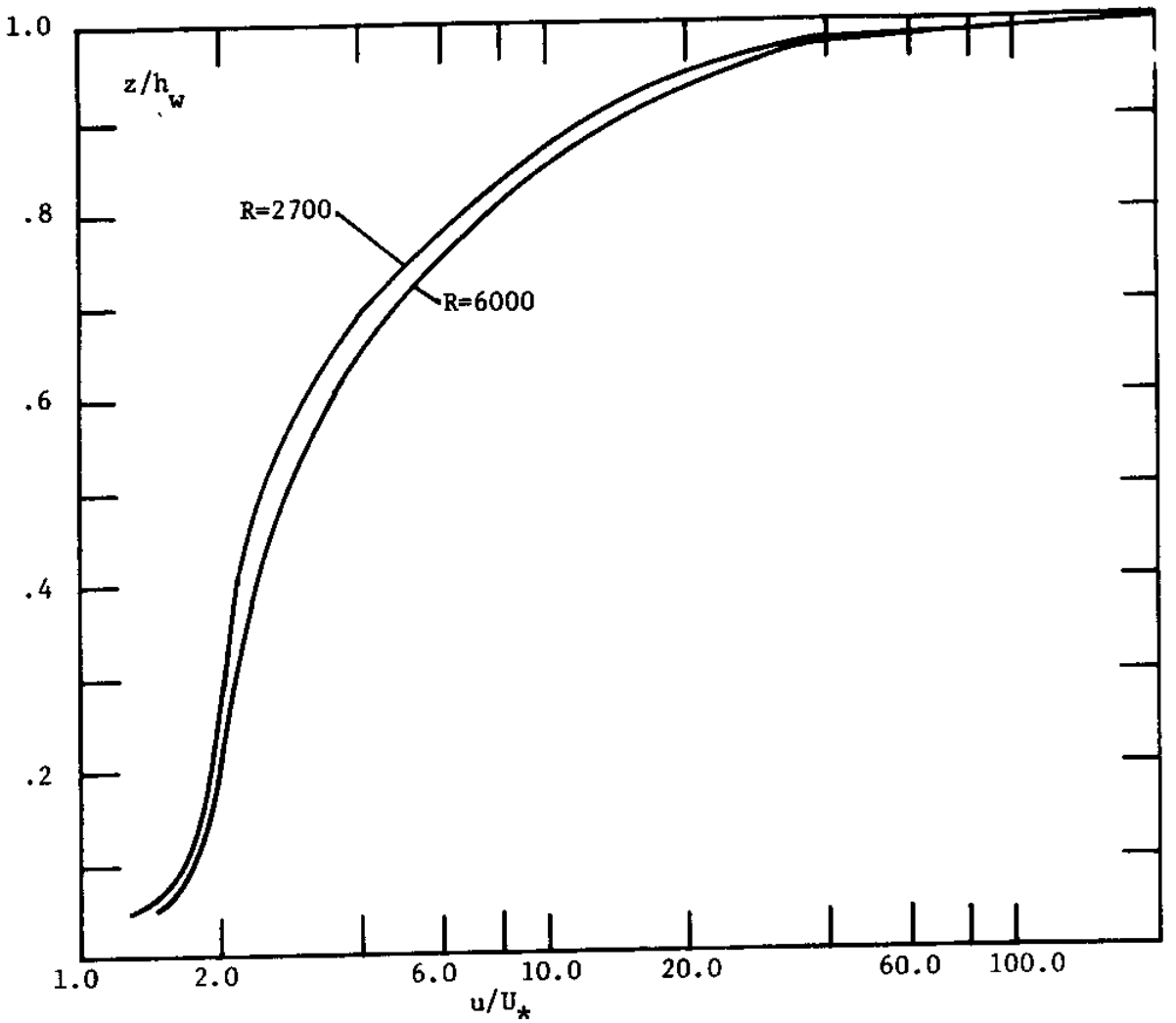

Figure 5.4 - Effect of Reynold's Number ($R=U_* h_w/\nu$) on Confined Flows having $(U_*/U_m)^2 = .98$, $h_g/h_w = 1$, $C_d h_g a = .5$ (runs 8,9)

conclusions of this chapter is presented.

5.3 Vertical Velocity Profiles

Figures 5.5-5.13 show non-dimensional velocity profiles for each of the three flow types in Figure 5.1, as well as for confined flows having both shear and pressure forces. Each figure illustrates the effect on the vertical velocity profile of varying one of the dimensionless parameters, as discussed below.

5.3.1 $C_d h_g a$

$C_d h_g a$ represents the effective area of the obstructions normal to the direction of flow per unit horizontal area. Representative values of $C_d h_g a$ for various canopies are .1 for salt marsh grass, 1 for corn (DenHartog & Shaw, 1975), 4 for bulrush millet (Begg et al, 1964), and 5 for beans (Thom, 1971).

The presence of obstructions in the flow causes a drag force to be exerted on the fluid, resulting in a decrease in the velocity, other factors being kept constant. The effect of $C_d h_g a$ on the velocity magnitudes for flow types I and II is shown in Figures 5.5 and 5.6. Assuming a constant U_m, the velocities in each figure may be directly compared. For $C_d h_g a$ about .1, the velocity in the pressure driven cases is reduced by about a factor of four from the equivalent non-obstructed flow situation; for shear driven flows, in contrast, the velocity is reduced by almost a factor of ten. The larger reduction

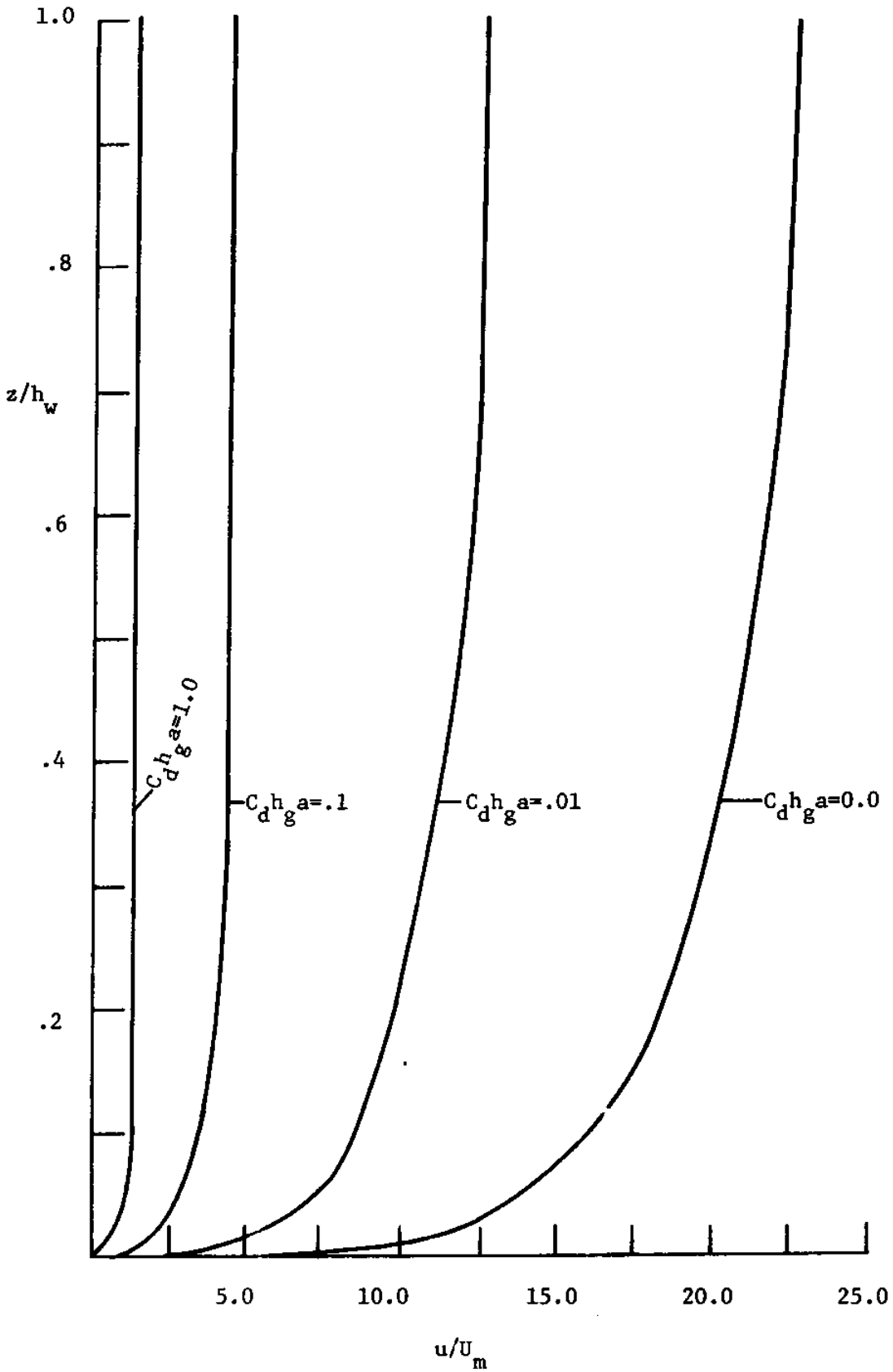

Figure 5.5 - Dimensionless Velocity Profiles for Type I Flow with h_g/h_w=1.0. (Runs 10-13).

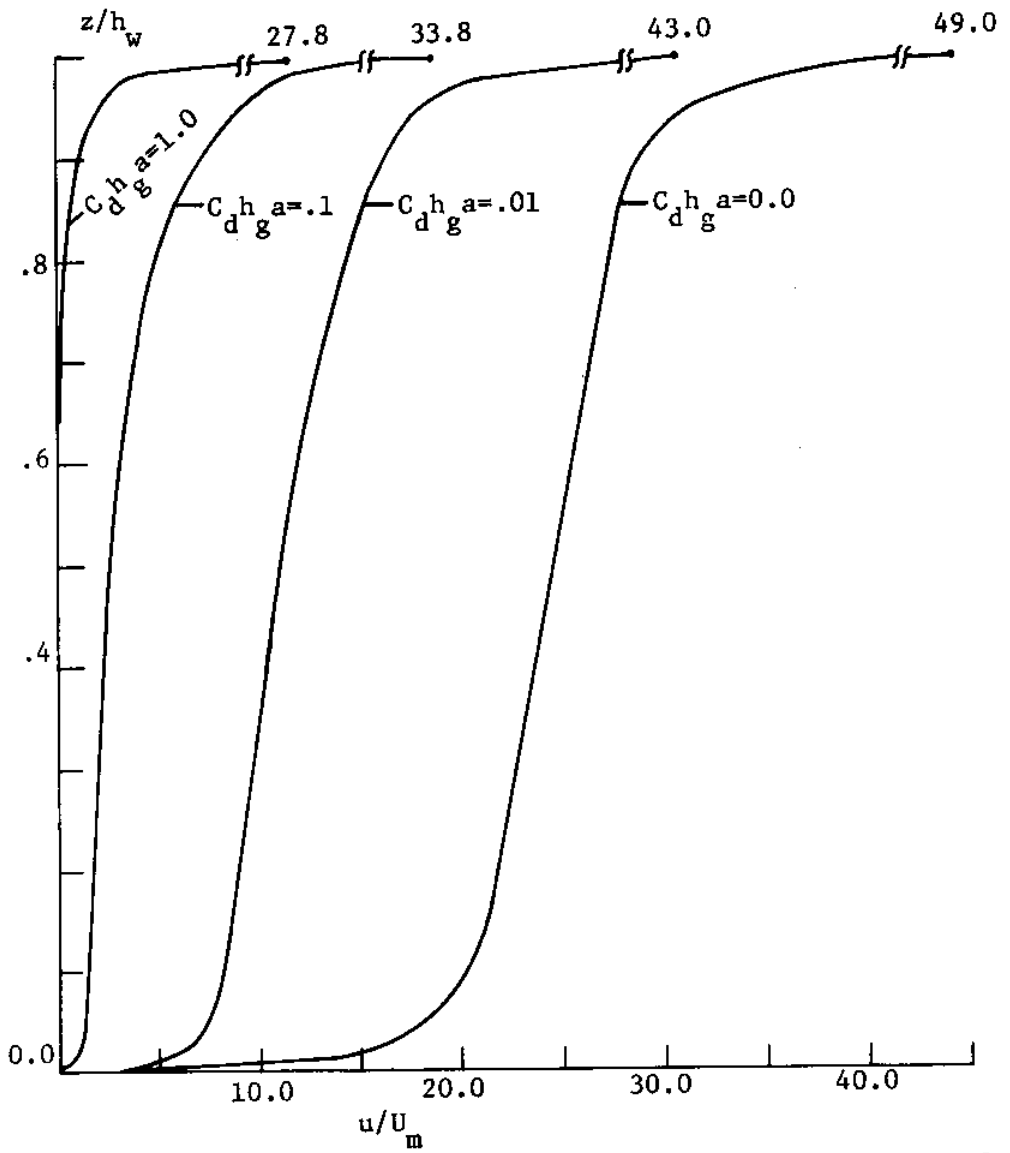

Figure 5.6 - Dimensionless Velocity Profiles for Type II Flow with h_g/h_w=1. (runs 14-17)

for wind driven flows is due to the fact that, unlike the pressure gradient ($g\frac{\partial \eta}{\partial x}$), which is uniform with depth, the stress driving the shear flow attenuates with depth.

As mentioned earlier, the velocity scale U_g is often appropriate for obstructed confined flow situations. The effect of $C_d h_g a$ on u/U_g for flow types I and II is shown in Figures 5.7 and 5.8. In Figure 5.7, u/U_g approaches one as $C_d h_g a$ increases; the reason is that, with denser obstructions, the shear effects become less important, leaving a balance in the momentum equation between drag and pressure. For $C_d h_g a$ greater than .1, the velocity is practically constant with depth. Many of the marsh flow cases examined in the previous chapter, having $C_d h_g a$ greater than .1, would fall in this category.

In contrast to the pressure drive flows, the ratio u/U_g for the shear driven flows becomes progressively less with $C_d h_g a$ (Figure 5.8), reflecting the reduced amount of energy that can diffuse downward to drive the flow.

Figure 5.9 shows the computed velocity profiles for unconfined (type III) flow. For $C_d h_g a=0$, the velocity profile has the expected logarithmic shape. As $C_d h_g a$ increases, the velocity within the obstructions decrease (assuming a constant value of U_a). As discussed later, the relatively uniform velocity in the obstructions, compared to the shear driven flows, is a result of increased diffusion of turbulent energy from above the obstructions. For $C_d h_g a=1$, the value of du/dlnz for $z/h_g > 10$,can be seen from Figure 5.9 to have a different value

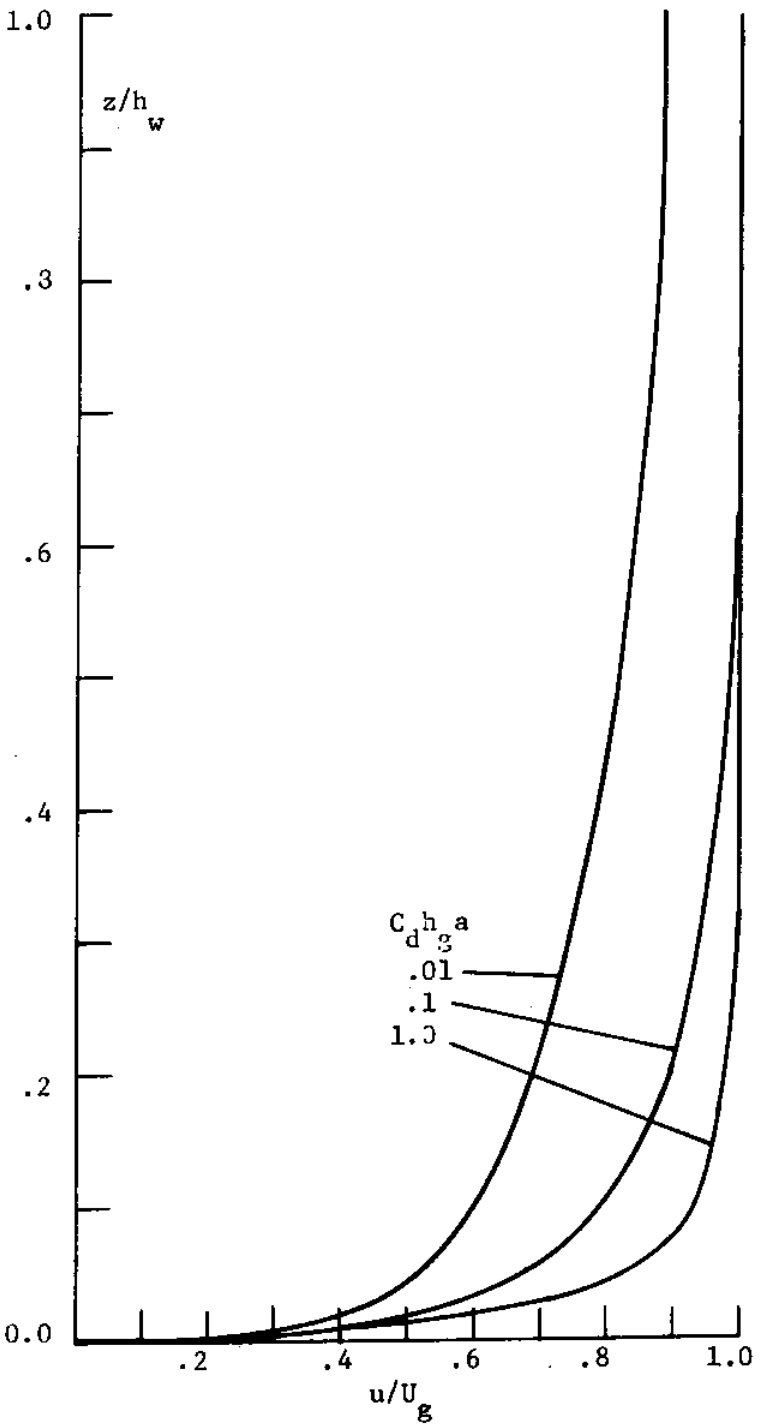

Figure 5.7 - Dimensionless Velocity Profiles for Type I flow with h_g/h_w=1 (Runs 11-13)

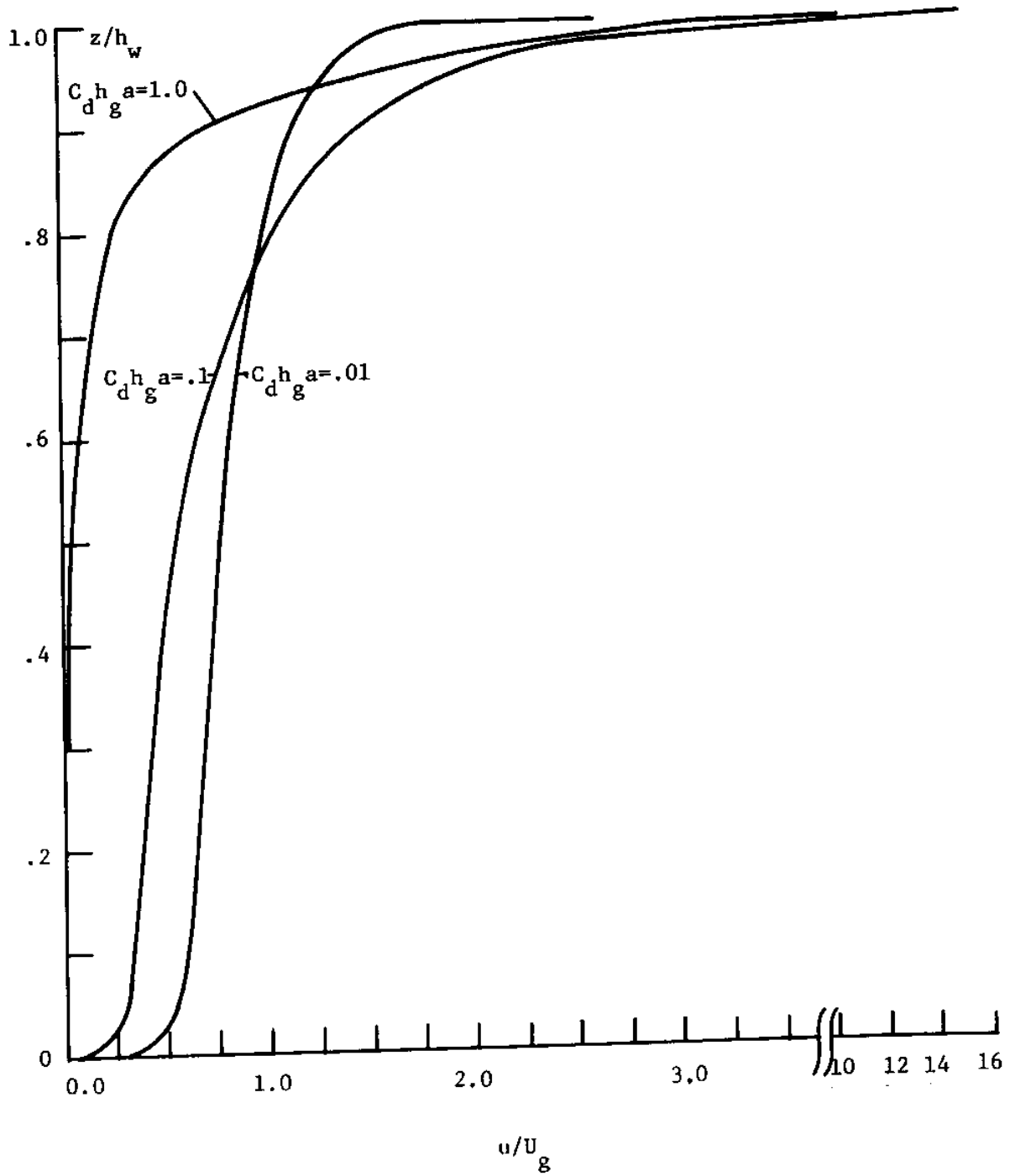

Figure 5.8 - Dimensionless Velocity Profiles for Type II Flows with h_g/h_w=1. (runs 15-17)

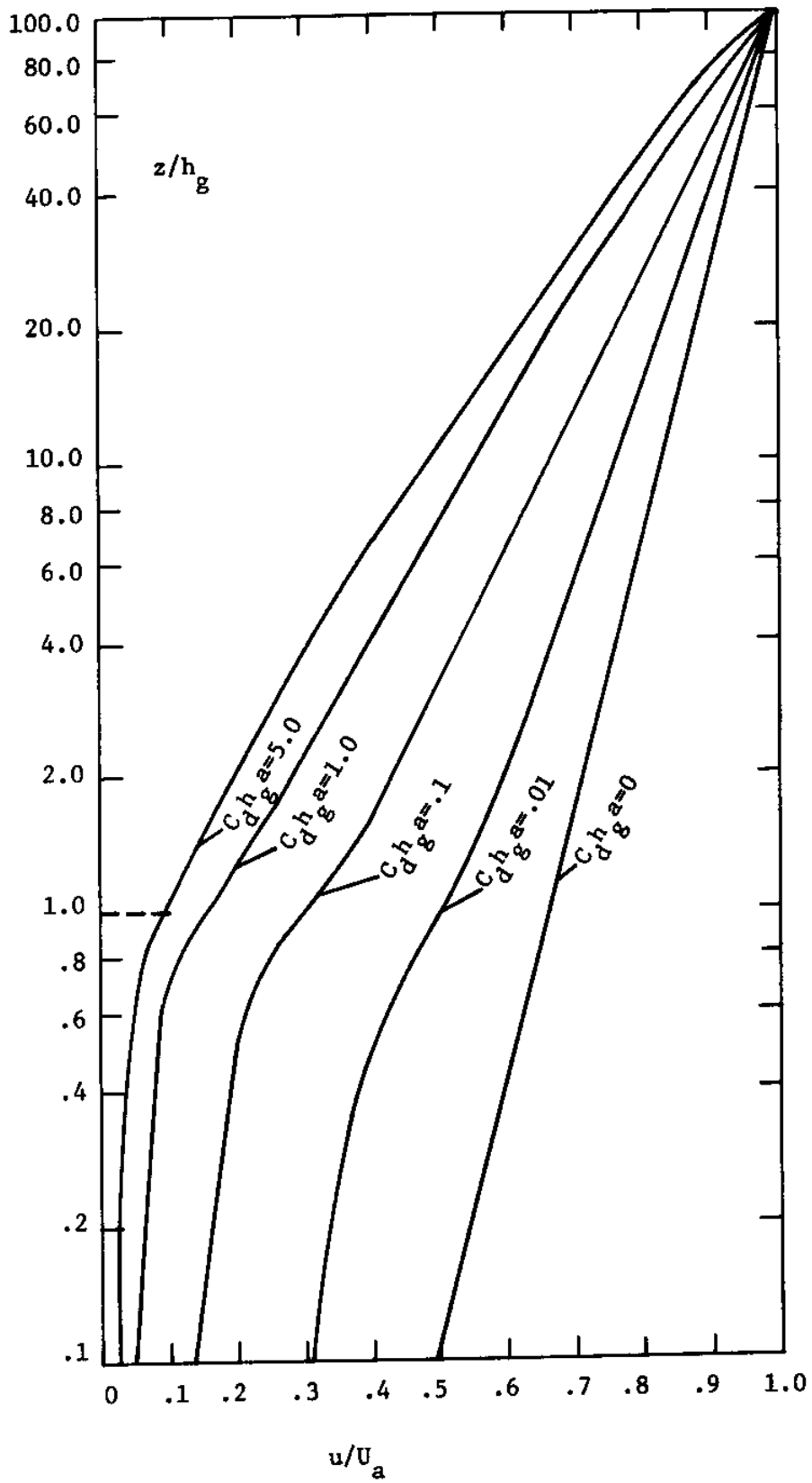

Figure 5.9 - Dimensionless Velocity Profiles for Type III Flow. (Runs 18-22).

than for $z/h_g < 10$, suggesting that the height above the obstructions at which the logarithmic profile begins may vary with vegetation density.

5.3.2 $(\frac{U_*}{U_m})^2$

The velocity profiles in Figure 5.10 correspond to confined flow situations having both shear and pressure driving forces. For $(U_*/U_m)^2=0$ (type I flow), the velocity is given by U_g, as discussed earlier. As $(U_*/U_m)^2$ increases above zero, the value of u/U_g becomes progressively smaller, reflecting the increased importance of the shear stress. At $(U_*/U_m)^2=.5$, corresponding to equal shear and pressure forces (i.e. $U_m^2=U_\eta^2$) the value of u/U_g is about .75 throughout most of the flow depth. For $(U_*/U_m)^2$ greater than about .8, the velocity profile is seen to be close to the completely shear driven case ($(U_*/U_m)^2=1$), indicating the dominant role of the shear forcing in these situations.

5.3.3 h_g/h_w

In general, the marsh vegetation may not protrude throughout the entire depth of the water column. The effect of h_g/h_w on confined flows is displayed in Figures 5.11 and 5.12. In Figure 5.11, corresponding to pressure driven flow, a progressively larger shear stress is induced in the obstructions as h_g/h_w decreases, thus causing velocities greater than those predicted by U_g. In Figure 5.12, corresponding to shear driven flows, the velocity is seen to drop off sharply for $h_g/h_w=1$. As h_g/h_w decreases, the profiles become more

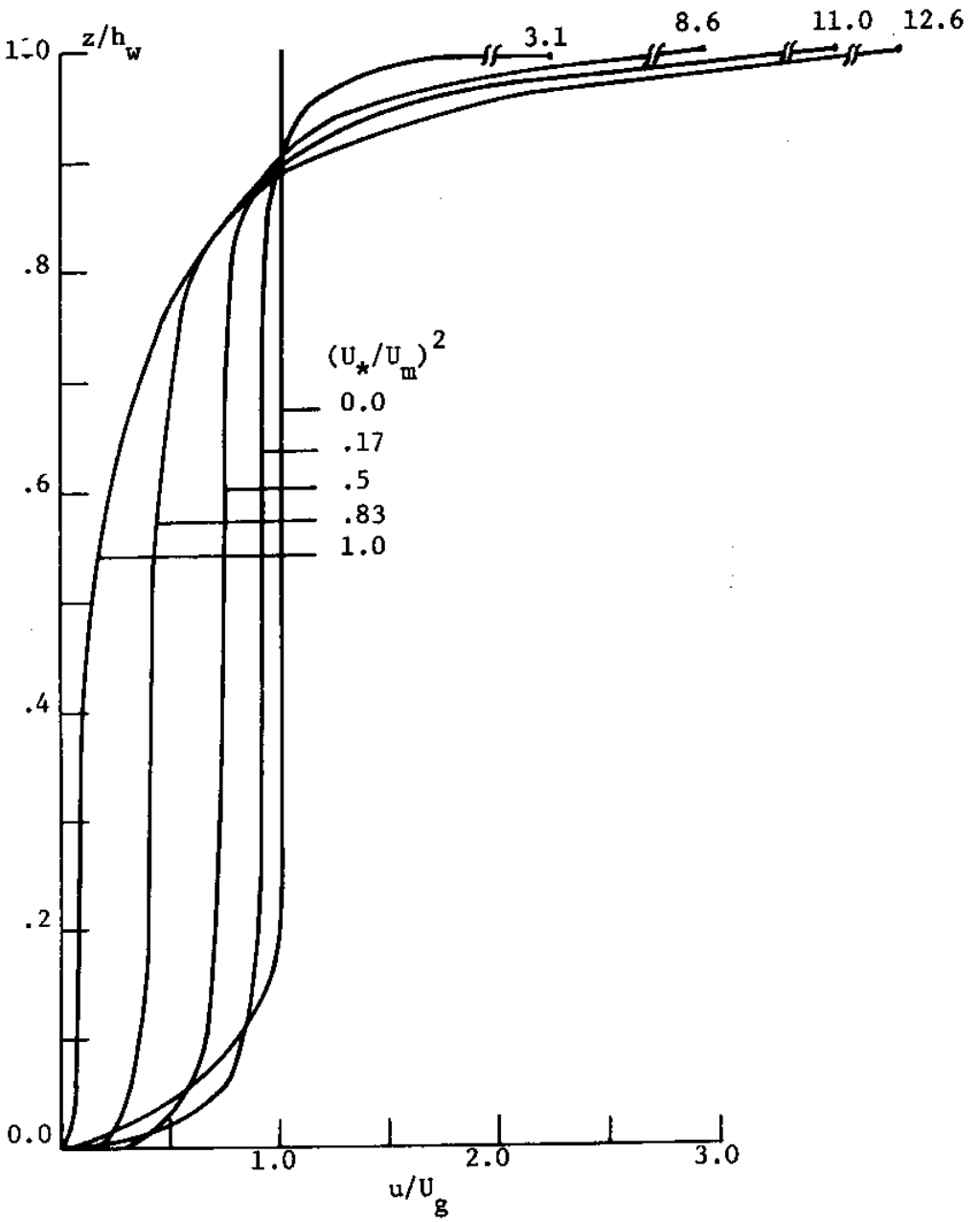

Figure 5.10 - Dimensionless Velocity Profiles for Confined Flow with h_g/h_w=1.0, $C_d h_g a$=.5 (runs 23-27)

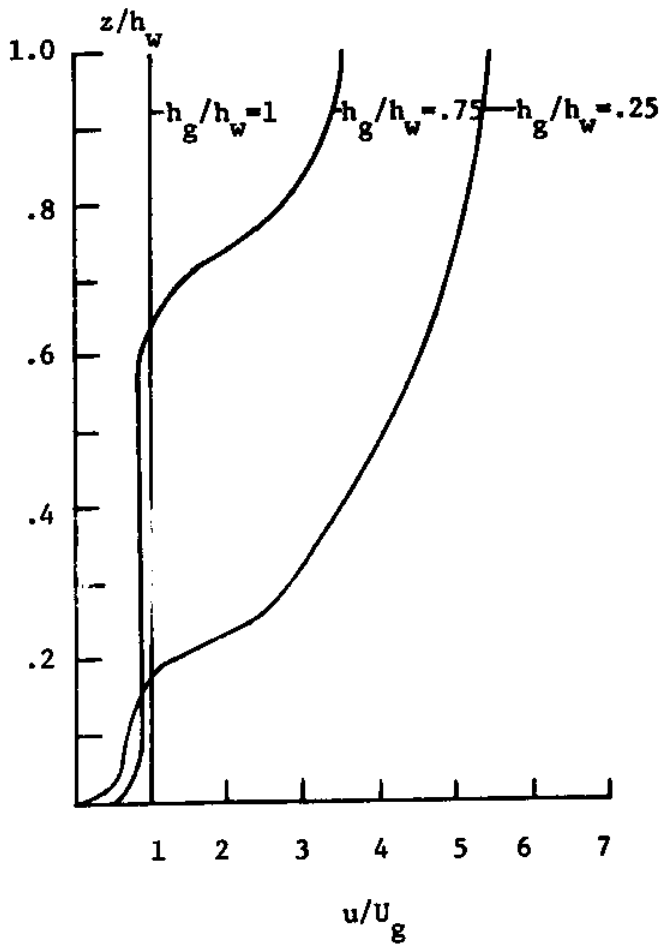

Figure 5.11 - Dimensionless Velocity Profiles for Type I Flows with $C_d h_g a$=1.0. (Runs 28-30).

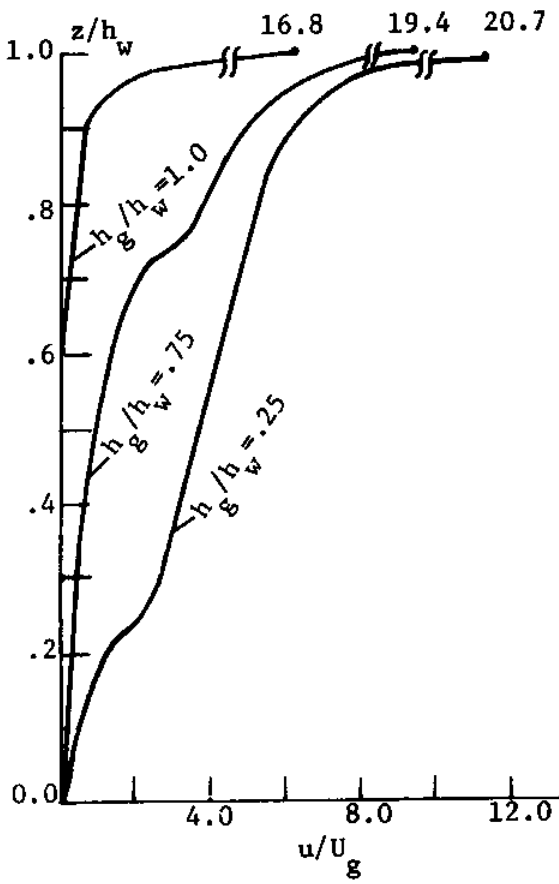

Figure 5.12 - Dimensionless Velocity Profiles for Type II flow with $C_d h_g a$=1.0 (runs 31-33)

uniform, reflecting the increased diffusion of turbulence from above the top of the obstructions.

5.3.4 h_a/h_w

The upper boundary conditions on k and ε for unconfined flow requires that the fluxes of these quantities are zero. To determine whether the height (h_a) at which this condition was applied might affect the calculations, model runs were performed with different values of h_a, while keeping h_g constant. The resulting velocity profiles are shown in Figure 5.13. The different runs were made to represent the same flow situation by using the velocities predicted with the largest h_a as the value of U_a in the other model runs. Thus, for instance, in the run with h_a/h_g=7.1, the predicted velocity at $h_a/2$ was taken as the value of U_a in the run with h_a/h_g=3.5. In this manner, the velocities from the different runs are directly comparable.

From Figure 5.13 it is seen that the velocity profile for the run with h_a/h_g=2.1 is about 10% different from that with h_a/h_g= 7.1. The reason for this effect deals with the fact that the fluxes of k and are not zero at short distances above the obstructions. As discussed later, turbulent diffusion in unconfined flows is important up to heights of about $3h_g$. Specification of h_a within this range, where the fluxes of k and $\tilde{\varepsilon}$ are non-zero, will thus produce different results than would higher values of h_a, where k and ε are more uniform, and the fluxes closer to zero.

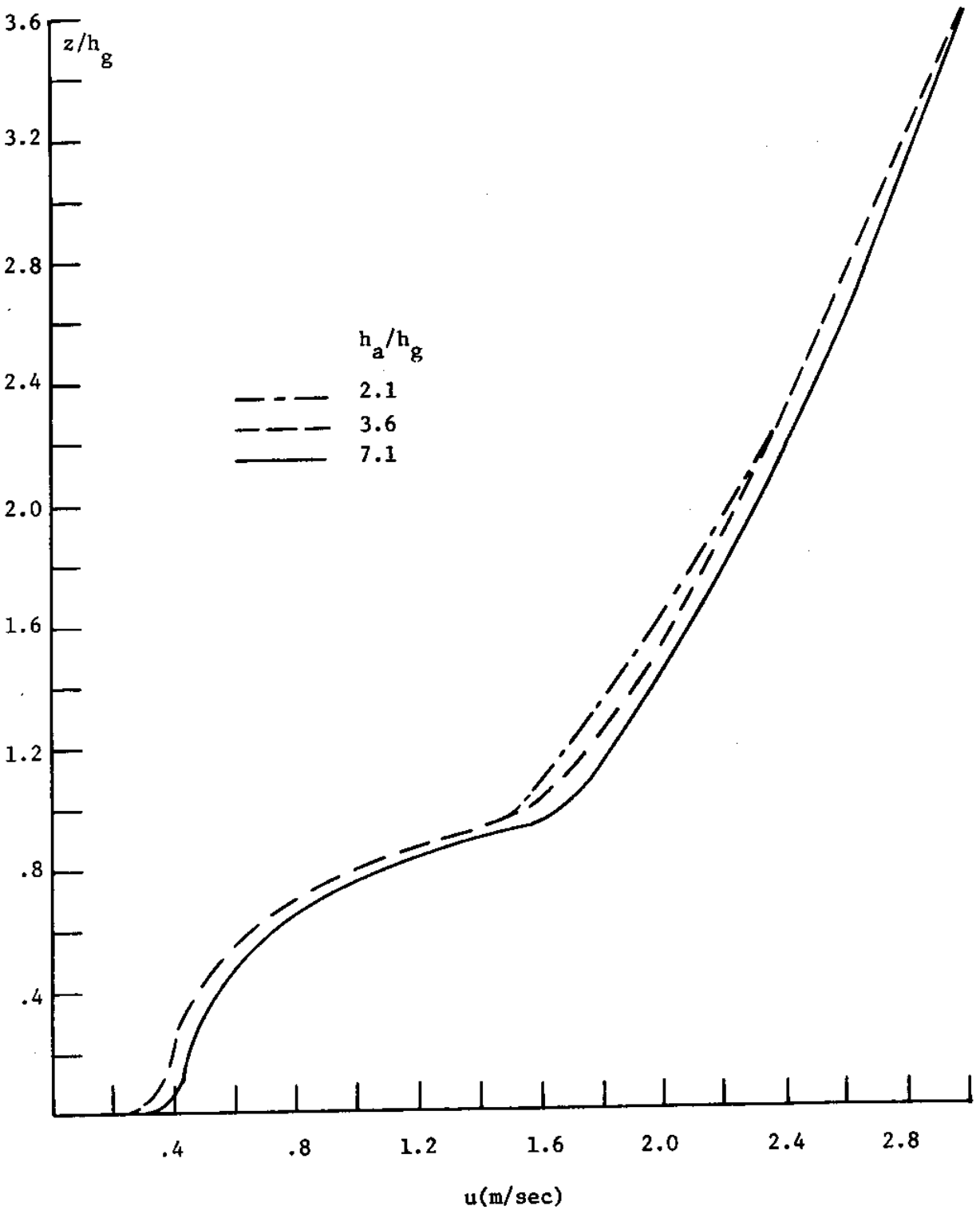

Figure 5.13 - Velocity Profiles for a Type III Flow with Different Values of h_a/h_g. (Runs 34-36).

5.4 Flow Conveyance

The total volume of water exchanged between different parts of the marsh will be influenced by the height, and density, of the vegetation. To investigate the effect of obstructions on flow conveyance, average velocities over the entire flow depth (U_t) were determined as functions of $C_d h_g a$ and h_g/h_w for both shear and pressure drive confined flows. The results are shown in Figures 5.14 and 5.15. Average velocities within the obstructions (U_ℓ) for these two types of flow, as well as for the unconfined flows, are shown in Figures 5.16-5.17.

For $h_g/h_w=0$, the value of (U_t/U_m) for both pressure and wind driven flows is about 25. This agrees with the value prediced by (3.31) for flow over smooth surfaces having $R \sim 2.7 \times 10^5$, which corresponds to the cases considered here.

For $h_g/h_w=1$, the averge velocity (U_t) for the pressure driven flow (Figure 5.14) is seen to approach U_g with increasing $C_d h_g a$. The flow reduction for the pressure driven flow is less than that for the shear driven flow cases (Figure 5.15), owing to the greater non-uniformity of the velocity profiles.

As h_g/h_w decreases below one, the value of (U_t/U_m) becomes progressively larger. For small h_g/h_w ($< .25$), the total flow conveyance for wind and pressure driven flows is about the same, indicating the equivalence of these forces for flow in which most of the depth is unobstructed.

The average velocities within the obstructiions (U_ℓ) for confined flows having h_g/h_w less than or equal to one are shown in Figures 5.16

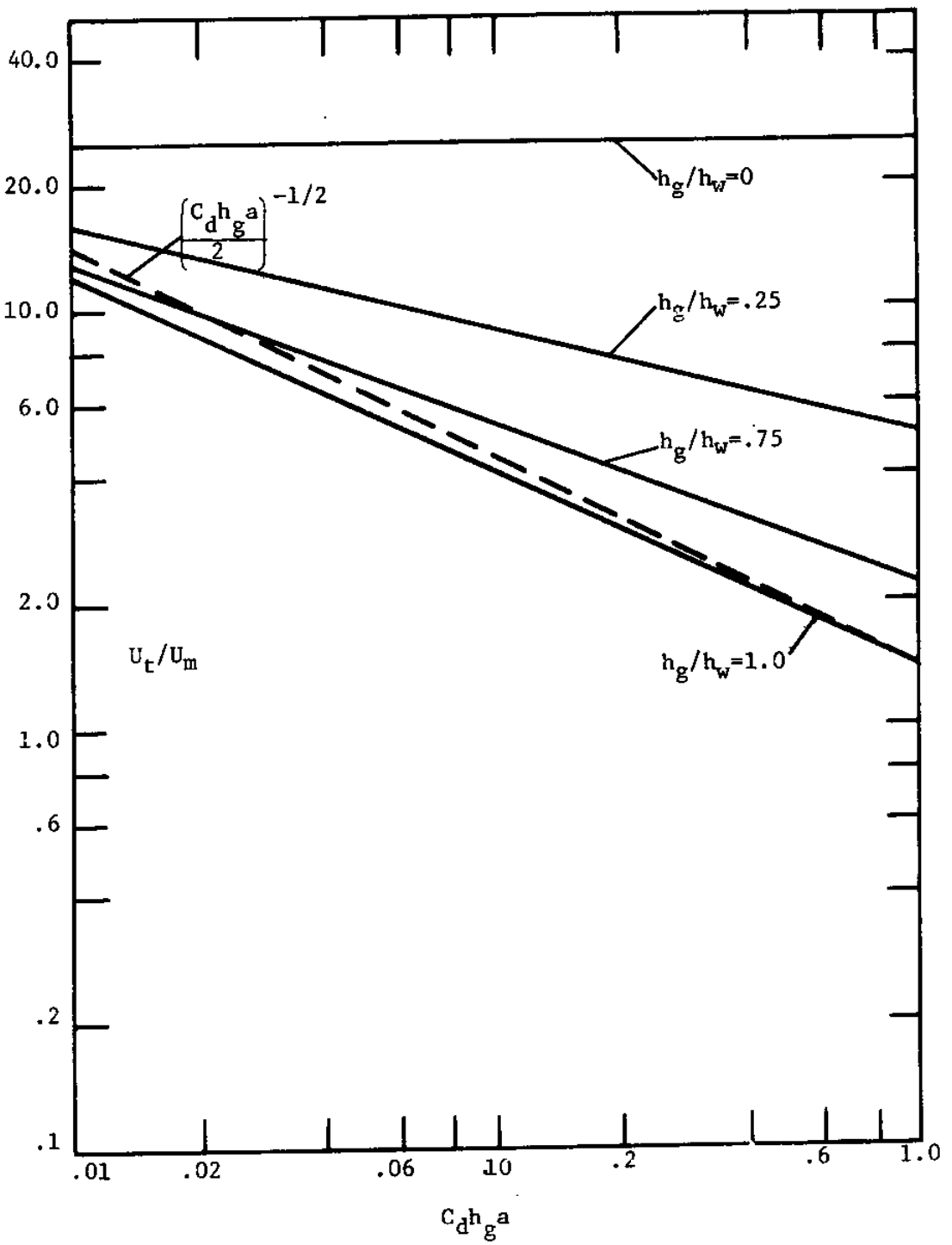

Figure 5.14 - U_t/U_m versus $C_d h_g a$ for Confined, Pressure-driven (Type I) Flows Having Different Values of h_g/h_w.

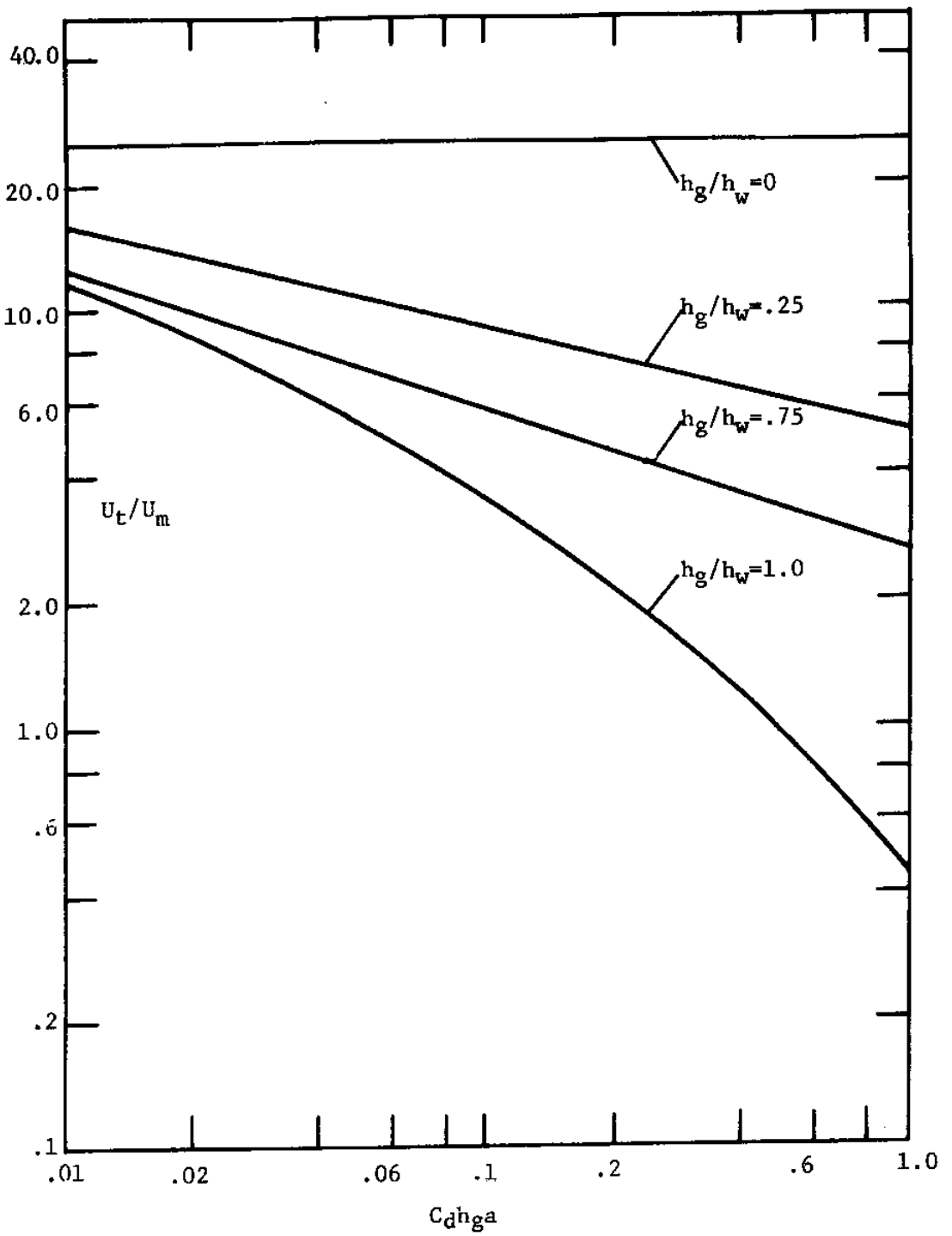

Figure 5.15 - U_t/U_m versus $C_d h_g a$ for Confined, Shear Driven (Type II) Flows having Different Values of h_g/h_w.

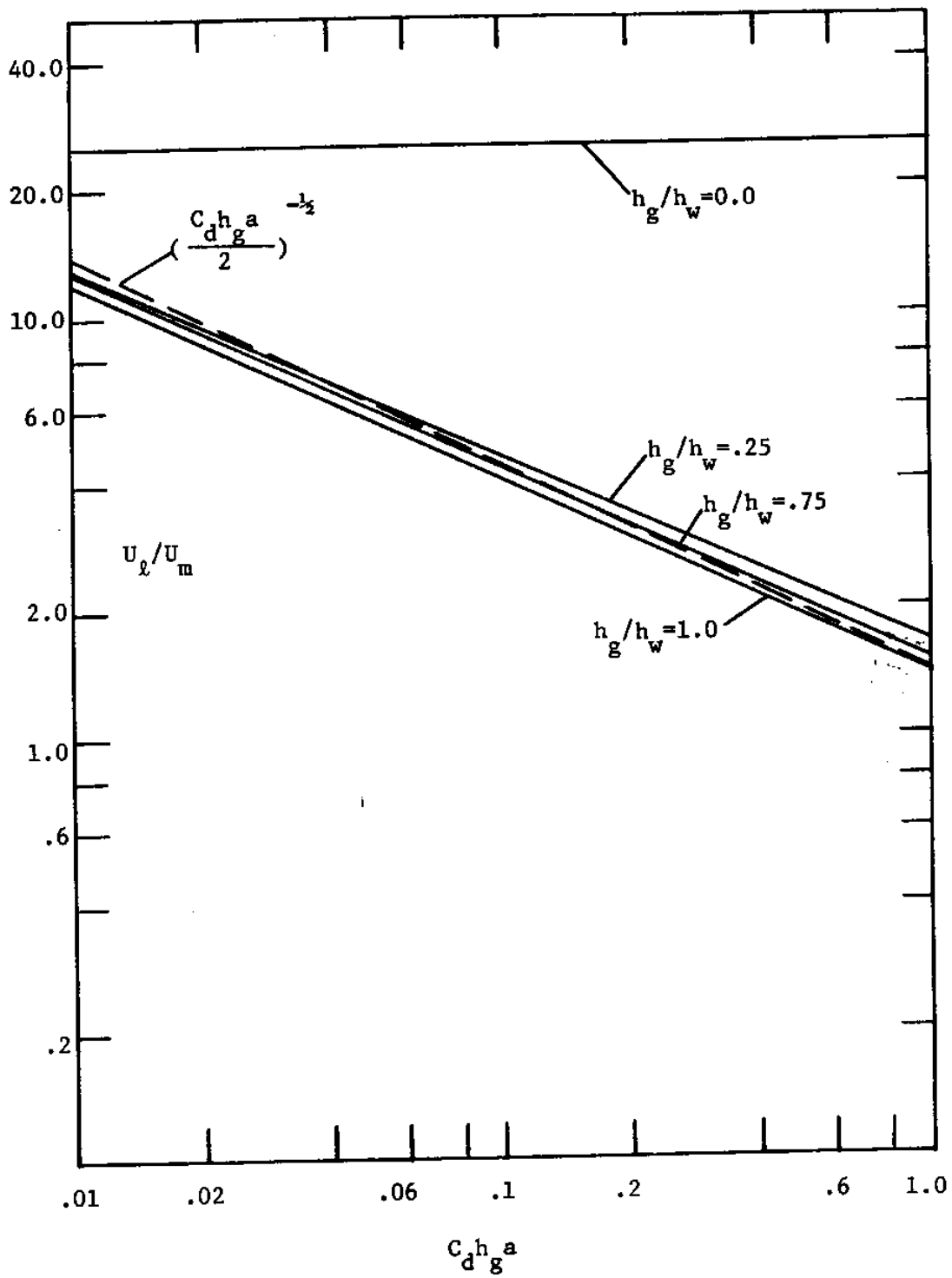

Figure 5.16 - U_ℓ/U_m for Confined, Pressure Driven (Type II) Flow.

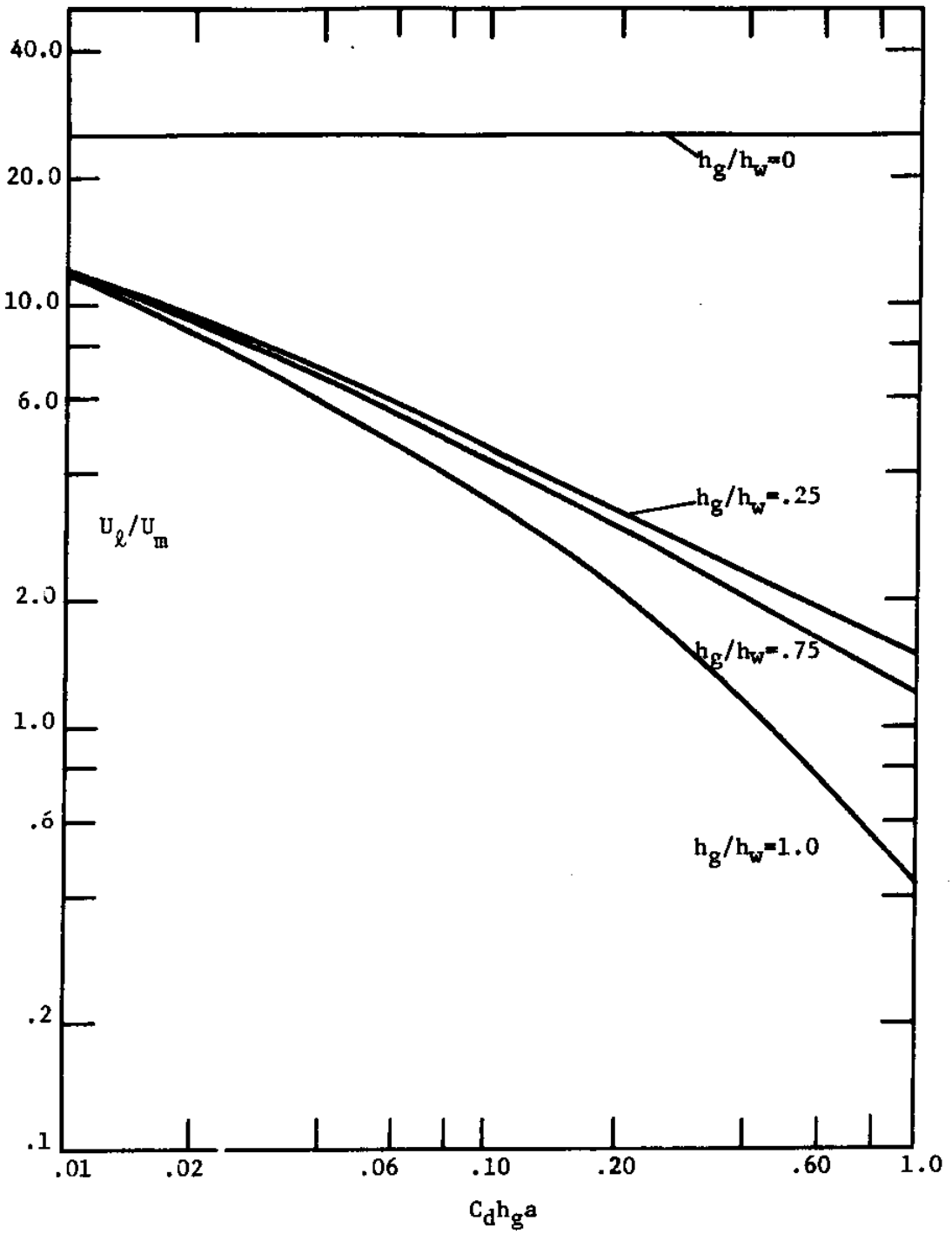

Figure 5.17 - U_ℓ/U_m versus $C_d h_g a$ for Confined, Shear Driven (Type II) Flows having Different Values of h_g/h_w.

and 5.17. For h_g/h_w less than about .75, the flow conveyance within the obstructions is nearly equal for both shear and pressure driven flows. Furthermore, the conveyance for these cases is approximately the same as that for the unconfined flows, shown in Figure 5.18. This is in accordance with the idea, mentioned earlier, that the unconfined flow provides the limiting case for confined flow as h_g/h_w goes to zero.

5.5 Turbulent Structure

The turbulent structure for non-obstructed flows such as channels is fairly well established (Townsend, 1976). When obstructions are introduced into the flow, momentum is absorbed by drag on the individual elements, thus causing a reduction in velocity, which in turn tends to reduce the level of turbulence. In opposition to this, the elements generate turbulent wakes, thereby tending to increase the level of turbulent energy. This section investigates the effect of $C_d h_g a$ on the turbulent structure of the three flow types considered here, and examines the differences with the non-obstructed cases. The vertical profile of turbulent diffusivity (μ_t) and length scale (ℓ) are examined with respect to simple turbulence concepts.

5.5.1 Kinetic Energy

Figures 5.19-5.21 show plots of kinetic energy, non-dimensionalized by U_m^2, or, in the case of the unconfined flows, by U_{*s}^2

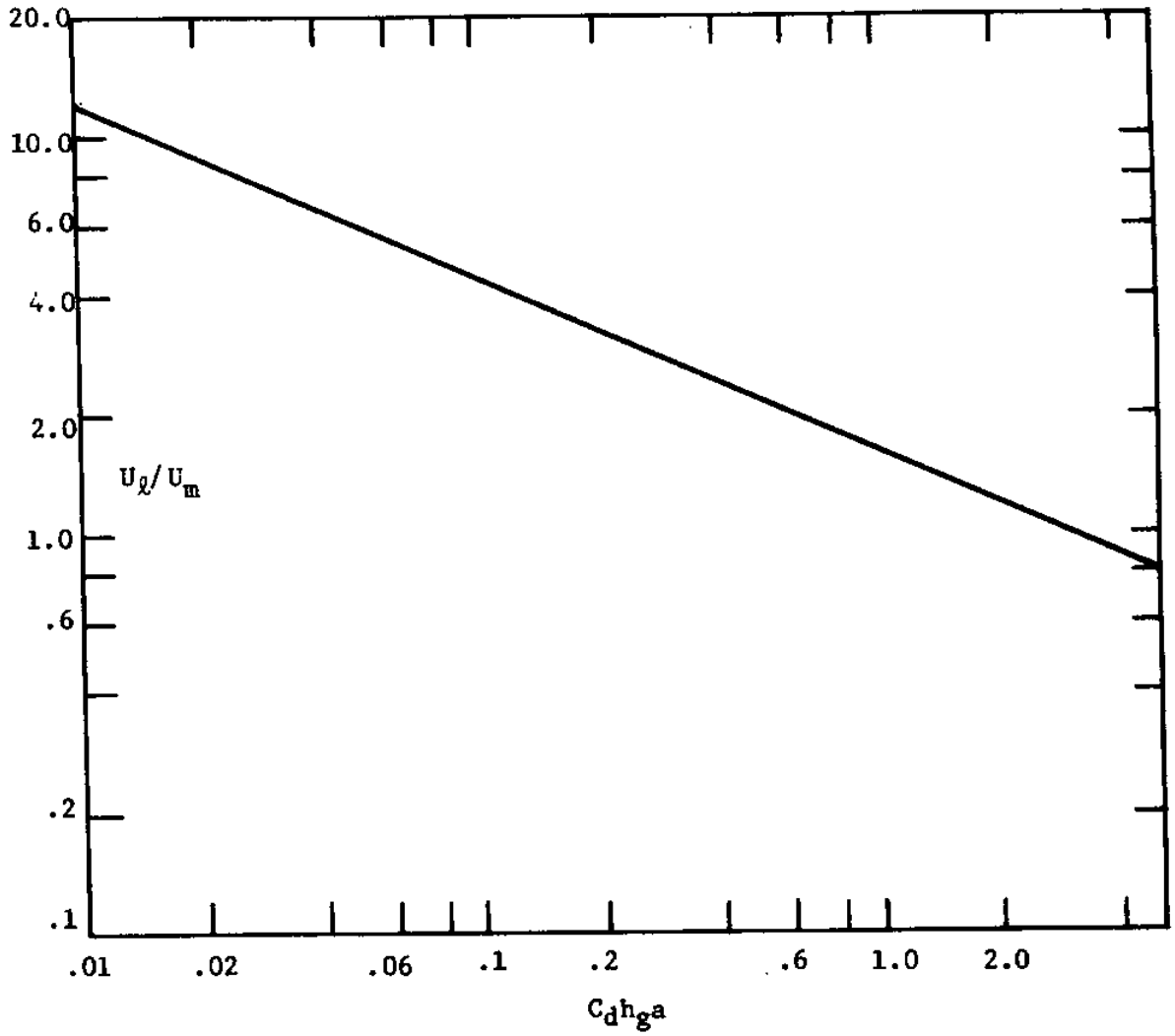

Figure 5.18 - U_ℓ/U_m versus $C_d h_g a$ for Unconfined (Type III) Flow

(the stress at the top of the obstructions). In each figure, k profiles for values of $C_d h_g a$ ranging from zero to one are presented. For the confined flows, k is zero at the top and bottom of the flow depth; for the unconfined flow, the flux of k is set to zero at $z/h_a=1$.

The k profiles share two general features:

(1) proportionality between k and the shear stress for the non-obstructed cases. Thus, for the pressure driven flows (Figure 5.19), k/U_m^2 decreases monotonically; for the shear driven cases (Figures 5.20, 5.21), where the shear stress is constant with depth, k/U_m^2, k/U_{*s}^2 is practically constant at 3.3, as predicted by (3.10). The proportionality between k and (τ/ρ) implies a negligible role of turbulent diffusion in the kinetic energy equation (3.14a), leaving a balance between production and dissipation (see Section 3.2.5).

(2) initial increase of k for low values of $C_d h_g a$, followed by a decrease as $C_d h_g a$ increases further. Assuming U_m^2 remains constant, the kinetic energy for $C_d h_g a=.01$ is seen to be generally greater than for the non-obstructed situation, reflecting the production of turbulence by the obstructions ($P_d \sim C_d a u^3$). As $C_d h_g a$ increases beyond .01, k starts to decline, owing to the reduction in velocity. In general, the value of k for $C_d h_g a=.01$ is 1.5-2 times greater than for $C_d h_g a=0$. It is likely that at slightly lower values of $C_d h_g a$, k may be even higher; the exact maximum, however, can not be determined from the given model runs.

The trend of increasing turbulence at low vegetation densities,

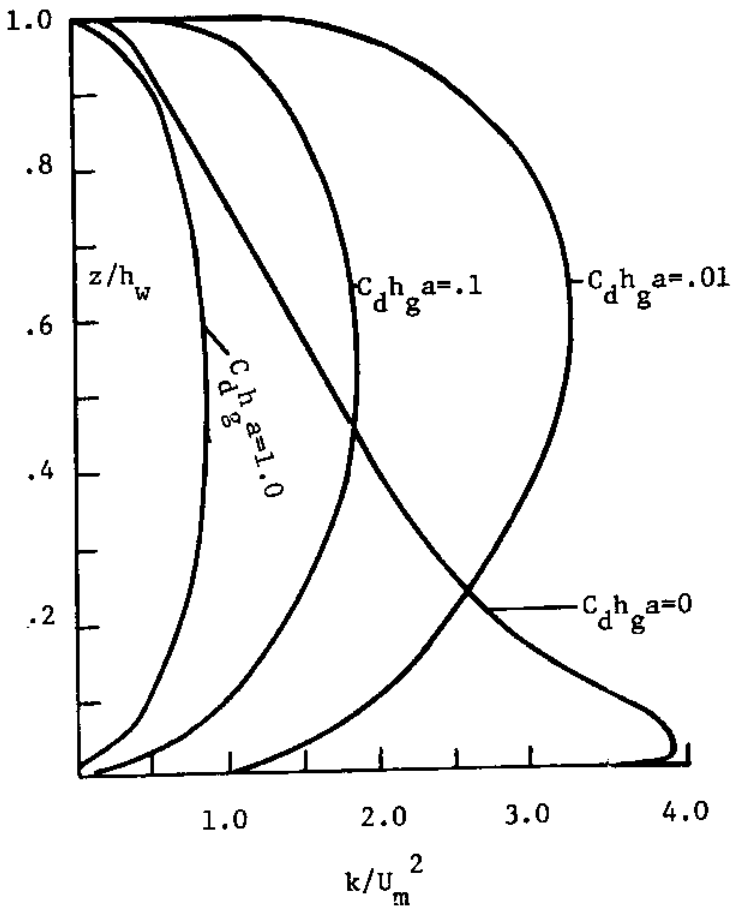

Figure 5.19 - Dimensionless Profiles of Kinetic Energy for Type I Flow with h_g/h_w=1.0. (Runs 10-13).

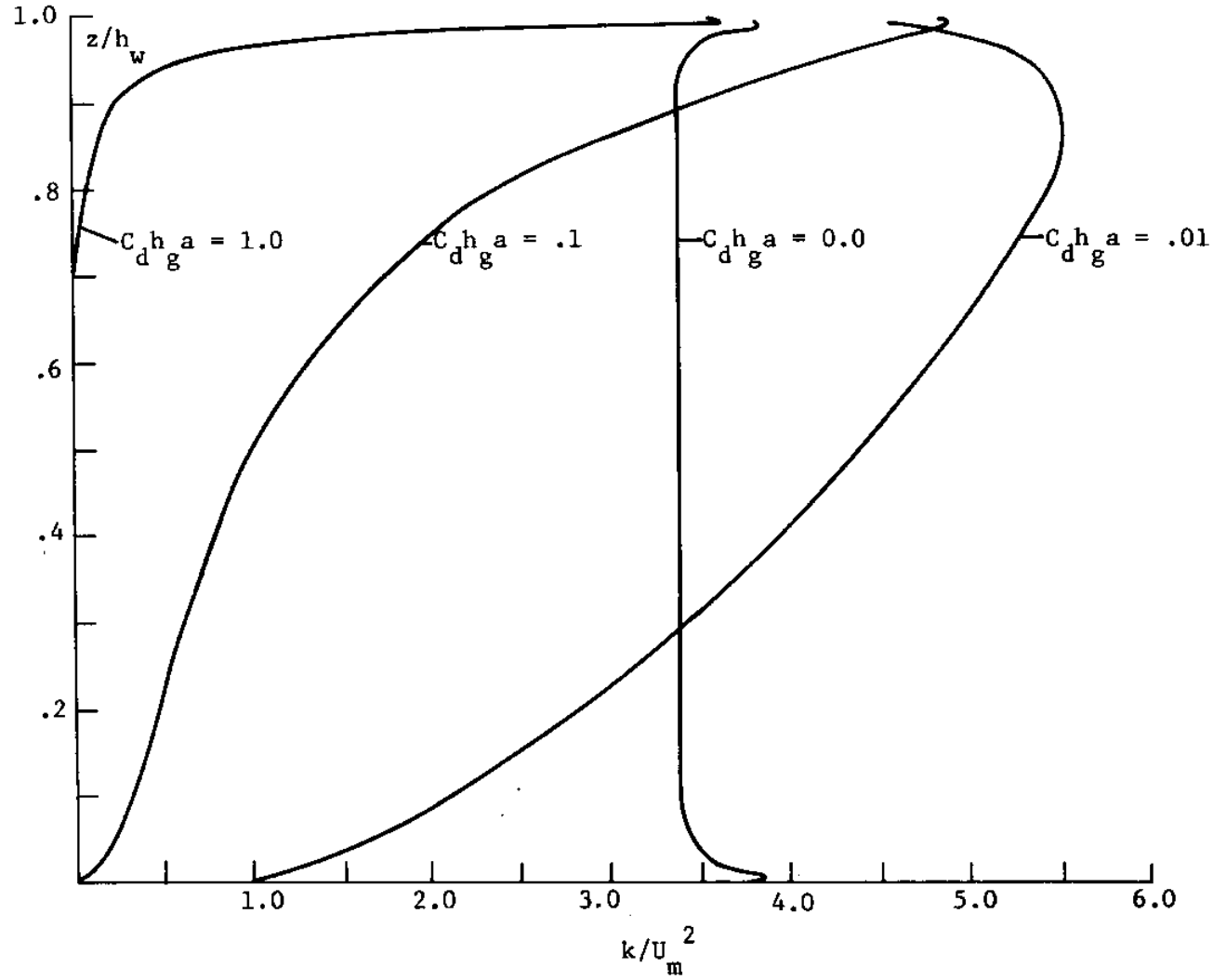

Figure 5.20 - Dimensionless Profiles of Kinetic Energy for Type II Flow with h_g/h_w=1. (runs 14-17)

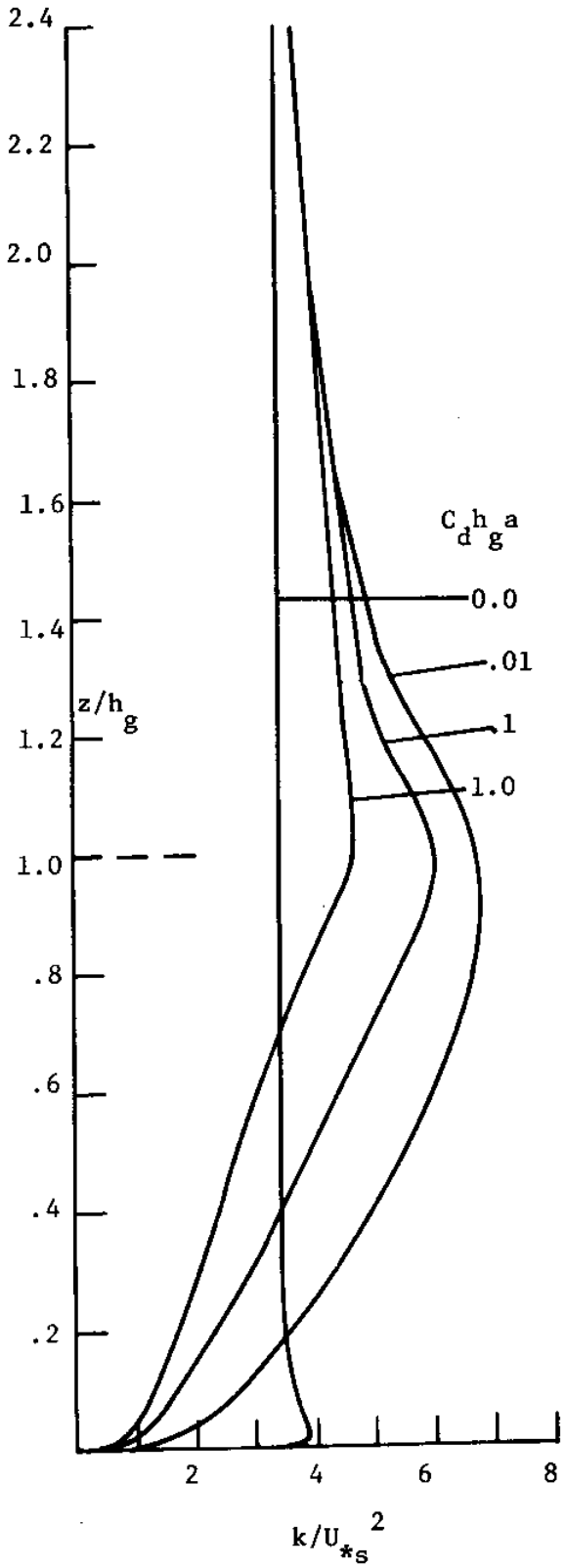

Figure 5.21 - Dimensionless Profiles of Kinetic Energy for Type III Flow. (runs 19-22)

other factors being kept constant, has implications for aquatic systems such as salt marshes, where the turbulence in the water motion may play an important role in the life processes of the vegetation. It suggests that areas of relatively lower vegetation density may be more turbulent than regions of no vegetation, or regions of very dense growth. In these low density, high turbulent regions, there may be enhanced rates of such processes as nutrient uptake, or exchange of gases or solutes. The effect of turbulence on aquatic plants has been studied by Anderson and Charters (1982), who found that a macro algae (Gelidium nudifrons) suppresses turbulence in the flow entering it's thallus, while at the same time generating turbulence of it's own, depending on the diameters and spatial density of the branches.

5.5.2 Dissipation

The vertical profiles of individual terms in the kinetic energy equation (3.14a) for the flows discussed above are shown in Figures 5.22-5.31. In the non-obstructed cases (Figures 5.22, 5.24, 5.28), the balance is seen to be almost entirely between production due to shear (P_s) and dissipation. The small role of turbulent diffusion in these flows was noted earlier as being responsible for the proportionality between k and (τ/ρ).

As obstructions are introduced into the flow, the relative magnitudes of the terms in the k equation changes dramatically. For the confined, pressure driven flows (Figure 5.23) the role of P_s decreses as $C_d h_g a$ goes from zero to .01. For greater values of $C_d h_g a$,

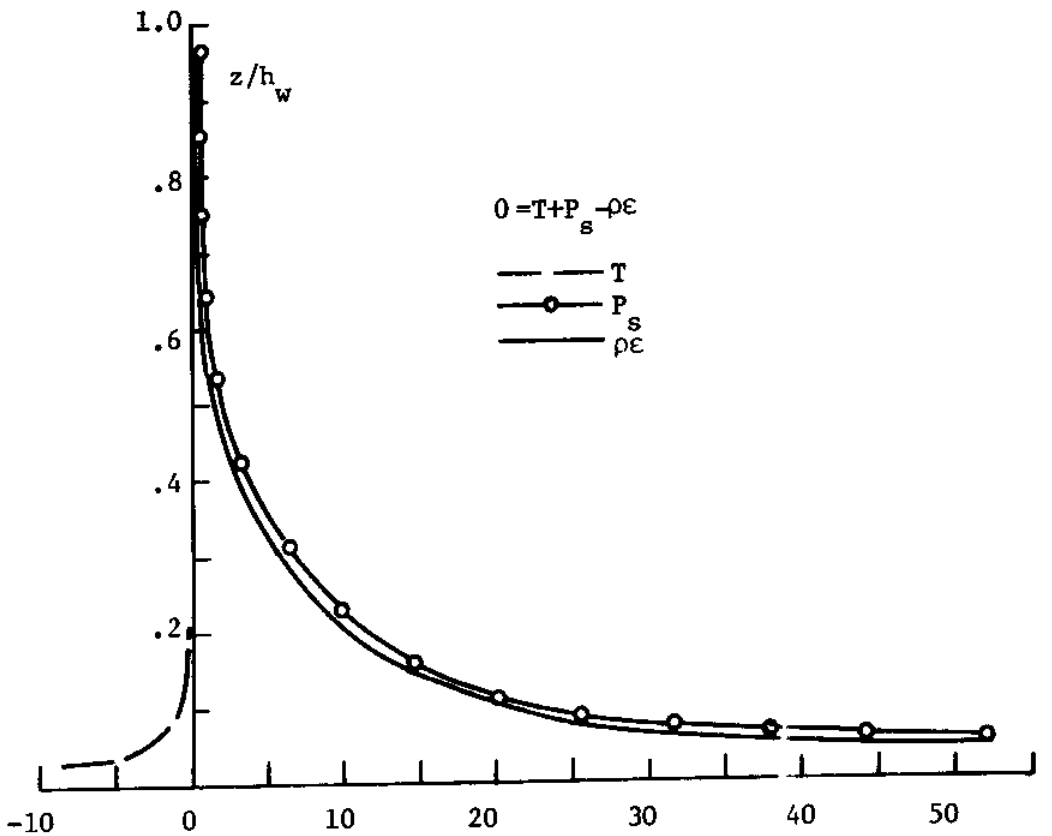

Figure 5.22 - Dimensionless Terms in Kinetic Energy Equation for Type I Flow with h_g/h_w=1.0, $C_d h_g a$=0.0 (run 10).

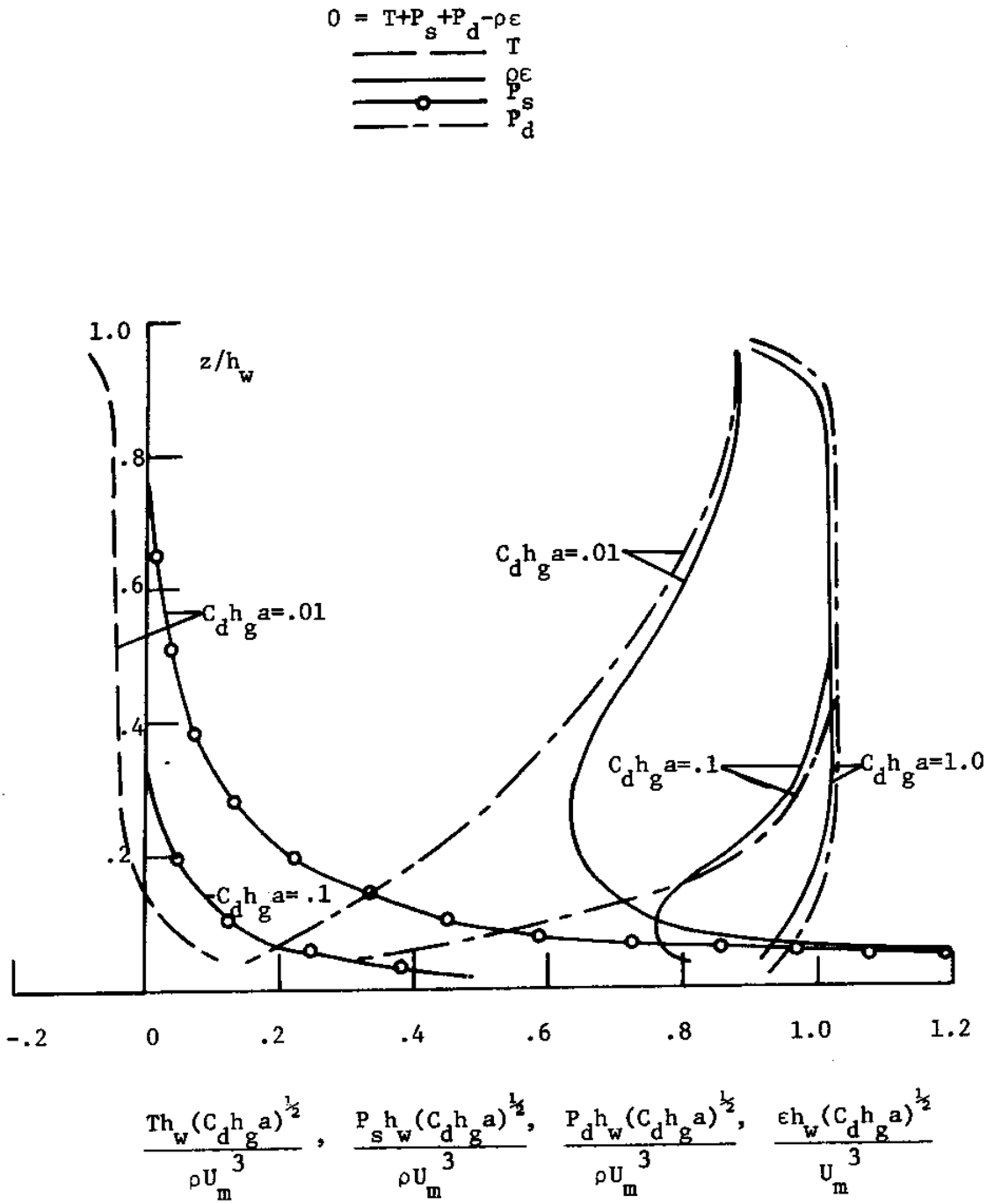

Figure 5.23 - Dimensionless Terms in Kinetic Energy Equation for Type I Flows with h_g/h_w=1.0, $C_d h_g a$=.01,.1,1.0. (Runs 11,12,13).

P_s becomes negligible as the production due to drag (P_d) takes over to become the dominant term balancing the dissipation. Remembering that $P_d \sim C_d a u^3$, and that the velocity under these conditions is given by U_g, it follows that the dissipation will vary as $a^{-1/2}$. This trend is observed in Figure 5.23.

For the shear driven confined flows (Figures 5.24-5.27), where the velocity gradients become larger near the top of the obstructions, neither P_s or turbulent diffusion are negligible, as in the pressure driven cases, and the dissipation no longer varies with $a^{-1/2}$.

Examining the results for the shear driven flows, it is seen that turbulent diffusion becomes relatively more important as $C_d h_g a$ increases, reflecting the progressively steeper gradients in the flow field. For the case with $C_d h_g a=1$, the terms fall by three orders of magnitude in the top thirty per-cent of the flow depth. In the lower part of the obstructions, the turbulence is so diminished that viscous effects become apparent.

In contrast to the confined shear driven flows discussed above, where turbulent diffusion is only important at relatively high values of $C_d h_g a$, the role of turbulent diffusion in unconfined flows is important at all values of $C_d h_g a$, as shown in Figures 5.29-5.31. Because of the relatively greater turbulent diffusion, the flow field in the unconfined flow cases is generally more uniform and fuller than in the confined flow cases mentioned above. For the unconfined flow cases (Figures 5.29-5.31), it is seen that within the obstructions the

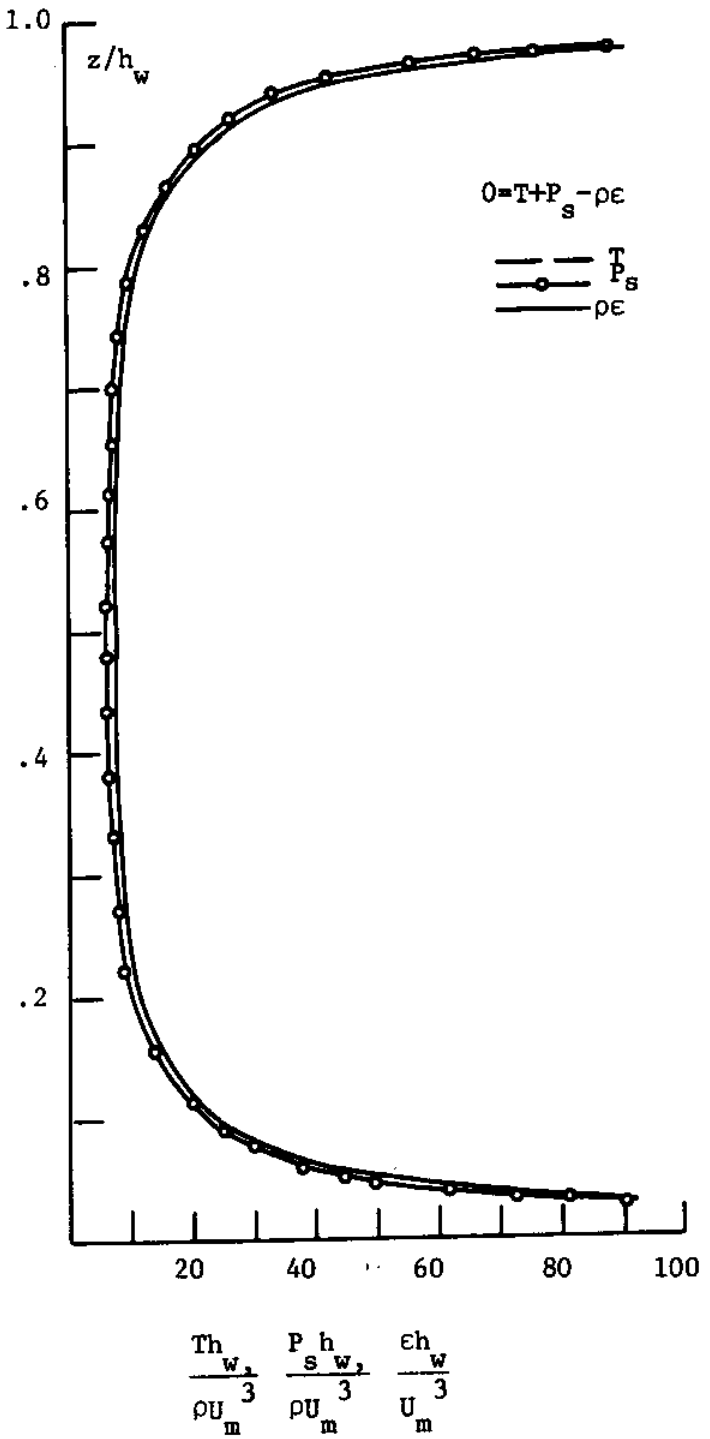

Figure 5.24 - Dimensionless Terms in Kinetic Energy Equation for Type II Flow with $h_g/h_w=1$, $C_d h_g a=0$ (run 14)

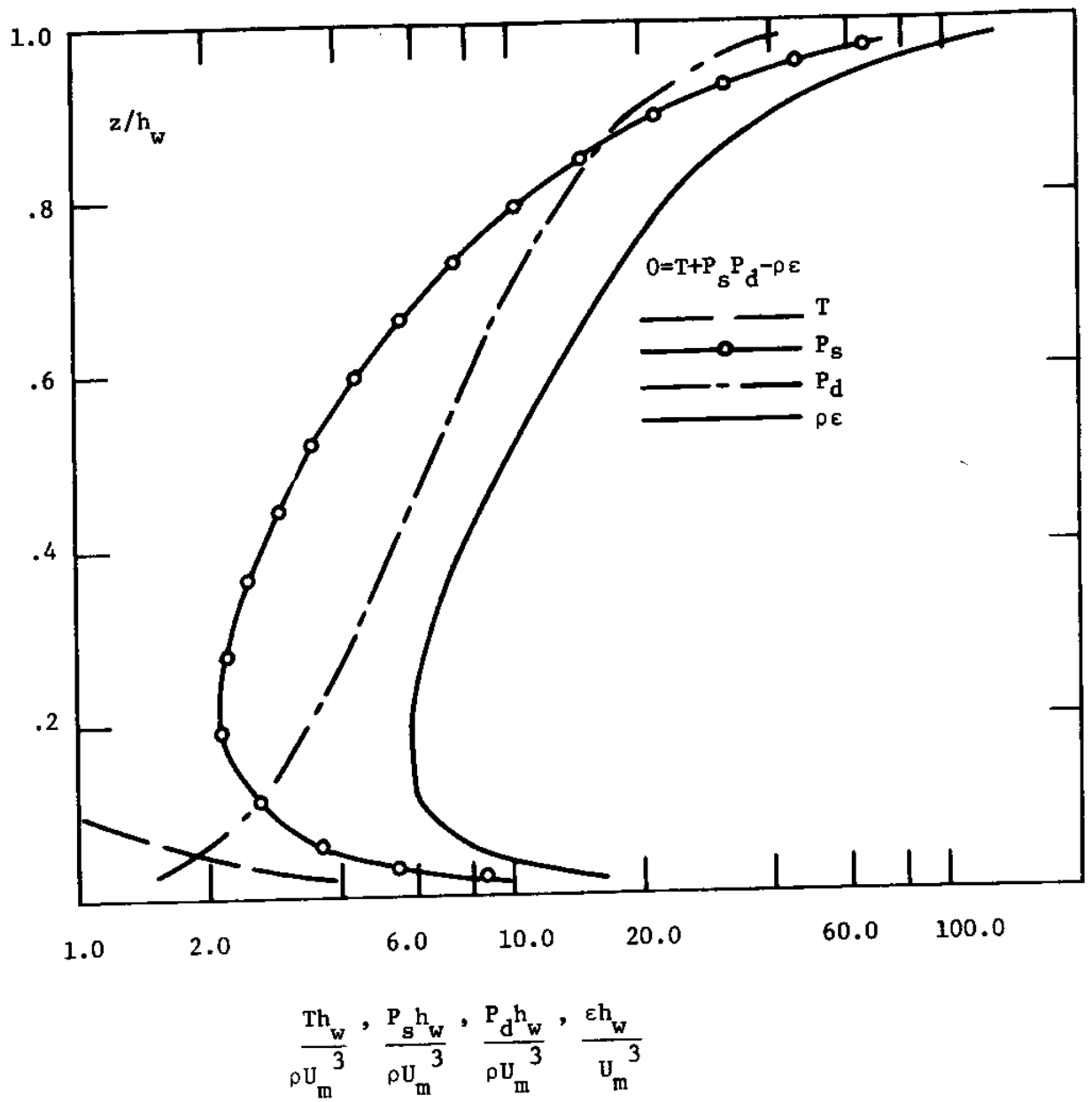

Figure 5.25 - Dimensionless Terms in Kinetic Energy Equation for Type II Flow with h_g/h_w=1.0, $C_d h_g a$=.01. (Run 15).

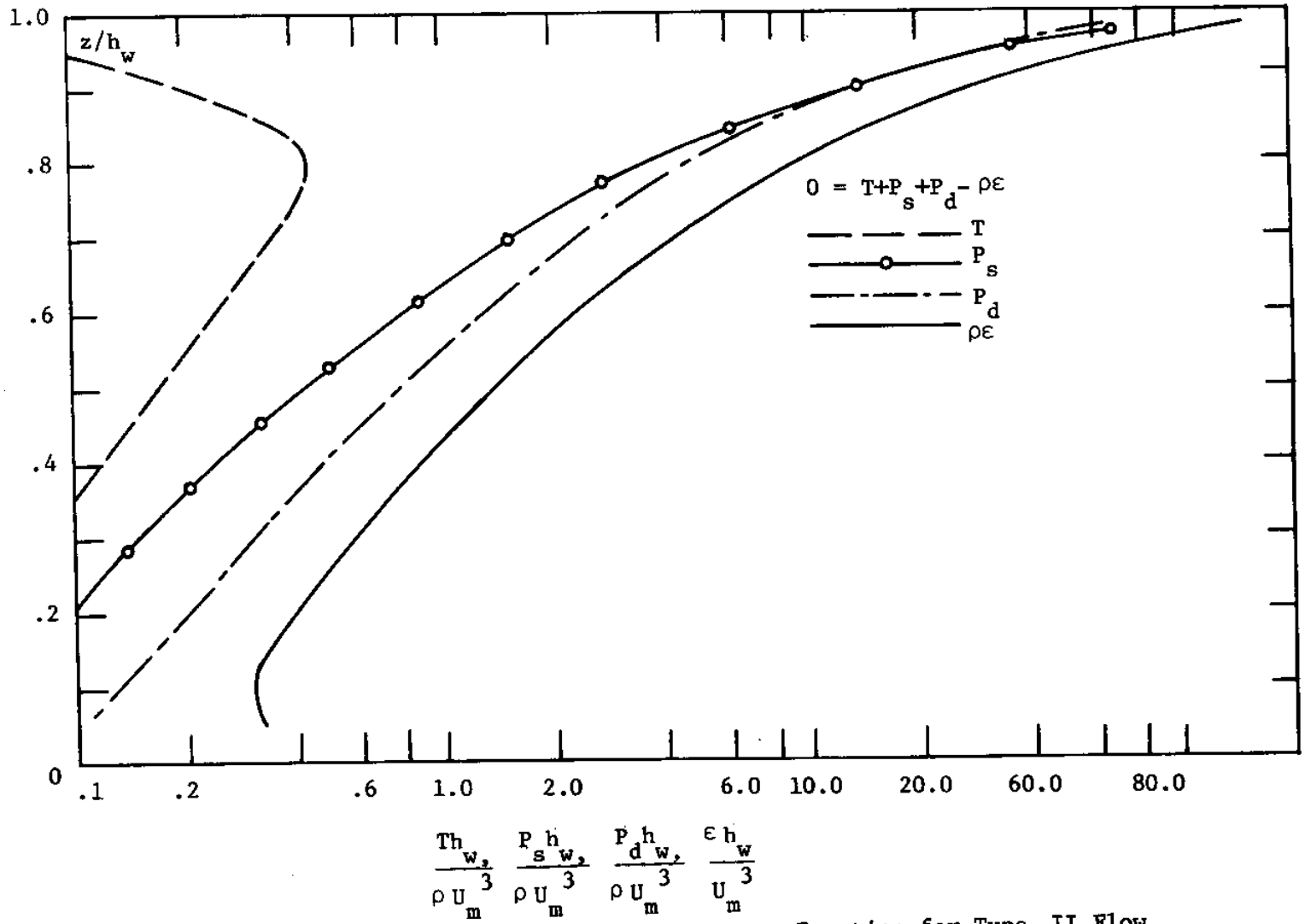

Figure 5.26 - Dimensionless Terms in Kinetic Energy Equation for Type II Flow with $h_g/h_w = 1.0$, $C_d h_g a = .1$ (run 16).

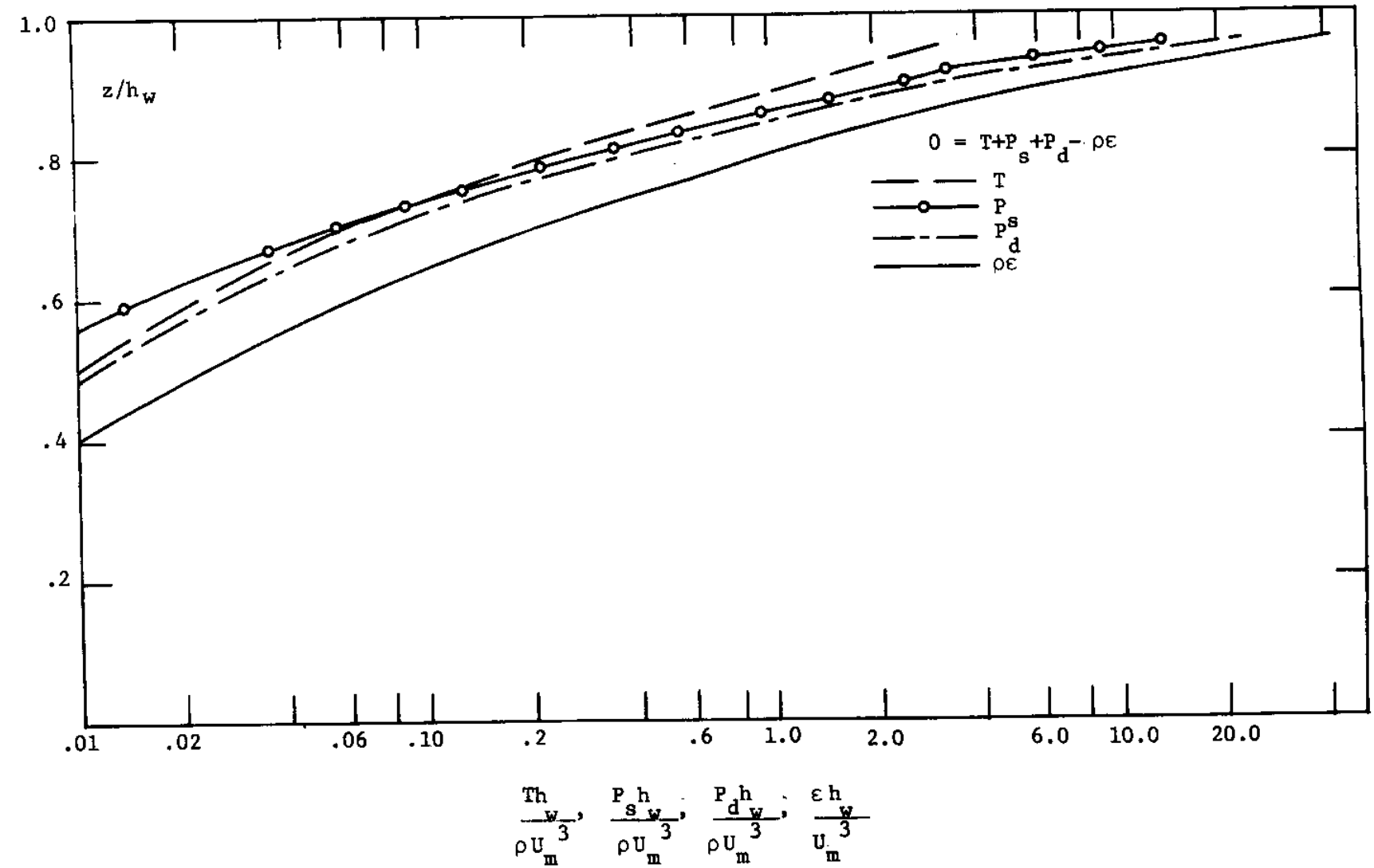

Figure 5.27 - Dimensionless Terms in Kinetic Energy Equation for Type II Flow with $h_g/h_w = 1.0$, $C_d h_g a = 1.0$ (run 17).

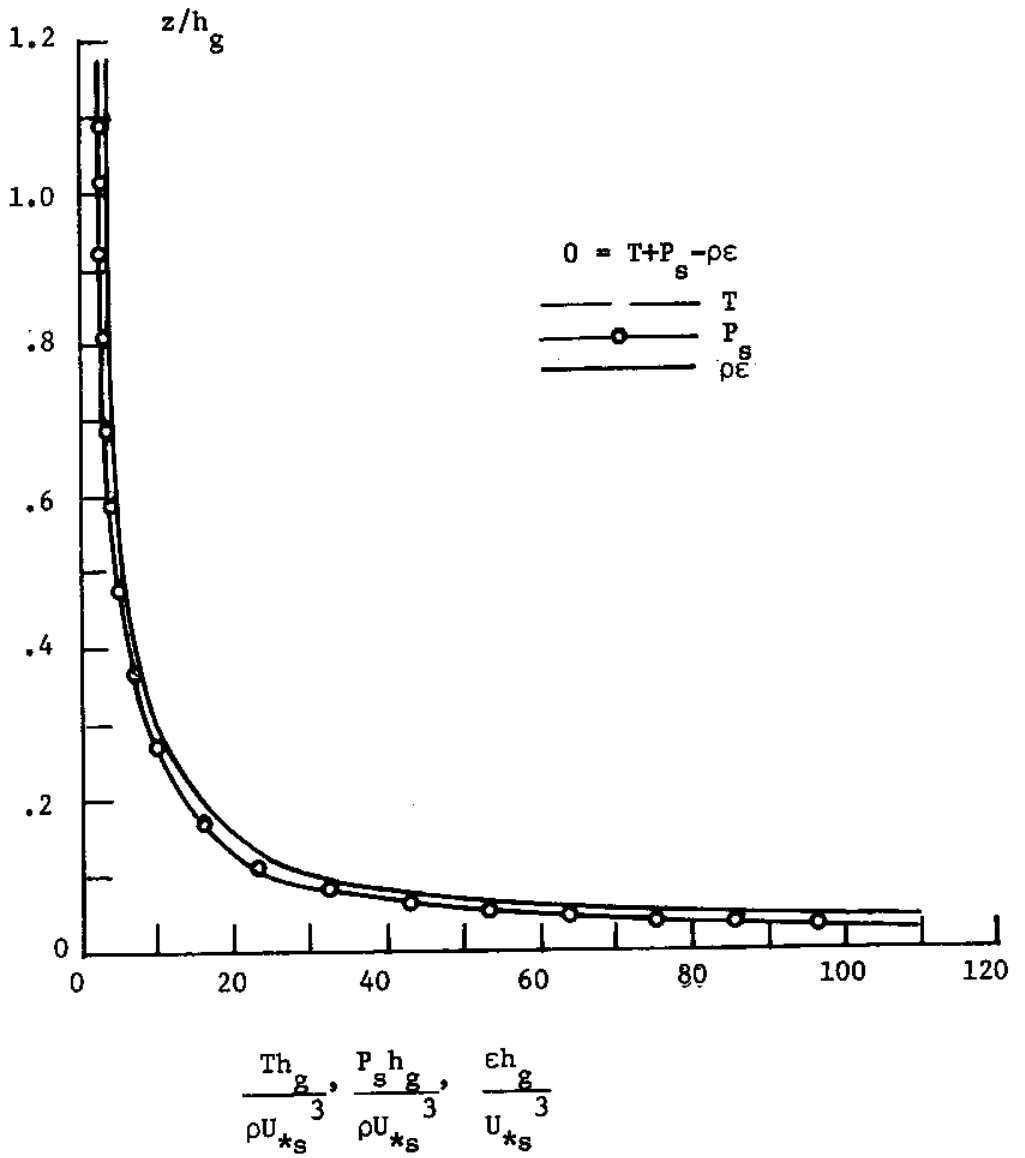

Figure 5.28 - Dimensionless Terms in Kinetic Energy Equation for Type III Flow with $C_d h_g a=0$ (run 18)

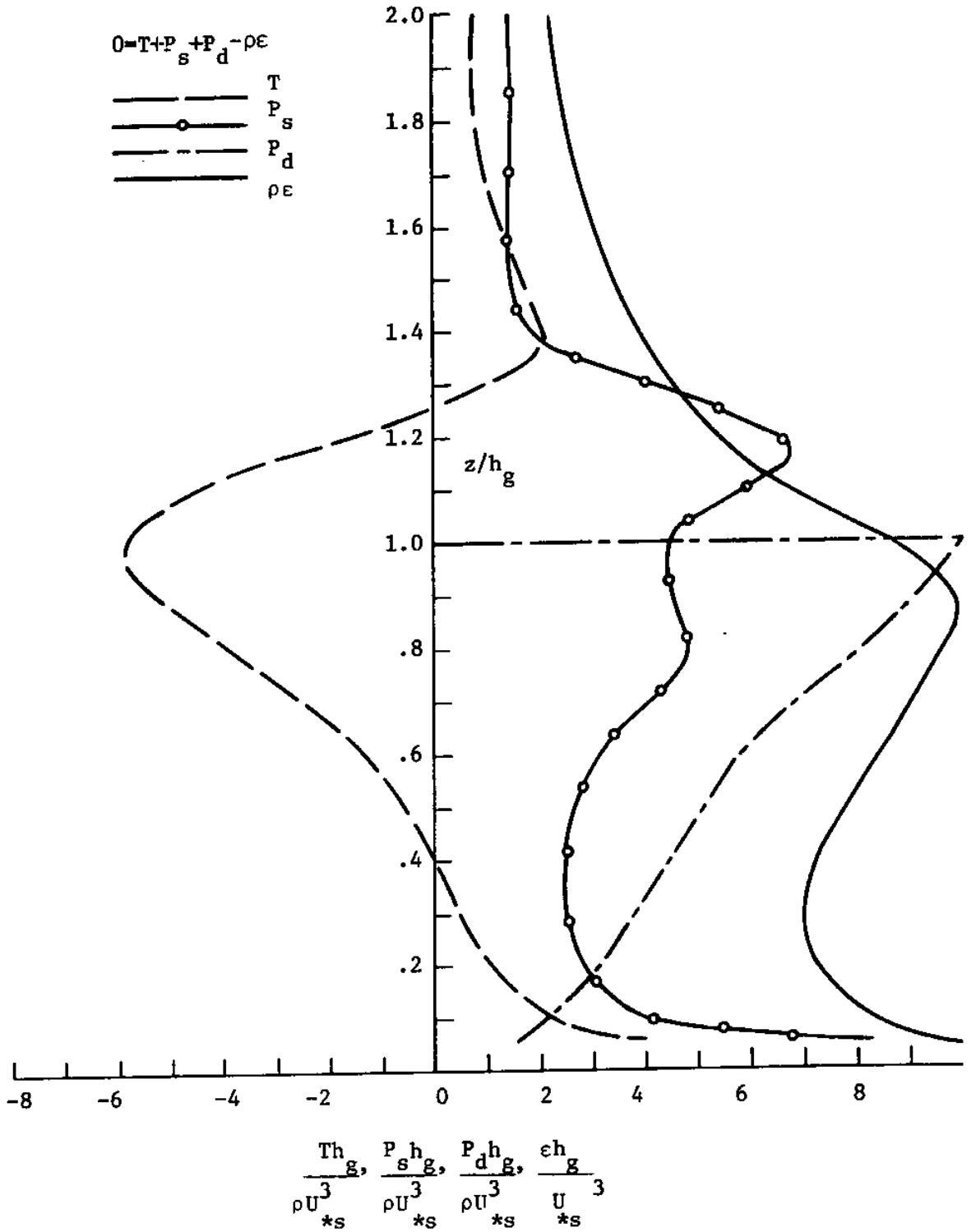

Figure 5.29 - Dimensionless Terms in Kinetic Energy Equation for Type III Flow with $C_d h_g a = .01$. (Run 19).

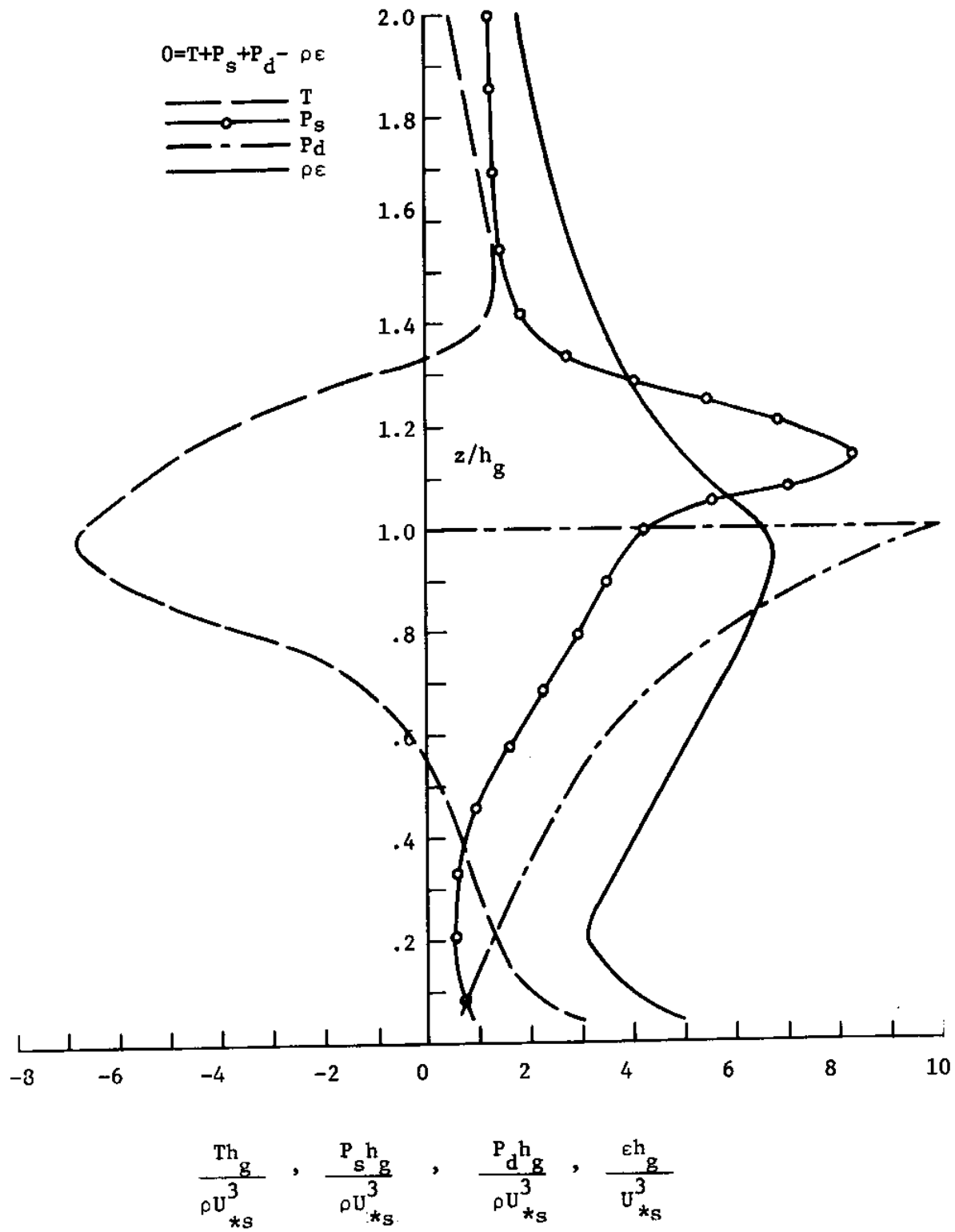

Figure 5.30 - Dimensionless Terms in Kinetic Energy Equation for Type III Flow with $C_d h_g a = .1$. (Run 20).

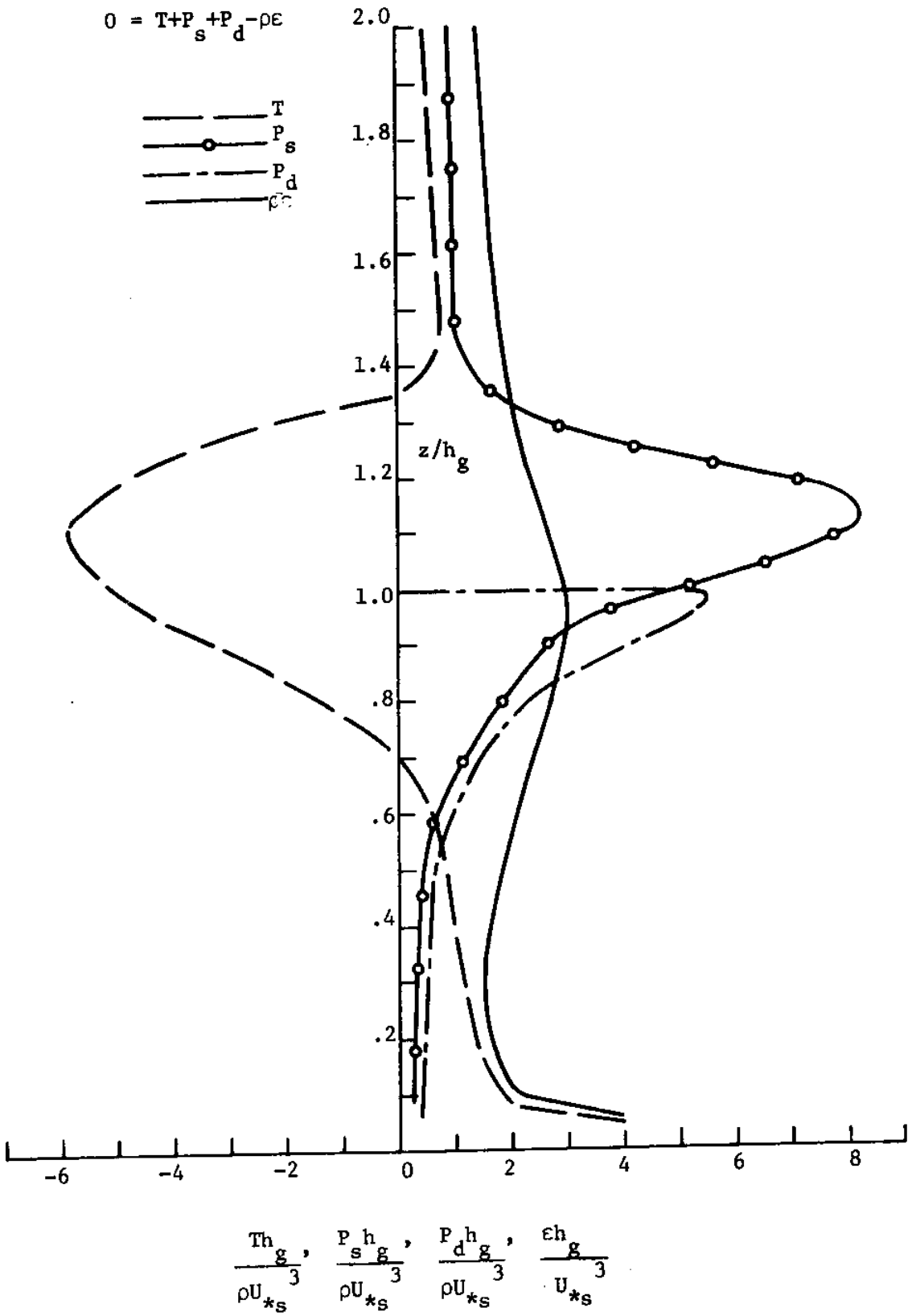

Figure 5.31 - Dimensionless Terms in Kinetic Energy Equation for Type III Flow with $C_d h_g a = 1.0$ (run 21).

production of k due to drag is almost always greater than that due to shear. The production due to drag ends abruptly at the top of the obstructions. Above this level, the turbulent diffusion gradually declines, leaving a balance between production due to shear and dissipation.

5.5.3 Turbulent Diffusivity and Length Scale

Figures 5.32-5.37 plot the turbulent diffusivity (μ_t) and length scale (ℓ) for each of the three types of flow. From Chapter Three, μ_t and ℓ are defined by the expressions

$$\mu_t = \frac{\rho C_\mu}{(1 + \frac{C_\mu' P_d}{\rho\tilde{\varepsilon}})} \frac{k^2}{\tilde{\varepsilon}} \qquad (3.14a)$$

$$\ell = \mu_t/\rho k^{1/2} \qquad (3.2)$$

Figures 5.32-5.35 show the vertical profiles of μ_t and ℓ for the confined pressure and shear driven flows. For $C_d h_g a=0$, the turbulent diffusivity in both types of flow is seen to increase linearly from each surface, reaching a maximum at about $z/h_g=.5$. For the shear driven flows, where k is constant, it follows from (3.2) that ℓ will exhibit a similar behavior. For pressure driven flows, in contrast, where k decreases monotonically, μ_t and ℓ do not have the same shape.

As $C_d h_g a$ increases above zero, the values of μ_t and ℓ for both types of confined flows start to decline, reflecting the changes in the

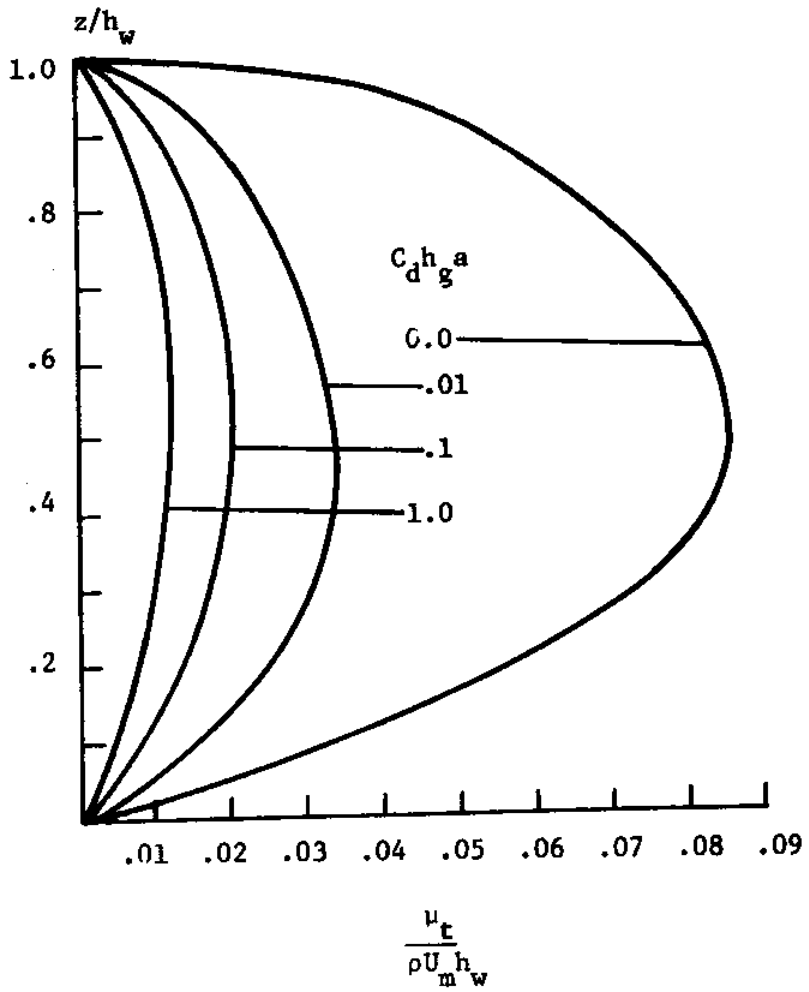

Figure 5.32 - Dimensionless Profiles of Turbulent Viscosity for Type I Flow with h_g/h_w=1. (Runs 10-13).

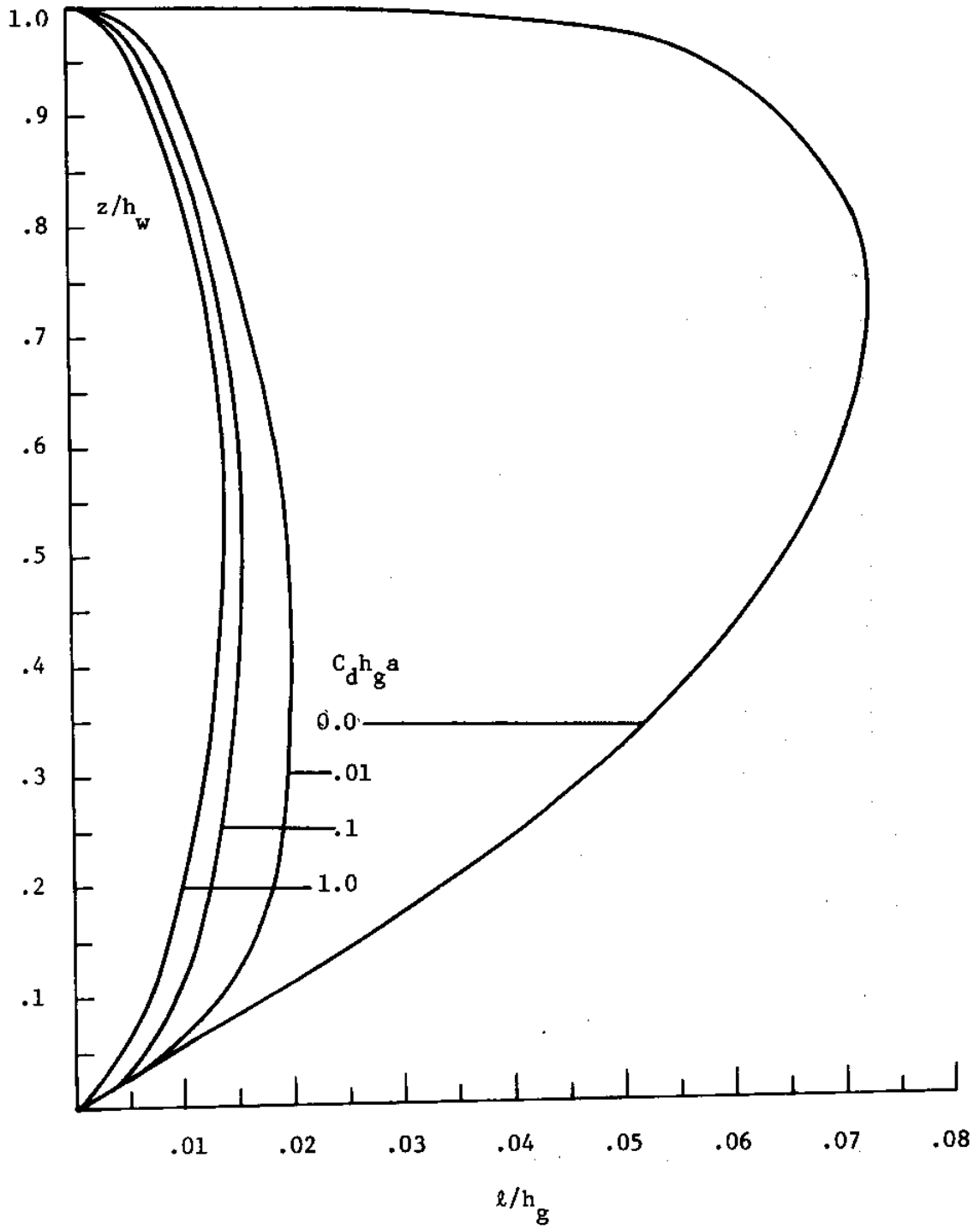

Figure 5.33 - Dimensionless Profiles of Turbulent Length Scale for Type I Flows with h_g/h_w=1. (Runs 10-13).

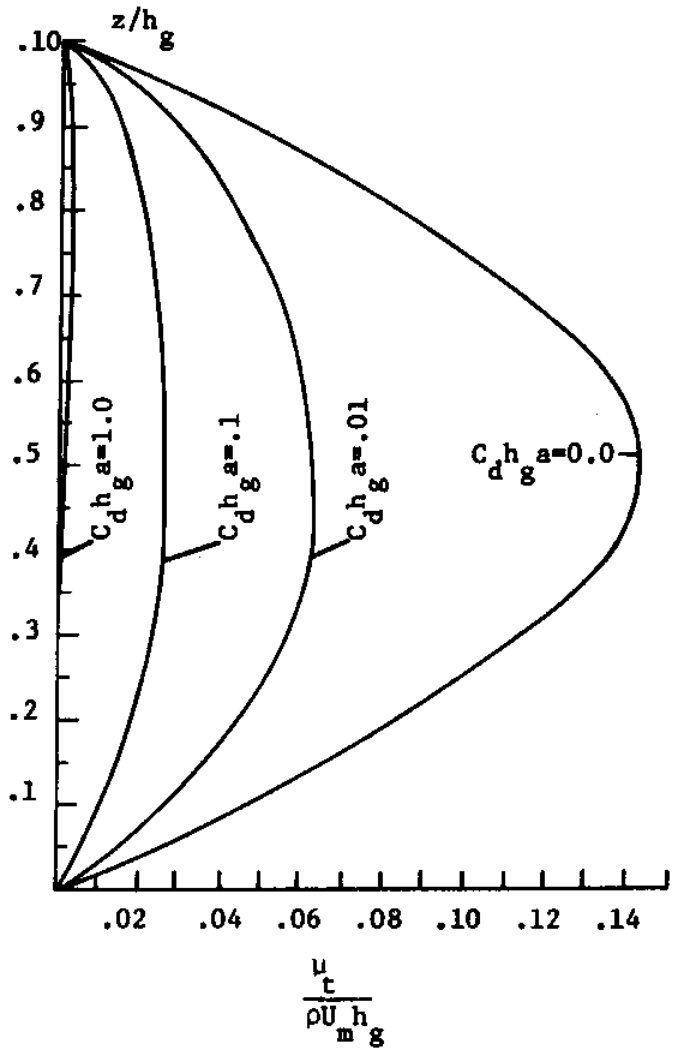

Figure 5.34 - Dimensionless Profiles of Turbulent Viscocity for Type II Flow with h_g/h_w=1.0 (runs 14-17).

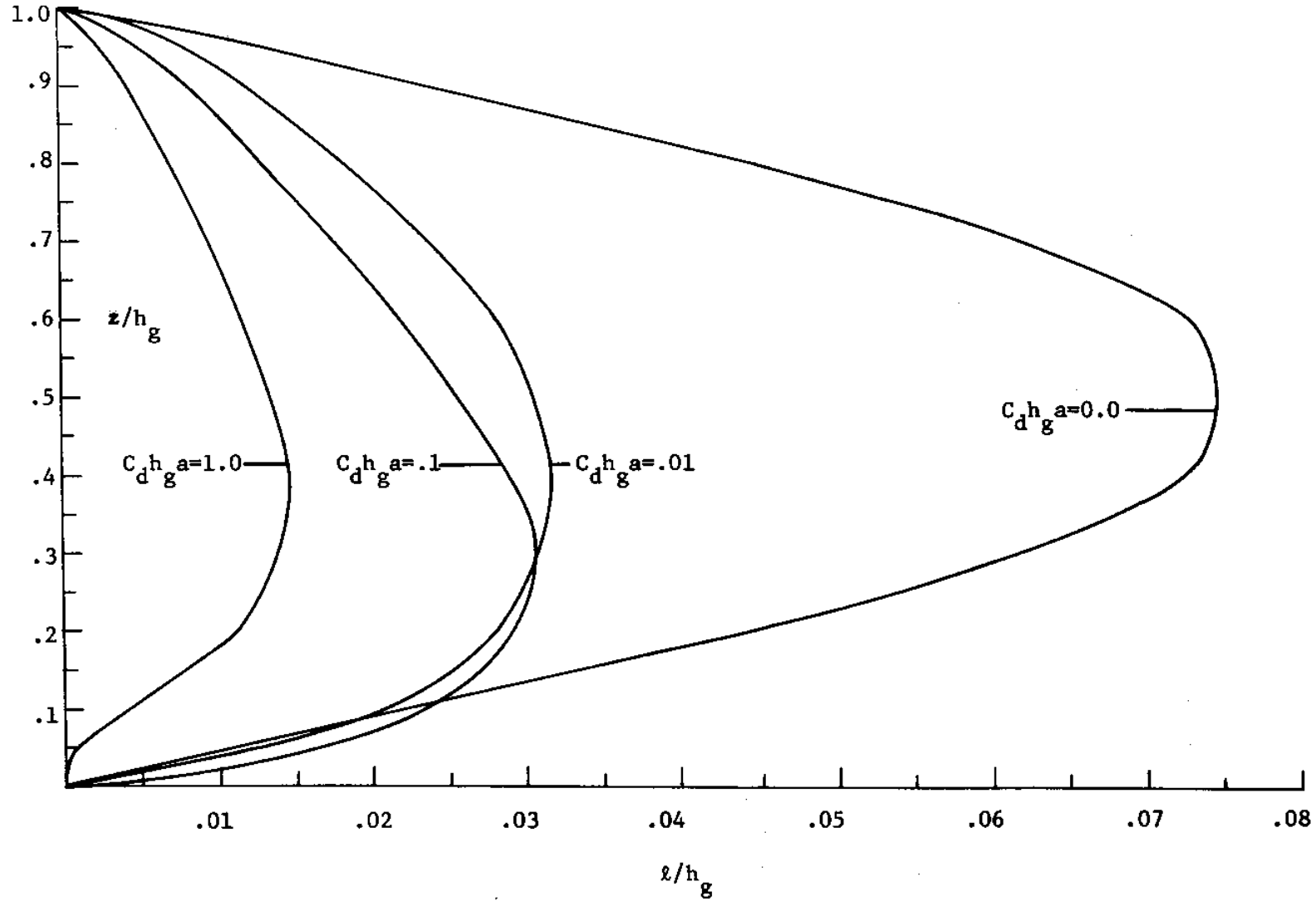

Figure 5.35 - Dimensionless Profiles of Turbulent Length Scale for Type II Flow with h_g/h_w=1.0 (Runs 14-17).

relative magnitudes of k and $\tilde{\varepsilon}$, discussed earlier. Within the obstructions, the turbulent scales are reduced below their non-obstructed values. In general, however, ℓ is not proportional to a single scale, such as (h_g) or (a). Thus, while (a) varies by a factor of 100, ℓ does not change by more than a factor of two or three.

Figures 5.36 and 5.87 show vertical profiles of μ_t and ℓ for the unconfined flow model cases. The sudden increase in these quantities at the top of the obstructions can be understood by referring to (3.14c) and (3.2), and by noting that at $z/h_g=1$, P_d drops suddenly to zero. Assuming that U_a remains constant, μ_t is observed to increase with $C_d h_g a$. (This is in contrast to the confined flow cases, where μ_t generally decreases with $C_d h_g a$, other factors being kept constant). The reason behind the increase in μ_t for the unconfined flow cases can be understood by noting that, to maintain a constant value of U_a as $C_d h_g a$ increases, a larger driving force will be required to overcome the additional drag. This larger driving force expresses itself through a large shear stress above the obstructions, leading to more diffusion of kinetic energy, and thus higher values of μ_t. The trend of increasing stress with $C_d h_g a$ for unconfined flows is considered in Section 5.6.

One of the major differences between the model proposed in this study and previous obstructed flow models, such as those reviewed in Chapter Two, concerns the manner in which the turbulent transport is parameterized. In simple diffusivity approaches, such as that of

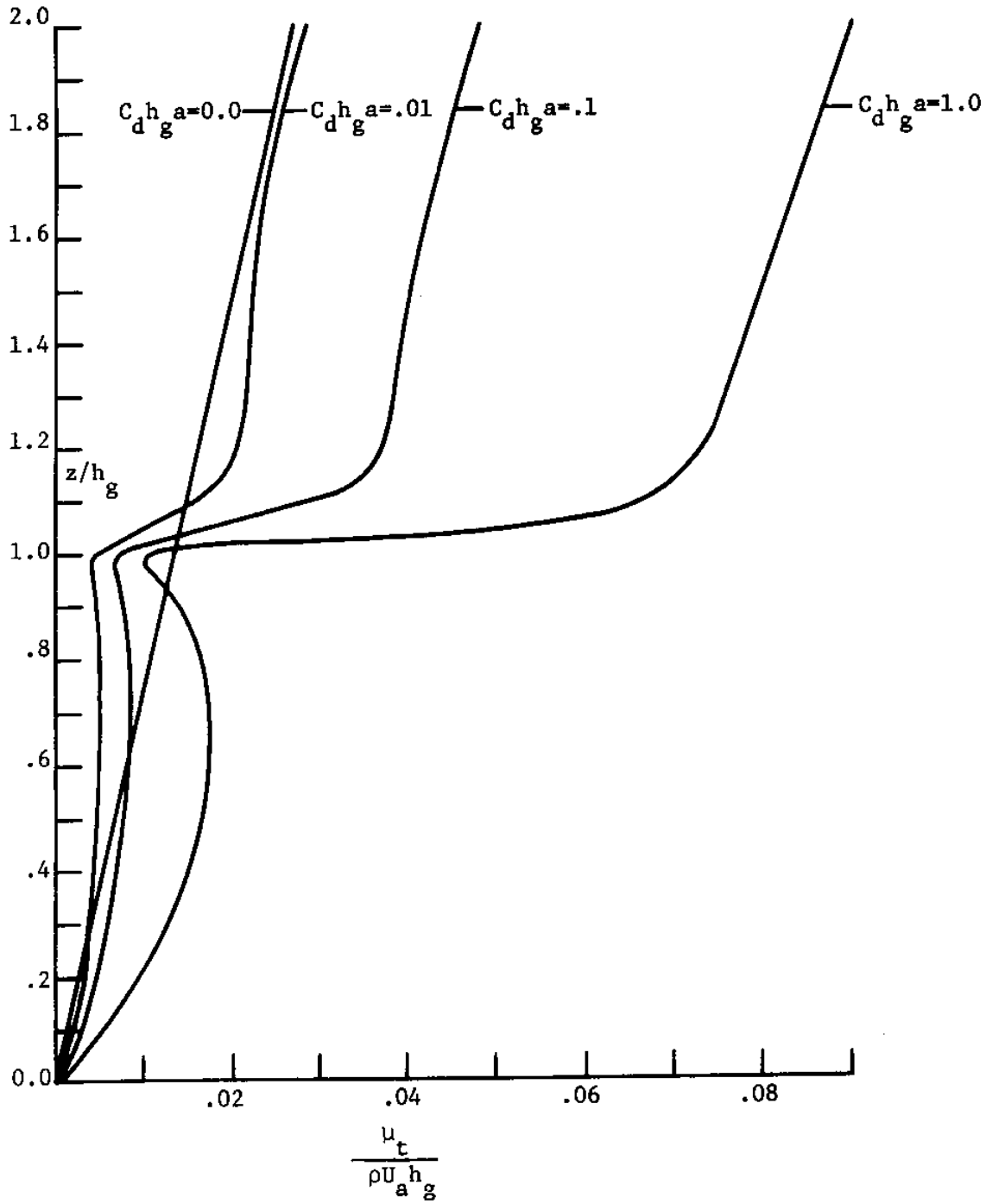

Figure 5.36 - Dimensionless Profiles of Turbulent Viscosity for Type III Flows. (runs 18 -21)

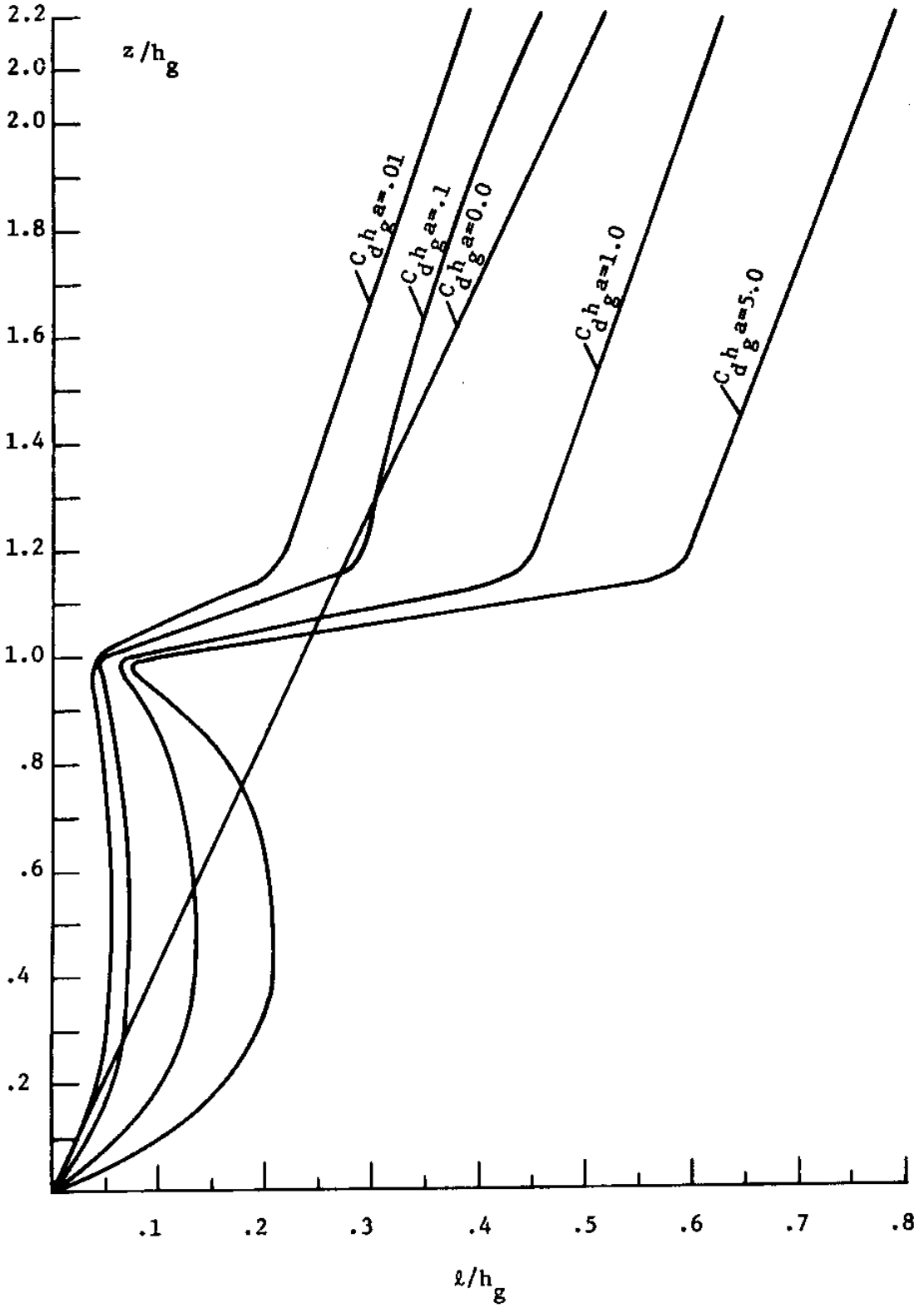

Figure 5.37 - Dimensionless Profiles of Turbulent Length Scale for Type III Flows. (Runs 18-22).

Cionco (1963) or Kondo (1976), the turbulent diffusivity is assumed proportional to the product of a single velocity scale and single length scale; the velocity scale is taken as being proportional to either the mean velocity gradient (mixing-length approach) or the friction velocity at the top of the obstructions (diffusivity approach). In one such model, Cionco (1963), using a mixing-length approach in which the mixing length (ℓ_c) was assumed constant, derived the expression

$$\frac{u}{u(h_g)} = \exp\ (\alpha_c(z/h_g - 1)) \tag{2.12}$$

where α_c is an empirical coefficient, equal to

$$\alpha_c = (\frac{1}{4}\ C_g h_g a\ (\frac{h_g}{\ell_c})^2)^{1/3} \tag{5.1}$$

Cionco's model was developed for unconfined flows only, and takes no account of a free surface. The velocity at the top of the obstructions ($u(h_g)$) must be prescribed, and is not determined by the model.

Comparison of ℓ_c and the turbulent length scale ℓ used in this study can be done by noting that

$$(\frac{\mu_t}{\rho})^2 = k\ell^2 = \ell_c^4\ (\frac{du}{dz})^2 \tag{5.2}$$

With $\frac{\tau}{\rho} = (\ell_c\ \frac{du}{dz})^2$, the above expression becomes

$$\ell = \ell_c \left(\frac{\tau/\rho}{k}\right)^{1/2} \tag{5.3}$$

For non-obstructed flows, where $\frac{\tau/\rho}{k} = C_u^{1/2}$ (from Section 3.2.5), and $\ell_c = \kappa z$, (5.3) reduces to $\ell = C_\mu^{1/4} \kappa z$, as derived earlier in Chapter Three.

The values of ℓ predicted by Cionco's model were calculated for the unconfined flow model cases treated previously. For each case, the value of ℓ_c was obtained from (5.1). (The determination of α_c is discussed in the next section.) Knowing ℓ_c, it was then possible to determine ℓ from (5.3). The results are shown in Figure 5.38, along with the values of ℓ predicted by this study. Note than Cionco's model makes no assumption about ℓ for $z/h_g > 1$.

Figure 5.38 demonstrates that for small values of $C_d h_g a$ (less than .1) the values of ℓ determined by (5.3) agree well with those determined from the unconfined flow model results. Considering that α_c was obtained by fitting the predicted model velocities to (2.12), as discussed later, this indicates that for small $C_d h_g a$ the velocity profile is exponential, and may be described by (2.12). As $C_d h_g a$ increases beyond .1, the agreement in ℓ profiles becomes progressively worse, indicating that the predicted velocity profile is approximated less accurately by (2.12), and that there is no simple length scale capable of predicting the flow field in these cases. In spite of the differences in the ℓ profiles, however, the velocity profiles for the unconfined flow model cases as determined by this study, and by (2.12),

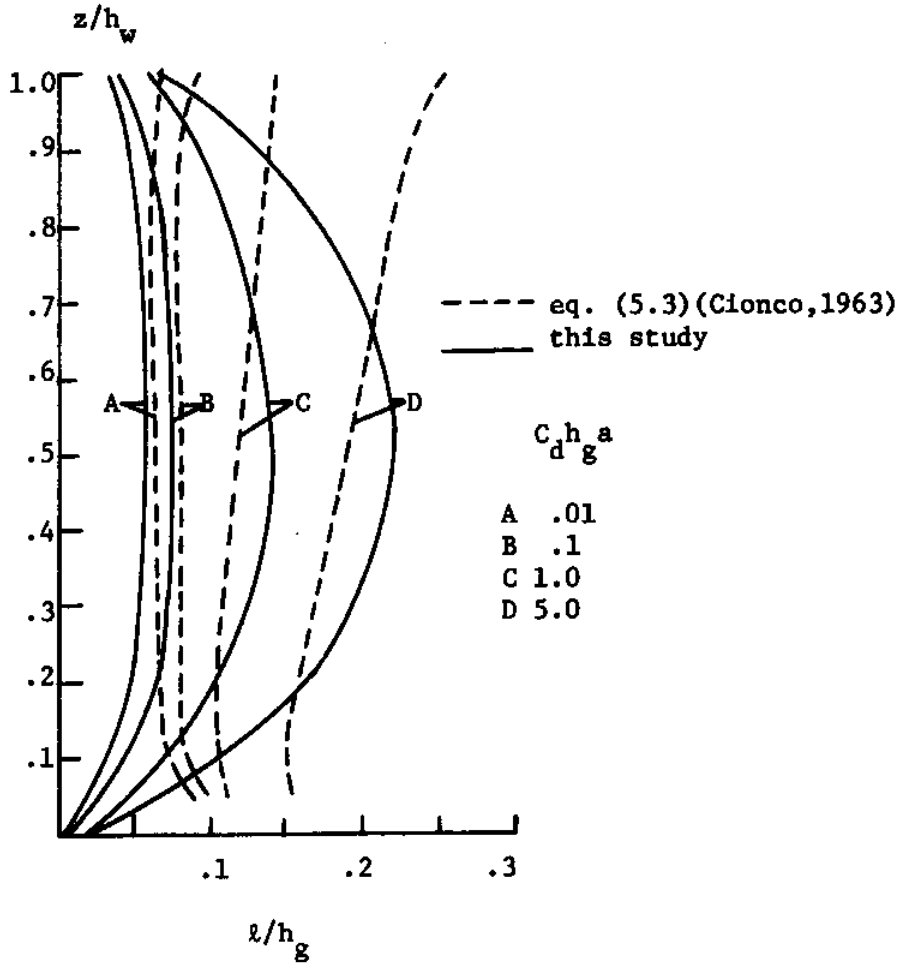

Figure 5.38 - Dimensionless Profiles of ℓ for Unconfined Flow Model Cases as Determined by Cionco (1963) and This Study.

are fairly similar in shape. As noted by Thom (1981), once $u(h_g)$ has been fit (as it has here by fitting α_c), then the velocity profile is fairly insensitive to the shape of ℓ. As discussed later, α_c is not a constant, but varies with $C_d h_g a$, as well as other parameters. To the extent that α_c must be redetermined for different applications, the predictive abilities of Cionco's model are restricted.

Cionco's model uses a turbulent diffusivity approach to parameterize the shear stress. More complex, higher order models, such as that of Wilson and Shaw (1976), solve for the individual stresses directly. This type of model generally requires some assumption about the dissipation. Wilson and Shaw assumed that

$$\varepsilon = \frac{k^{3/2}}{\Lambda \ell\omega} \tag{5.4}$$

where $\Lambda = 5.9$ and $\ell\omega$ was prescribed as being the maximum value allowed by

$$\ell\omega = 0 \qquad @\ z=0$$

$$\left|\frac{d\ell\omega}{dz}\right| < \kappa$$

$$\ell\omega < \frac{\alpha}{C_d a}$$

The empirical coefficient $\alpha = .12$ was determined by fitting the model results to the velocity data in a corn crop, having $h_g a$ of about one.

Recalling that in the model proposed here the dissipation is related to ℓ by

$$\varepsilon = \frac{C_\mu}{(1 + \frac{C'_\mu P_d}{\rho \tilde{\varepsilon}})} \frac{k^{3/2}}{\ell}$$

it follows from (5.4) that

$$\ell = \frac{C_\mu}{\left(1 + \frac{C' P_d}{\rho \tilde{\varepsilon}}\right)} \Lambda \ell\omega \qquad (5.5)$$

Using the above expression, the length scale ℓ as determined by Wilson and Shaw's model was determined for the unconfined flow model cases. Values of $\ell\omega$ for each case are presented in Figure 5.39. With these values, and the model results for P_d and $\tilde{\varepsilon}$, the profiles of ℓ were determined for each case using (5.5). The results are shown in Figure 5.40. Examining this figure, the following points are observed:

(1) For the non-obstructed flow case, ℓ = .53kz. In the absence of obstructions P_d=0, so that from (5.5) $\ell = C_\mu \Lambda \ell\omega$ = .53kz (C_μ=.09). This is analogous to the result derived in Section 3.2.5, where it was shown that in flows having negligible diffusion $\ell \sim C_\mu^{1/4} kz$ = .55kz (see Figure 5.37). Thus, in the absence of obstructions, the turbulent length scale as determined by Wilson and Shaw agrees with that predicted by this study. This result is not surprising, but serves as a check on the calculations.

(2) For $C_d h_g a$=.01, .1, the turbulent length scale above the obstructions is the same as if the flow were non-obstructed. For higher values of $C_d h_g a$, the turbulent length scale within the obstructions is roughly proportional to $(C_d a)^{-1}$, as might be expected

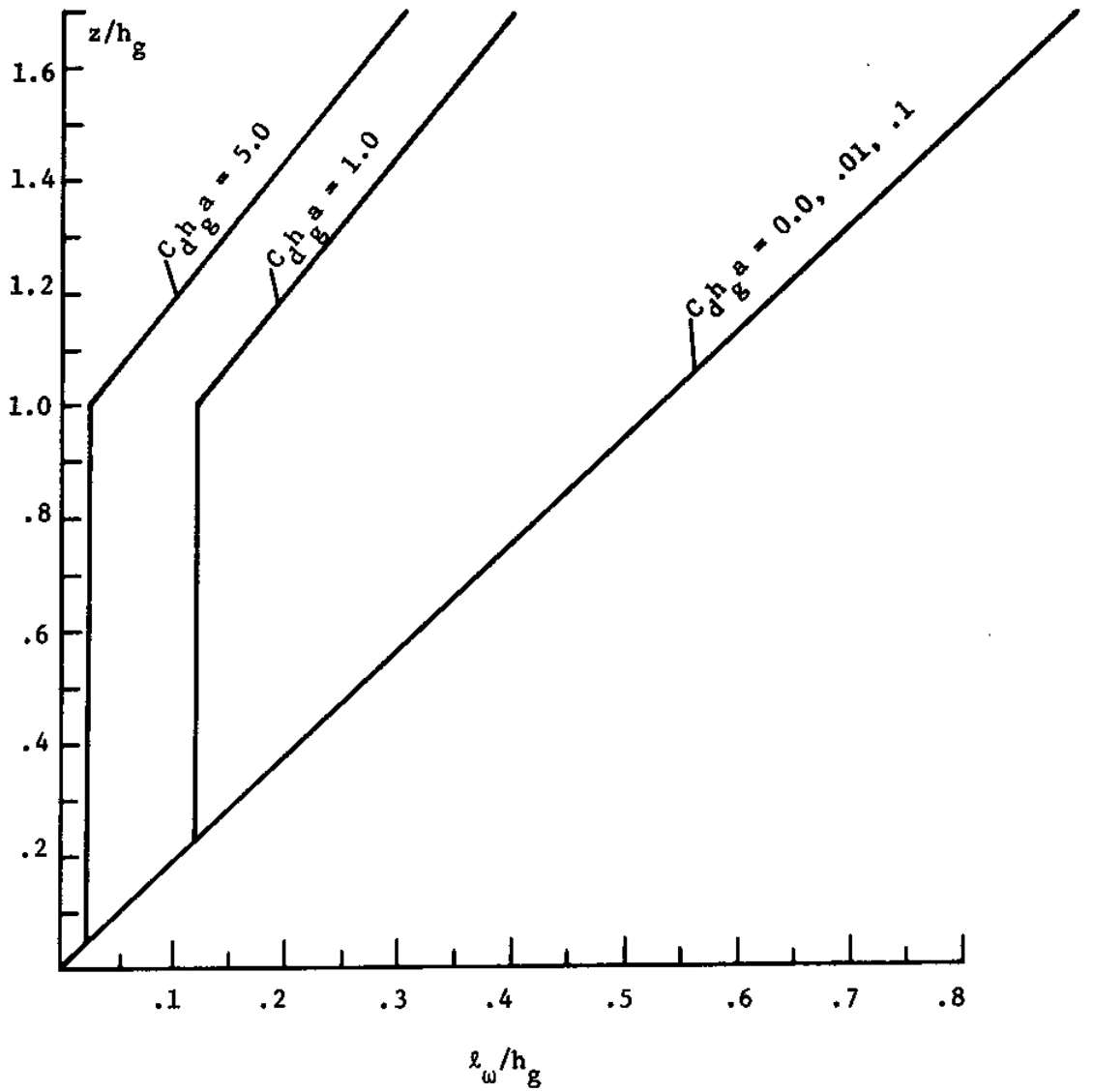

Figure 5.39 - Profiles of ℓ_ω/h_g for Unconfined Flow Cases as Prescribed by Wilson and Shaw (1976).

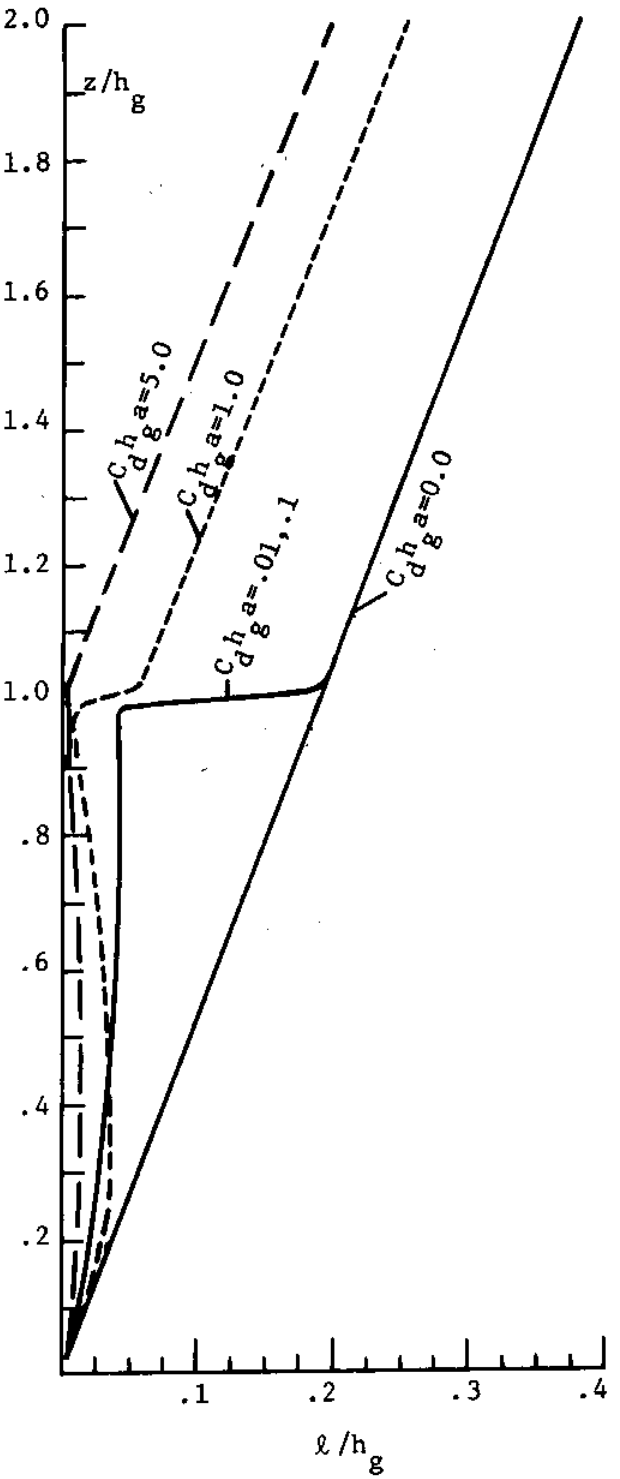

Figure 5.40 - Dimensionless Profiles of the Turbulent Length Scale as determined by Wilson and Shaw (1976) for Unconfined Flow Model Cases.

from the manner in which $\ell\omega$ is determined.

(3) The values of ℓ are less than those predicted in this study. By prescribing the length scale algaebraically, Wilson and Shaw do not allow it to be influenced by diffusion.

In general, the values of ℓ determined by previous obstructed flow models do not agree with the results found in this study, owing to the assumptions used to parameterize the turbulent transport. As discussed earlier, turbulent diffusion is usually an important factor in obstructed flows; this disagrees with the simple diffusivity approaches, in which no consideration is given to the influence of diffusion on the length or velocity scales.

A second area of disagreement with previous models concerns the assumption that the turbulent length scales is proportional to either h_g or $(C_d a)$. As determined in this study, ℓ is not generally proportional to either of these scales. Thus, for instance, in the confined and unconfined model flow cases treated previously, (a) changed by a factor of 100, while ℓ only changed by about a factor of three.

A third discrepancy, referring specifically to Wilson and Shaw's model, concerns the result that small values of $C_d h_g a$ do not affect the turbulent structure above the obstructions. This contrasts with the findings of this study, which indicate that even relatively sparse canopies will alter the nature of the turbulence from it's non-obstructed situation.

In summary, the turbulent structure of obstructed flows has been found to reflect the separate infuence of the two length scales h_g and (a), as well as the influence of diffusion. These factors will interact with each other in potentially complicated ways, making it doubtful whether a simple concept of μ_t or ℓ, ignoring diffusion, or the presence of more than one length scale, would be practicable under the varying situations of interest in this study.

5.6 Determination of Empirical Parameters in Analytical Expressions for Unconfined Flow (Type III)

In contrast to confined obstructed flow, which has received relatively little attention in the past, considerable effort has been aimed at trying to understand unconfined flows, both above and within the obstructions. Much of this research has been directed toward analytical expressions, which contain empirical coefficients obtained by observation. It is interesting to use the dimensionless parameters and the model proposed here to determine these coefficients, and to compare the results with observed values.

5.6.1 Inertial Sublayer

The flow in the inertial sublayer overlying obstructions in unconfined flow may be described by the semi-log law, given in Chapter Two as

$$\frac{u}{u_*} = \frac{1}{\kappa} \ln \left(\frac{z-d}{z_o}\right) \qquad (2.10)$$

where u_* is the friction velocity at the top of the obstructions, z_o is the roughness length, and d is the zero plane displacement height. Typically, u_* and z_o are determined by fitting velocity measurements to (2.10), after making some assumption about d. The following discussion presents values of shear stress (ρu_*^2) and z_o determined for the unconfined flow model cases, and examines how the predicted z_o compares with observed values.

Figure 5.41 presents the stress at the top (U_{*S}^2) and bottom $(U_{*B})^2$ of obstructions for the unconfined flow model cases. The stress is non-dimensionalized by U_a^2; assuming U_a remains constant, the stress at the top of the obstructions is seen to increase with $C_d h_g a$, reflecting the increased stress necessary to achieve the velocity U_a over a surface of increasing roughness. For small $C_d h_g a$, the stress at the top and bottom of the obstructions approaches the same value. As $C_d h_g a$ increases, the two stresses become increasingly far apart. At typical marsh values of $h_g a$ (about .1), the top and bottom stress will differ by almost a factor of ten.

Figure 5.41 also shows values of z_o/h_g for the unconfined flow cases, as determined from (2.10), with u,z obtained from model values at a height of ten meters. In the calculations, d was set equal to $2h_g/3$ (Brutsaert, 1982). Since d appears in (z-d), the determination of z_o will not be very sensitive to the value of d, provided $z \gg z_o$.

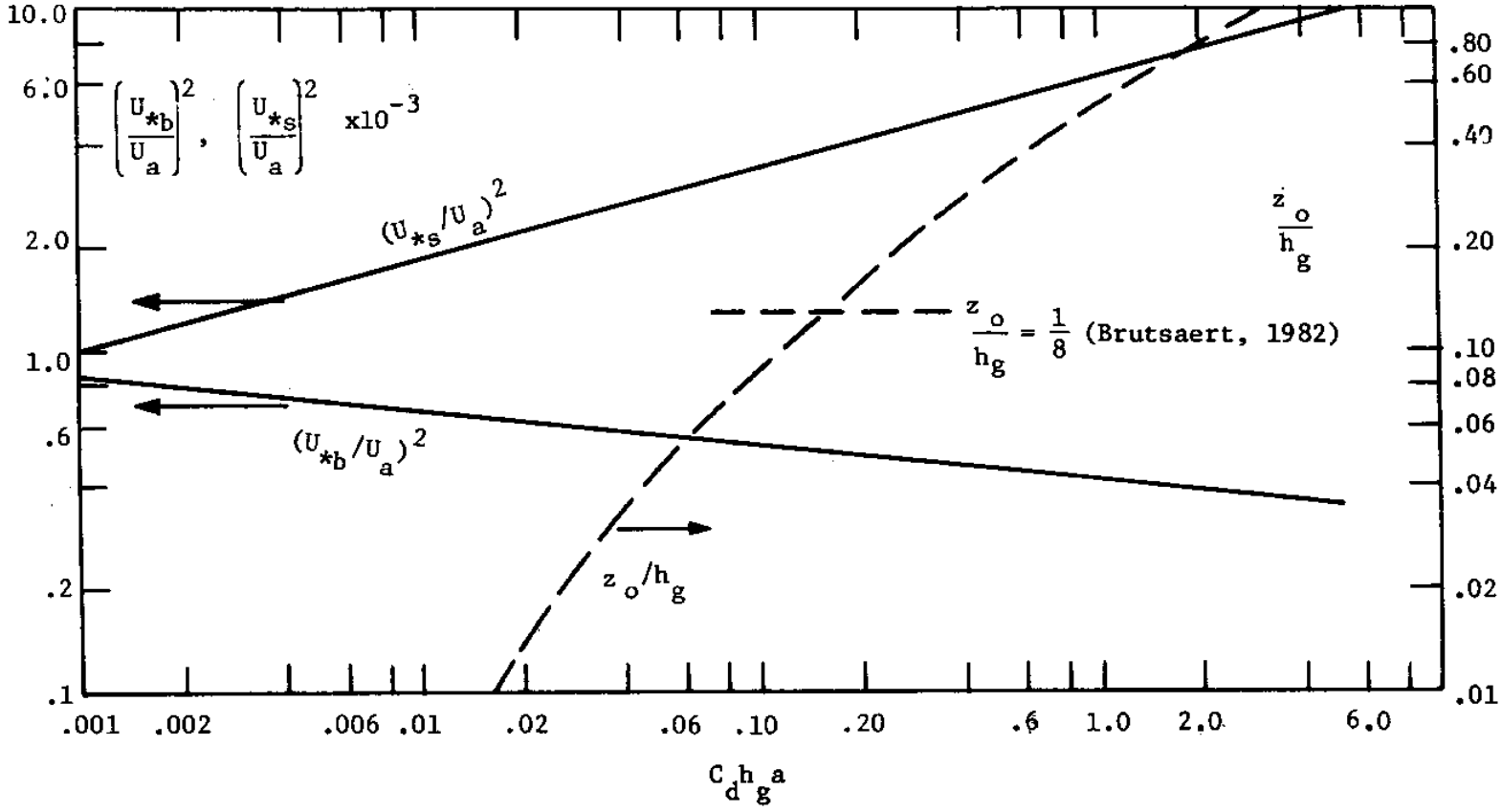

Figure 5.41 - Variation of $(U_{*s}/U_a)^2$, $(U_{*b}/U_a)^2$, and (z_o/h_g) with $C_d h_g a$ fpr Type III Flows.

Also shown in Figure 5.41 is the value z_o/h_g=1/8, as recommended by Brutsaert (1982) for vegetation such as grasses, shrubs, and bushes, having $h_g a$ between .1 and 1. Over this range, the model values are seen to be in fairly good agreement with the analytical expression.

The values of z_o/h_g for the unconfined flow model cases are also exhibited in Figure 5,42, along with values for a variety of boundary roughnesses, and 3D obstructions. This figure was taken largely from Seginer (1974).

From Figure 5,42, it is seen that for $C_d h_g a$ less than about .3, the model values of z_o/h_g for unconfined flow agree with those of other studies. For larger $C_d h_g a$, several of the curves reach a maximum, and then start to decline. This trend does not hold for the unconfined model cases, in which z_o/h_g increases monotonically over the range of $C_d h_g a$ considered.

The interpretation of the peak in the z_o/h_g curve is that, as the density of sparsely-placed obstructions increases, the drag increases, and thus so does z_o; when (a) becomes very large, and the obstructions are densely packed together, the flow skims over the tops of the obstructions, without penetrating downward, thus causing a decrese in z_o.

Of the curves in Figure 5.42 that exhibit a maximum, only one corresponds to obstructions having a comparable geometry to that of the unconfined flow model cases. This is the wind tunnel study of cylindrical pegs, done by Kawatini and Meroney (1970). In this study,

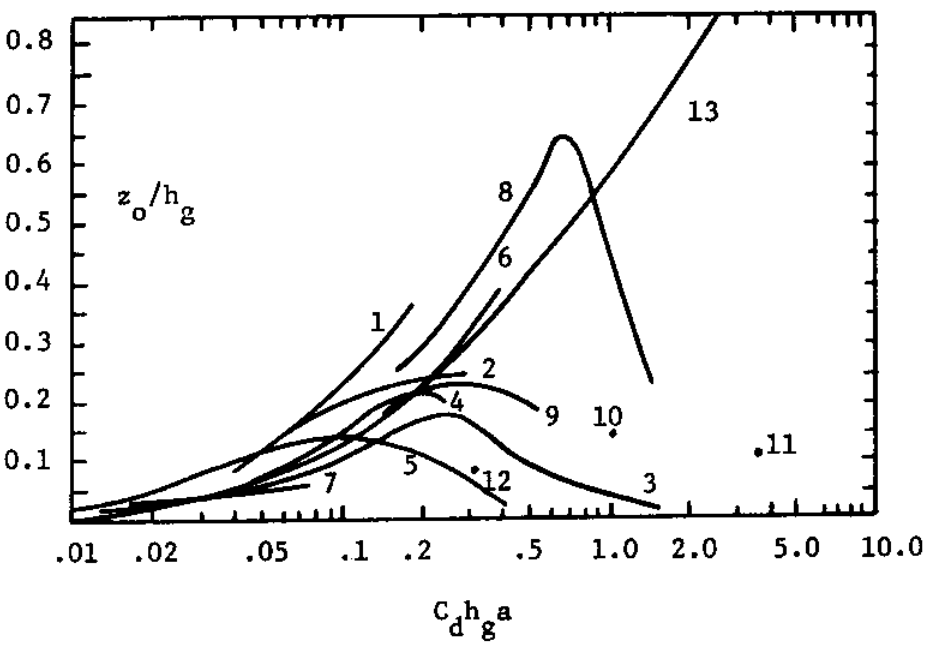

Figure 5.42 - The Relative Roughness Length z_o/h_g as a function of $C_d h_g a$. 1,2: Sayre and Albertson (1961), 3-D, baffles; 3: Robertson et al. (1968), 2-D slats; 4: Robertson et al. (1968), 2-D, Rods; 5: Robertson et al. (1968), 3-D, Spheres; 6: Lettau (1969), 3-D, baskets; 7: Robertson et al. (1968), 3-D, hemispheres; 8: Kawatani and Meroney (1970), 3-D, pegs; 9: Chamberlain (1968), 2-D, rods; 10: Plate and Quraishi (1965), 3-D, strips; 11: Thom (1971), 3-D, rods; 12: Seginer (1976) 3-D, rods; 13: this study, 3-D, rods. (taken largely from Seginer (1974)).

z_o and u_* were determined by fitting the velocity data above the obstructions to (2.10), with d being taken as h_g. As a test, the friction velocity was also estimated in one case from measurements of the drag force on the pegs by means of a shear plate. The difference between the friction velocities calculated from (2.10) and the drag force was about 30% of the value obtained from the drag force. Considering that z_o will be fairly sensitive to u_*, which appears in e^{-u/u_*}, it seems likely that a thirty percent error in u_* could substantially alter the results, and may exlain the observed maximum in Kawatini and Meroney's data.

Aside from experimental errors, there is the question of whether z_o/h_g is a function only of $C_d h_g a$. Inspecting Figure 5.42, it is seen that in the wind tunnel studies of Thom (1971), Plate (1965), and Seginer (1976), (for which good model agreement was found in Chapter Two), the values of z_o/h_g do not generally agree with those of Kawatini and Meroney at the same value of $C_d h_g a$. This suggests that z_o/h_g may depend on other factors besides $C_d h_g a$, such as Reynold's number effects, or h_g/h_w, which ranged in the above wind tunnel studies from 3 to 14.

Wind tunnels are essentially confined flow situations, and may not duplicate the exact conditions of unconfined flow. This is corroborated by noting that, in modeling the wind tunnel studies of Chapter Two, unsatisfactory agreement was obtained by treating the flows as being unconfined. As discussed previously, there is generally

more diffusion in unconfined than confined flows. This could explain the generally higher values of z_o/h_g observed in the unconfined model flow cases. Under unconfined flow conditions, having relatively more diffusion, there would likely be more penetration into the obstructions, and thus higher z_o.

5.6.2 Flow Profiles in Obstructions

The roughness length (z_o) was used in (2.10) to determine the flow above obstructions in unconfined flow. Within the obstructions, a commonly used relationship to obtain the velocity is

$$\frac{u}{u(h_g)} = \exp\ (\alpha_c(z/h_g - 1)) \qquad (2.12)$$

where α_c is the extinction coefficient, defined in Chapter Two. The velocity at the top of the obstructions ($u(h_g)$) must be known beforehand, and is not predicted by the model.

The extinction coefficient α_c is commonly determined by taking the slope of the plot of $\ln(u)$ versus $(z/h_g - 1)$. This procedure was followed for the unconfined flow model cases, the results of which are shown in Figure 5.43. The trend of increasing α_c with $C_d h_g a$ observed in the model results has been noted by Cionco (1972). In his review, Cionco (1972) concluded that α_c varies between .4 and .8, approximately, for rigid elements, such as citrus orchards, wooden pegs, plastic strips, or bushel basket. This range agrees with the values determined for the flow model cases.

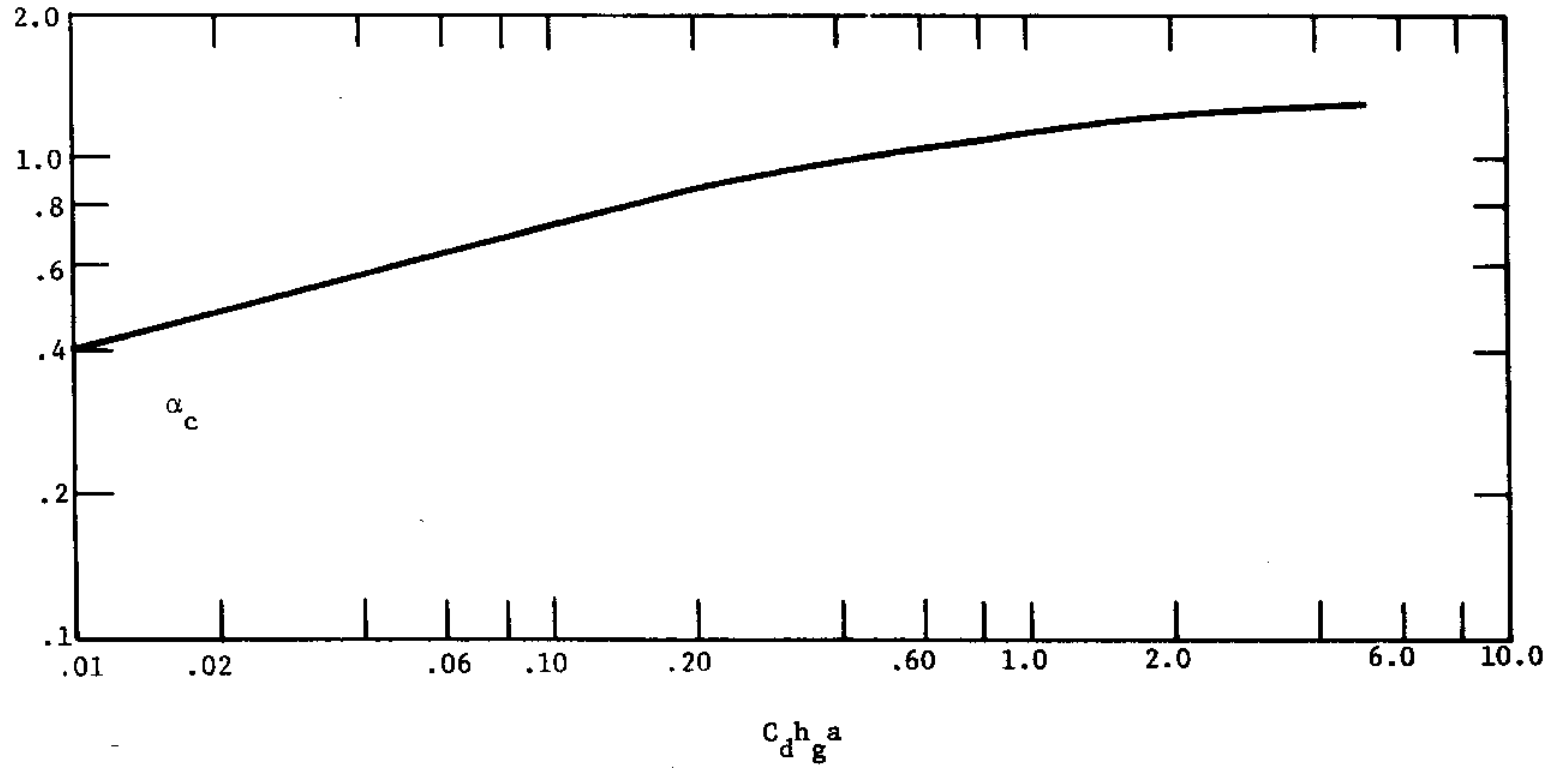

Figure 5.43 - Extinction Coefficient (α_c) as a Function of $C_d h_g a$ for Unconfined Model Flow Cases.

5.7 Conclusions

The variables governing both confined and unconfined obstructed flow may be arranged into the following dimensionless parameters

$$\frac{h_a}{h_g}\ ,\ \frac{h_w}{h_g}\ ,\ C_d h_g a,\ \frac{U_*^2}{U_m^2}\ ,\ \frac{\hat{U}\hat{h}}{\nu}$$

where $U_m = (U_\eta^2 + U_*)^{1/2}$, and $\hat{U}$, $\hat{h}$ are appropriate scales for defining a Reynold's number. Simulations in which all parameters but $\frac{\hat{U}\hat{h}}{\nu}$ were held constant show that Reynold's number effects have relatively little influence on the major flow features. In a similar fashion, the ratio h_a/h_g was found to be unimportant, leaving three parameters representing grass density, grass height and the relative importance of shear. The relationship between these dimensionless parameters and various flow field characteristics was then investigated through a series of model runs. On the basis of these simulations, the following conclusions concerning the effect of obstructions on the flow field may be drawn. (Unless other specified, $h_g/h_w=1$)

(1) For $C_d h_g a$ of about .1, the velocity is reduced below it's non-obstructed value by approximately a factor of four for pressure driven flows, and by almost a factor of ten for shear driven flows. The greater reduction for wind driven flows is due to the fact that, unlike the pressure gradient ($g\frac{\partial n}{\partial x}$), which is uniform with depth, the stress driving the shear flow attenuates with depth.

(2) The scale $U_g=U_m(2/C_d h_g a)^{1/2}$ approximates the velocity of pressure driven flows in which $C_d h_g a > .1$. This result does not apply

to shear driven flows, owing to the non-uniformity in the velocity profiles.

(3) For small values of h_g/h_w (<.25), the variation of the dimensionless total flow conveyance (U_t/U_m) with $C_d h_g a$ is about the same for both shear and pressure driven flows, indicating the equivalence of these two forces when most of the flow depth is unobstructed. For h_g/h_w less than about .75, the variation of U_ℓ/U_m with $C_d h_g a$ is approximately equal for both confined flow and unconfined flow; this is in accordance with the idea that unconfined flow is a limiting case of confined flow in which h_g/h_w approaches zero.

(4) As obstructions are introduced into the flow, the turbulent kinetic energy k increases, reaching a maximum for $C_d h_g a$ between zero and .01, and then starts to decline for larger $C_d h_g a$. The increased levels of k for low vegetation densities has implications for aquatic plants, whose life processes may be enhanced by turbulent motion in the surrounding fluid.

(5) The presence of obstructions dramatically alters the relative magnitudes of the terms in the kinetic energy equation from that in non-obstructed flows, where the major balance is between production due to shear (P_s) and dissipation. For pressure driven confined flows (with $C_d h_g a > .1$), the major balance is between production due to drag (P_d) and dissipation, from which it follows that dissipation varies with $a^{-1/2}$. This result does not apply to shear driven flows, where P_s and turbulent diffusion are generally not

negligible. For unconfined flows, turbulent diffusion is one of the leading terms within the obstructions because of transport from above the obstructions; as a result, the flow field is more uniform than in the confined pressure driven flows.

Reviewing the above discussion shows that for $C_d h_g a$ greater than about .1, the flow field characteristics, including vertical profiles of u, k, u_t, and ℓ are significantly different from the equivalent non-obstructed flows. This result applies for each of the types of flow in Figure 5.1, and is thus of sufficient generality to say that the motion of a fluid passing between obstructions having $h_g a$ greater than about .1 will share few of the characteristics of conventional open-channel flow, and may be classified as being obstruction-dominated.

In addition to flow field characteristics, this chapter also examined the concepts underlying other obstructed flow models, and compared the values of empirical coefficients appearing in previous studies with those predicted by the model proposed here. The results of this analysis may be summarized as follows:

(1) The turbulent structure within obstructed flow will generally be influenced by both turbulent diffusion and the two length scales (h_g) and (a), thus precluding simple turbulence models that do not account for these factors.

(2) Observed values of the empirical coefficients z_o and α_c, which appear in analytical expressions for unconfined flow above and within obstructions, were found to be in generally good agreement with predicted model results.

CHAPTER VI

EPILOGUE

This study has taken the low Reynold's number k-ε model, as developed by other researchers for non-obstructed flows, and extended it's capabilities to include obstructed flow processes. The ability of the model to reproduce the vertical variation of horizontal velocity, as well as more general turbulent properties such as kinetic enenrgy and dissipation, has been demonstrated by comparison with a wide variety of labortory and field studies, ranging from a water flume experiment of flow through plastic strips, to airflow through bean and corn crops. The generally good agreement found in these comparisons between observed and predicted results warrants the use of the model in a predictive mode. This is further supported by noting that the model contains no adjustable constants, and requires no computational fitting of parameters to experimental data, as is necessary in many previous obstructed flow schemes.

In addition to model comparisons against experimental studies, the flow algorithm proposed here was also used in investigations considering the sensitivity of the flow field to the relevant parameters governing obstructed flow situations, these parameters being defined in Chapter Five. The sensitivity studies provided insight into the various flow regimes encountered in natural systems, such as

tidally inundated salt marshes.

While this report has sought to provide a better understanding of obstructed flow processes, there are still many issues remaining to be considered. In particular, further study is merited in the following areas.

(1) Improvements in the basic model formulation

There are three major ways in which the model formulation could be improved. First, a better knowledge is needed of the relationships between the turbulent parameters (appearing as coefficients in the model) and the physical nature of the obstructions. Thus, for instance, more work could be done on the dependence of the drag coefficient (C_d) on the obstruction geometry (i.e. rod or leaf), flexibility, and density. As discussed in Chapter Two, the drag coefficient applied to a group of obstructions has been found to be generally less than that for a single element. Typically, however, the data relating to this sheltering effect is mentioned as a side-note in a larger study of flow through vegatative canopies, where the primary interest is in the velocity. Laboratory investigations focusing solely on this question would be worthwhile. One possibility would be to conduct a series of water flume tests through artificial vegetation, such as circular cylinders, having roughly the same geometry and spacing as marsh grass. In conjunction with these tests, it might be feasible to measure the drag coefficient on live marsh grass set up in the flume.

The second area in which the model formulation could be improved concerns the addition of terms representing the effect of skin friction. In it's current form, the model proposed in this study takes no account of skin friction drag on the obstructions, or the dissipation of kinetic energy due to skin friction. Inclusion of these effects would likely increase the model's capability to predict the flow through vegetative canopies having large, leafy surfaces.

Third, the model could be improved through the development of a technique allowing the empirical treatment of the viscous regions near boundaries. At present, the model extends the calculations through the viscous zones, requiring a relatively large number of grid points to cover the flow depth, as discussed below. The viscous zone could be avoided altogether through the development of universal wall functions, analogous to those used in non-obstructed flows. These functions might be derived by analyzing the model predictions of the near-wall turbulent structure in obstructed flow situations, and trying to find general patterns in the vertical distributions of the variables. As the parameter $C_d h_g a$ goes to zero, the variables will exhibit the same trends as observed in non-obstructed flows. To avoid the complexities associated with the transition from obstructed to non-obstructed conditions, only obstruction dominated flows, having $C_d h_g a$ greater than .1, should be examined initially.

(2) Improvements in the model's computational efficiency

In addition to improvements in the model formulation, there are

also changes that could be made to increase the efficiency of the flow algorithm. One area of improvement deals with the grid spacing. Adequate resolution of the viscous zone near solid walls, or other interfaces, requires a fine grid spacing, resulting in a large number of grid points. As discussed in Chapter Three, 137 nodes are currently being used to cover a flow depth of .2m with a viscous zone at each end having 10 points within the region $R_t < 1$ (R_t is the turbulent Reynold's number, defined as $R_t = k^2/\nu\varepsilon$).

It seems possible that the number of grid points within the viscous zone could be relaxed without a disproportionate loss in solution accuracy. Ideally, the viscous zone could be passed over altogether through the use of universal wall functions, as described above.

A second area in which work could be done to improve the model's efficiency deals with the underrelaxation scheme. At present, the underrelaxation coefficient α for the dependent variables u,v,k, and is held constant at a value of .75; for the turbulent diffusivity α=.5. (The lower the value of α, the less change that occurs in the variable between iterations). A more efficient approach, in terms of the number of iterations required to reach a solution, would be to have a different value of α for each variable, as determined by the sensitivity of the solution process to the variable in question. Thus, for instance, it seems likely that α could be greater for u or v, than for k or ε, in accordance with the fact that the k and ε equations are

more non-linear than the generally well behaved momentum equations. The value of α used to underrelax (μ_t) should probably be the smallest, as μ_t plays a central role in almost all the non-linear terms of the model equations. Experience has shown that underrelaxation of μ_t, in addition to k and ε, is essential if instabilities and non-convergence is to be avoided.

In addition to having different values of α for each variable, it might also be worthwhile to make α a function of the turbulent Reynold's number R_t. In regions of low turbulence, such as near walls or interfaces, where change is propagated primarily by viscous effects, α could probably be greater than in highly turbulent regions, where the flow field would respond relatively quicker to any perturbations, thus increasing the likelihood of instabilities.

(3) Field Data

The field study of free surface properties in Great Sipewissett Marsh described in Chapter Four was biased toward conditions of pressure driven flow, where the wind stress had generally little importance, and where the grass usually extended throughout the entire water column. Under these conditions, the velocity is fairly uniform, and is given by (4.6). It would be useful to investigate the marsh conditions at the other extreme, i.e., flows driven mainly by wind stress, or in which the grass is well submerged below the water surface.

Another worthwhile task relating to future field work would be to study the relationships in the marsh between vegetation density, type of grass, and position on the marsh surface. This could be done using the technique described by Schaefer et al (1982), who measured the vertical (a) distribution in a limited number of sites in Great Sippewissett Marsh, all but one of which corresponded to the grass type Spartina alterniflora.

(4) Model Applications

The model cases considered in this study corresponded to conditions of uni-directional flow. To extend it's range of applications, the model might be used to simulate obstructed flow in a dead end channel, having zero net transport, and in which there would thus be a flow reversal . This situation was studied experimentally by Tickner (1956), who measured the effects of wire screens on the wind set-up in a model channel. Reid and Whitaker (1976) used Tickner's data as the basis for determining the empirical coefficients in their obstructed flow model. Specificlly, Reid and Whitaker divided the flow depth into two layers, the bottom layer extending through the obstructions, and the top layer occupying the region from the top of the obstructions to the free surface. The stress at the top of the obstructions was parameterized as being proportional to the square of the velocity difference between the two layers times an empirical coeficient. The value of the coefficient was determined by fitting model results to one of Tickner's cases. It would be interesting to

compare this value with that predicted by the model proposed here, and to observe how the coefficient varies with the flow geometry.

In addition to being applied to other types of flow, the model might also serve as a sub-model in a larger scheme for predicting the distribution of horizontal velocity $\bar{q}(x,y,z,t)$ within a region of marsh grass for specified boundary conditions on the water surface elevation $\eta(x,y,t)$ at the boundaries of the region and for specified wind speed $U_a(t)$ (or equivalent surface stress). The horizontal connection between various parts of the marsh would be determined through solution of the vertically integrated mass conservation equation, given as

$$(\nabla \cdot h_w \bar{\bar{q}}) + \frac{\partial \eta}{\partial t} = 0$$

where

$$\bar{\bar{q}} = \frac{1}{n} \int_0^{\eta} \bar{q} dz = \text{depth average velocity}$$

$$\bar{q} = \bar{q}(z, \nabla_\eta, U_a) = \text{vertical velocity distribution}$$

The vertical velocity distribution $\bar{q}$ would be computed using the algorithm presented in this study. The time dependence is seen to enter the problem through the continuity relationship.

On a larger scale, the flow model for the grassy marsh area could then be linked to a scheme for computing the flow in the marsh channels and creeks as a function of the tidal forcing at the ocean boundary condition. In this way, the entire free surface flow regime of the marsh could be simulated.

A two-dimensional circulation model such as that described above would provide the basis for dispersion and diffusion calculations aimed at determining the horizontal distribution of dissolved constituents. Specifically, the concentration of the constituent would be obtained through solution of the mass conservation equations, requiring knowledge of the velocity as well as the lateral dispersion coefficient; both of these quantities are readily available from the algorithm proposed here. Such a transport model would be a requisite in the development and analysis of new technologies for effective sewage distribution systems that would enhance the productivity of the marsh without overloading it's capacity, or endangering public health.

A mass transport model, based on the model proposed here, could also be used to help study poorly understood physical, chemical, and biological aspects of marsh ecology, such as the circulation paterns of crucial nutrients. A somewhat more immediate application of the model presented in this report, relating to the ecology of marsh systems, concerns the idea that the turbulence levels in the microenvironment of aquatic plants will largely control the rates of various processes essential to the plant's growth. Use of the model to determine the

vegetation density providing the maximum turbulent levels, and comparison of the resulting (a) values with those observed in nature would help to quantify the importance of turbulence in determining the optimum plant density.

REFERENCES

Anderson, S.M., and A.C. Charters, 1982. A fluid dynamics study of seawater flow through Galadium nudifrons. Limnol. Oceanogr. 27:399-412.

Brutsaert, W.H., 1982. Evaporation into the atmosphere; theory, history, and applications. D. Reidel Company, Boston, 299 pages.

Chou, P.Y, 1945. On the velocity correlations and the solution of the equations of turbulent fluctuation. Quart. Appl. Math., 3:38.

Cionco, R.M., 1965. A mathematical model for airflow in a vegetative canopy. J. Appl. Meteorol., 4:517-522.

Cionco, R.M., 1972. A wind-profile index for canopy flow. Boundary Layer Meteorology, 3:255-263.

Cowan, I.R., 1968. Mass, heat and momentum exchange between stands of plants and their atmospheric environment. Quart. J. Roy. Meteorol. Soc., 94:318-332.

Daily, J.W., and D.R.F. Harleman, 1966. Fluid Dynamics. Addison-Wesley, Reading, MA, 454 pages.

den Hartog, G., and R.H. Shaw, 1975. A field study of atmospheric exchange processes within a vegetative canopy. In D.A. deVries and N.H. Afgan, eds., Heat and Mass Transfer in the Biosphere. John Wiley and Sons.

Emmons, H.W., 1954. Shear flow turbulence. Proc. 2nd U.S. Congress of Applied Mechanics, ASME.

Fischer, H.B., E.J. List, R.C.Y. Koh, J. Imberger, N.H. Brooks, 1979. Mixing in inland and coastal waters. Academic Press, New York, 483 pages.

Geiger, R., 1950. The Climate Near the Ground. Harvard University Press, Cambridge, MA.

Gerard, V., and K.H. Mann, 1979. Growth and production of Laminaria longicuris populations exposed to different intensities of water movement. J. Phycol. 15:33-41.

Gosman, A.D., E.E. Khalil, and J.H. Whitelaw, 1979. The calculation of two-dimensional recirculating flows. Turbulent Shear Flows I, Springer Verlag, Heidelberg.

Hanjalic, K., 1970. Two-dimensional asymmetric turbulent flow in ducts. Ph.D. Thesis, University of London.

Hanjalic, K., and B.E. Launder, 1972. A Reynold's stress model of turbulence and it's application to asymmetric shear flows. J. Fluid Mechanics, 52:609.

Harlow, P.H., and P.I. Nakayams, 1968. Transport of turbulence energy decay rate. Los Alamos Sci. Lab. Univ. California Rep La-3854.

Henderson, F.M., 1966. Open Channel Flow. MacMillan Publishing Co., New York, 522 pages.

Hinze, J.O., Turbulence, McGraw-Hill, New York, 790 pages.

Inoue, E., 1963. On the turbulent structure of airflow within crop canopies. J. Meteorol. Soc. (Jpn). 41:317-326.

Jones, W.P., and B.E. Launder, 1972. The prediction of laminarisation with a 2-equation model of turbulence. Int. J. Heat Mass Transfer, 15:301-313.

Jones, W.P., and B.E. Launder, 1973. The calculation of low-reynold's number phenomena with a two-equation model of turbulence. J. of Heat Mass Transfer, 16:1119-1130.

Kouwen, N., T.E. Unny, and H.M. Hill, 1969. Flow retardance in vegetated channels, J. of the Irrigation and Drainage Div., ASCE, Proc. Paper 6633, 95(IR2):329-324.

Kondo, J., and S. Akeshi, 1976. Numerical studies of the two-dimensional flow in horizontally homogeneous canopy layers. Boundry Layer Meteorology, 10:255-272.

Landsberg, J.J., and A.S. Thom, 1971. Aerodynamic properties of a plant of complex structure. Quarterly Journal of the Royan Meteorological Society. 97:565-570.

Launder, B.E., 1975. On modelling role of pressure fluctuations in turbulent shear flows. Imperial College, Mechanical Engineering Department Rep.

Launder, B.E., 1976. Progress in the modeling of Turbulent Transport. McGill University. Notes of a short course given at McGil University.

Launder, B.E., and D.B. Spalding, 1974. The numericl computation of turbulent flows. Computer Methods in Applied Mechanics and Engineering, pages 269-289.

Launder, B.E., and B.I. Sharma, 1974. Application of the energy-dissipation model of turbulence to flow near a spinning disc. Letters in Heat and Mass Transfer, 2.

Leendertse, J.J., 1970. A water quality simulation model for well-mixed estuaries and coastal seas. Vol. 1. Principles of computations. Rand Corporation RM-6230-RD.

Lemon, E., L.H. Allen, and L. Mueller, 1970. Carbon dioxide exchange of a tropical rain forest, Part II. Bioscience, 20:1054-1059.

Lewellen, W.S., and Y.P. Sheng, 1980. Modeling of dry deposition of SO_2 and sulfate aerosols. Aeronautic Research Associates of Princeton, Inc., Princeton, N.J.

Monin, A.S., and A.M. Yaglom, 1971. Statistical Fluid Mechanics, MIT Press, Cambridge, MA, 768 pages.

Nagakawa, H., I. Nexu, H. Ued and H. Ueda, 1975. Turbulence in open channel flow over smooth and rough beds. Proc. of Jap. Soc. Civ. Eng., 241:155-168.

Nixon, S.W., 1980. Between coastal marshes and coastal waters - a review of twenty years of speculation andn research on the role of salt marshes in estuarine productivity and water chemistry. In P. Hamilton and K. MacDonald, eds., Estuarine and Wetland Processes - with an Emphasis on Modeling. Plenum Press, New York.

Oliver, H.R., 1971. Wind profiles in and above a forest canopy. Quart. J.R. Met. Soc. 97:548-553.

Oliver, H.R., 1975., Ventilation in a forest. Agric. Meteorol., 14:347-355.

Patankar, S.V., 1980. Numerical Heat Transfer and Fluid Flow. Hemisphere Publishing Corporation, New York, 197 pages.

Plate, E.J., and A.A. Quraishi, 1965. Modeling of velocity distributions inside and above tall crops. J. Appl. Meteorology, 4:400-406.

Raymer, W.G., 1962. Wind resistance of conifers. NPL Aero. Rep. No. 1,008, 5 pages.

Ree, W.O., 1958. Retardation coefficients for row crops in diversion terraces. Transactions of the American Society of Agricultural Engineers 1:78-80.

Ree, W.O., and V.J. Palmer, 1945. Flow of water in channels protected by vegetative linings. U.S. Dept. of Agriculture, 115 pages.

Ree, W.O., and F.R. Crow, 1977. Friction factors for vegetated waterways of small slope. U.S. Dept. of Agriculture, ARS-S-151.

Reid, R.O., and R.E. Whitaker, 1976. Wind-driven flow of water influenced by a canopy. Journal of the Waterways, Harbors and Coastala Engineering Division, ASCE, Proc. Paper 11926(WWI):61-77.

Robertson, J.M., 1959. On turbulent plane-covette flow. Proceedings, 6th Midwestern Conference on Fluid Mechanics, University of Texas.

Rodi, W., 1975. A note on the empirical constant in the Kolmogorov-Prandtl eddy-viscosity expression, J. of Fluids Engg., Trans. ASME, 386-389.

Rodi, W., 1976. A new algebraic relation for calculating the Reynolds stresses, ZAMM 56, T219-1221.

Rodi, W., 1980. Turbulence models and their application on hydraulics. Institut fur Hydromechanik and Sonderforschungsbereich, University of Karlsruhe, Karlsruhe, Federal Republic of Germany, 103 pages.

Rodi, W., 1981. Turbulence models and their application in hydraulics. Institut fur Hydromechanik and Sonderforschungsbereich 80, University of Karlsruhe, Karlsruhe, Federal Republic of Germany, 103 pages.

Schaefer, M., and K. Stolzenbach, 1982. A photographic technique for the measurement of vegetation density. In preparation.

Schlichting, H., 1968. Boundary-layer Theory. McGraw-Hill, New York, 745 pages.

Seginer, I., 1974. Aerodynamic roughness of vegetated surfaces. Boundary Layer Meteorology 5:383-393.

Seginer, I., P.J. Mulhaern, E.F. Bradley and J.J. Finnegan, 1976. Turbulent flow in a model plant canopy. Boundary Layer Meteorology, 10:423-453.

Shaw, R.H., 1977. Secondary wind speed maxima inside plant canopies. J. Appl. Meteorol., 16:514-521.

Shaw, R.H., G. den Hartog, K.M. King, and G.W. Thurtell, 1974. Measurements of mean wind flow and three-dimensional turbulence intensity within a mature corn crop. Agric. Meteorology, 13:419-425.

Steever, E.Z., R.S. Warren, and W.A. Niering, 1976. Tidal energy subsidy and standing crop production of Spartina alterniflora. Est. Coast. Mar. Sci., 4:473-478.

Stephenson, P.L., 1976. Theoretical study of heat transfer in two-dimensional turbulent flow in a circular pipe and between parallel and diverging plates. Int. J. Heat Mass Transfer, 19:413-423.

Stewart, J.B., and A.S. Thom, 1973. Energy budgets in pine forests. Quart. J. Roy. Meteorol. Soc., 99:154-170.

Tennekes, H., and J.L. Lumley, 1972. A First Course in Turbulence. MIT Press, Cambridge, MA, 300 pages.

Thom, A.S., 1968. The exchange of momentum, mass, and heat between an artificial leaf and the airflow in a wind-tunnel. Quarterly Journal of the Royal Meteorological Society, 94:44-55.

Thom, A.S., 1971. Momentum absorption by vegetation. Quart. J. Royal Met. Soc. 97:414-428.

Thom, A.S., and M.R. Raupach, 1981. Turbulence in and above plant canopies, Annual Review of Fluid Mechanics, 13:97-129.

Topping, J., 1972. Errors of Observation and their Measurement. John Wiley and Sons, New York.

Turner, A.B., 1971. Local heat transfer measurements on a gas turbine in blade. J. Mech. Eng., 13.

Valiela, I., J.M. Teal, and W. Sass, 1973. Nutrient retention in salt marsh plots experimentally fertilized with sewage sludge. Est. Coast. Mar. Sci. 1:262-269.

Valiela, I., J.M. Teal, S. Volkmann, D. Shafer, and E.J. Carpenter, 1978. Nutrient and particulate fluxes in a salt marsh ecosystem: Tidal exchange and inputs by precipitation and groundwater. Limnol. Oceanogr. 23(4):798-812.

Wang, S.Y., C.A. Brebbia, C.V. Alonso, W.G. Gray, and G.F. Pinder, 1980. Finite Elements in Water Resources. School of Engineering, The University of Mississippi, Mississippi, U.S.A.

Wilson, N.R., and R.H. Shaw, 1977. A higher order closure model for canopy flow. J. Applied Meteorol., 16:1197-1205.

Windon, H.L., 1975. Heavy metal fluxes through salt marsh estuaries. In Estuarine Research, L.E. Cronin, ed., 1:137-152. Academic Press, New York.

Woodwell, G.M., and D.E. Whitney, 1977. Flax pond ecosystem study: exchanges of phospherous between a salt marsh and the coastal waters of Long Island Sound. Mar. Bio., 41:1-6.

Wu, J., 1969. Wind stress and surface roughness at air-sea interface. J. Geophys. Res., 74:449.